# Highly charged dendritic polyelectrolytes: Competitive ion binding and charge renormalization

## Dissertation

zur Erlangung des akademischen Grades

DOCTOR RERUM NATURALIUM

(Dr. rer. nat.)

im Fach Physik

eingereicht an der

Mathematisch-Naturwissenschaftlichen Fakultät

der Humboldt-Universität zu Berlin

von

**Herrn M.Tech. Rohit Nikam**

Präsident der Humboldt-Universität zu Berlin

Prof. Dr.-Ing. Dr. Sabine Kunst

Dekan der Mathematisch-Naturwissenschaftlichen Fakultät

Prof. Dr. Elmar Kulke

Gutachter: 1. Prof. Dr. Joachim Dzubiella

     2. Prof. Dr. Roland Netz

     3. Dr. Stefan Kirstein

Tag der mündlichen Prüfung: 15.12.2020

# List of publications

Chapter 4 [I, IV], chapter 5 [II] and chapter 6 [III] in this thesis contain work from the following original papers published in peer-reviewed journals:

[I]   R. Nikam, X. Xu, M. Ballauff, M. Kanduč, and J. Dzubiella. "Charge and Hydration Structure of Dendritic Polyelectrolytes: Molecular Simulations of Polyglycerol Sulphate". *Soft Matter* 14.21 (2018), pp. 4300–4310.

[II]  R. Nikam, X. Xu, M. Kanduč, and J. Dzubiella. "Competitive sorption of monovalent and divalent ions by highly charged globular macromolecules". *J. Chem. Phys.* 153.4 (2020), p. 044904.

[III] J. Walkowiak, R. Nikam, J. Dzubiella, and M. Ballauff. "Competitive Sorption of $Mg^{2+}$ and $Na^+$ Ions on Dendritic Polyglycerol Sulphate (dPGS)" (2020). *Manuscript in preparation.*

[IV]  X. Xu, Q. Ran, P. Dey, R. Nikam, R. Haag, M. Ballauff, and J. Dzubiella. "Counterion-Release Entropy Governs the Inhibition of Serum Proteins by Polyelectrolyte Drugs". *Biomacromolecules* 19.12 (2018), pp. 409–416.

Not included in this thesis are:

[V]   S. W. Coles, C. Park, R. Nikam, M. Kanduč, J. Dzubiella, and B. Rotenberg. "Correlation Length in Concentrated Electrolytes: Insights from All-Atom Molecular Dynamics Simulations". *J. Phys. Chem. B* 124.9 (2020), pp. 1778–1786.

# Statement of author's contribution

Some parts of the dissertation are contributed to by other authors, as the publications the thesis is based on are joint works and collaborations. I hereby identify my and the other author's contributions.

1. The entire research presented in this thesis and in publications [I, II, III] has been conducted under the supervision of Prof. Dr. J. Dzubiella. The research presented in the manuscript [III] has been conducted under the joint supervision of Prof. Dzubiella and Prof. Dr. M. Ballauff.

2. All classical atomistic molecular simulations, the related data analysis and evaluations have been performed by myself. All the theoretical modelling has been performed by myself with the direction provided by Prof. Dzubiella. I have contributed the most to the discussions.

3. Chapter 4 of the thesis is based on the publication [I]. All co-authors have contributed to the discussion of publication [I].

4. Chapter 5 of the thesis is based on the manuscript [II], which has been submitted for publication. Dr. X. Xu has performed the coarse-grained simulations. All co-authors have contributed to the discussion of the manuscript [II].

5. Chapter 6 of the thesis is based on the manuscript [III]. Isothermal titration calorimetry was performed by J. Walkowiak and supervised by Prof. Dr. M. Ballauff. The manuscript for this work is currently in preparation and will be finished shortly after the submission of this dissertation. All co-authors have contributed to the discussion of the manuscript [III].

## Abstract

Polyelectrolytes (PEs) represent a broad and interesting class of materials that are getting an increasing attention in the scientific community. Quintessential roles of PEs range from the information encapsulators (DNA, RNA) to the architects of cellular life (proteins) in biological world and from the superabsorbers to the drug delivery agents in the artificial world. However, despite extensive theoretical and experimental research, the understanding of PE solutions has been relatively poor compared to their neutral counterparts. The main difficulty in their theoretical treatment arises from the long-range nature of electrostatic interactions between the charged groups and ions, which becomes more prominent issue for highly charged PEs, and puts forth challenges towards the theoretical rationalization of the subsequent counterion condensation and charge renormalization. Moreover, the counter-intuitive footprint of PE–water thermodynamics, and the simultaneous presence of the divalent and the monovalent counterions in the solution, as is reminiscent of many biological environments, escalates the complexity and richness of the problem. This affects the subsequent complexations of the PE with other biologically relevant molecules such as proteins, and thus the functions, applications of such complexes in biomedicine and biotechnology.

In this thesis, we conducted a comprehensive analysis of the charge and hydration structure of dendritic PEs in a monovalent salt using all-atom explicit-water molecular dynamics (MD) computer simulations and semi-analytical theoretical approaches, and investigated a competitive sorption of mono- versus divalent ions on globular PEs using mean-field theoretical models, all-atom and coarse-grained (CG) simulations and calorimetry experiments. Atomic specificity and explicit treatment of water in MD simulations allows us to characterize the PE by calculating molecular distributions and to rationalize the energetics of PE–water interaction. In particular, owing to the charged renormalization of the PE induced by condensed counterions, we address the challenges of how to obtain a well-defined effective charge and surface potential of the PE for practical applications using the implicit- and explicit-solvent approaches. We present a novel two-state binding model as an extension of one component conventional Langmuir binding model, to study the competitive ion sorption, ensuring a meaningful comparison between theory, simulations and experiments.

This thesis lays out a systematic methodological demonstration of the PE electrostatic characterization, explores PE–water thermodynamic signature, and shows a comprehensive analysis of the competitive binding of divalent and monovalent counterions on the PE. The theoretical and simulation analysis provides a deeper insight into the physicochemi-

cal aspects of PE–counterion and PE–water interactions on the atomistic and mesoscopic level, which has a potential to contribute in propelling a new perspective for the rational design of PEs on a targeted application basis.

**Keywords**: Dendritic polyelectrolytes, Counterion condensation, Charge renormalization, Competitive ion sorption, Effective charge, All-atom simulations, Hydration

## Zusammenfassung

Polyelektrolyte (PEs) bilden eine große und wichtige Klasse von Materialien, die in der wissenschaftlichen Forschung immer mehr Beachtung findet. PEs haben wichtige Aufgaben sowohl in der biologischen Welt, z.B. bei der Informationskapselung (DNA, RNA) oder beim Aufbau des zellulären Lebens (Proteine), als auch in der künstlichen Welt wie bei Superabsorbern oder medizinischen Wirkstoffen. Trotz umfangreicher theoretischer und experimenteller Untersuchungen sind PE-Lösungen im Vergleich zu ihren neutralen Gegenstücken noch relativ schlecht verstanden.

Die größte Schwierigkeit bei ihrer theoretischen Beschreibung ergibt sich aus der langen Reichweite der elektrostatischen Wechselwirkungen zwischen den geladenen Gruppen und den Ionen, was besonders für stark geladene PEs zum Problem werden kann und die theoretische Behandlung der anschließenden Kondensation und Renormalisierung der Gegenionen erschwert. Die Komplexität des Problems wird noch zusätzlich durch die gleichzeitige Anwesenheit monovalenter und divalenter Gegenionen in der Lösung, was vielen biologische Umgebungen entspricht, erhöht. Dies beeinflusst die Komplexierungen der PEs mit anderen Biomolekülen wie z.B. Proteinen und damit die Funktionen und Anwendungen solcher Komplexe in der Biomedizin und Biotechnologie.

In dieser Arbeit führen wir eine umfassende Analyse der Ladungs- und Hydratationsstruktur von dendritischen PEs in einem monovalenten Salz unter Verwendung von atomistischen Moleklardynamik (MD) Computersimulationen mit explizitem Wasser durch. Die atomistische Auflösung und die explizite Behandlung des Wassers ermöglichen es, die PEs anhand von Molekülverteilungen und PE-Wasser-Wechselwirkung zu charakterisieren. Insbesondere aufgrund der durch kondensierte Gegenionen induzierten Ladungsrenormalisierung der PEs befassen wir uns mit der Frage, wie eine genau definierte effektive Ladung und ein genau definiertes Oberflächenpotential der PEs für praktische Anwendungen unter Verwendung von impliziten und expliziten Lösungsmittelansätzen bestimmt werden können. Darüber hinaus untersuchen und klären wir die Physik hinter der kompetitiven Adsorption der monovalenten und divalenten Gegenionen am PE mit Hilfe theoretischer Mean-Field-Modelle, vergröberter und atomistischer (expliziter) Wasser-Simulationen und Kalorimetrie-Experimenten. Wir präsentieren ein kompetitives Zwei-Zustands-Bindungsmodell als Erweiterung des konventionellen einkomponentigen Langmuir-Bindungsmodells, das einen aussagekräftigen Vergleich zwischen Theorie, Simulationen und Experimenten gewährleistet.

Diese Arbeit stellt eine systematische methodische Demonstration der elektrostatischen Beschreibung von PE vor, untersucht die thermodynamische PE-Wasser Signatur

und analysiert die kompetitiven Bindung von monovalenten und divalenten Gegenionen an PEs. Die theoretische Analyse in dieser Arbeit bietet einen tieferen Einblick in die physikalisch-chemischen Aspekte von PE-Gegenion- und PE-Wasser-Wechselwirkungen auf atomistischer und mesoskopischer Ebene. Hiermit eröffnen wir neue Perspektiven für das rationale Design von PEs für spezifische Anwendungen.

**Stichwörter**: Dendritischen polyelektrolyte, Gegenionskondensation, Effektive Ladung, Ladungsrenormierung, Kompetitiven Adsorption, Atomistischen Simulationen, Hydration

# Contents

# 1  Introduction

Polyelectrolytes (PEs) have been principle components responsible for the conception of life forms on earth. Majority of naturally occurring polymers ranging from the information-encapsulating polymers such as DNA, RNA to the multi-functional polypeptide chain linked protein molecules and glycosidic chain linked polysaccharides, that constitute the design of organisms and their functions, are highly charged PEs. The existence of these types of polymers originates from billions of years ago. In spite of the modest performance in comparison to such naturally occurring highly charged PEs, human species have achieved spectacular advancements in manufacturing the PE-based systems, with technologically pertinent properties. Owing to the polymer science and technology, there has been a revolution in the design, fabrication and processing of modern PEs, which form the integral part of everyday life [1]. A plethora of artificially synthesized macromolecules such as poly(styrene sulphonate) (PSS) and polyacrylic acid (PAA) are a part of highly charged PEs. The industrial applications of these PEs range from colloidal stabilization, flocculation, flow modification to super-absorbent gels (diapers being a prominent example), leak protection, viscosity modification, etc. [2, 3]. Newer PEs with diverse functionalities continue to emerge from the laboratories, helping towards the enhancement of human health care and the sustainability of the planet, thereby paving the way our civilization is being driven.

In spite of such advancements, there is a lack of full understanding of the PE behaviour. Due to the overwhelming number of non-linearly coupled variables controlling the PE phenomena, a theoretical description of PEs is one of the demanding tasks today, in both the artificial and biological realms. The major actively interacting forces in a system of PE solutions are evident also in a system of a single isolated PE molecule. Such systems are furnished with long-range electrostatic forces (as a result of the charged groups on the PE molecule, counterions and salt ions), dipolar interactions and hydrogen-bonding (water), van der Waals interactions associated with the excluded volume effects, and the chemical covalent bonds connecting the PE atoms together. The system endowed with the richness and combination of such effects has a potential to exhibit wealth of functionalities.

The systems of PEs with ionic salts in polar solvents such as water, are important and ubiquitous in biological as well as synthetic world [1, 2, 4, 5, 6, 7, 8]. The long-range electrostatic interactions regulated by free ions and water in such environments play a dominant role in shaping the structural and electrostatic characteristics of the PE, and

the subsequent function of the system [1, 2, 4]. Such interactions are also prominent in a general PE–ligand complexation processes, such as protein–ligand interactions. Although the net protein–ligand interaction is complex, the often highly protonated state of the protein molecule and the multivalent electrostatic charge on the ligand are responsible for leading contribution of electrostatics in the overall interaction. As another example, the protein–DNA interaction directing the genome information storage, is significantly contributed by electrostatics [9], since the interaction sites on the protein are primarily composed of charged patches [10]. Other preliminary examples include the interaction of antibody–antigen, enzyme–inhibitor, potassium channel–peptide inhibitor and so forth [11, 12]. These phenomena, apart from the ligand–substrate charge–charge interactions, are also the result of hydrogen bonding, salt bridges and metal interactions [13].

The electrostatic attraction between the isolated PE molecule and the oppositely charged counterions in the solution, leads to the counterion condensation on the molecule, thereby significantly modifying its interaction with other charged molecules (*e.g.* proteins, DNA, etc.) and its electric properties such as electrophoric mobility in external electric field [1, 6, 8]. Therefore, understanding the counterion condensation is of utmost importance in order to understand the properties of PEs and their implications in biological and artificial environments [1, 14]. The basic idea is that a highly charged object exerts such a long-range attraction onto its counterions that a proportion gets enacted upon a high electrostatic coupling with the object, thereby condensing onto the surface and effectively neutralizing an equivalent amount of the structural charge $Z_d$ [15, 16]. The charged substrate plus its confined counterions, may be considered as a single entity with an effective (or renormalized) charge $Z_{eff}$, which is significantly lower than the bare structural charge $Z_d$. We then identify the difference $Z_d - Z_{eff}$ as the amount of counterions "condensed" onto the surface [17].

The phenomenon of counterion condensation and the effect of ionic strength on the configurational properties of different types of PE molecules such as chains [7, 8, 14, 18, 19, 20, 21, 22, 23], brushes [24, 25, 26, 27, 28] and PE nanogels [29, 30, 31] have been studied extensively in the past. Through the knowledge of the distribution of the salt ions around the PE, *e.g.*, measured in terms of the radial distribution function in simulations and experiments, important properties such as charge–charge correlation, osmotic compressibility and shear viscosity of the system can be derived [32]. Muthukumar, in his extensive and comprehensive review of the experimental, theoretical and simulation based research done on PE chains, described the effect of salt concentration, valency of counterions, chain length and PE concentration on the counterion condensation [4, 33]. Besides

the properties of a single isolated PE molecule, the ionic strength of the solution also influences the interaction of PEs with other entities, such as adsorption on substrates [34, 35, 36, 37, 38, 39], formation of ultra-thin PE multilayer membranes [40, 41, 42, 43, 44], structure and solubility of PE complexes [45, 46, 47, 48, 49] or coacervates [50, 51, 52, 53].

As an emerging class of functional PEs, PE nanogels [29, 30, 31] and dendritic or hyperbranched PEs [54, 55, 56, 57, 58] have attracted considerable interest in the scientific community in the last years due to their multifaceted bioapplications, such as biological imaging, drug delivery and tissue engineering [59, 60, 61]. Dendritic PEs (charged dendrimers), are known as a group of synthetic macromolecules with a globular hyperbranched (tree-like) topology emerging from the central core. The overall size, the total number of branching chemical units and the total number of charged groups on the dendrimer are associated with its generation index. The higher the generation of the dendrimer, the higher is its size, total number of branching units it comprises of, etc. As an example, a generation zero dendrimer contains a multi-functional core connected to one layer of dendritic branching units via chemical bonds. The higher generations are then structured by creation of successive layers by iterative addition of branching units to those of the layer underneath [12] *cf.* Fig. 1.1(a). The dendrimers possessing irregularities in the structure in terms of linear defects are termed as hyperbranched dendrimers. Nevertheless, dendrimers in general can be synthesized on a kilogram scale and in a large range of molecular weights, which is aided by their homogeneous structure. The multi-functional groups on dendrimers, which are exemplified by the terminal segments predominantly drive the dendrimer properties. The dendrimer becomes a PE soluble in a polar solvent, if the terminal groups can be dissociated to acidic/basic forms.

Owing to the unique topological features, dendrimers facilitate a range of applications. Polyamidoamine (PAMAM) is the very first synthesized and now commercialized charged dendrimer [12, 63]. They are the most studied dendrimer PEs for drug delivery applications [64]. Cationic PAMAM, which contains primary amine groups, undergoes electrostatic complexation with naturally occurring PEs such as DNA, siRNA and proteins [65]. In particular, due to the excellent DNA complex forming ability of the PAMAM dendrimers, they are widely used as commercial DNA transfection kits [66]. The complexation with the dendrimer PEs is not always biocompatible. PAMAM dendrimers at low pH conditions possess cationic amine groups and as a result, are generally haemolytic and cytotoxic [67]. As an example, erythrocyte membrane protein molecules, upon the interaction with PAMAM dendrimers (2nd, 3rd and 4th generations) undergo a change

3

**(a)**



**(b)**     **PETIM**
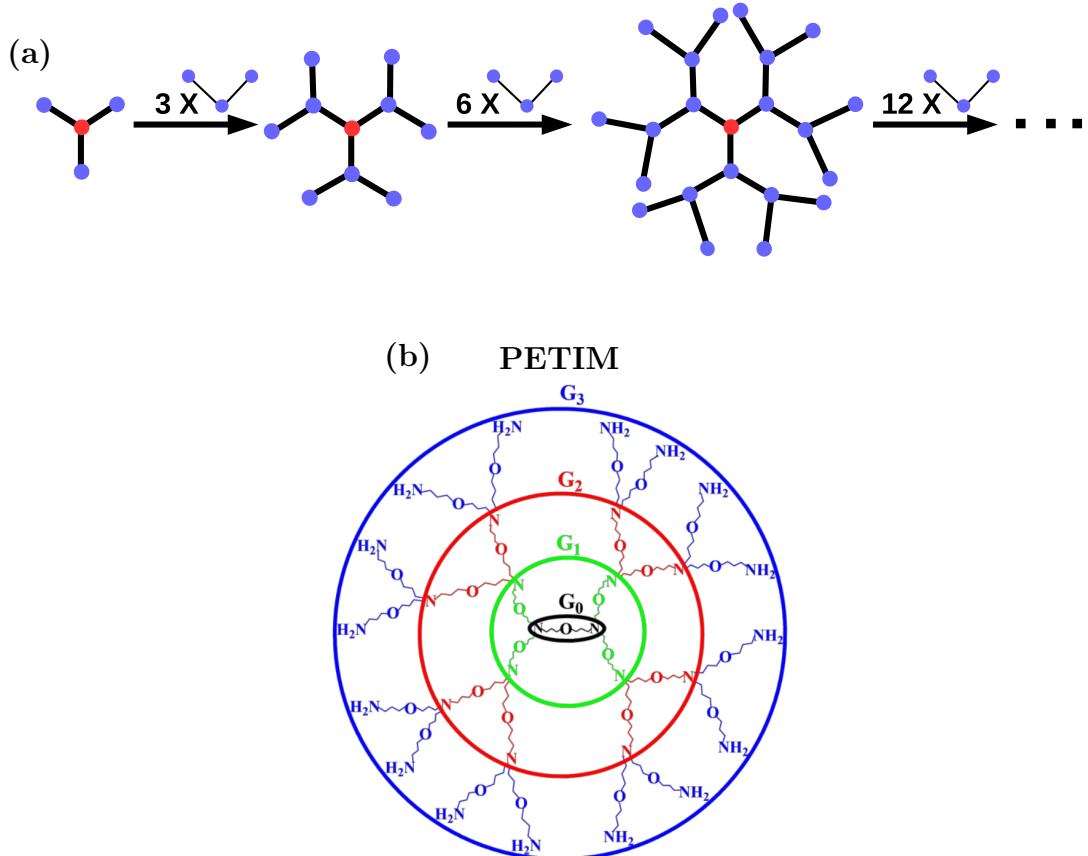


Figure 1.1: (a) Schematic process of the growth of the dendritic structure in terms of generation. The red and blue spheres indicate the core group of atoms and the branching chemical unit respectively. (b) Chemical structure of different generations of poly(propyl ether imine) (PETIM) dendrimer [62]. Adapted with permission from Kanchi et al. Copyright © 2015 American Chemical Society.

in confirmation. Such biologically relevant issues have largely been unexplained in detail. Compared to PAMAM, dendrimer PEs with lower cytotoxicity, called Poly(propyl ether imine) (PETIM) dendrimers with oxygen or nitrogen cores have emerged as a new subclass of dendrimer since past two decades *cf.* Fig. 1.1(b) [62]. Another unique structural feature of dendrimers is the presence of internal cavities, as a result of which, charged dendrimers with the aid of electrostatic complexation, can successfully encapsulate other charged molecules. This gives charged dendrimers an excellent basis to act as a drug delivery platforms. The capture and release of drug molecules from charged dendrimers can be controlled by studying their structural characteristics in detail. It has been found that the spatial structure of charged dendrimers is sensitive to the solution ionic strength, temperature and pH of the solution [60, 68, 69].

The important applications of dendritic macromolecules in general have initiated substantial efforts towards their detailed molecular-level characterization by theory and computer simulations [60, 61]. A large number of fully atomistic computer simulations, for example, of PAMAM-based dendrimers have been performed [70, 71, 72, 73, 74, 75, 76], some of them with particular focus on solvent effects and structural features [77, 78, 79, 80, 81, 82, 83, 84]. On the other hand, to overcome the limitation of the system size of atomistic simulations, coarse-grained (CG) monomer-resolved models which contain various levels of specific chemical features have led to plentiful structural insight on larger scales [85, 86, 87, 88, 89, 90, 91, 92, 93, 94, 95, 96, 97, 98, 99, 100, 101, 102, 103, 104, 105, 106, 107, 108, 109, 110].

One of the notable dendrimer PE species of vital importance are the hyperbranched or dendritic polyglycerol sulphates (hPGS or dPGS), which are found to possess strong anti-inflammatory properties [57, 58], can act as a transport vehicle for drugs towards tumor cells [56, 111, 112], and can also be used as an imaging agent for the diagnosis of rheumatoid arthritis [112]. Fig. 1.2(a) shows the chemical structure of $G_1$-dPGS. As shown, dPGS comprises of a carbon core, glycerol group ($C_3H_5O-$) as a branching unit and sulphate ($-OSO_3$) as the terminal monovalent negatively charged groups. dPGS generations 0 to 3 are shown in Fig. 1.2(b), indicating spherically symmetric structural growth of the scaffold. The anti-inflammatory properties of dPGS are attributed to its strong binding affinity with the cell adhesion molecules such as L- and P-selectin proteins situated at the endothelial cells, which diminishes the inflammatory response and reduces the leukocyte extravasation associated with acute and chronic inflammatory diseases [113]. Another way the dPGS fights against inflammation is by acting as a drug delivery agent. As an example, dPGS offers a delivery platform for the anticancer, tubulin-binding drug
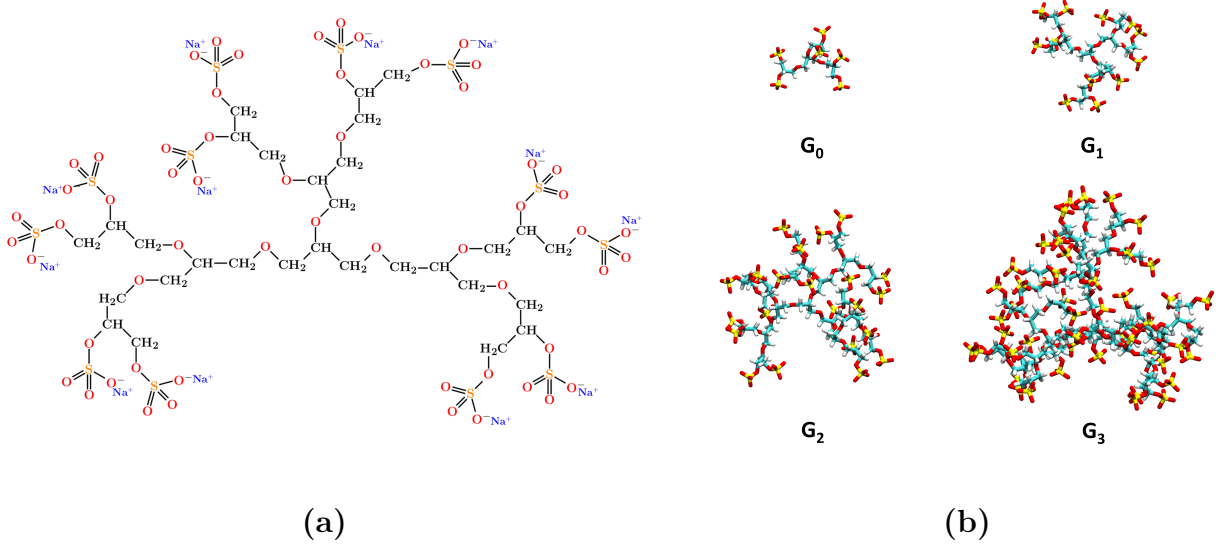
Figure 1.2: (a) Illustration of the dendritic PGS (dPGS) with an example of the chemical structure of $G_1$-dPGS along with counterions ($Na^+$) of the respective sulphate groups. (b) Simulation snapshots of dPGS from generations 0 to 3 [I].

Paclitaxel (PTX) with a linear, non saturable uptake kinetics in tumor cells [111]. This wide variety of applications, thus, have proven dPGS to be a high potential candidate for the use in medical treatments [55]. Hence, the understanding of dPGS interaction with *in vivo* environment becomes important. The globular dendritic topology, terminated with monovalent negatively charged sulphate groups, makes dPGS an excellent representative model in the class of highly charged globular PEs [114, I], and thus in this dissertation, dPGS fulfills such role.

For the case of (internally or surface) charged globular dendrimers such as dPGS, one important focus in the literature has been set on the dominant role of condensed counterions (as introduced earlier) and the charge renormalization [15, 16, 17, 115, 116, 117, 118, 119, 120, 121] in modulating the conformation and effective charge of the dendrimers [106, 107, 108, 109, 110]. Indeed, as mentioned earlier, for highly charged PEs, electrostatic effects naturally dominate the interactions with proteins and have complex dependencies on the effective size, charge, flexibility, shape and charge heterogeneity of the interaction partners [122, 123, 124, 125, 126, 127, IV]. However, a thorough understanding in this area remains a challenge, due to the long-range nature of Coulombic interactions in the dilute salt regime, where $\kappa R_m \ll 1$ ($R_m$ is the radius of the PE) ensuring that the interactions are highly non-linear [121]. Also it remains challenging to characterize the

6

open-structure nanogel particles or dendrites such dPGS, which are partially penetrable to ions and whose surface structure is not well defined, *cf.* Fig. 1.2 [128]. The resultant challenges in simulations are the integration of very heterogeneous and long-ranged charge distributions of all constituents as well as finding a reasonable or at least practical definition for the surface potential and its precise location. Therefore, despite the large body of studies on dendrimers, apart from a notable exception of the work by Maiti and Messina [76], there have hardly been any simulation studies defining and determining the effective surface potential (and its location) of charged dendrimers so far, despite its significance for the electrostatic interaction with macromolecules or the response to electric fields. Recently, Xu et al. thoroughly reconsidered and investigated the key electrostatic features of charged dendrimers, based on previous works by Alexander et al. and Belloni [15, 16], at hand of dPGS using CG computer simulations [114]. In these implicit-solvent/explicit-salt Langevin dynamics simulations, dPGS was studied up to its sixth generation, and it was argued that a systematic mapping of the long-range decay of the calculated electrostatic potentials onto the Debye–Hückel form for simple charged spheres serves as the most practical definition for their effective electrostatic properties seen in the far-field regime. This scheme is widely known as the Alexander prescription [15, 17, 129, 130], that led to the determination of well-defined effective net charges and corresponding radii, surface potentials, and surface charge densities of dPGS. The latter were found to be up to one order of magnitude smaller than the bare values, consistent with previously derived theories on charge renormalization [17, 120, 119] and weak saturation for high dendrimer generations (charges). The surface potentials of dPGS were found to agree with electrophoretic experiments, while still some tolerance in the comparison had to be imposed to leave room for the hydration effects [114]. Nonetheless, based on this criterion, a systematic electrostatic characterization of dPGS has been performed via CG [114] and all-atom (AA) [I] simulations by defining the condensed (bound) ions.

This significant charge renormalization of dPGS in presence of salt is a direct culmination of the counterion condensation, and thus governs binding mechanisms of highly charged PEs such as dPGS to proteins. It is already established that the interaction of proteins with strongly charged linear PEs is resulted due to the renormalized charge on the PE [131], where the binding of protein releases a few condensed counterions on the PE, and the charged patch on the protein takes their place while acting as a multivalent counterion for the PE [132, IV]. The other notable examples of such interactions are the binding of dPGS with proteins such as human serum albumin (HSA) which is the most abundant protein found in human blood plasma [133], lysozyme which is also available in

abundant amounts and forms a part of innate immune system in animals [134], and cell adhesion proteins such as L- and P-selectins [IV].

While the influence of a few released counterions and a subsequent entropic gain is worth noting while discussing the driving forces behind the PE complexation, it is crucial to focus on the role of water – the common environment for most biological phenomena, in this process [135, 136, 137, 138]. Before the complexation, both of the PE molecules are hydrated, stronger around the polar or charged groups. During the complexation, the water molecules engaged in hydration and the hydrogen-bonding networks around the PEs, undergo spatial and configurational rearrangements, yielding mutually compensating (and, frequently, canceling) enthalpic and entropic contributions to the free energy of binding, the phenomenon widely known as the enthalpy–entropy compensation [134, 135, 136, 137, 138, 139, 140, 141, 142, 143, 144]. This role of water can be manifested as a passive player or as a driving player in the complexation processes, and is a highly system specific issue. It depends on the specific physicochemical properties of the environment as well as on the biomolecular geometry of the binding patches. This hydration thermodynamics gives a more detailed knowledge and real perspective on the biomolecular complexation processes. However it is challenging to explore and predict from a simulation standpoint due to insufficient sampling issues and deeply coupled contributions from water and solutes [138, 139].

The aqueous PE solutions in a biological environment often consist of ions of varying charge valencies, some of which can act as counterions. PEs such as dPGS, considering the variety of their medicinal applications as mentioned earlier, interact with physiological ionic solutions. Thus, apart from monovalent counterions (*e.g.* $Na^+$, $K^+$, etc.) it is important to study their interactions with the *divalent metal cations, viz.* magnesium(II) and calcium(II) ions. $Mg^{2+}$ is essential for the stabilization of proteins, polysaccharides, lipids and DNA/RNA molecules, while $Ca^{2+}$ is critical for bone formation and plays a key role in signal transduction [145, 146]. Human serum blood contains approximately $0.75-0.95\,mM$ $Mg^{2+}$ ions, $1-4\,mM$ $Ca^{2+}$ ions and around $150\,mM$ NaCl salt in a dissociated form. [147, 148] Thus, upon the administration of dPGS into the human biological environment, it is imperative for the competitive sorption between the divalent ($Mg^{2+}/Ca^{2+}$) and monovalent ($Na^+$) counterions to establish on the dPGS molecule, which can change the effective charge, and subsequently the interaction properties of dPGS with other charged entities such as proteins. The competitive sorption here essentially refers to the divalent counterions binding to dPGS, thereby displacing the bound monovalent counterions when the divalent salt is introduced in varying amounts to the dPGS solution with a monovalent

8

salt. The basic physics behind this ion-exchange relies on the competition between the electrostatic energy gain of the sorbed ions and the translational entropy of the free ions. This microscopic mechanism has a potential to significantly alter the attributes of the complexes of dPGS with other molecules, such as the protein corona around dPGS. Proteins typically bind strongly to the macromolecular surface, thereby forming a protein 'corona', a dense shell of proteins that can entirely coat the macromolecule [149, 150, 151, 152, 153, 154, 155]. The alteration in the properties of this dPGS-protein corona complex can change the biological immune response to it, its metabolic fate, and the function of such complex in biomedical and biotechnological applications, since once the dPGS is introduced in the solution whether its *in vivo* or *in vitro*, the solution environment does not 'see' dPGS but the protein corona. The competitive ion binding can be observed in a wide variety of the biological and industrial ion-exchange processes such as the alkaline-earth/alkali-metal ion-exchange onto PEs [156], desalination of saline water to produce potable water [157], demineralization of whey, acid and alkali recovery from waste acid [158] and alkali solutions [159] by diffusion dialysis [160], etc.

The competitive sorption of the divalent and monovalent counterions on the PEs such as DNA, RNA and proteins has been studied in the past via X-ray scattering, conductometry and potentiometry experiments [156, 161, 162, 163, 164, 165], AA [166, 167] and CG simulations [8, 22, 168, 169, 170, 171]. Interactions of multivalent ions with PE solutions have also been theoretically studied in the past, using well known methods such as the Poisson–Boltzmann (PB) theory [172, 173, 174, 175, 176] and two-state models [177, 178, 179]. Since the traditional experimental techniques are unable to explore the ionic local structural details surrounding the PE, PB theory – a mean-field approximation to the spatial ionic density distribution within a continuum solvent model, has become a well known tool that estimates the ionic structure and double-layer characterization in electrochemistry, colloidal science or biological and geological physics [2, 180]. Hence, today this model has becomes a standard by which PE electrostatic interactions are treated. However, in spite of its extensive use, PB theory assumes a constant dielectric constant throughout the domain and excludes ion–ion correlation effects, thus failing to display the non-ideal microscopic picture of the system. Some of the other notable studies that apply the models other than the PB theory, focus on the investigation of the thermodynamic properties of PE systems [181], ionic and potential distributions [182], accurate calculation of the PE effective charge [183], and the effect on the interaction between PE macromolecules [184, 185, 186, 187].

In comparison, AA Molecular Dynamics (MD) simulations can serve as an "atomistic

microscope" and offer a high spatially and temporally resolved data, that cannot be accessed through experimental or theoretical means. The downside of AA simulations, however, is that in order to have an accurate representation of the ionic effects, an accurate and realistic effective, classical interaction potentials *i.e.* force-fields are needed. The challenge, in particular, is to reproduce the required fine balance between ion–ion, ion–water and water–water interactions. Especially, how to incorporate the notable contribution from the polarization effects in the conventional non-polarizable force-fields, is still an open question, which is largely relevant to the multivalent metal ions such as $Mg^{2+}$, $Ca^{2+}$, etc. Today, most of the AA MD simulations are performed using non-polarizable force-fields such as AMBER [188], CHARMM [189], GROMOS [190] and OPLS [191]. The term "non-polarizable force-fields" essentially means that these force-fields partially incorporate the effects of electronic polarization and the screening of electrostatic interactions through the effective charges on atoms and other empirical parameters [192]. Monovalent ions such as $Na^+$ or $K^+$ have been satisfactorily modeled in all of the aforementioned force-fields, in terms of predictions of binding affinities with proteins [193], salt solubilities, activity coefficients, and chemical potentials [194, 195, 196, 197, 198, 199]. However, these force-fields fail to model multivalent ions and usually overestimate ion–protein and ion–peptide interactions [200, 201]. As an example, AMBER force-field uses Joung–Cheatham [202] parameters for monovalent alkali metal ions, which are optimized based on solvation free energies, lattice energies and inter-ionic distances of alkali-halide crystals, and provide satisfactory results. However, there is a fairly common use of the Åqvist parameters [203] adopted in AMBER for divalent metal cations, even though they fail to reproduce thermodynamic or ion-specific effects at finite concentrations [204, 205, 206, 207, 208]. Especially the parametrizations for $Mg^{2+}$ and $Ca^{2+}$ ions in AMBER and CHARMM force-fields result in significant artifacts such as unphysical cluster formations with acetate, phosphate and chloride ions [208, 209]. On the other hand, due to the deficiency of accurate parametrization for multivalent ions in the literature, some focus has been directed towards correction strategies such as the implementation of polarizable force-fields [210, 211, 212], numerical scaling of ionic charges to account for electronic polarization effects (discussed in detail in Sec. 3.2.6.1) [192, 213, 214], and adjustments of ionic sizes [204, 215, 216].

# 2 Aims of the dissertation

PEs are identified not only as the molecular constituents that participate in the biological mechanisms that shape the structure and function of life forms on earth, but also as a part of the solution for modern day issues of healthcare and planet sustainability. Aqueous PE solutions with ionic salt are one of such systems most commonly found in both the biological and artificial realms. However, in order to attain a grasp on the basis of their functionalities and to replicate likewise systems for future purposes, it is important to build an understanding over the physical processes and mechanisms responsible on a molecular level, such as counterion condensation and hydration properties of the PE. In this dissertation, we aim to explore such systems with the exemplification of the PE as dendritic polyglycerol sulphate (dPGS), which has a huge potential in the medicinal field in terms of its anti-inflammatory and drug delivering properties, owing to its high charge, the unique ion-specific attributes of charged groups and the dendritic topology of the molecule. Such prospect motivates the consideration and the development of computational tools such as AA MD simulations and theoretical methods. Two major themes of the dissertation are ($i$) Employing AA, explicit water MD simulations in order to rationalize and obtain insights about the dPGS–counterion and dPGS–water interactions, and their contribution to the electrostatic properties of dPGS and the thermodynamic signature of water, respectively, and ($ii$) the theoretical rationalization of the competitive binding of mono- and divalent counterions to dPGS, with the help of mean-field continuum and discrete binding site models. The details of these research goals are as follows:

Due to the high charge valency on dPGS, when the net inter-molecular interactions are considered, electrostatics dominates over the excluded volume and other non-electrostatic contributions. However, due to the non-linear nature of electrostatics, especially in a dilute salt case which is reminiscent of the biological environments, it is challenging to electrostatically characterize PEs such as dPGS. Recently, a systematic electrostatic characterization of dPGS in terms of the determination of well-defined effective net charges and corresponding radii, surface potentials, and surface charge densities of dPGS, has been performed via CG simulations by defining the condensed (bound) ions based on the Alexander prescription and the inflection point criterion [15, 16, 114]. The latter work was based on a CG force field where the explicit action of water was neglected and the charged atoms were clumped together in beads. Then always the questions remains, how do these

results compare to fully resolved, explicit-water simulations and what are the details of the water structural effects [84]? In the **chapter 4**, we aim to address this question with a focus on electrostatic properties, and revisit the electrostatic dendrimer problem with a fully atomistic representation of dPGS of generations 0 to 3 in an explicit-water and electrolyte (NaCl) solution. The inclusion of water gives rise to larger complexity in the problem, in particular due to explicit and local screening effects, which are absent in the implicit-solvent simulations. We re-address the challenges of how to obtain a well-defined effective charge and surface potential of dPGS for practical applications and compare CG, implicit-, and explicit-solvent approaches. In addition, we seize the opportunity and take a closer look at the solvent accessible area and volume in the dendritic interior as well as the thermodynamics of water insertion into the dPGS environment [78, 137, 138]. Water insertion and release into and from the penetrable dendrimer may lead to significant contributions in the thermodynamic signatures of binding of the dendrimers to proteins [133].

As described earlier, dPGS, owing to its effective use in the medicinal treatments, often comes in contact with *in vivo* aqueous biological environments such as intra- or extracellular fluids, or human blood serum, which, apart from the monovalent NaCl salt, also consist of the divalent metal cations *viz.* $Mg^{2+}$ and $Ca^{2+}$ that can act as counterions to dPGS. Therefore, considering its significance in the medicinal and pharmaceutical field, in order to mimic the physiological ionic environment, we aim to study this crucial interaction of dPGS with divalent cations, in the presence of monovalent salt, which results in the competitive sorption of mono- and divalent ions on dPGS. In the **chapter 4**, we deploy AA MD simulations to study this phenomenon. The challenge for AA MD simulations, however, is that the nature of inter-molecular interaction is highly sensitive to the choice of the force-field employed. In particular, the parametrizations for divalent ions according to the well-known non-polarizable force-fields fail in terms of incorporating the notable contribution from their polarization effects. We aim to demonstrate the developments in the parametrizations for divalent ions by comparing the quantitative performances of force-fields optimized according to several latest works [191, 201, 208, 217, 218]. These performances are quantified in terms of the ionic distributions and the distance-resolved electrostatic potential profiles around dPGS.

While the AA simulations are able to provide useful physical insights on an atomistic scale, it is important to interpret the culminations of these results on a mesoscale correctly with the help of a suitable binding model. In the **chapter 5**, we thus aim to theoretically analyze the competitive sorption of mono- and divalent ions on dPGS with the help

of mean field continuum and discrete binding site models, inform these models via the coarse-grained computer simulation data, and use the models to predict the competitive ion sorption for different salt concentrations and PEs of different sizes. We then aim to utilize the developed models to fit and interpret the competitive ionic sorption isotherm obtained from the isothermal titration calorimetry, in the **chapter 6**. Such knowledge can help predict the biological immune response to the PE, its metabolic fate, and the efficacy of the PE drug in different environments for biomedical and biotechnological applications.

# 3 Basic principles and methods

This chapter introduces the basic theoretical principles, simulation methods and the analytical framework needed to study the systems in chapters 4, 5, and 6. We start with the theoretical treatments in the section 3.1. The introduction to simulations, including the basics, and advanced methods are described in the section 3.2.

## 3.1 Theoretical treatment

### 3.1.1 Basic statistical mechanics

Consider a canonical system of an electroneutral medium having a dielectric constant $\varepsilon_r$, containing a molecule with a fixed charge distribution $c_f(r)e$ (where $e$ is the electronic charge) and $N$ mobile point-particles (counterions and coions) having positions $\vec{r_i}$, mass $m$, momentum $\vec{p_i}$, enclosed in a volume $V$ and at temperature $T$. The Hamiltonian $H$ of the system is then the sum of the potential energy $U$ and the kinetic energy $K$ of the system [3], *i.e.*,

$$
\begin{aligned}
H &= K(\vec{p_1}, \cdots, \vec{p_N}) + U(\vec{r_1}, \cdots, \vec{r_N}) \\
&= \sum_{i=1}^{N} \frac{|\vec{p_i}|^2}{2m} + \frac{1}{2} \sum_{i=1}^{N} \sum_{j=1, j \neq i}^{N} \frac{z_i z_j e^2}{4\pi\varepsilon_0\varepsilon_r|\vec{r_i} - \vec{r_j}|} + \sum_{i=1}^{N} z_i \int_V \frac{c_f(\vec{r})e^2}{4\pi\varepsilon_0\varepsilon_r|\vec{r_i} - \vec{r}|} \, \mathrm{d}^3r
\end{aligned}
\tag{3.1}
$$

where $\varepsilon_0$ is the permittivity of vacuum and $z_i$ is the charge valency of particle $i$. The classical analog of the canonical partition function of the system is then given by

$$
\mathcal{Z} = \frac{1}{h^{3N}N!} \int \cdots \int e^{-\beta H(\vec{r_1}, \cdots, \vec{r_N}, \vec{p_1}, \cdots, \vec{p_N})} \, \mathrm{d}^3r_1 \cdots \mathrm{d}^3r_N \, \mathrm{d}^3p_1 \cdots \mathrm{d}^3p_N = \mathcal{Z}_U \mathcal{Z}_K
\tag{3.2}
$$

where $h$ is the Planck constant and $\beta^{-1} = k_B T$ is the thermal energy. The observables – position $\vec{r}$ and momentum $\vec{p}$, commute in the partition function $\mathcal{Z}$ and hence can be factored out. Thus, $\mathcal{Z}_U = \int \cdots \int e^{-\beta U(\vec{r_1}, \cdots, \vec{r_N})} \, \mathrm{d}^3r_1 \cdots \mathrm{d}^3r_N$ is called the configurational partition function and $\mathcal{Z}_K = \frac{1}{h^{3N}N!} \int \cdots \int e^{-\beta K(\vec{p_1}, \cdots, \vec{p_N})} \, \mathrm{d}^3p_1 \cdots \mathrm{d}^3p_N$ is the momentum part of the partition function $\mathcal{Z}$, which is simply a product of $N$ identical Gaussian integrals.

The free energy of the system is given by

$$\beta \mathcal{F} = -\ln \mathcal{Z} \tag{3.3}$$

The canonical probability density for the system to be at a certain configurational state [219, 220] is then expressed as

$$\mathcal{P}_N(\vec{r_1}, \cdots, \vec{r_N}) = \frac{e^{-\beta U(\vec{r_1}, \cdots, \vec{r_N})}}{\mathcal{Z}_U} \tag{3.4}$$

### 3.1.1.1 Radial distribution function (RDF)

Based on the probability density $\mathcal{P}_N$ given as Eq. (3.4), the $N$-particle distribution function $P^{(N)}(\vec{r'}, \vec{r''}, \cdots, \vec{r^{N\prime}})$ is then given by [219, 220]

$$P^{(N)}(\vec{r'}, \vec{r''}, \cdots, \vec{r^{N\prime}}) =$$
$$\int \cdots \int \mathcal{P}_N(\vec{r_1}, \cdots, \vec{r_N}) \delta(\vec{r_1} - \vec{r'}) \delta(\vec{r_2} - \vec{r''}) \cdots \delta(\vec{r_N} - \vec{r^{N\prime}}) \, \mathrm{d}^3 r_1 \cdots \mathrm{d}^3 r_N \tag{3.5}$$

Similarly, the specific pair distribution function, *i.e.*, the probability density of simultaneously locating particle 1 at $\vec{r'}$ and particle 2 at position $\vec{r''}$ is given as [219, 220]

$$P^{(2)}(\vec{r'}, \vec{r''}) = \int \cdots \int \mathcal{P}_N(\vec{r_1}, \cdots, \vec{r_N}) \delta(\vec{r_1} - \vec{r'}) \delta(\vec{r_2} - \vec{r''}) \, \mathrm{d}^3 r_1 \cdots \mathrm{d}^3 r_N \tag{3.6}$$

The single particle distribution function $P^{(1)}(\vec{r})$ is then defined as

$$P^{(1)}(\vec{r}) = \int \cdots \int \mathcal{P}_N(\vec{r_1}, \cdots, \vec{r_N}) \delta(\vec{r_1} - \vec{r}) \, \mathrm{d}^3 r_1 \cdots \mathrm{d}^3 r_N \tag{3.7}$$

The generic pair distribution function is related to $P^{(2)}(\vec{r'}, \vec{r''})$ as

$$c_2(\vec{r'}, \vec{r''}) = N(N-1)P^{(2)}(\vec{r'}, \vec{r''}) \tag{3.8}$$

Equivalently, $P^{(1)}(\vec{r})$ is proportional to the number density (or generic singlet distribution function) $c_1(\vec{r}) = c(\vec{r})$

$$P^{(1)}(\vec{r}) = \frac{c(\vec{r})}{\int_V c(\vec{r}) \, \mathrm{d}^3 r} = \frac{c(\vec{r})}{N} \tag{3.9}$$

Under the assumption that the distance $r = \left|\vec{r'} - \vec{r''}\right|$ between two particles is very large (equivalent to the mean-field assumption), their spatial correlation becomes weak and $c_2(\vec{r'}, \vec{r''})$ becomes

$$c_2(\vec{r'}, \vec{r''}) = c_1(\vec{r'})\, c_1(\vec{r''}) = c(\vec{r'})\, c(\vec{r''}) \tag{3.10}$$

However, at a finite distance, this assumption is not valid. Hence, the generic pair distribution function (in a homogeneous system described here) can be expressed as

$$c_2(\vec{r'}, \vec{r''}) = c(\vec{r'})\, c(\vec{r''})\, g(\vec{r'}, \vec{r''}) = c^{\mathrm{b}^2}\, g(\vec{r'}, \vec{r''}) \tag{3.11}$$

where $g(\vec{r'}, \vec{r''})$ is defined as the pair correlation function which measures the extent of deviation from Eq. (3.10) [220]. The second equality in Eq. (3.11) holds in the case of a spatially homogeneous distribution of particles within the domain, where the uniform number density $c^{\mathrm{b}} = c(\vec{r'}) = c(\vec{r''})$ is the bulk particle number density in the far-field. This will be the key assumption behind all analysis methods mentioned in this work.

The function $g(\vec{r'}, \vec{r''})$ is only a function of a scalar distance $r = \left|\vec{r'} - \vec{r''}\right|$. Hence $g(\vec{r'}, \vec{r''}) = g(r)$ is defined as the *radial distribution function* (RDF) and contains all the essential information in deriving the inter-particle interactions. Another important definition related to the RDF is the Potential of Mean Force (PMF), defined as the work required to bring two selected particles from the infinite separation to the separation distance $r$. Under the assumption of the two-body interaction in a system described here, PMF is given as a Boltzmann inversion [221, 222] of $g(r)$

$$\beta V(r) = -\ln g(r) \tag{3.12}$$

### 3.1.2   Theory of electrostatic interactions

#### 3.1.2.1   Poisson–Boltzmann theory

Given the knowledge of the Hamiltonian (Eq. (3.1)), the PB equation free energy functional can now be constructed using mean-field approximations to the $N$-particle distribution function $P^{(N)}$ (Eq. (3.5)) and the method of variation in order to derive the PB equation.

In statistical mechanics, the free energy $\mathcal{F}$ of any system such as the one presented in the section 3.1.1 at an arbitrary energy state with a probability $\mathcal{P}_0$, satisfies the inequality [3]

$$\beta\mathcal{F} \leq \beta\langle H\rangle_0 - \frac{S_0}{k_{\mathrm{B}}} \tag{3.13}$$

where $\langle H\rangle_0 = \int\int \mathcal{P}_0 H\,\mathrm{d}\vec{r}\,\mathrm{d}\vec{p}$ is the average total energy and $H$ is the Hamiltonian. $S_0 = -k_{\mathrm{B}}\int \mathcal{P}_0 \ln\mathcal{P}_0\,\mathrm{d}\vec{r}$ is the system entropy at that state. Eq. (3.13) is termed in the literature as the Gibbs–Bogoliubov inequality and it serves as an effective way of deriving mean-field theories from a variational principle [223]. The equality in Eq. (3.13) is satisfied if and only if the probability of the state equals the canonical probability as expressed in Eq. (3.4). Eq. (3.5) is complicated to solve, due to the coupled (correlated) particle positions $\vec{r}_i$. The mean-field approximation eliminates these correlations between the particles and it can be done in the present context by assuming the $N$-particle distribution function $P^{(N)}(\vec{r_1}, \cdots, \vec{r_N})$ (Eq. (3.5)) as a product of $N$ single particle distribution functions $P^{(1)}(\vec{r_i})$ (Eq. (3.9))

$$P^{(N)}(\vec{r_1}, \cdots, \vec{r_N}) \xrightarrow{\text{mean-field}} P^{(1)}(\vec{r_1})\,P^{(1)}(\vec{r_2})\cdots P^{(1)}(\vec{r_N}) \tag{3.14}$$

This assumed state of the system, if used as a trial state in the Gibbs–Bogoliubov inequality (Eq. (3.13)), gives the maximum value allowed for the free energy [3, 223]. The canonical partition function $\mathcal{Z}$ can now be factorized into an ideal (purely entropic) and an excess contribution [224]. Hence, the Helmholtz free energy from Eq. (3.3) can be rewritten as

$$\mathcal{F}_{\mathrm{PB}} = \mathcal{F}_{\mathrm{id}} + \mathcal{F}_{\mathrm{ex}} \tag{3.15}$$

where $\mathcal{F}_{\mathrm{PB}}$ is the PB approximation of the Helmholtz free energy $\mathcal{F}$. Eq. (3.13) along with the above conditions gives the upper limit for the free energy as

$$\beta\mathcal{F} \leq \beta\mathcal{F}_{\mathrm{PB}}\left[c(\vec{r})\right] \tag{3.16}$$

where the $\mathcal{F}_{\mathrm{PB}}$ is evaluated as

$$\beta\mathcal{F}_{\mathrm{PB}}\left[c_{\pm}(\vec{r})\right] =$$
$$\int_V \left\{ \sum_{i=\mathrm{f},+,-} c_i(\vec{r})\left[\ln\left(c_i(\vec{r})\Lambda^3\right) - 1\right] + \phi(\vec{r})\left[\frac{1}{2}\sum_{i=+,-} z_i c_i(\vec{r}) + c_{\mathrm{f}}(\vec{r})\right]\right\}\mathrm{d}^3 r \tag{3.17}$$

where $\phi$ (scaled by $k_\mathrm{B}T/e$) is the dimensionless electrostatic potential and $\Lambda$ indicates the thermal de Broglie wavelength. The task now is to find the single particle number density distribution $c_\pm(\vec{r})$, which minimizes the density functional $\mathcal{F}_\mathrm{PB}$. The mean-field assumption thus, leads to the variational problem of minimization of the density functional. The PB equation thus, is a result of equating the functional derivative $\delta\mathcal{F}_\mathrm{PB}[c_\pm]/\delta c_\pm$ to zero, along with ($i$) imposing the relationship between the charge density and the electrostatic potential via the Poisson's equation (mentioned below) and ($ii$) constraining the total number of particles $i$ to $N_i$. The constrain of the total particle number is achieved by adding the term $\beta\mu^0_\pm \left(c_\pm(\vec{r}) - N_\pm/V\right)$ to the integrand in Eq. (3.17), where $\mu^0_\pm$ is the Lagrange multiplier. The functional derivative is then

$$\frac{\delta\beta\mathcal{F}_\mathrm{PB}\left[c_\pm(\vec{r})\right]}{\delta c_\pm(\vec{r})} = \beta\mu^0_\pm + z_\pm\phi(\vec{r}) + \ln\left(c_\pm(\vec{r})\Lambda^3\right) \overset{!}{=} 0 \tag{3.18}$$

Eq. (3.18) indicates the model for a "charged ideal gas". The right hand side of the equation has two quantities – one is the electrostatic energy of the mobile charges based on their spatial distribution $c_\pm(\vec{r})e$ in the presence of the potential created by itself ($\phi$). The second quantity is the entropy of the ideal gas with a density distribution $c_\pm(\vec{r})$. Eq. (3.18) can now be rewritten as

$$c_\pm(\vec{r}) = \Lambda^{-3}\,\mathrm{e}^{-z_\pm\phi(\vec{r})-\beta\mu^0_\pm} = c^\mathrm{b}_\pm\mathrm{e}^{-z_\pm\phi(\vec{r})} \tag{3.19}$$

where $c^\mathrm{b}_\pm = \Lambda^{-3}\,\mathrm{e}^{-\beta\mu^0_\pm}$ and $\mu^0_\pm$ are the particle density and the chemical potential in the bulk, respectively, where $\phi = 0$. $c^\mathrm{b}_\pm$ or $\mu^0_\pm$ can be determined by the constraint that the number of particles in the ensemble is conserved, $i.e.$, $\int_V c_\pm(\vec{r})\,\mathrm{d}^3r = N_\pm$. Eq. (3.19) indicates that the particle density locally depends on the Boltzmann factor.

The Poisson's equation relating the net electrostatic potential and the particle density distribution is given by

$$\nabla^2\phi(\vec{r}) = -4\pi l_\mathrm{B}\sum_{i=\mathrm{f},+,-} z_i\,c_i(\vec{r}) \tag{3.20}$$

where $l_\mathrm{B} = \beta e^2/4\pi\varepsilon_0\varepsilon_\mathrm{r}$ is the Bjerrum length. Combining Eqs. (3.19) and (3.20) leads to the PB equation

$$\nabla^2\phi(\vec{r}) = -4\pi l_\mathrm{B}\left(\sum_{i=+,-} z_i c^\mathrm{b}_i\mathrm{e}^{-z_i\phi(\vec{r})} + c_\mathrm{f}(\vec{r})\right) \tag{3.21}$$

The PB equation (3.21) is the second order partial differential equation and thus can be analytically solved for selective cases, where the fixed charge distribution of the molecule $c_f(r)e$ is taken into account via the Neumann or Dirichlet boundary conditions, so that $c_f(r) \equiv 0$ within the computational domain of interest [3]. $c_f(r)$ will be later attributed to the volume charge density of dPGS in the penetrable PB model, introduced in the chapter 5.

Note that the PB theory, unlike the PMF (or the RDF) described in the section 3.1.1.1, partially captures the enthalpic contribution to the inter-particle/inter-atomic interaction by assuming it to be purely electrostatic in origin and approximates the entropic contribution by treating the particles/atoms as an ideal gas. PMF, on the other hand, includes both short and long-range enthalpic effects, as well as non-ideal contributions to the entropic effects. Part of the short-range effects include the ion-specific effects, which have been incorporated in the standard PB theory in the past [173, 180, 225, 226]. These additional effects have been attempted to be captured and thus the standard PB model described here is expanded in the penetrable PB model, introduced in the chapter 5.

Despite its simplicity, the PB equation has been proven to be extremely important step forward as a mean-field approach in the understanding of the charged systems. The description above shows how the particle–particle correlations are neglected in the theory (assumption (3.14)). This assumption exclusively makes the solution for the theory tractable, and even enables the exact analytical form of the solution to be evaluated for systems containing only monovalent ions. However, it is also one of the significant drawbacks of the theory, and can lead to errors in the systems of highly concentrated electrolyte systems or systems involving multivalent ions. Assuming the ions modeled as particles in this model, the absence of ion-specific interactions has a potential to result in unrealistically high ion condensation and overestimated electrostatic screening on the highly charged surface. Therefore, the PB approach is found to be most appropriate for the systems having an electrolyte concentrations smaller than $0.2\,\mathrm{M}$ [227]. For example, PB equation relatively works well in the physiological conditions with ionic strengths of approximately $0.1\,\mathrm{M}$ [228].

### 3.1.2.2   Linearized PB equation: Debye–Hückel theory

For the case of the low magnitude of electrostatic potential $\phi$, a very vital approximation to the Boltzmann ansatz (Eq. (3.19)) can be made. If $|\phi| \ll 1$, *i.e.* if $|\psi| \ll k_B T$ (or if $|\psi| \ll 25\,\mathrm{mV}$), the PB equation (3.21) can be linearized (incorporating the fixed charge distribution into the boundary conditions, as shown below), resulting in the famous

Debye–Hückel (DH) theory [219, 229]

$$\nabla^2 \phi(\vec{r}) = \left( 4\pi l_{\mathrm{B}} \sum_i z_i^2 c_i^{\mathrm{b}} \right) \phi(\vec{r}) = \kappa^2 \phi(\vec{r}) \tag{3.22}$$

where $\kappa = \sqrt{8\pi l_{\mathrm{B}} I}$ is the *inverse DH screening length*, with $I = \frac{1}{2} z_i^2 c_i^{\mathrm{b}}$ as the total ionic strength in the bulk of the electrolyte solution. In the case of a simple homogeneously charged sphere with a bare charge valency $Z$, radius $R$, the boundary conditions can be formulated as

$$\frac{\mathrm{d}\phi(r)}{\mathrm{d}r}\bigg|_{r=R} = -\frac{Z l_{\mathrm{B}}}{R^2}, \quad \phi(r)|_{r\to\infty} = 0 \tag{3.23}$$

and the solution of Eq. (3.22) leads to the well known Yukawa potential [230]

$$\phi_{\mathrm{DH}} = \frac{Z l_{\mathrm{B}}}{1 + \kappa R} \frac{\mathrm{e}^{-\kappa(r-R)}}{r} \sim \frac{\mathrm{e}^{-\kappa r}}{r} \tag{3.24}$$

The behavior of Eq. (3.24) indicates that the interaction between any pair of ions at a distance $r$ decays exponentially due to the screening by the cloud of cations and anions surrounding the ionic pair [228]. For $r < \kappa^{-1}$, the Coulombic interaction is only slightly screened ($\sim r^{-1}$), while for $r > \kappa^{-1}$, it is exponentially screened.

The resultant ionic density distribution around the sphere in a DH context is given by

$$c_i(r) = c_i^{\mathrm{b}} \left( 1 - z_i \phi_{\mathrm{DH}} \right) = c_i^{\mathrm{b}} \left( 1 - \frac{z_i Z l_{\mathrm{B}}}{1 + \kappa R} \frac{\mathrm{e}^{-\kappa(r-R)}}{r} \right) \tag{3.25}$$

DH theory, being the linearized version of the PB theory, neglects any non-linear effects arising from the short-range ion–sphere interactions, and thus is only valid in the case of weakly charged spheres. Both DH and PB theories can be utilized to evaluate the potential distribution also in a more realistic system, such as using the ionic number distribution profiles obtained as a result of simulations, which involve not only the monopole contributions, but also the multipole contributions from the molecules [231].

### 3.1.2.3 Counterion condensation on linear PEs: Onsager–Manning–Oosawa condensation

Ionic distribution around PEs has been a subject of considerable interest for a long time in the PE community, starting with the pioneering work by Fuoss et al. [232] who studied

the counterion distribution around rod-like PEs using the PB theory. It was first realized by Onsager and later analyzed by Manning [233] and Oosawa [234] that, in the limit of the vanishing radius and infinite salt dilution, the rod-like PEs act as charged cylinders with an associated logarithmic potential that may be strong enough to "condense" counterions [235]. This consequently leads to the renormalization of bare charges of the PE by the counterion charges. Below is a short mathematical description of how this concept was introduced by Manning [233].

We consider a realistic situation where we have a linear PE of radius $r_0$ with a line charge density $\lambda > 0$, and length $L$ immersed in a solvent characterized by a Bjerrum length $l_{\mathrm{B}}$. We assume a simplistic situation with no salt and only monovalent counterions ($z = -1$) mobile within the domain cell, which is also characterized as cylindrical with radius $R$ and length $L$. Assuming the cell radius $R$ to be smaller than the persistence length of the PE, thereby neglecting the bending on the large length scale, a linear PE can simply be referred to as a "charged rod". If the end effects are neglected, $i.e.$, $L \to \infty$, cylindrical symmetry is acquired and the counterion distribution $c$ is only a function of the perpendicular distance from the charged rod, $i.e.$, $c = c(r)$. Taking these approximations into consideration, the PB equation can be written for the region of $r_0 < r < R$ as,

$$\left( \frac{\mathrm{d}^2}{\mathrm{d}r^2} + \frac{1}{r} \frac{\mathrm{d}}{\mathrm{d}r} \right) \phi(r) = \kappa^2 \mathrm{e}^{\phi(r)} \tag{3.26}$$

where $\kappa = \sqrt{4\pi l_{\mathrm{B}} c(R)}$ is an inverse of the Debye length and $\phi$ (scaled by $k_{\mathrm{B}} T/e$) is the dimensionless potential assumed to be zero at $r = R$. We now introduce a new dimensionless parameter and define it as Manning parameter [233, 236, 237, 238], which will be useful later and is given as

$$\zeta = \frac{\lambda l_{\mathrm{B}}}{e} \tag{3.27}$$

which essentially indicates the number of charges within the Bjerrum length along the rod, and is an alternative dimensionless way to measure $\lambda$. Given the following boundary conditions

$$\frac{\mathrm{d}\phi(r_0)}{\mathrm{d}r} = -\frac{2\zeta}{r_0} \quad \text{and} \quad \frac{\mathrm{d}\phi(R)}{\mathrm{d}r} = 0 \tag{3.28}$$

The analytical solution for Eqs. (3.26) and (3.28) is given by [232, 236, 237, 239]

$$\phi(r) = -2\ln\left\{\frac{\kappa r}{\gamma\sqrt{2}}\cos\left(\gamma\ln\frac{r}{R_{\mathrm{M}}}\right)\right\} \tag{3.29}$$

where $\gamma$ and $R_{\mathrm{M}}$ can be evaluated by substituting Eq. (3.29) to the boundary conditions Eq. (3.28), resulting in the two coupled transcendental equations

$$\gamma\ln\frac{r_0}{R_{\mathrm{M}}} = \arctan\frac{1-\zeta}{\gamma} \qquad \text{and} \qquad \gamma\ln\frac{R}{R_{\mathrm{M}}} = \arctan\frac{1}{\gamma} \tag{3.30}$$

The counterion radial density distribution is given by $c(r) = c(R)e^{\phi(r)}$, where $c(R)$ is the bulk counterion density. The fraction of the counterions $f(r)$ that can be found between $r_0$ and $R$ is then given by

$$f(r) = \frac{e}{\lambda}\int_{r_0}^{r} c(r')2\pi r'\,\mathrm{d}r' = 1 - \frac{1}{\zeta} + \frac{\gamma}{\zeta}\tan\left(\gamma\ln\frac{r}{R_{\mathrm{M}}}\right) \tag{3.31}$$

Note that $f(R_{\mathrm{M}}) = 1 - 1/\zeta$, implying that at $r = R_{\mathrm{M}}$, the fraction $1 - 1/\zeta$ of counterions can be found, which also indicates that $r_0 \leq R_{\mathrm{M}} < R$. Owing to the importance of this fraction in the Manning theory of counterion condensation, $R_{\mathrm{M}}$ is sometimes referred to as the "Manning radius" [3].

The counterion density distribution around charged cylindrical rods shows a peculiar characteristic which can be displayed under the following conditions. We take the limit of infinitely dilution to the point that there is just one counterion. In the canonical ensemble, its RDF is simply given by $e^{-\beta H(r)}/\int e^{-\beta H(r)}\,\mathrm{d}V$ where, upto the kinetic energy and the additive constant, the Hamiltonian $\beta H(r) = 2\zeta\ln(r/r_0)$, is the electrostatic energy of the counterion, and the denominator is the electrostatic contribution to the statistical-mechanical phase integral, which can be rewritten as

$$\int e^{-\beta H(r)}\,\mathrm{d}V = \int_{r_0}^{\infty} e^{-2\zeta\ln(r/r_0)}2\pi r\,\mathrm{d}r = 2\pi r_0^2\int_0^1 x^{1-2\zeta}\,\mathrm{d}x \tag{3.32}$$

which diverges for $\zeta < 1$. This means that the radial density distribution cannot be normalized, and that in the limit of infinite dilution, charged rods with $\zeta < 1$ cannot localize counterions, while rods with $\zeta > 1$ can. With this result, Manning postulated that the charged rods with $\zeta > 1$ "condense" a fraction $1 - 1/\zeta$ of total counterions, in turn, reducing (or "renormalizing") $\zeta$ to an effective value of 1, while the rest of the counterions

remain "free" [233]. This concept has been widely knows as "Manning condensation" and is proven to be an elegantly simple path to obtain qualitative insights into the physical chemistry of the linear PEs. While so, the theory is still being contested within the scientific community due to the flexibility of most of the industrial and biological PEs and unclear understanding of the state of condensed counterions [177, 240, 241, 242, 243].

### 3.1.2.4 Counterion condensation around spherical objects

Relative to that in the cylindrical geometry, the notion of counterion condensation in the spherical geometry is less clear. However, based on the variety of approximations proposed, previous works more or less agree on the idea that counterions condense near the spherical charged surface, renormalizing its original (bare) charge. The terminology "condensation" here should be used keeping in mind that, except in the cylindrical geometry, there is *no* physical condensation (defined as the existence of a non-vanishing quantity of counterions in a layer of vanishing thickness around the polyion) [17, 232, 244, 245]. The decorated object (charged sphere *plus* captive counterions) thus acts as a single entity with an effective charge valency $Z_{\text{eff}}$ lower than the bare valency $Z_{\text{d}}$ [15, 117, 118, 119, 120]. This so-called charge renormalization effect has been extensively studied and wide variety of theories have been developed for the effective charge and size of simple charged spheres with smooth surfaces [16, 17, 115, 119, 120, 121]. The subsections below give brief descriptions of the some of these works. The basic premise behind these approaches is that, as far as the far-field effects from the colloid are concerned, the DH-like linearized PB approaches, which are unable to explain the non-linear counterion condensation effects in the vicinity of the colloid, can still be used if the structural bare charge valency $Z_{\text{d}}$ of the colloid can be replaced with the effective valency $Z_{\text{eff}}$. $Z_{\text{eff}}$ is then attempted to be estimated a priori.

### 3.1.2.4.1 Alexander prescription

Alexander et al. [15] proposed that the effective colloidal charge valency $Z_{\text{eff}}$ can be obtained by asymptotically matching the solution $\phi$ of full non-linear PB equation (Eq. (3.21)) (*i.e.*, the local, radially symmetric electrostatic potential $\phi$ in the long-range) to the solution of the linearized PB (DH) form *with an effective charge valency $Z_{\text{eff}}$* [246], given

as [15, 16, 114, I]

$$\phi_{\mathrm{DH}}(r) = Z_{\mathrm{eff}} l_{\mathrm{B}} \frac{\mathrm{e}^{\kappa r_{\mathrm{eff}}}}{1 + \kappa r_{\mathrm{eff}}} \frac{\mathrm{e}^{-\kappa r}}{r}. \tag{3.33}$$

where $\phi_{\mathrm{DH}}$ is the dimensionless DH potential (scaled by $k_{\mathrm{B}}T/e$) applicable to a smooth charged sphere with valency $Z_{\mathrm{eff}}$ and radius $r_{\mathrm{eff}}$ (effective radius, discussed below). In other words, in the long-range,

$$\ln \left| r\phi(r) \right| \underset{\kappa r \to \infty}{=} \ln \left| Z_{\mathrm{eff}} l_{\mathrm{B}} \frac{\mathrm{e}^{\kappa r_{\mathrm{eff}}}}{1 + \kappa r_{\mathrm{eff}}} \right| - \kappa r \tag{3.34}$$

where the right-hand side turns out to be a linear function with a negative slope defined by the inverse Debye length $\kappa$. Eq. (3.34) applies, *i.e.*, $\phi_{\mathrm{DH}}$ approaches to $\phi$ only for the distance $r > r^*$ where non-linear effects, including the correlation and condensation for ions, subside. In practice, an energy criterion (*e.g.* 50% of $k_{\mathrm{B}}T$) can be established in order to compare $\phi$ and $\phi_{\mathrm{DH}}$ and evaluate $r^*$. Thus, $r^* = r_{\mathrm{eff}}$ is eligible to serve as the effective radius $r_{\mathrm{eff}}$ of the sphere, *i.e.*, the counterions residing within the distance $r \leq r_{\mathrm{eff}}$ are designated as *condensed*. Having found $r_{\mathrm{eff}}$, the effective charge valency $Z_{\mathrm{eff}}$ can be obtained from the y-intercept of Eq. (3.34), or from the total cumulative charge distribution $Z_{\mathrm{acc}}(r)$ (*cf.* Sec. 3.2.5.1 and Eq. (3.66)) as $Z_{\mathrm{eff}} = Z_{\mathrm{acc}}(r_{\mathrm{eff}})$. The effective surface potential of the sphere obtained from simulations is defined as $\phi_{\mathrm{eff}} = \phi(r_{\mathrm{eff}}) = \phi_{\mathrm{DH}}(r_{\mathrm{eff}})$.

In general, $\phi(r)$ can be in principle directly evaluated from the simulations, *i.e.*, replacing the Boltzmann ansatz for the concentration profiles of charged species $c_i(r)$ in Eq. (3.21) with the respective radial density distributions obtained from the simulations, as shown in the section 3.2.5.1, and also in the work by Xu et al. [114]. Apart from the electrostatic contribution on the DH-level, this approach incorporates the electrostatic and steric correlations among the charged species as well as the discrete solvent effects in the vicinity of the macromolecule that contribute to $Z_{\mathrm{eff}}$ and $r_{\mathrm{eff}}$. The reference for Alexander prescription for further mentions in this thesis will be thus alluded to this approach. An equivalent approach can also be seen in the section 3.1.2.4.3.

### 3.1.2.4.2 Inflection point criterion

As proposed by Belloni [16, 114, 117, 121], an effective radius $r_{\mathrm{eff}}$ for a highly charged PE can be defined as an inflection point in the plot of the total cumulative charge valency $Z_{\mathrm{acc}}$ (described in Eq. (3.66), Sec. 3.2.5.1) vs. the inverse radial distance $1/r$. From the

PB and counterion-condensation theory it follows that the condition

$$\left.\frac{\mathrm{d}^2 Z_{\mathrm{acc}}(r)}{\mathrm{d}\left(\frac{1}{r}\right)^2}\right|_{r=r_{\mathrm{inf}}} = 0 \tag{3.35}$$

leads to a radius definition $r_{\mathrm{inf}}$ within which ions are assumed to be *condensed* and separates the linear DH regime from the non-linear regime.

### 3.1.2.4.3 PMF method

Using simulations, the structure of the electrolyte solution surrounding the macromolecule/colloid is analysed by calculating the RDFs of ions with respect to the center-of-mass (COM) of the macromolecule $g_i(r)$, where $i$ are the ionic species. Considering Eq. (3.12), the PMF of the ions (or RDF) $V_i(r)$ can be decomposed into short-ranged and long-ranged contributions as [219, 247, 248]

$$V_i(r) = V_i^{\mathrm{sr}}(r) + V_i^{\mathrm{lr}}(r) \tag{3.36}$$

where the short-range part $V_i^{\mathrm{sr}}(r)$ includes all the non-linear effects due to specific macromolecule–ion interactions and ion–ion correlations. The long-range part $V_i^{\mathrm{lr}}(r)$ can be typically approximated by a dimensionless DH type of potential $\phi_{\mathrm{DH}}(r)$ of the form [219, 229]

$$\beta V_i^{\mathrm{DH}}(r) = z_i \phi_{\mathrm{DH}}(r) \tag{3.37}$$

where $z_i$ is the charge valency of ionic species $i$. Eq. (3.37) can be rewritten similar to Eq. (3.34) as [249]

$$\ln\left|\beta r V_i^{\mathrm{DH}}(r)\right| \underset{\kappa r \to \infty}{=} \ln\left|z_i Z_{\mathrm{eff}} l_{\mathrm{B}} \frac{\mathrm{e}^{\kappa r_{\mathrm{eff}}}}{1 + \kappa r_{\mathrm{eff}}}\right| - \kappa r \tag{3.38}$$

This construction was introduced by Kalcher and Dzubiella [249] for infinitely dilute electrolyte systems, to calculate the short-ranged part of specific ion–ion interactions by subtracting the linear DH fit from the full PMF. In the chapter 4, it will also serve as a method to identify the location where the linear long-ranged DH decay crosses over to non-linear behavior. This should be in principle one possible reasonable definition for an effective size in the DH picture, $r_{\mathrm{eff}}$ in Eq. (3.33), of the macromolecule with respect to charge properties.

### 3.1.2.4.4 Manning model

Manning [120] extended his famous standard counterion condensation theory on linear PEs to charged spheres immersed in dilute salt solutions, giving results consistent with the previous theories presented in different limits [116]. In this mean-field theory, the free energy of a counterion is constructed, that points to the competition between the electrostatic binding of the counterions and their entropy in the bulk. The free energy is then minimized in order to optimize the unknown fraction of condensed counterions $\Theta$ that is assumed at an outset. Considering an impenetrable sphere of radius $r_{\mathrm{eff}}$ with $N$ unit charges $e$ on the surface, immersed in an infinite solution of a bulk simple electrolyte having an inverse Debye length $\kappa$, the electrostatic surface free energy of the sphere is obtained by applying a standard charging procedure to the solution of the DH linearization of the PB equation [250],

$$\beta G^{\mathrm{el}} = \frac{N l_{\mathrm{B}} (1 - z\Theta)^2}{2 r_{\mathrm{eff}} (1 + \kappa r_{\mathrm{eff}})} \tag{3.39}$$

where $z$ is the counterion valency. The lost entropy of $N\Theta$ condensed counterions, with $c$ as the salt concentration, is then given by

$$\beta G^{\mathrm{tr}} = -N\Theta \ln c \tag{3.40}$$

With the aim to explore the conditions for which the number of condensed counterions is greater than zero, *i.e.*, $1 - z\Theta \leq 1$, the total free energy $G^{\mathrm{tot}} = G^{\mathrm{el}} + G^{\mathrm{tr}}$ is minimized with respect to $\Theta$ to derive the minimum surface charge density $\sigma_{\mathrm{crit}}$ needed to start the counterion condensation in the asymptotic limit of $\kappa r_{\mathrm{eff}} \ll 1$ as [120]

$$\sigma_{\mathrm{crit}} = -\frac{e \ln (\kappa r_{\mathrm{eff}})}{2\pi z l_{\mathrm{B}} r_{\mathrm{eff}}} \tag{3.41}$$

In the asymptotic limit of $\kappa r_{\mathrm{eff}} \gg 1$, $\sigma_{\mathrm{crit}}$ becomes [120]

$$\sigma_{\mathrm{crit}} = -\frac{e(1 + \kappa r_{\mathrm{eff}}) \ln(\kappa l_{\mathrm{B}})}{2\pi z l_{\mathrm{B}} r_{\mathrm{eff}}} \tag{3.42}$$

Some of the other key works about the counterion condensation on spherical objects have proposed the expressions for colloidal effective charge under different conditions. Early approaches include the work by Ohshima et al. [115] who proposed approximate solutions for non-linear PB equation for single spheres in the limit $\kappa r_{\mathrm{eff}} \geq 1$. Ra-

manathan [118] in his extensive study on the PB equation around a single charged sphere in the limit of $\kappa r_{\text{eff}} \ll 1$, also derived Eqs. (3.41) and (3.42), and presented the dependence of $Z_{\text{eff}}$ on the sphere size and salinity of the solution. Bocquet et al. [17], in the limit of $\kappa r_{\text{eff}} \gg 1$ put forward a simple method to estimate the effective charge of highly charged colloidal objects, while Netz and Orland [119], using the field-theoretic formulation of the variational theory, proved the existence of the effective charge on spheres and proposed that in the limit of $\kappa r_{\text{eff}} \to 0$, the effective charge density $\sigma_{\text{eff}} = Z_{\text{eff}} e / 4 \pi r_{\text{eff}}^2$ of the sphere explicitly depends upon its bare charge valency, $Z_{\text{d}}$.

As described in the introduction, the dPGS microscopic morphology consists of a carbon-core surrounded by dendritic branches which are terminated by the charged sulphate groups (see Fig. 1.2). The spread of this topology in three dimensions, and the presence of charged sulphate groups at the terminal positions of dendritic branches allow dPGS to be modeled as a uniform sphere charged at the surface. However, there is a significant void available within the structure for water molecules or ions to penetrate in. Since defining the concepts of counterion condensation and effective charge to such complex structure is challenging, we resort to the approaches mentioned in this section, such as Alexander prescription [15], the inflection point criterion [16, 121, I], the PMF method [249] (*cf.* chapter 4) and the Manning model [120] for the counterion condensation on charged spheres (*cf.* chapter 5).

### 3.1.2.5 Donnan theory

The phenomenon of ion partitioning was studied a century ago by Donnan, in the area of thermodynamic equilibrium involving ions and electrolytes, where two electrolyte solutions are separated by a porous membrane freely permeable to small ions, but impermeable to macromolecules, as shown in Fig. 3.1 [251]. This leads to interesting results, which include the electrostatic potential difference and different ionic densities between the two phases. The description of membrane equilibrium by Donnan constitutes a relatively simple model, as a first development in understanding the gradients in ionic densities and potentials in biological systems [252, 253].

Consider a system of salt ions partitioned in two compartments (with the right compartment as a reservoir) by a membrane permeable to small ions, while impermeable to macroions, as shown in Fig. 3.1. All ions are considered as monovalent. All small cations and anions can freely move across both phases (unlike the macroions, which are spatially constrained to the left hand side, owing to their size), hence they are in an electrochemical equilibrium. The confined domain for the macroions thus prompts the movement
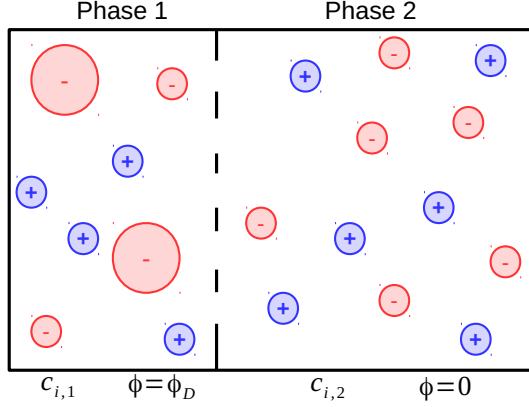
Figure 3.1: Illustration of a system exhibiting the Donnan equilibrium. The two electroneutral and mutually exclusive phases (phase 1 and 2) are partitioned by a semipermeable membrane (permeable to the small ions but not to the macroions). The concentrations of the ionic species are indicated as $c_{i,1}$ and $c_{i,2}$ ($i = \pm$), while the electrostatic potentials are shown as $\phi = \phi_{\mathrm{D}}$ and $\phi = 0$, in the phases 1 and 2, respectively.

of cations to the left side in order to charge-neutralize them, resulting in the *Donnan potential* ($\phi_{\mathrm{D}}$) among the two partitions. The two partitions can now be seen as the two mutually exclusive and electroneutral phases with the phase 1 at the Donnan potential $\phi = \phi_{\mathrm{D}}$, and the phase 2 at zero potential $\phi = 0$. Now, similar to Eq. (3.18) in the PB theory, the balance of electrochemical potential for both mobile cations and anions is performed resulting in

$$
\begin{aligned}
\ln c_{\pm,1} \pm \phi_{\mathrm{D}} &= \ln c_{\pm,2} \\
\implies c_{\pm,1} &= c_{\pm,2}\, e^{\mp \phi_{\mathrm{D}}}
\end{aligned}
\tag{3.43}
$$

where $\phi_{\mathrm{D}}$ (scaled by $k_{\mathrm{B}}T/e$) is the dimensionless Donnan potential. The electroneutrality conditions in phase 2 (reservoir) results in $c_{+,2} = c_{-,2} = c_2$, and in phase 1,

$$
c_{+,1} - c_{-,1} - c_m = 0
\tag{3.44}
$$

where $c_m$ is the macroion concentration in phase 1. Assuming a known reservoir concentration $c_2$ and thus, substituting Eq. (3.43) in Eq. (3.44), the Donnan potential is thus given by [254]

$$
\phi_{\mathrm{D}} = \ln \frac{c_2}{c_{+,1}} = -\ln\left(-\frac{\sqrt{1+\chi^2}+1}{\chi}\right)
\tag{3.45}
$$

where $\chi = -2c_2/c_m$. A scenario equivalent to the one described in Fig. 3.1, and that deserves Donnan treatment, is that of an ionic solution surrounding an isolated single

PE. The charged groups on the PE, similar to the macroions in phase 2 in Fig. 3.1, are chemically bonded to the macromolecule core, and hence, cannot go into the solution. Thus the purpose of the "membrane" is served by the chemical bonds between the charged groups and the macromolecule core. The salt ions, on the other hand, are free to navigate throughout the system domain. This positional constraint on macromolecular charged groups along with the electrostatic interaction between the charged groups and the counterions leads to similar consequences as in the membrane equilibrium described above, *i.e.*, the Donnan potential across the macromolecule and bulk solution phases is developed. The implementation of the Donnan theory in this context can be seen in the chapter 5.

### 3.1.3 Standard Langmuir isotherm

Consider a canonical ligand–substrate system with a volume $V$ containing one substrate unit (with negligible volume compared to $V$) and $n$ ligand molecules. The substrate possesses $N$ independent and identical binding sites, available for the binding with ligands. Considering a state where $N^{\mathrm{b}}$ ligands are bound to the substrate, the extent of binding is defined as the coverage $\Theta = N^{\mathrm{b}}/N$. The corresponding degeneracy of the binding state is then given by [254, 255, 256]

$$W = \frac{\gamma^{N^{\mathrm{b}}} N!}{N^{\mathrm{b}}! \left(N - N^{\mathrm{b}}\right)!} \tag{3.46}$$

$W$, in other words, is the combinatorial possibilities of distributing $N^{\mathrm{b}}$ identical and indistinguishable ligands among $N$ binding sites. $\gamma$ is defined as the partition sum of a single ligand in its bound state. The associated Boltzmann entropy is now defined as

$$\frac{S_{\mathrm{b}}}{k_{\mathrm{B}}} = \ln W \tag{3.47}$$

The entropy per binding site is then given by

$$\frac{S_{\mathrm{b}}}{N k_{\mathrm{B}}} = -\Theta \ln \Theta - (1 - \Theta) \ln (1 - \Theta) + \Theta \ln(v_0/\Lambda^3) \tag{3.48}$$

where $\gamma = v_0/\Lambda^3$ is re-defined as the ratio of the effective configurational volume $v_0$ to the cube of thermal de Broglie wavelength $\Lambda$. The effective configurational volume $v_0$ takes into consideration the vibrational and rotational degrees of freedom of a ligand in its bound state, and can be computed via simulations. According to the convention in

experiments, $v_0 = 1\,\mathrm{M}^{-1} \simeq 1.6\,\mathrm{nm}^3$ is designated as the standard volume, corresponding to the standard ligand concentration $c^{\mathrm{std}} = 1\,\mathrm{M}$ [257, 258, 259]. More discussion in this regard can be seen in the chapter 5.

The canonical ideal gas translational free energy of free ligands is given by

$$\beta\mathcal{F}_{\mathrm{tr}} = (n - N_{\mathrm{b}})\left[\ln\left(\frac{(n - N^{\mathrm{b}})\Lambda^3}{V}\right) - 1\right] \tag{3.49}$$

The total canonical Helmholtz free energy of the system is then given by

$$\beta\mathcal{F} = \beta\mathcal{F}_{\mathrm{tr}} - \frac{S_{\mathrm{b}}}{k_{\mathrm{B}}} + \beta N^{\mathrm{b}}\Delta\mu_{\mathrm{bind}} \tag{3.50}$$

where $\Delta\mu_{\mathrm{bind}}$ is defined as the total binding free energy of corresponding to the binding of one ligand to its associated binding site. The free energy per binding site is then given by

$$\beta\widetilde{\mathcal{F}} = \frac{\beta\mathcal{F}}{N} = \left(\frac{n}{N} - \Theta\right)\left[\ln\left(\frac{(n - N^{\mathrm{b}})\Lambda^3}{V}\right) - 1\right]$$
$$+ \Theta\ln\Theta + (1 - \Theta)\ln(1 - \Theta) - \Theta\ln(v_0/\Lambda^3) + \beta\Theta\Delta\mu_{\mathrm{bind}} \tag{3.51}$$

The variation of the free energy $\widetilde{\mathcal{F}}$ with respect to the number of bound ligands $N^{\mathrm{b}}$ results in the expression for the standard Langmuir isotherm, in the form of a binding constant $K$. $K$ depends on the extent of binding $\Theta$ and the independent variables such as the free ligand concentration $c^{\mathrm{b}} = (n - N^{\mathrm{b}})/V$.

$$K = v_0 \mathrm{e}^{-\beta\Delta\mu_{\mathrm{bind}}} = \frac{\Theta}{c^{\mathrm{b}}(1 - \Theta)} \tag{3.52}$$

$\Delta\mu_{\mathrm{bind}}$ in this standard Langmuir isotherm is resolved into the DH-level electrostatic and ion-specific contributions, as well as the isotherm is extended to the heterogeneous binary ligand binding in order to study the competitive ionic sorption in the chapter 5.

## 3.2 All-atom (AA) simulations

In this work, the systems of atomistically resolved dPGS surrounded by counterions and salt ions immersed in an explicitly modeled water molecules, are simulated using the GROMACS MD simulation package [260, 261, 262, 263] version 5.0.6. In MD, the classical

Newtonian equations of motions are solved for a finite number of atoms, each with a point charge and finite volume. Through pair-potentials, atoms interact with each other in a periodic box of cubic volume $V$. The fundamental simulation results are obtained as time trajectories of all atoms in the box and their interaction energies. The typical time scale for the performed AA simulations is 100–200 nanoseconds.

## 3.2.1  Equations of motion

Consider a canonical system of $N$ mobile atoms. Each atom $j$ in the simulation box is represented by mass $m_j$, and a partial charge $q_j$ located at its center. The Hamiltonian of the system is then given by

$$H = \sum_j^N \frac{\left|\vec{p_j}\right|^2}{2m_j} + \sum_{i \neq j \neq k \neq l}^N V(r_{ij}, \theta_{ijk}, \Phi_{ijkl}) \tag{3.53}$$

where the first term indicates the kinetic energy associated with the atom $j$ and the second term indicates the interactions between any two atoms $i$ and $j$ with respect to their relative distance $r_{ij} = |\vec{r_i} - \vec{r_j}|$ (bonded atoms or non-bonded interactions), three adjacent atoms $i$, $j$ and $k$ (angular interactions) as well as four adjacent atoms $i$, $j$, $k$ and $l$ (dihedral interactions), as defined by the potential function $V$. The potential function incorporates Lennard-Jones (LJ) and Coulomb electrostatic (non-bonded) potentials as pair additive and centro-symmetric nonbonded interactions, and harmonic potentials for intramolecular (bonded) interactions such as bonds, angles or dihedrals. The angular and dihedral interactions depend on third or fourth adjacently bonded atoms, the identities of which are founds via neighbour-lists. In order to mimic the macroscopic properties, or the infinite bulk environment around each atom, periodic boundary conditions (PBC) are employed for all atoms. The potential function $V$ then is given as

$$V(r_{ij}, \theta_{ijk}, \Phi_{ijkl}) = V_{\text{bonded}}(r_{ij}, \theta_{ijk}, \Phi_{ijkl}) + V_{\text{nonbonded}}(r_{ij}) \tag{3.54}$$

$$V(r_{ij}, \theta_{ijk}, \Phi_{ijkl}) = \frac{1}{2}K_{ij}^{\text{b}}(r_{ij} - r_{\text{eq}})^2 + \frac{1}{2}K_{ijk}^{\theta}(\theta_{ijk} - \theta_{\text{eq}})^2 \tag{3.55}$$

$$+ \frac{1}{2}K_{ijkl}^{\Phi}\left[1 + \cos(n\Phi_{ijkl} - \gamma)\right] \tag{3.56}$$

$$+ 4\varepsilon_{ij}\left[\left(\frac{\sigma_{ij}}{r_{ij}}\right)^{12} - \left(\frac{\sigma_{ij}}{r_{ij}}\right)^6\right] + \frac{1}{4\pi\varepsilon_0\varepsilon_{\text{r}}}\frac{q_i q_j}{r_{ij}} \tag{3.57}$$

where the cross LJ parameters $\sigma_{ij}$ and $\varepsilon_{ij}$ are calculated using Lorentz–Berthelot combination rule for each single-particle LJ parameters, *i.e.*, van der Waal radius $\sigma_j$ and the depth of potential well $\varepsilon_j$ [264]. $q_i$ and $q_j$ are the partial charges of atoms $i$ and $j$ related to electrostatic Coulomb potential, $\varepsilon_0$ is the relative permittivity of a vacuum and $\varepsilon_{\mathrm{r}}$ is a dielectric constant of a simulation medium. In view of atomistic simulations, the background medium is vacuum, hence $\varepsilon_{\mathrm{r}}$ is set as 1. $K_{ij}^{\mathrm{b}}$ and $K_{ijk}^{\theta}$ represent the bond and angular force constants, along with $r_{\mathrm{eq}}$ and $\theta_{\mathrm{eq}}$ as the equilibrium bond length and angle respectively. $\theta_{ijk}$ represents the angle between bonds $i - j$ and $j - k$. $K_{ijkl}^{\Phi}$ indicates the dihedral interaction parameter along with $\Phi_{ijkl}$ as the dihedral angle between $ijk$ and $jkl$ planes and $\gamma$ as the initial phase angle. In the simulations performed, the bond vibrations are constrained using LINCS [265] algorithm. The total force on each atom $j$ generated according to the potential function $V$ is then given by

$$
\vec{F}_j = - \sum_{i}^{N} \frac{\partial V(r_{ij}, \theta_{ijk}, \Phi_{ijkl})}{\partial r_{ij}} \hat{r_{ij}} - \sum_{i \neq k}^{N} \frac{\partial V(r_{ij}, \theta_{ijk}, \Phi_{ijkl})}{\partial \theta_{ijk}} \hat{\theta_{ijk}}
$$
$$
- \sum_{i \neq k \neq l}^{N} \frac{\partial V(r_{ij}, \theta_{ijk}, \Phi_{ijkl})}{\partial \Phi_{ijkl}} \hat{\Phi_{ijkl}}
$$

(3.58)

where $\hat{a}$ represents a unit vector in the direction of vector $\vec{a}$. An atomic trajectory can thus be obtained by integrating Newton's equation of motion

$$
m_j \frac{\mathrm{d}^2 \vec{r}_j}{\mathrm{d}t^2} = \vec{F}_j
$$

(3.59)

## 3.2.2   Force-field

One of the most crucial aspects to consider before performing the AA simulations for production is the choice of the force-field. A classical force-field essentially refers to the Hamiltonian function used to generate the potential energies and forces (as described in Sec. 3.2.1), and the parametrization that constructs this Hamiltonian. This parametrization involves the empirical values of the interaction parameters such as the LJ parameters and electrostatic charges for the non-bonded interactions, and the force constants for the bonded, angular and dihedral interactions. There are multiple force-fields available in the literature, and the choice of the force-field depends on the system properties one is interested in. This is why, pertaining to a specific system property of interest, it is important to look for an accurate and reliable force-field. In the area of the AA simulations of biological and synthetic PEs in explicit-water, some of the well known classical force-fields are

Assisted Model Building and Energy Refinement (AMBER) [188] (widely used for proteins and DNA), Chemistry at HARvard Molecular Mechanics (CHARMM) [189] (widely used for both small molecules and macromolecules), Optimized Potential for Liquid Simulations (OPLS) [191] (known for the experimental properties of liquids, *e.g.*, density and heat of vaporization), GROningen MOlecular Simulation (GROMOS) [190] (united atom force field optimized with respect to the condensed phase properties of alkanes), etc.

### 3.2.3 Numerical scheme: Leapfrog integrator

Eqs. 3.53, 3.58 and 3.59 collectively represent the equations of motion for each atom within the simulation box. There exist several numerical discretization techniques to solve this system of differential equations, out of which, GROMACS implements the leapfrog algorithm which is a second-order method and is much more stable than the first-order Euler method. After choosing the simulation time step $\Delta t$, which is in the range of $1-2\,\mathrm{fs}$, the positions of all atoms $\vec{r}_j$ are calculated as and with the known positions of atoms $\vec{r}_j$ and velocities $\vec{v}_j$ at time $t$, the positions and velocities at time $t + \Delta t$ are given according to the leapfrog algorithm by

$$\vec{v}_j\left(t + \frac{1}{2}\Delta t\right) = \vec{v}_j\left(t - \frac{1}{2}\Delta t\right) + \frac{\Delta t}{m_j}\vec{F}_j\left(t\right) \tag{3.60}$$

$$\vec{r}_j\left(t + \Delta t\right) = \vec{r}_j\left(t\right) + \Delta t \cdot \vec{v}_j\left(t + \frac{1}{2}\Delta t\right) \tag{3.61}$$

The velocities at time $t + \frac{1}{2}\Delta t$, $\vec{v}_j\left(t + \frac{1}{2}\Delta t\right)$ are calculated using the force at time $t$, $\vec{F}_j(t)$, which in turn, is calculated using the positions at time $t$, $\vec{r}_j(t)$ and the velocities at time $t - \frac{1}{2}\Delta t$, $\vec{v}_j\left(t - \frac{1}{2}\Delta t\right)$. The positions at time $t + \Delta t$, $\vec{r}_j\left(t + \Delta t\right)$ are then evaluated using $\vec{v}_j\left(t + \frac{1}{2}\Delta t\right)$.

### 3.2.4 Simulation techniques

#### 3.2.4.1 Constant temperature simulations

Implementing the above MD equations in the microcanonical ($NVE$) ensemble cannot conserve energy for long time simulations due to the energy leakage occurring as a result of the time accumulation of numerical errors (or also called numerical friction) induced by the discretization scheme, and also due to the interaction cut-off artifacts [266, 267, 268]. In comparison, it is easier to simulate canonical ($NVT$) or isobaric-isothermal ($NPT$) ensembles. Due to above mentioned reasons, the atomic velocities in these ensembles are

exerted upon by the numerical friction, rendering the total kinetic energy of the system *i.e.*, the system temperature to go down. Hence, to maintain the constant temperature, the equations of motion are coupled with a thermostat. There are a number of thermostat schemes available, some of which are Berendsen [269], Nosè–Hoover [270, 271], Andersen [272], and velocity rescaling [273]. As as example, Berendsen algorithm assumes the simulation box to be in a constant contact with a external heat bath having a target temperature as $T_0$.

$$\frac{\mathrm{d}T}{\mathrm{d}t} = \frac{T_0 - T}{\tau} \tag{3.62}$$

where $\tau$ and $T$ are the time constant and the current temperature of the simulation box, respectively. Eq. (3.62) basically states that the difference between the system and the target temperature decreases with time in an exponential manner, with a time constant $\tau$. This relaxes the system faster and hence is considered to be more suitable for the equilibration phase of the simulation protocol.

### 3.2.4.2   Constant pressure simulations

In the $NPT$ ensembles, constant pressure is maintained in the simulation box by dynamic adjustment of its size and rescaling of coordinates of all atoms (apart from the fixed atoms). Analogous to the Berendsen temperature thermostat, the Berendsen barostat considers coupling the system with a first order kinetic relaxation of the pressure as

$$\frac{\mathrm{d}P}{\mathrm{d}t} = \frac{P_0 - P}{\tau_p} \tag{3.63}$$

Thus, the Berendsen barostat, instead of manipulating the atom velocity, scales the box vectors and atomic coordinates by a factor $\mu$, where $\mu$ is a function of the characteristic time scale $\tau_p$ and the instantaneous pressure $P(t)$ of the system.

   In spite of its stability and the ability to generate an average constant pressure, Berendsen is a weak pressure coupling algorithm and fails to generate true $NPT$ ensemble. In comparison, Parrinello–Rahman pressure coupling produces correct $NPT$ ensemble [274, 275].

### 3.2.4.3   Particle mesh Ewald

In a nanometer sized simulation box, the number of atoms increases as $\sim L^3$, where $L$ is the box length. The simulation of a large systems, say $10 - 20\,\mathrm{nm}$ sized box, causes one

to indulge in costly computations, thus necessitating schemes of minimum computational cost and minimum subsequent error. The computational cost of simulating $N$ particles is $N^2$, which is undesirable for large systems. The effort of computing the particle trajectory primarily goes into the calculation of particle-particle interaction energies, which include short range interactions such as Van der Waal interactions and long range interactions like Coulomb interactions. Van der Waal interaction decays as $r^{-6}$, where $r$ is the inter-particle distance. This allows an opportunity to minimize its computational cost by the application of cut-off distance, *i.e.*, maximum distance till which mutual interactions are calculated. The Coulomb interactions, on the other hand, decay as $r^{-1}$, which is much slower. Hence, implementing a cut-off distance scheme here would result in significant errors in the particle trajectories. This motivates the division of the total interaction space into the short-range ($r < r_{\mathrm{coulomb}}$) and long-range ($r > r_{\mathrm{coulomb}}$) part, where $r_{\mathrm{coulomb}}$ is introduced as a Coulomb cut-off distance. Subsequently, the Coulomb interactions are divided as

$$V(\vec{r}) \equiv V_{\mathrm{sr}}(\vec{r}) + V_{\mathrm{lr}}(\vec{r}) \tag{3.64}$$

In Eq. (3.64), the short range part of the interaction $V_{\mathrm{sr}}(\vec{r})$ (applicable in $r < r_{\mathrm{coulomb}}$) is calculated in real space. The problem arises in the computation of the long-range part $V_{\mathrm{lr}}(\vec{r})$ (applicable in $r < r_{\mathrm{coulomb}}$), which is not convergent if summed up in real space. Hence, this part is treated in a Fourier space, where a single sum of the wave vectors of the reciprocal grid is used to evaluate the discretized PB equation, obtaining the electrostatic potential. This sum over wave vectors converges faster and also requires small number of wave vectors in order to maintain sufficient accuracy. One of the algorithms adopting this idea to calculate long-range Coulomb interactions is Particle Mesh Ewald algorithm (PME) [276, 277].

### 3.2.5   Analysis of simulation data

#### 3.2.5.1   Electrostatic potential and cumulative charge

RDFs of charged species $g_i(r)$ (*cf.* Sec. 3.1.1.1) with respect to the macromolecule-COM, obtained from simulations, provide the respective radial density distributions $c_i(r)$ using the relation $c_i(r) = c_i^{\mathrm{b}} g_i(r)$. For all ionic species, $c_i(r)$ reaches the bulk number density $c_i^{\mathrm{b}}$ in the far-field. $c_i(r)$ can then be utilised to calculate the local charge accumulation (or running ion coordination) and electrostatic potential distribution around

the macromolecule, using the Poisson's equation (3.20) where the summation runs over all atomic species $i$ with a non-zero partial charge, which involve dPGS atoms and ions for "implicit-water" integration (*cf.* Sec. 3.2.5.2.2) and all charged species including hydrogen and oxygen atoms of water for "explicit-water" integration (*cf.* Sec. 3.2.5.2.1). Eq. (3.20) is numerically integrated twice to obtain $\phi(r)$, which is then compared with the dimensionless DH potential $\phi_{\mathrm{DH}}$, according to the Alexander prescription described in the section 3.1.2.4.1, in order to calculate the effective radius $r_{\mathrm{eff}}$ of the macromolecule.

In addition to the potential profile, the running coordination number of species $i$ as a function of the distance $r$ from the macromolecule-COM is defined as,

$$N_{\mathrm{acc},i}(r) = \int_0^r c_i(r')4\pi r'^2 \mathrm{d}r' \tag{3.65}$$

This motivates the definition of total cumulative charge valency as

$$Z_{\mathrm{acc}}(r) = \sum_i z_i N_{\mathrm{acc},i}(r) \tag{3.66}$$

With that, the number of the bound ions and the effective charge valency of the dPGS follow as $N_i^{\mathrm{b}} = N_{\mathrm{acc},i}(r_{\mathrm{eff}})$ and $Z_{\mathrm{eff}} = Z_{\mathrm{acc}}(r_{\mathrm{eff}})$, respectively.

### 3.2.5.2   Implicit vs. explicit-water integration

In order to better scrutinize the explicit-water effects, the two approaches of calculating the radial electrostatic potential and the total cumulative charge are compared using the charge integration and mapping, as described in sections 3.2.5.1 and 3.1.2.4. The comparison is based on the inclusion/exclusion of the radial density distributions of the partial charges of water as follows:

### 3.2.5.2.1   "Explicit-water" approach

Here the partial charges of all the atoms are included in the simulation box, which include the macromolecule atoms, counterions, coions and the partial charges of water molecules. This basically assumes a multi-ingredient mixture of different charged species in vacuum, thus taking the dielectric constant of unity (*i.e.*, $l_{\mathrm{B}} = 56\,\mathrm{nm}$ at $T = 300\,\mathrm{K}$) while calculating the electrostatic potential.

### 3.2.5.2.2 "Implicit-water" approach

This approach assumes an implicit-water in terms of implementing the partial charges in the Poisson's equation for calculating the electrostatic potential (Eq. (3.20)), *i.e.*, the partial charges of water are excluded while calculating the potential; thereby the dielectric constant of the medium is chosen as 72 [278] [*i.e.*, $l_B = 0.72\,\text{nm}$ (corresponding to the SPC/E water model used in the simulations) and at $T = 300\,\text{K}$]. The charge density distributions of all other species (*i.e.*, macromolecule atoms and ions) are deployed to calculate the potential.

Note that the PMF method described in the section 3.1.2.4.3 is essentially an explicit-water approach as it directly works on the ionic profiles, not integrated potentials. Therefore, no approximation is made concerning the dielectric properties as in the implicit approach to the potential.

### 3.2.5.3 Gibbs dividing surface and partial molar volume

In equilibrium conditions, the description of a macromolecule–water interface in terms of the radial density distribution of water around the macromolecule-COM allows us to consider the phase dividing surface as a separate thermodynamic system that is in equilibrium with its adjoining macromolecule and water phases. This thermodynamic interface, *i.e.*, the radial Gibbs dividing surface [279, 280, 281, 282, 283, 284] (GDS) assuming its spherical nature, is given by [285]

$$\frac{4\pi}{3} r_{\text{GDS}}^3 = K_{\text{w}} \tag{3.67}$$

where $K_{\text{w}}$ is the Kirkwood–Buff integral [205] and defines the excess volume of the solution [286] in the limit of an infinite dilution, given by

$$K_{\text{w}} = \Delta V_{\text{ex}} = \int_0^\infty (1 - g_{\text{w}}(r)) 4\pi r^2 \, \text{d}r \tag{3.68}$$

where $g_{\text{w}}(r)$ is the RDF of water molecules with respect to the macromolecule-COM. The variation in volume when $1\,\text{mol}$ of solute is added to an infinite amount of solution, defines the partial molar volume that is decomposed in an ideal solution contribution and the excess volume $\Delta V_{\text{ex}}$ [287, 288, 289]. Using Kirkwood–Buff theory [205], an expression for

the partial molar volume of macromolecule is given by

$$\overline{V}_{\mathrm{d}} = \Delta V_{\mathrm{ex}} + \kappa_T^0 \, k_{\mathrm{B}} T \tag{3.69}$$

where $\kappa_T^0$ is the isothermal compressibility of water at $300\,\mathrm{K}$. Eq. (3.69) essentially describes the effective volume occupied by the macromolecule on account of the displacement of water by the molecule. The number of replaced water molecules then would be $\Delta n_w = c_{\mathrm{w}}^{\mathrm{b}} \overline{V}_{\mathrm{d}}$, with $c_{\mathrm{w}}^{\mathrm{b}}$ as the bulk density of water.

#### 3.2.5.4 Water penetration thermodynamics

The thermodynamic signature of the macromolecule–water association can be obtained by the temperature-dependence of the PMF, thereby obtaining the distance-resolved profiles of the free energy, enthalpy, and entropy at the atomistic level [138, 290, 291, 292]. Once the distance-resolved PMF is identified, $V_{\mathrm{w}}(r)$, from macromolecule-COM as the macromolecule–water (Gibbs) free energy of association $G_{\mathrm{w}}(r)$, the corresponding entropy can be determined via the temperature dependence of free energy,

$$S_{\mathrm{w}}(r) = -\left(\frac{\partial G_{\mathrm{w}}(T, r)}{\partial T}\right)_{N,P} \tag{3.70}$$

The corresponding distance-resolved water enthalpy is then

$$H_{\mathrm{w}}(r) = G_{\mathrm{w}}(r) + T S_{\mathrm{w}}(r) \tag{3.71}$$

### 3.2.6 Further topics

#### 3.2.6.1 Electronic continuum correction (ECC)

AA MD simulations have become an essential component of the tools used in the study of biomolecular as well as synthetic systems. The time scales used in the simulation systems studied today go up to microseconds [293] or even milliseconds [294], while containing over a million atoms [295, 296, 297]. The atomistic trajectories are governed by the Hamiltonian Eq. (3.53) and the two-body interaction parameters needed in the Hamiltonian, collectively called a force-field, are empirically optimized based on benchmarking certain experimentally evaluated physical or chemical properties of the target system. Today, most of the MD simulations are performed using non-polarizable force-fields (*i.e.*, with fixed atomic partial charges) such as AMBER [188], CHARMM [189], GROMOS [190] and

OPLS [191]. These force-fields partially incorporate the effects of electronic polarization and the screening of electrostatic interactions through the effective charges on atoms and other empirical parameters [192]. In spite of these oversimplified parametrizations, the above mentioned non-polarizable force-fields have accurately modeled complex molecular systems [192, 298]. For instance, the hydration free energies and the properties of liquid water have been modeled fairly accurately without incorporating electronic polarizability in an explicit way [299, 300].

However, the implementation of non-polarizable force-fields in certain systems results in serious inaccuracies. For instance, the unaccountability of electronic polarization in the non-polarizable force-fields results in the failure in capturing the complex features connected with the hydration of divalent ions such as $Ca^{2+}$ [203, 216, 301, 302, 303, 304, 305, 306]. Owing to their high charge densities, the divalent cations such as $Ca^{2+}$ and $Mg^{2+}$ are capable of powerfully polarizing surrounding water molecules [301], with even a possibility of a potential charge transfer [307]. In a study of the interaction between the Drude-2013 polarizable protein force-field and several biologically important ions such as $Na^+$, $K^+$, $Ca^{2+}$ and $Cl^-$, it was concluded that the electronic polarization effects accounted for as much as 30% of the total protein–$Ca^{2+}$ binding energy of complexation, highlighting how traditional non-polarizable fixed charge force-fields cannot account for an ion binding in a strongly polarizable microenvironments [297]. The exclusion of electronic polarizability in the non-polarizable force-fields is also responsible for inaccurate structural and ion-pairing description of electrolytes containing monovalent ions with high charge densities, such as $Li^+$ [308]. The polarizable force-fields with the dynamic atomic charges are able to solve this issue, and are being actively explored [309, 310, 311, 312, 313, 314, 315]. However, the disadvantage of such force-fields is that they are computationally much more expensive, since the self-consistency of polarization needs to be achieved at all polarization sites, and at every MD time step [192]. As a result, polarizable force-fields cannot sample the time scales as non-polarizable ones, which is crucial if one needs to study, say biomolecular complexation phenomena, which occur at time scales from nanoseconds to microseconds. Besides, the parameter space required for polarizable force-fields is larger, in order to tune or to develop the parameters derived from quantum mechanical calculations.

As an alternative to the polarizable force-fields, Leontyev and Stuchebrukhov proposed a simple model, called molecular dynamics electronic continuum (MDEC), for accounting electronic polarization in the non-polarizable MD simulations [192]. MDEC model works well both in high- and low-dielectric media and is a low-cost alternative to fully

polarizable MD force-fields. The electronic polarization is, in essence, a distortion of the electron cloud of the medium molecules, and under the linear response approximation, it is considered to be an additive quantity [192]. The electronic subsystem of the medium molecule is much swifter compared to the nucleic motion of the molecule, due to smaller mass of electrons and high electron velocity. Therefore, electrons react instantaneously to any perturbation in the form of change in the position of medium nucleus or the change in external electric field. Hence, the total polarization is partitioned into the slow "inertial" polarization, or also termed as nuclear polarization, which depends on the configuration of medium nuclei, and fast "inertia-less" pure electronic polarization. The nuclear polarization also includes that from their electronic subsystem, which is in equilibrium with its corresponding nucleus position [192].

In the traditional non-polarizable force-fields, the pure electronic polarization part of the total polarization is completely neglected, and the remaining electronic part of nuclear polarization is incorporated in terms of the effective partial charges and other non-electrostatic parameters. For example, in a polar medium like water, the missing pure electronic polarization effect, or in other words explicit polarizability, is corrected via the modification of the solute–solvent electrostatic and Van der Waal interactions [192, 213]. Hence, to account for the consistency in the treatment of the electrostatic interactions between the solute and solvent, effective charges that incorporate explicit polarizability should be used for both [316]. Assuming the electronic polarization response as continuum, the effective atomic charges are simply the actual charges scaled by $1/\sqrt{\varepsilon_e}$, where $\varepsilon_e$ is the part of the dielectric constant contributed by the electronic degrees of freedom ($\varepsilon_e = 1.78$ for water) [192, 213, 316]. This adjustment in the atomic partial charges can also be interpreted as an explicit initiation of the electronic dielectric continuum [214, 316], and in the chapter 4, this model will be referred to as the Electronic Continuum Correction (ECC) model.

## 3.3 Coarse-grained (CG) simulations: Basics

AA MD simulations involve atomistically resolved degrees of freedom including those of solvent molecules, which renders them as computationally costly. In this scenario, the minimization of the computational effort and a broader perspective on the electrostatic properties of the system can be achieved by coarse-graining the molecules, modeling the solvent by a dielectric background continuum, and employing the Langevin dynamics (also termed as stochastic dynamics (SD)) simulations. These simulations are then based on
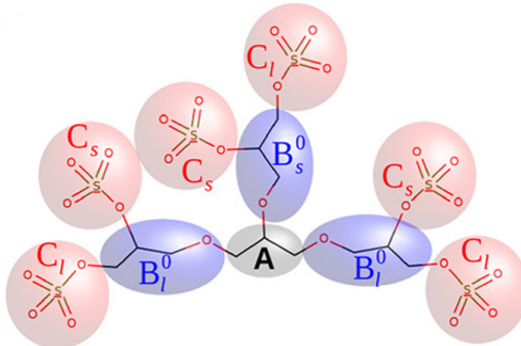
Figure 3.2: Atomistic and CG structure of the $G_0$-dPGS molecule. We depict the atomistic subunits $C_3H_5$, $-C_3H_5O-$, and $-OSO_3$ corresponding to the CG bead types $A$, $B_i$, and $C_i$ ($i = s, l$). Reprinted with permission from Xu et al. [114] Copyright © 2017 American Chemical Society.

the Langevin equation of motion given as

$$m_i \frac{\mathrm{d}^2 \vec{r}_i}{\mathrm{d}t^2} = -m_i \zeta_i \frac{\mathrm{d}\vec{r}_i}{\mathrm{d}t} - \nabla_i U + \vec{R}_i(t) \tag{3.72}$$

where $\zeta_i$ is the relaxation rate of the $i$th CG bead. $U$ is the system potential energy, which includes harmonic bonded interactions between neighbouring beads, dihedral potentials and inter-atomic Lennard-Jones (LJ) between all non-neighbouring beads. The force $\vec{R}_i(t)$ is a time dependent Gaussian noise process that mimics the solvent impacts and satisfies the fluctuation-dissipation theorem

$$\beta \left\langle \vec{R}_i(t) \cdot \vec{R}_j(t') \right\rangle = 2m_i \zeta_i \delta(t - t') \delta_{ij} \tag{3.73}$$

Note that the solvent in Langevin dynamics is modeled as a continuous medium, thus the electrostatic interaction should be scaled with static dielectric constant $\varepsilon_r$. CG models are typically used for molecular modeling of biomolecules at different resolutions [317, 318]. A wide range of coarse-grained models are available in the literature. Some of the examples are the computational models of specific molecules such as proteins [317, 318], nucleic acids [319, 320], lipid membranes [318, 321], carbohydrates [322] or water [323]. In the chapter 5, we study the competitive ion binding on dPGS using its CG model. The example of CG $G_0$-dPGS model is shown in Fig. 3.2.

## 3.4   Isothermal titration calorimetry (ITC) experiments

Macromolecular binding in the biological and physicochemical systems can be reliably characterized by the isothermal titration calorimetry (ITC). ITC can directly provide the

thermodynamic analysis of the binding in the form of the heat of binding, stoichiometry, binding constant, Gibbs free energy, and entropy changes.

An ITC apparatus consists of two identical and highly thermally conductive cells which are embedded in an adiabatic chamber [324]. A sample cell contains the macromolecule solution (substrate), while the other cell, called the reference cell, contains the buffer or water without the macromolecule. Constant heat is supplied to both cells initially. The temperature within the sample cell is maintained by detecting its temperature difference with the reference cell using sensitive thermocouple circuits and then by regulating the power supply using the feedback mechanism. During the titration, the ligand solution in a precise concentration is injected through a syringe into the sample cell. Based on the exothermic or endothermic nature of the substrate–ligand binding process, the resultant heat exchange takes place with the surroundings in the sample cell. The time-dependent power supply needed for the sample cell to maintain its temperature same as that of the reference cell is then recorded. The experimental raw data is the time series of peaks of heat required to balance the temperature of the sample cell, with each peak representing an injection process. The time integral of the peaks gives the heat exchange $Q$ during the titration.

The adsorption of a ligand on the macromolecule (substrate) is associated with the heat exchange $Q$, which is measured in the ITC experiments vs. the total ligand concentration $c^0$. The ITC analysis of adsorption of one component ligand on the macromolecule is given in previous works by Dzubiella [254, IV, 325]. Defining the total macromolecule (substrate) concentration in the titration volume $V$ as $c_d$, and introducing the molar ratio $x = c^0/c_d$, $Q$ is given by [254, IV, 325]

$$Q(x) = c_d V \int_0^x dx' \frac{\partial H(N^b(x'))}{\partial x'} \tag{3.74}$$

where $H(N^b)$ is the total heat exchanged *per macromolecule* on adsorption of $N^b$ ligands and $N^b(x)$ depicts the binding isotherm, *i.e.*, the number of bound ligands as a function of the molar ratio $x$ at a fixed temperature.

In order to track the changes in the heat exchange during the titration, differential heat $Q'(x) = dQ/dx$ is typically measured, as the ligand is incrementally supplied to the solution. $Q'(x)$ is given as

$$\frac{1}{c_d V} Q'(x) = \frac{\partial H(N^b(x))}{\partial N^b} \frac{\partial N^b(x)}{\partial x} \tag{3.75}$$

The function $H(N^{\mathrm{b}})$ is typically not known due to the complex interactions governing the ligand binding on the macromolecule, and it is in practice assumed to be linearly proportional to $N^{\mathrm{b}}$, *i.e.*, $H(N^{\mathrm{b}}) = \Delta H N^{\mathrm{b}}$, where $\Delta H$ (heat exchanged *per bound ligand*) is constant and independent of the already bound ligands. This modifies Eq. (3.75) as

$$\frac{1}{c_{\mathrm{d}}V}Q'(x) = \Delta H \frac{\partial N^{\mathrm{b}}(x)}{\partial x} \tag{3.76}$$

Eq. (3.76) connects the differential heat exchange during the binding of the ligand to the one component ligand binding model $N^{\mathrm{b}}(x)$.

In the chapter 6, we study a competitive sorption of $Mg^{2+}$ and $Na^{+}$ cations on $G_2$-dPGS via ITC experiments. Owing to the different chemical identities of these counterions (ligands), here we extend the one component ligand binding model described above to a two component ligand binding model, in a preliminary fashion. For the case of two ligands, which we designate here as $++$ and $+$ corresponding to $Mg^{2+}$ and $Na^{+}$ cations, respectively, Eq. (3.76) changes as

$$
\begin{aligned}
\frac{1}{c_{\mathrm{d}}V}Q'(x) &= \Delta H_{++} \frac{\partial N^{\mathrm{b}}_{++}(x)}{\partial x} + \Delta H_{+} \frac{\partial N^{\mathrm{b}}_{+}(x)}{\partial x} \\
&= (\Delta H_{++} + \lambda \Delta H_{+}) \frac{\partial N^{\mathrm{b}}_{++}(x)}{\partial x}
\end{aligned}
\tag{3.77}
$$

where $x = c^0_{++}/c_{\mathrm{d}}$ is the molar ratio of $Mg^{2+}$ to that of dPGS in the solution. $\lambda = \frac{\partial N^{\mathrm{b}}_{+}(x)}{\partial N^{\mathrm{b}}_{++}(x)}$ is the ratio of differential amount of bound $Na^{+}$ to dPGS to that of $Mg^{2+}$ counterions, or simply called an exchange ratio. $\lambda$ is negative due to the competitive ligand binding and is assumed to be constant throughout the titration. Eq. (3.77) thus represents two component ligand binding in terms of a *pseudo one component* ligand binding model with a constant binding enthalpy $\Delta H_{++} + \lambda \Delta H_{+}$ per bound $Mg^{2+}$ cations to the dPGS.

In terms of numerical differences, Eq. (3.77) can be rewritten as

$$\frac{1}{\eta}\frac{\Delta Q}{\Delta x} = \frac{\Delta N^{\mathrm{b}}_{++}(x)}{\Delta x} \tag{3.78}$$

where $\eta = c_{\mathrm{d}}V(\Delta H_{++} + \lambda \Delta H_{+})$ is a constant. The incremental heat exchange $\Delta Q$ is thus directly proportional to that in the number of bound $Mg^{2+}$ cations $\Delta N^{\mathrm{b}}_{++}$. Hence, assuming the heat exchange corresponding to the $k^{\mathrm{th}}$ titration step ($k = 1, 2, \cdots n$) as $\Delta Q_k$ and the respective differential number of bound ligands as $\Delta N^{\mathrm{b}}_{++}(x_k)$, the differential number of bound $Mg^{2+}$ cations in $k+1^{\mathrm{th}}$ titration step are related to those from $k^{\mathrm{th}}$ titration step

as

$$\Delta N^{\mathrm{b}}_{++}(x_{k+1}) = \frac{\Delta Q_{k+1}}{\Delta Q_k} \Delta N^{\mathrm{b}}_{++}(x_k) \tag{3.79}$$

One important key assumption made here is that the amount of $Mg^{2+}$ cations during the first titration step $(k = 1)$ are entirely bound to the dPGS. In other words, the entire amount of $Mg^{2+}$ cations introduced in the titration cell after the first titration step is depleted from the bulk, $i.e.$, $\Delta N^{\mathrm{b}}_{++}(x_1) = x_1 = c^0_{++,1}/c_{\mathrm{d}}$. The subsequent differential numbers of bound $Mg^{2+}$ cations are then evaluated using Eq. (3.79). The obtained $Mg^{2+}$ binding isotherm $N^{\mathrm{b}}_{++}(x)$ is then compared with the theoretical binding models in the chapter 6.

# 4 Charge and hydration structure of dendritic polyelectrolytes: Molecular simulations of polyglycerol sulphate

Macromolecules based on dendritic or hyperbranched PEs have been emerging as high potential candidates for biomedical applications. In this chapter, the charge and solvation structure of dendritic polyglycerol sulphate (dPGS) of generations 0 to 3 in aqueous monovalent salt (sodium chloride) solution is studied using AA, explicit-solvent MD computer simulations. The dPGS is characterized by calculating several important properties such as molecular distributions, Solvent Accessible Surface Area (SASA), and the partial molar volume. In particular, as the dPGS exhibits high charge renormalization effects, the challenges of how to obtain a well-defined effective charge and surface potential of dPGS for practical applications, are addressed. The implicit- and explicit-solvent approaches in the results obtained from the AA simulations performed in this work with the CG simulations in Xu et al., are compared. Consistent values are found for the effective electrostatic size (i.e., location of the effective charge of a DH sphere) within all the approaches, deviating by mostly the size of a water molecule. The excess chemical potential of water insertion into dPGS and its thermodynamic signature are also presented and rationalized. Further, owing to the presence and significance of divalent ions in biological realm, dPGS is electrostatically characterized in a solution mimicking an aqueous physiological solution containing a mixture of divalent and monovalent salts (magnesium and sodium chloride). Performances of several recently advanced non-polarizable force-fields for magnesium(II) cations are quantitatively compared, and the competitive sorption isotherm of magnesium(II) and sodium cations on dPGS, along with the corresponding qualitative trends in dPGS electrostatics are rationalized. Note that part of the descriptions and figures in this chapter are taken almost directly from our previous publication [I].

## 4.1 dPGS in monovalent salt

### 4.1.1 Atomistic simulations method

Initial atomistic structures of all generations ($n = 0 - 3$) of the PGS dendrimers (*cf.* Fig. 1.2(b)) were constructed using the Marvin software [Marvin 16.4.11.0, 2016, ChemAxon
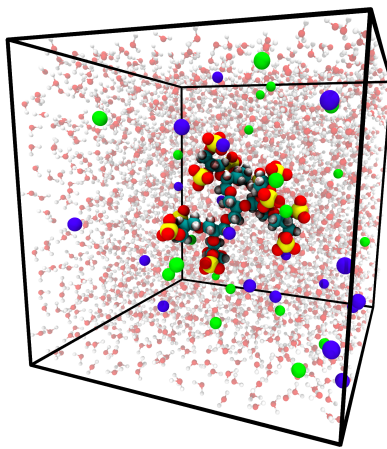
Figure 4.1: Simulation snapshot of the simulation box of 15.7 nm size, showing $G_1$-dPGS with $Na^+$ (violet spheres) and $Cl^-$ (green spheres) ions acting as counter- and co-ions, respectively. Water is also shown in the background (not to scale).

(www.chemaxon.com)]. $Na^+$ and $Cl^-$ ions were used as counterions and coions, respectively. MD simulations were performed using the GROMACS 5.0.6 platform [260, 261, 262, 263], employing the General Amber Force Field (GAFF) [326, 327] for dPGS and ions. Partial charges for dPGS atoms were calculated using AM1-BCC quantum mechanical charge model [328], which is compatible with GAFF. The antechamber package [327, 329] from USCF Chimera software [330] was used to assign the partial charges which are summarized along with the force-field parameters in Appendix A.1.1.

The structures were subject to a series of initialization and equilibration protocols. First, the dendrimer was immersed in a cubic simulation box filled with the water molecules of Simple Point Charge-Extended (SPC/E) model [331]. Pertaining to the aim of studying the electrostatic potential distribution around dPGS dendrimer and in order to curb finite size effects, large sizes of the boxes were used ranging from 13 nm for $G_1$-dPGS to 26 nm for $G_3$-dPGS (*cf.* Table 4.1). The appropriate numbers of $Na^+$ and $Cl^-$ ions are then inserted to ensure electroneutrality and a bulk salt concentration of 25 mM. The system was then subject to energy minimization and 100 ns equilibration in the $NPT$ ensemble at 1 bar and 300 K. The production MD simulations in the same $NPT$ ensemble for each of the dendrimers were subsequently performed for 150 ns. Bonds involving hydrogens were constrained by the LINCS algorithm [332]. The electrostatic interactions were calculated with the Particle Mesh Ewald method [277] using 1 nm as a short-range cut-off. The short-range Lennard-Jones cut-off was set to 1 nm. The details of the simulation conditions for all generations are summarized in Table 4.1 and the simulation snapshot for $G_1$-dPGS is shown in Fig. 4.1.

| dPGS Generation | dPGS atoms | number of water molecules | Box length (nm) | number of cations | number of anions |
|---|---|---|---|---|---|
| 0 | 65 | 66,394 | 12.6 | 32 | 26 |
| 1 | 149 | 128,075 | 15.7 | 101 | 89 |
| 2 | 317 | 308,645 | 21.0 | 163 | 139 |
| 3 | 653 | 583,725 | 25.9 | 313 | 265 |

Table 4.1: System details for the simulations of the four different generations. The pressure and temperature are fixed to 1 bar and $T = 300\,\mathrm{K}$ in the simulations, respectively, and the bulk salt concentration is 25 mM.

## 4.1.2 Density distribution functions

### 4.1.2.1 Terminal groups

Fig. 4.2 shows the atomic radial density distributions with respect to the dPGS-COM. The radial density of the terminal sulphur is inhomogeneous and has pronounced peak(s) as shown in Fig. 4.2(a). Excluded volume interactions along with bond constraints and charge repulsion lead to shifts of the positions of maxima with generations to larger distances. A single peaked distribution is found for generations $G_0$ and $G_1$ indicating that most of the terminal sulphur atoms stay on the molecular surface. The breadth of distribution increases with generation. For generations $G_2$ and $G_3$, the distribution becomes bimodal with a minor peak at $r = 0.6\,\mathrm{nm}$. This indicates that fraction of total sulphate groups reside in the interior of the dendrimer. This penetration of terminal groups into the interior volume called "backfolding" has already been observed in previous literature [333, 334, 335, 336]. The increase in the number of terminal sulphate groups with higher generation leads to higher charge density in the dPGS corona [114], leading to higher electrostatic repulsion that essentially leads to backfolding. The major peak position of the distribution is used to define the "structural" or "intrinsic" dPGS radius $r_{\mathrm{d}}$ (*cf.* Table 4.2). A monotonic increase in $r_{\mathrm{d}}$ with generation is observed, from $r_{\mathrm{d}} = 0.66\,\mathrm{nm}$ for $G_0$ to $r_{\mathrm{d}} = 1.4\,\mathrm{nm}$ for $G_3$. These quantities are also compared to the standard radius of gyration in Table 4.2.

With the knowledge of the intrinsic dPGS radius $r_{\mathrm{d}}$, along with the bare charge valency $Z_{\mathrm{d}}$, estimates of the effective charge valency $Z_{\mathrm{eff}}$, the dPGS bare charge density $\sigma_{\mathrm{d}} = Z_{\mathrm{d}}e/4\pi r_{\mathrm{d}}^2$ and effective surface charge density $\sigma_{\mathrm{eff}} = Z_{\mathrm{eff}}e/4\pi r_{\mathrm{eff}}^2$ can be defined, respectively. The number of terminal sulphate groups increases with generation, thus increasing $\sigma_{\mathrm{d}}$, on the other hand, the tendency of backfolding of the terminal groups also
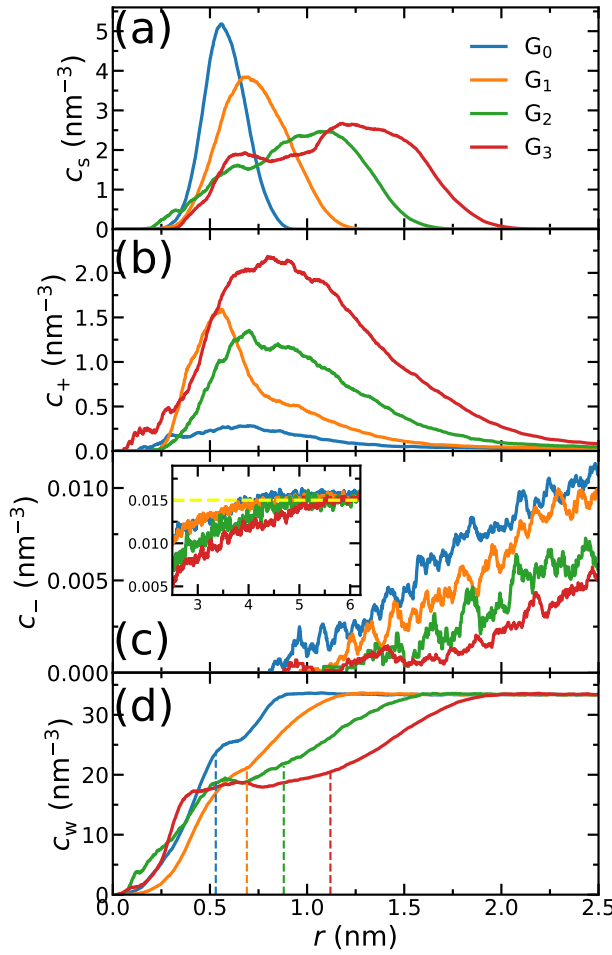
Figure 4.2: Radial density distributions $c_i(r)$ with respect to the dPGS-COM of (a) sulphur atoms of the terminal sulphate groups, $i = S$, (b) cations (counterions; $i = Na^+$), (c) anions (coions; $i = Cl^-$), and (d) water molecules for all four generations. In the inset of panel (c) the anion density profiles at larger distances are shown, with the bulk density $c_-^b = 25\,mM$ marked by a dashed horizontal line. (d) Water radial density distribution. The vertical dashed lines indicate the location of dPGS–water Gibbs dividing surface $r_{GDS}$ for each generation (*cf.* Sec. 3.2.5.3 and Table 4.3).

| | $G_0$ | $G_1$ | $G_2$ | $G_3$ |
|---|---|---|---|---|
| MW (kDa) | 0.79 | 1.72 | 4.10 | 8.32 |
| $r_d$ (nm) | 0.66 | 0.86 | 1.16 | 1.40 |
| $Z_d$ | $-6$ | $-12$ | $-24$ | $-48$ |
| $\sigma_d$ ($e\,nm^{-2}$) | $-1.08$ | $-1.30$ | $-1.41$ | $-1.93$ |
| $R_g$ (nm) | 0.57 | 0.75 | 1.03 | 1.28 |

Table 4.2: Intrinsic parameters of atomistic dPGS. MW is the molecular weight of the molecule while $r_d$ and $Z_d$ stand for the intrinsic radius (defined by the terminal sulphur peak position in the density distribution (*cf.* Fig. 4.2(a)) and bare charge valency, respectively, leading to the bare dPGS surface charge density $\sigma_d$. $R_g$ is the radius of gyration.

increases with generation, thus hampering the growth of $\sigma_\mathrm{d}$. Table 4.2 shows that the net result is a monotonic increase in $\sigma_\mathrm{d}$ implying minor contribution of backfolding.

### 4.1.2.2 Counterions and salt

Fig. 4.2(b) shows the counterion density distributions which exhibit a single peak and decay in the exponential (DH-like or Yukawa) fashion for $r \gtrsim r_\mathrm{d}$, while reaching bulk concentration at large distances. Whereas the electrostatic attraction of the terminal sulphate groups drives counterions towards dPGS, excluded volume restricts their entropy. This combined effect leads to the non-monotonic distribution. Co-ions, on the other hand, as indicated in Fig. 4.2(c), are depleted from the dPGS interior due to electrostatic repulsion.

### 4.1.2.3 Water

Apart from the open morphology of dPGS, which is favourable for the water uptake, the electrostatic repulsion between like-charged terminal sulphate groups and their polar nature facilitate their interaction with water. Hence, water penetrates into dPGS interior as depicted in Fig. 4.2(d), which shows the radial density of water as a function of distance from the dPGS-COM for all generations. The water density gradually rises as on going radially outward from dPGS-COM and reaches its bulk value. It is seen that, besides the water penetration into the dendrimer interior, the density profile starts to develop a peak with increasing generation at the region around 0.6 nm. This could be attributed to the backfolding of sulphate groups in the interior region of dendrimer, since water indulges in a preferential interaction with sulphate groups due to their polar nature. The dashed lines represent the locations of Gibbs dividing surfaces $r_\mathrm{GDS}$ (*cf.* Sec. 3.2.5.3) of individual generations reported in Table 4.3. It can be seen that $r_\mathrm{GDS}$ increases almost linearly with generation and is roughly 80% of the bare radius $r_\mathrm{d}$ for all generations (*cf.* Table 4.2 and 4.3).

Another effective means to characterize dendrimer hydration properties is by calculating the solvent accessible surface area (SASA) and the solvent excluded volume (VSE), which can also be deduced by observing Fig. 4.2(d) that there is a significant water uptake by dPGS molecules. Although the outer surface of dPGS is available for interaction with water and ionic species, there still remains significant accessible internal surface area in a dendrimer immersed in water. To evaluate the SASA and VSE, each dendrimer atom is assumed as a sphere with the radius $r_i$ being the sum of the van der Waals radius of that

|  | $G_0$ | $G_1$ | $G_2$ | $G_3$ |
|---|---|---|---|---|
| $r_{\mathrm{GDS}}$ (nm) | 0.53 | 0.69 | 0.88 | 1.12 |
| SASA (nm$^2$) | 9.56 | 16.60 | 34.38 | 61.16 |
| $\overline{V}_{\mathrm{d}}$ (nm$^3$) | 0.64 | 1.34 | 2.83 | 5.88 |
| $\Delta n_{\mathrm{w}}$ | 21.24 | 44.35 | 91.32 | 197.55 |

Table 4.3: dPGS–water interaction parameters. $r_{\mathrm{GDS}}$ stands for the Gibbs dividing surface (*cf.* Sec. 3.2.5.3). SASA is the SASA of dPGS evaluated with the probe radius of 0.15 nm which is approximately the radius of one water molecule [337]. $\overline{V}_{\mathrm{d}}$ is the partial molar volume of dPGS (*cf.* Sec. 3.2.5.3) and $\Delta n_{\mathrm{w}}$ denotes the corresponding number of water molecules replaced by dPGS.

atom, $r_{vdW}$, and a water 'probe' radius $r_p$, i.e., $r_i = r_{vdW} + r_p$. The dendrimer is thus assumed as a union of such fused spheres. The SASA is defined as the surface traced by spherical solvent probe as it rolls around the van der Waals spheres of the dendrimer [77]. The values of the SASA for a typical probe radius of 0.15 nm (length scale of a water molecule) for all generations are listed in Table 4.3.
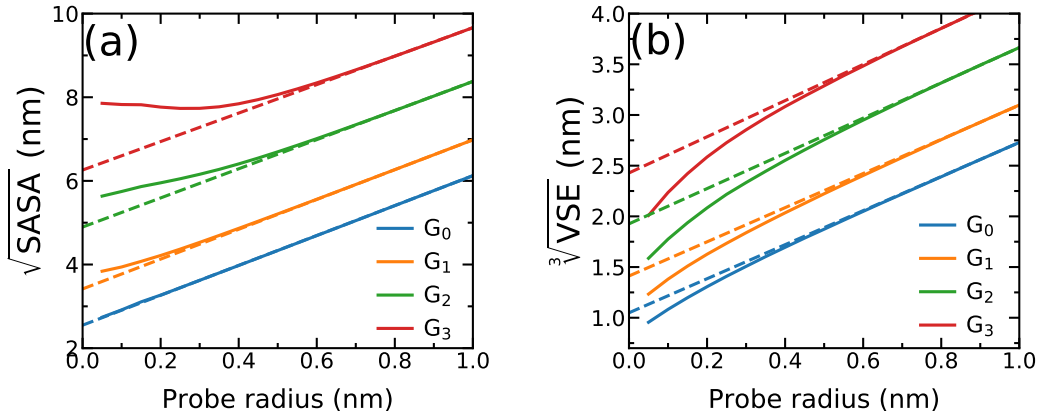


Figure 4.3: (a) $\sqrt{\mathrm{SASA}}$ and (b) $\sqrt[3]{\mathrm{VSE}}$ as a function of probe radius $r_p$. The linear behaviour in the high $r_p$ range is extrapolated to $r_p = 0$ (shown by dashed lines) to acquire the dendrimer surface area and volume in the absence of internal pores and voids.

Fig. 4.3 plots $\sqrt{\mathrm{SASA}}$ and $\sqrt[3]{\mathrm{VSE}}$ as a function of probe radius for all generations. We can see that both quantities increase with higher dendrimer generation and also increase linearly with the probe radius (except for small probe radius) [77]. For small probe radius we see deviations from linear behavior of $\sqrt{\mathrm{SASA}}$ due to the extra surface in the interior of dendrimer, and $\sqrt[3]{\mathrm{VSE}}$ due to exclusion of the volume of interior voids. Assuming the shape of the dendrimer to be spherical, we can estimate the exterior surface area and the size of the dendrimer from these plots using linear regression. For such a case SASA and VSE are given by $4\pi(R_{\mathrm{SA}} + r_p)^2$ and $4\pi(R_{\mathrm{VSE}} + r_p)^3/3$, respectively. The intercept at zero probe radius leads to the estimate of surface area and volume of the dendrimer

|  | $G_0$ | $G_1$ | $G_2$ | $G_3$ |
|---|---|---|---|---|
| $R_{SA}$ (nm) | 0.72 | 0.96 | 1.38 | 1.76 |
| $R_{VSE}$ (nm) | 0.65 | 0.87 | 1.19 | 1.50 |
| $\Sigma$ (nm$^2$) | 0.00 | 0.20 | 2.50 | 14.00 |
| $\Lambda$ (nm$^3$) | 0.00 | 0.02 | 0.07 | 0.09 |

Table 4.4: Results of SASA and VSE calculations for dPGS–water interaction (*cf.* Fig. 4.3). $R_{SA}$ and $R_{VSE}$ stand for the radius of dPGS estimated via calculation of SASA and of VSE, respectively. $\Sigma$ and $\Lambda$ define the surface area and volume of dPGS interior voids respectively.

excluding the voids and pores inside. The radii of the dendrimer $R_{SA}$ and $R_{VSE}$ found this way are given in Table 4.4. The difference between the calculated points and regression line gives the internal area $\Sigma$ and volume $\Lambda$ of the pores and interior voids, which are are listed for different generations in Table 4.4 for a probe radius of 0.15 nm.

### 4.1.3   Electrostatic properties of dPGS

#### 4.1.3.1   Effective size and charge: PMF method

We start the electrostatic characterization of dPGS by defining its effective size and charge via the PMF method described in the section 3.1.2.4.3. The structure of the electrolyte solution surrounding the dPGS is analysed by calculating the RDFs between the dPGS-COM and ions/water $g_i(r)$ [$i = +(Na^+), -(Cl^-)$, water]. The long-range part of the dPGS–counterion PMF $V_+(r)$ obtained by Boltzmann inversion of counterion radial number distribution $g_+(r)$ (Eq. (3.12)), is then quantitatively mapped onto the basic DH theory (Eq. (3.38)). Note again that here no assumptions have to be made on the dielectric constant of water. Fig. 4.4 shows the logarithm of a rescaled PMF, $r\beta V_+(r)$, as a function of distance from dPGS-COM for all generations. It is seen that at large distances, the profiles decay linearly for all generations with a slope $\kappa = 0.52\,\text{nm}^{-1}$ corresponding to salt concentration $c_+^b = 25\,\text{mM}$. As opposed to the exponential behavior at large distances, the PMF reaches a maximum at smaller distances before it decreases to almost zero close to the dPGS core. This highly non-linear behavior is expected to be attributed to high electrostatic and steric correlations between dPGS atoms and counterions. As shown in Fig. 4.4, the boundary can now be set between the long-range ($r > r_{eff}$) DH-like PMF $V^{DH}(r)$, which decays linearly and the short-range ($r_d < r < r_{eff}$) PMF, which is non-linear. As a criterion, $r_{eff}$ is defined as the shortest distance where the DH fit (minimizing the root mean square deviation to the PMF) and PMF cross before the maximum
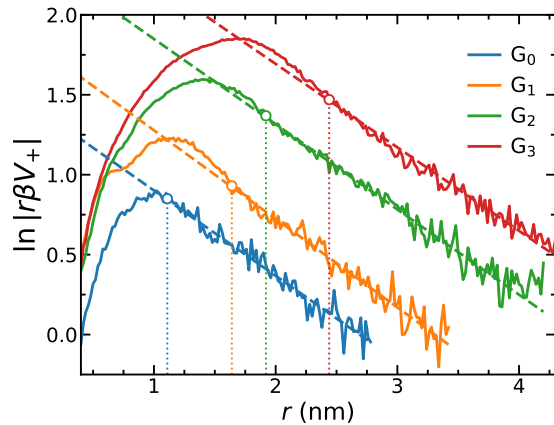
Figure 4.4: The rescaled PMF $V_+(r)$ between dPGS and $Na^+$ ions plotted for all generations. The dashed lines are fits of Eq. (3.38) in the far-field. Their slopes determine the inverse Debye length $\kappa = 0.52\,\mathrm{nm}^{-1}$ corresponding to the bulk salt concentration $c_+^b = 25\,\mathrm{mM}$. The dotted vertical lines indicate the effective radius of dPGS, $r_{\mathrm{eff}}$, which separates the non-linear short-range nature of electrostatic potential regime from the long-range linear DH regime (see also text). The corresponding values such as effective dPGS charge valency $Z_{\mathrm{eff}}$, the number of bound counterions $N_+^b$, and effective charge density $\sigma_{\mathrm{eff}}$ are summarized in Table 4.5.

of the PMF [114]. This formulation treats the dPGS as homogeneously charged sphere of effective radius $r_{\mathrm{eff}}$ at which the effective surface charge valency $Z_{\mathrm{eff}}$ can be defined. Fig. 4.4 shows the location of $r_{\mathrm{eff}}$ for each generation with vertical dotted lines. The corresponding electrostatic properties are listed in Table 4.5.

### 4.1.3.2 Effective size and charge: Alexander prescription

The radial density distributions of charges can be now utilised to calculate the local charge accumulation (or running ion coordination) and electrostatic potential profile around dPGS. Following the "implicit-water" approach described in sections 3.2.5.1 and 3.2.5.2.2, the total cumulative charge valency distribution $Z_{\mathrm{acc}}(r)$, or in other words the local net charge valency (Eq. (3.66)) is shown in Fig. 4.5(a). On probing away from dPGS-COM, the charge build-up due to dPGS terminal groups and coions leads to more negative $Z_{\mathrm{acc}}$ close to dPGS. Subsequently, a reversal in its profile is seen at a distance where counterion accumulation starts becoming dominant and the magnitude of $Z_{\mathrm{acc}}$ tends to decrease onwards. This so-called charge renormalization effect has been extensively studied and wide variety of theories have been developed for the effective charge and size of simple charged spheres with smooth surfaces [16, 17, 115, 120, 121]. A comparison of the cumulative charge valency $Z_{\mathrm{acc}}$ distributions of the implicit versus explicit-water integrations agrees in the long-range decay. The explicit-route profiles are very noisy, however, due to strong water fluctuations (see Appendix A.1.3). A comparison of implicit and explicit
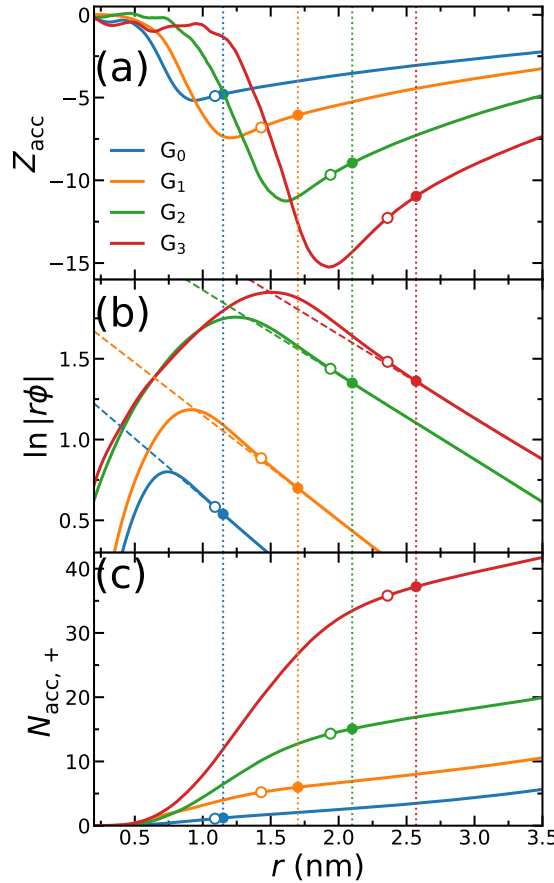
Figure 4.5: Using the "implicit-water" approach (including charge density distributions of all species except water and assuming $\varepsilon_{\mathrm{w}} = 72$), (a) net cumulative charge valency $Z_{\mathrm{acc}}(r)$ as a function of distance $r$ from dPGS-COM, (b) Alexander prescription (*cf.* Sec. 3.1.2.4.1) showing the logarithm of the rescaled electrostatic potential. The dashed lines are fits of Eq. (3.33) to the MD results in the far-field. (c) Cumulative counterion coordination $N_{\mathrm{acc},+}(r)$. The vertical dotted lines denote the effective radii of dPGS, $r_{\mathrm{eff}}$, intersecting the curves in filled circles. Empty circles denote radii $r_{\mathrm{inf}}$ according to the inflection point criterion (*cf.* Sec. 3.1.2.4.2). The two circle types (corresponding to the Alexander prescription and the inflection point criterion) thus indicate effective charge valency $Z_{\mathrm{eff}}$, effective potential $\phi_{\mathrm{eff}}$ and number of condensed counterions $N_{+}^{\mathrm{b}}$ on the respective vertical axes in (a), (b), and (c), respectively.

approaches on the level of the electrostatic potential will be discussed later.

One of the aims of this chapter is to define the effective charge valency of the dendrimer $Z_{\mathrm{eff}}$ and effective surface potential $\phi_{\mathrm{eff}}$ within the linear DH picture. The DH theory works well in the far-field limit whereas the short-range non-linear effects arising from condensed counterions are neglected and absorbed in the effective charge (as demonstrated, *e.g.*, by solutions of the full non-linear PB theory [15, 16, 17, 115, 118] discussed in Sec. 3.1.2.4). Hence, instead of mapping to ionic PMFs, it was showed in the section 3.1.2.4.1 that equivalently, a direct mapping of the long-range decay of the total electrostatic potential onto the spherical DH form (Alexander prescription) may also serve as a practical defining equation for the effective properties seen in the far-field and thus can quantify the diffusive

double-layer behavior with high accuracy [114]. This tool can thus be used to define the location $r_{\text{eff}}$ of the interface between the diffusive counterion layer in the DH sense and the non-linear behavior of the correlated and condensed ions deep in the surface layer.

Adopting this approach and assuming an implicit-water with $\varepsilon_{\text{w}} = 72$ ($l_{\text{B}} = 0.72\,\text{nm}$), a logarithm of the rescaled potential $\left|r\phi(r)\right|$ is plotted as a function of distance from dPGS-COM for all generations as shown in Fig. 4.5(b). At large distances, the profiles decay linearly for all generations with the slope $\kappa = 0.52\,\text{nm}^{-1}$, corresponding consistently to the bulk salt concentration of $c_+^{\text{b}} = 25\,\text{mM}$. Hence, it is possible in this approach to define the effective electrostatic surface potential $\phi_{\text{eff}}$ as the potential at $r_{\text{eff}}$ ($\phi_{\text{eff}} = \phi(r_{\text{eff}}) = \phi_{\text{DH}}(r_{\text{eff}})$). As before, $r_{\text{eff}}$ is defined as the shortest distance where the DH fit (minimizing the root mean square deviation to the PMF) and PMF cross before the maximum of the PMF (*cf.* Sec. 3.1.2.4.1) [114]. The location of $r_{\text{eff}}$ for each generation is shown in Fig. 4.5 by vertical dotted lines. The intersection points in Figs. 4.5(a) and (c) denote $Z_{\text{eff}}$ and the number of cumulative counterions at $r_{\text{eff}}$, $N_+^{\text{b}} = N_{\text{acc},+}(r_{\text{eff}})$, respectively. It is seen that $r_{\text{eff}}$ increases with generation. Comparing $Z_{\text{eff}}$ values with the corresponding bare charge valency $Z_{\text{d}}$ values (*cf.* Tables 4.5 and 4.2) a significant charge renormalization can be realized.

### 4.1.3.3 Effective size and charge: inflection point criterion

As described in the section 3.1.2.4.2, it is also customary to define the crossover radius from diffusive to condensed ionic layers as an inflection point in the plot of $Z_{\text{acc}}$ vs. the inverse radial distance $1/r$ [16, 114, 121]. Inflection points are shown in Fig. 4.5 as empty circle symbols. The corresponding effective potential and the number of condensed counterions can be read from circle symbols at the respective vertical axes in Figs. 4.5(b) and (c), respectively.

### 4.1.3.4 Discussion

Table 4.5 summarizes the electrostatic attributes of dPGS stemming from their different definitions. An increase in $r_{\text{eff}}$ and the magnitude of $Z_{\text{eff}}$ is observed with increasing dPGS generation along with substantial charge renormalization. As an example, $G_3$-dPGS has a bare charge valency $Z_{\text{d}}$ of $-48$ (*cf.* Table 4.2), which is effectively renormalized to $Z_{\text{eff}} \sim -11$ at larger distances $r > r_{\text{eff}}$ according to the Alexander prescription. A clear trend in $Z_{\text{eff}}$ with respect to dPGS generation is observed, which shows that the counterion condensation increases with generation due to corresponding higher charge density of

| Method | Label | $G_0$ | $G_1$ | $G_2$ | $G_3$ |
|---|---|---|---|---|---|
| | $r_{\text{eff}}$ (nm) | 1.05 | 1.63 | 1.94 | 2.47 |
| PMF method [249] | $Z_{\text{eff}}$ | $-4.98$ | $-6.20$ | $-9.59$ | $-11.39$ |
| | $\sigma_{\text{eff}}$ ($e\,\text{nm}^{-2}$) | $-0.36$ | $-0.18$ | $-0.20$ | $-0.14$ |
| | $r_{\text{eff}}$ (nm) | 1.15 | 1.70 | 2.10 | 2.57 |
| Alexander | $Z_{\text{eff}}$ | $-4.80$ | $-6.06$ | $-8.95$ | $-10.96$ |
| prescription [15] | $\sigma_{\text{eff}}$ ($e\,\text{nm}^{-2}$) | $-0.29$ | $-0.17$ | $-0.16$ | $-0.13$ |
| | $\phi_{\text{eff}}$ | $-1.56$ | $-1.30$ | $-1.78$ | $-1.52$ |
| | $r_{\text{inf}}$ (nm) | 1.09 | 1.43 | 1.94 | 2.36 |
| Inflection | $Z_{\text{inf}}$ | $-4.90$ | $-6.80$ | $-9.67$ | $-12.27$ |
| point [16] | $\sigma_{\text{inf}}$ ($e\,\text{nm}^{-2}$) | $-0.33$ | $-0.26$ | $-0.20$ | $-0.17$ |
| | $\phi(r_{\text{inf}})$ | $-1.72$ | $-1.82$ | $-2.12$ | $-1.86$ |
| | $r_{\text{eff}}$ (nm) | 0.70 | 1.60 | 1.90 | 2.40 |
| Xu et al. [114] | $Z_{\text{eff}}$ | $-6.00$ | $-7.30$ | $-10.60$ | $-14.30$ |
| CG simulation | $\sigma_{\text{eff}}$ ($e\,\text{nm}^{-2}$) | $-0.97$ | $-0.23$ | $-0.23$ | $-0.20$ |
| ($c_+^{\text{b}} = 10\,\text{mM}$) | $\phi_{\text{eff}}$ | $-4.20$ | $-2.12$ | $-2.37$ | $-2.22$ |

Table 4.5: Electrostatic parameters of dPGS obtained using the PMF method [249], Alexander prescription [15] and the inflection point criterion [16] evaluated at the bulk salt concentration of $c_+^{\text{b}} = 25\,\text{mM}$. Values from previous CG simulations by Xu et al. [114] are also compared. Here, $r_{\text{eff}}$ is the effective dPGS radius. $Z_{\text{eff}}$ stands for the effective dPGS charge valency after charge renormalization due to counterions. $\sigma_{\text{eff}}$ thus is the effective surface charge density while $\phi_{\text{eff}} = \phi(r_{\text{eff}})$ (or $\phi(r_{\text{inf}})$) is the effective electrostatic potential at $r_{\text{eff}}$ (or $r_{\text{inf}}$).

dPGS corona. This agrees with the consistent shift away from dPGS, in the inflection point of the cumulative charge valency $Z_{\mathrm{acc}}$ as shown in all panels of Fig. 4.5 and with the plot of $N_{\mathrm{acc},+}(r)$ in panel (c), where an increased deviation from DH behavior is observed, thus indicating higher counterion condensation with generation. This also explains the striking agreement between $r_{\mathrm{eff}}$ values from the Alexander prescription and the PMF method. Owing to the fact that the PMF method plots PMF calculated by Boltzmann inversion of counterion RDF, while the Alexander prescription plots electrostatic potential calculated by solving Poisson's equation, the results show that the PMF between dPGS and salt ions is predominantly of electrostatic nature.

Tables 4.2 and 4.5 show that the effective surface charge density $\sigma_{\mathrm{eff}}$ is about an order of magnitude lower than $\sigma_{\mathrm{d}}$ and also, unlike the trend of $\sigma_{\mathrm{d}}$ values with generation, $\sigma_{\mathrm{eff}}$ decreases with generation. Experiments on carboxyl-terminated dendrimers at almost fully ionized state also found higher effective charge densities for a lower generation $G_2$ than for $G_5$ [338]. However, $\sigma_{\mathrm{eff}}$ saturates to a fixed value for higher generations $G_5$ and $G_6$ [114].

In their CG simulations at $10\,\mathrm{mM}$ bulk salt concentration, Xu et al. [114] also found that $r_{\mathrm{eff}}$ and $\sigma_{\mathrm{eff}}$ depend weakly on salt concentration, which allows us to compare them with our simulations at $c_+^{\mathrm{b}} = 25\,\mathrm{mM}$ salt concentration. Within a reasonable error, both $r_{\mathrm{eff}}$ and $\sigma_{\mathrm{eff}}$ evaluated from previous CG simulations by Xu et al. [114] are in a good reasonable agreement with other approaches used in our work. An exception is seen for the case of $G_0$ where charge renormalization has not been observed in CG simulations. It is also noticed that the trend in $\sigma_{\mathrm{eff}}$ with respect to generation found in CG simulations from Xu et al. is in agreement with those found using approaches employed here. Another consequence of the charge renormalization is the weak dependence of $\phi_{\mathrm{eff}}$ with generation, which is observed in all approaches.

### 4.1.3.5 Comparison of implicit and explicit routes to the potential

Fig. 4.6 shows the comparison of the electrostatic potentials from explicit and implicit-water integration approaches, described in the section 3.2.5.2. The long-range electrostatic potential obtained from the explicit-water approach also exhibits the long-range DH behavior but with more statistical fluctuations and visible deviations from strict linearity. The slope, *i.e.*, the inverse Debye length, is in most cases consistently close to the expected $\kappa = 0.52\,\mathrm{nm}^{-1}$, corresponding to $c_+^{\mathrm{b}} = 25\,\mathrm{mM}$. It is found that the occurring wiggles and deviations are caused by the large water fluctuations in the far-field regime, rendering the integration prone to large errors (see also the electrostatic fields shown in the Ap-
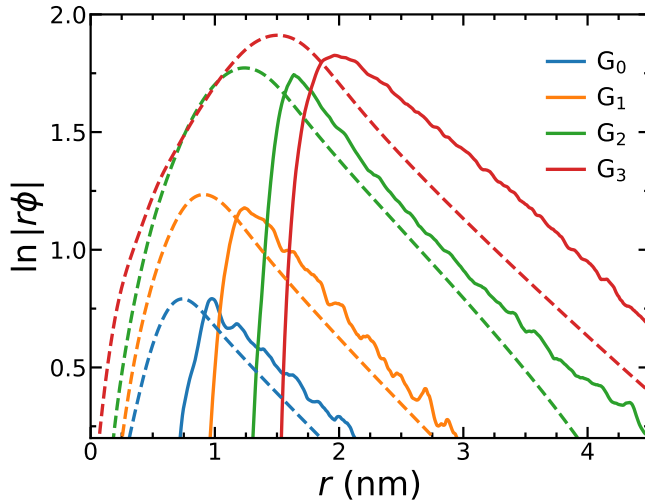
Figure 4.6: Comparison of electrostatic potential profiles with respect to distance from dPGS-COM from implicit and explicit-water approaches, denoted by dashed and solid lines, respectively. The implicit-water approach (same as Fig. 4.5(b)) only takes dPGS and ion charges in a uniform dielectric medium ($\varepsilon_{\mathrm{w}} = 72$) into account, while the explicit-water approach additionally includes partial charges of water in vacuum permittivity ($\varepsilon_{\mathrm{r}} = 1$).

pendix A.1.3). While the values of $r_{\mathrm{eff}}$ from the implicit approaches are not contradicting the explicit-route curves, no meaningful comparison can be made on a quantitative level. Although the curves from the explicit-route seem consistently shifted to larger distances by about the size of one water molecule, *i.e.*, $\simeq 0.3\,\mathrm{nm}$. It is concluded that, after all, all approaches give consistent values for the effective charge and size but within an uncertainty window of the size of one water molecule. More accurate quantifications are probably not so meaningful to attempt, as they are obviously hampered by systematic uncertainties induced by continuum assumptions and microscale fluctuations.

## 4.1.4 Thermodynamic signature of dPGS–water interaction

In this section, the thermodynamic signature of dPGS–water association is calculated using an approach based on the temperature dependence of the water PMF [137, 138]. As an illustrative example, a system of $G_2$-dPGS in 25 mM NaCl aqueous solution was simulated at two different temperatures 283 K and 310 K, while keeping all other parameters constant and simulation protocol the same (*cf.* Sec. 4.1.1). The PMFs of the dPGS–water interaction $V_{\mathrm{w}}(r)$ are evaluated using Eq. (3.12) for the two temperatures. Using finite differences in Eq. (3.70), the entropy profile $S_{\mathrm{w}}(r)$ is evaluated, whereas the enthalpy is determined using Eq. (3.71) at the mean temperature 296.5 K. Fig. 4.7 shows the distance-resolved profiles of the free energy in the form of the water PMF $V_{\mathrm{w}}(r)$. Monotonically increasing PMFs with decreasing distance towards dPGS-COM indicate a
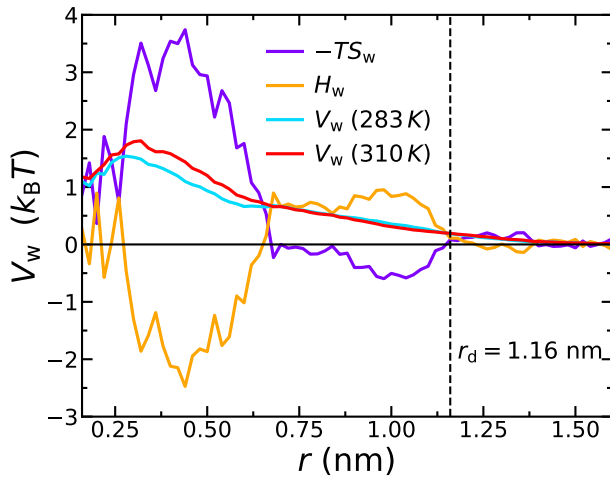
Figure 4.7: Distance resolved thermodynamic signature profile for water binding to $G_2$-dPGS. PMF $V_w(r)$ at $T = 283\,\mathrm{K}$ and $T = 310\,\mathrm{K}$, entropic term $-TS_w$ and enthalpy $H_w$ (both at $296.5\,\mathrm{K}$)of interaction have been presented. The dashed vertical line is the bare radius $r_d$ of $G_2$-dPGS.

net repulsion between dPGS and water. The corresponding changes in the system enthalpy $H_w$ and the entropic term $-TS_w$ of the dPGS hydration are also displayed. They show at first an increase of $H_w$ (and decrease of $-TS_w$) until $\sim 1\,\mathrm{nm}$ when approaching from larger distances. Since this location corresponds to the high density of terminal sulphate groups (*cf.* Fig. 4.2), this observation could be attributed to their ion-specific (Hofmeister) effects due to their chaotropic nature [339, 340, 341, 342, 343]. Unlike the kosmotropic divalent sulfates, the monovalent sulphates exhibit weaker interactions with water than water with itself and thus disturb the hydrogen-bond network of surrounding water. Consequently, this leads to water with a higher configurational freedom and thus higher entropy, simultaneously resulting in enthalpic penalty for breaking water–water hydrogen bonds. The increase of $H_w$ until $\sim 1\,\mathrm{nm}$ is then followed by a rapid exchange of favourable/unfavourable compensating components at $\sim 0.6\,\mathrm{nm}$. The unfavourable $V_w$ is dominated by the entropic term with a counterbalancing enthalpy $H_w$. The molecular origin of this effect could be credited to the dPGS interior environment rich of dPGS-oxygens, which is favourable for additional hydrogen bonds. However, simultaneously a steric hindrance of the dPGS core towards water and possibly localized dPGS–water hydrogen bond formation results in an entropic penalty. Ultimately the entropic contribution dominates the dPGS–water interaction in the interior, consequently resulting in an unfavourable free energy. Surprisingly, despite significant chemical difference of the dendrimers, very similar signatures were observed in explicit–water simulations of the PAMAM dendrimer [78].

## 4.2 dPGS with protein in monovalent salt

Section 4.1 discusses various approaches of comprehensive structural and electrostatic characterization of dPGS in an aqueous monovalent salt solution. This identification of dPGS is essential in the context of its principle application in the medicinal field as an anti-inflammatory agent for the acute and chronic inflammatory diseases, as discussed in the section 1. The microscopic mechanism behind this effect traces back to the dPGS inhibiting the binding between the leukocytes and the cell adhesion proteins situated on the endothelial cells, such as L- and E-selectins [113]. Inflammatory diseases trigger the dysregulated immune response from the body, in the form of the massive influx of the leukocytes towards the inflammation sites, thereby contributing to further escalate the inflammation. dPGS, by acting as a ligand to L- and E-selectins, prevents leukocyte-selectin binding and thus the inflammation.

Motivated by the clear identification dPGS atomistically [I] and in CG fashion [114], along with the applications of its binding with proteins, Xu et al. (our other work) [IV], attempted to quantitatively understand the dPGS–protein interaction in a monovalent salt at a physiological ionic strength, with the help of CG, AA MD simulations and calorimetry experiments. It was demonstrated that the complexation of proteins and highly charged dendritic macromolecules, especially at physiological ionic strength, is largely dominated by the entropic counterion release mechanism [IV]. The counterion release mechanism here refers to the purely entropic effect that a few counterions condensed on the dPGS are liberated when the protein binds, whereupon an oppositely charged protein patch becomes a multivalent counterion for the dPGS. Implicit-water, explicit salt CG simulations of $G_3$-dPGS with L-selectin in 150 mM NaCl are performed to calculate PMF profiles, binding free energies and release counterions. It was found that approximately 3–4 $Na^+$ counterions are released when $G_3$-dPGS and L-selectin undergo complexation [IV]. AA, explicit-water MD simulation of $G_3$-dPGS and L-selectin was performed in identical conditions, in order to supplement the CG results.

### 4.2.1 Atomistic simulation method

The final complex structure of $G_3$-dPGS and L-selectin was simulated via a standard, AA MD simulations built on the Optimized Potentials for Liquid Simulations 'All-Atom' (OPLS-AA) [191] force-field as included in GROMACS and the extended simple point charge (SPC/E) water model. We assigned the partial atomic charges for the $G_3$-dPGS

61

inner core according to the OPLS-AA force-field. The missing charges on sulphate atoms in the OPLS are taken according to AA simulations on $G_0$ and $G_1$ from Xu et al. that agree with recent work [344] which has been applied, for instance, the simulations of sodium dodecyl sulphate micelles [345]. The initial configurations of $G_3$-dPGS are constructed in a vacuum with the program ChemDraw [346]. The equilibrated structure of $G_3$-dPGS is obtained after a 30 ns equilibration in the isobaric $NPT$ ensemble at conditions of $P = 1$ bar and $T = 293$ K. The partial charges for L-selectin were taken at physiological pH, resulting in a net charge of zero. The protein initial structure refers to the Protein Data Bank with Number 3CFW consistent with CG simulation. A cutoff distance 1 nm for both the PME summation and van der Waals interactions was used in a cubic box of side-length 10.7 nm. For the atomistic simulation, the condensed counterions of the $G_3$-dPGS are defined as those within the distance $r_{\text{eff}} = 2.4$ nm with respect to the dPGS-COM [114]. The difference of the condensed counterions between the unbound and bound state leads to the released counterions number. The bound state was obtained via AA MD simulations by placing the dPGS initially close to the binding patch observed in the CG simulations and let the system bind and equilibrate within 30 ns. The final statistics were generated from a canonical $NVT$ simulation with a working trajectory of 30 ns.

### 4.2.2 Discussion

Compared to the CG simulation, we find that the number of released counterions as well as the structure of the complex is virtually the same, regardless of the inclusion of the explicit solvent and atomistic structure, *cf.* Fig. 4.8. We find 3.3 liberated counterions in the AA simulation and 3.6 for the CG simulation [IV]. However, the CG model, where each amino acid is replaced by a simple bead, to some extent brings small deviations to the surface geometry as compared to the fully atomistic protein structure: we find that in the AA simulations two more amino acids R14 and K8 of L-selectin can interact with the dPGS, *cf.* Fig. 4.8(b) and (d). Nevertheless, apparently this deviation in the binding interface does not much affect the mean number of released ions. This clear mechanistic picture described in Xu et al. [IV] behind the dPGS–protein complexation as well as its predictive value for the calculation of binding affinities are important for the rational optimization of dendritic PEs as potential drugs and nanocarrier systems, which define their overall biological identity *in vivo* by their interactions and coating with proteins [150, 151, 152, 153].
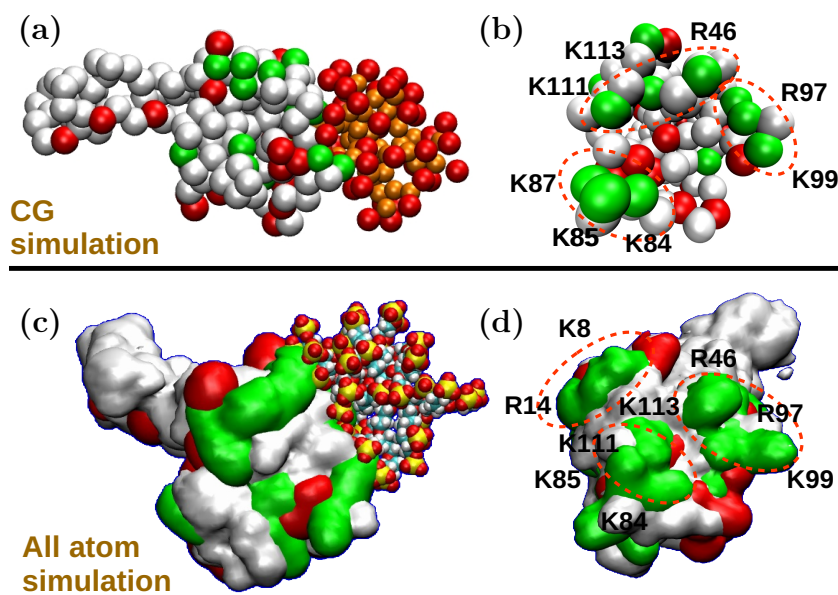
Figure 4.8: (a,c) Snapshots of the L-selectin/$G_3$-dPGS binding complex: CG versus AA MD simulations. Green colored beads or regions depict domains of positive charge. (b,d) The corresponding snapshots of the L-selectin binding patch. The responsible basic amino acids shown to be interactive with dPGS are labeled and highlighted. Reprinted with permission from Xu et al. [IV]. Copyright © 2018 American Chemical Society.

## 4.3 dPGS in a mixture of mono- and divalent salts

When a highly charged globular macromolecule, such as a dendritic polyelectrolyte or charged nanogel, is introduced into a physiological electrolyte solution, monovalent and divalent counterions from the solution sorb into the macromolecule in a certain ratio and thereby almost electroneutralize it. For charged macromolecules in biological media this ratio can be decisive for the desired function. As discussed earlier, the divalent ions play a critical role in the structure and function of the PE systems. dPGS, in particular, owing to its medicinal applications, is naturally exposed to the biological fluid environments and thus prone to undergo an interaction with its constituents. For example, divalent ions such as $Mg^{2+}$ and $Ca^{2+}$ are essential components of the human serum blood as well as intra- and extracellular fluids. Thus, having performed a comprehensive electrostatic characterization of dPGS in a monovalent (NaCl) salt, we now turn our attention to the quantitative rationalization of the competitive sorption of $Mg^{2+}$ and $Na^+$ cations on dPGS, which can significantly alter the biological footprint of dPGS, via its consequential interactions with biomolecules such as proteins (*e.g.* L-selectin, *cf.* Sec. 4.2). The basic physics behind this ion-exchange relies on the competition between the electrostatic energy gain of the sorbed ions and the translational entropy of the free ions. However, the ion-

specific interactions between the charged terminal sulphate groups and the counterions, in the form of the steric or hydration effects can play a pivotal role in characterizing the dPGS electrostatic features such as effective charge. The impact of such effects can be studied in detail via AA, explicit-water MD simulations which offers a highly resolved spatial and temporal data.

However, as discussed in the section 1, identifying or optimizing an accurate non-polarizable force-field for divalent cations is a challenge, due to their ability to polarize the surrounding media, especially polar solvents such as water. While the conventional non-polarizable force-fields struggle to reproduce divalent ion properties, there have been several recent attempts to incorporate corrections in their parametrization [201, 208, 217, 218]. Current section describes the results of the AA, explicit-water MD simulation of the system containing $G_2$-dPGS along with $Na^+$ and $Mg^{2+}$ counterions (with $Cl^-$ as coions) by employing these force-fields in order to evaluate the dPGS–counterion interaction. We compare the performances of the force-fields in terms of their effect on dPGS electrostatic properties such as effective charge, surface potential, the number and the composition of condensed counterions (divalent vs. monovalent). The description of the force-fields employed is as follows–

### 4.3.1 Mamatkulov et al. force-field

Currently available non-polarizable force-fields [203, 347, 348, 349] fail to reproduce several thermodynamic properties of ionic solutions at finite concentrations. The reason for it is that they were developed to reproduce only a single-ion thermodynamic properties such as the solvation free energy, the first peak of the ion–water RDF, crystal lattice parameters, etc., which makes them, in principle, credible only in simulations at low salt concentrations. As an example, mainstream force-fields such as CHARMM, GROMOS, and AMBER fail to model ion-specific effects in ion channels [216]. Mamatkulov et al. [217] offer a divalent cation force-field obtained by concurrent optimization with respect to the solvation free energy and the activity coefficient of an ion, to ensure accurate representation of the ion–water and ion–ion interaction potentials at finite ion concentrations. Similar procedure is applied to optimize the force-field for sulphate ($SO_4^{2-}$) ions, in combination with the SPC/E water model [216, 350, 351, 352]. The optimization of the ionic force fields is done in two consecutive steps. First, the cation solvation free energy is determined as a function of the LJ parameters. The peak in the ion–water RDF is used as a check of the structural properties of the ions. Second, the activity derivatives of the

electrolytes $MgY_2$, $CaY_2$, activity derivatives are determined for the restricted set of LJ parameters which reproduce the exact $BaY_2$, $SrY_2$ are determined through Kirkwood–Buff solution theory, where $Y = Cl^-$, $Br^-$, $I^-$. The optimal ion parameters are those that match the experimental activity data and therefore simultaneously reproduce single-ion and ion-pair thermodynamic properties.

### 4.3.2   Naleem et al. (Kirkwood–Buff integral) force-field

Similar to Mamatkulov, Fyta, and Netz, Naleem et al. [201] offer an alkaline earth metal ion force-field optimized in order to ensure a reasonable balance between ion–ion, ion–water and water–water interactions. Taking SPC/E water model, the force field parameters are specifically developed to reproduce the experimental Kirkwood-Buff integrals for aqueous solutions and thereby the experimental activity derivatives, partial molar volumes, and excess coordination numbers. The strong polarization of the medium by the divalent cations is taken into account by increasing their degree of solvation, which is achieved by scaling of the ion and water oxygen interaction strength. Apart from the fact that this force-field gives confidence in the underlying ion–ion, ion–water and water–water interactions, it is also able to reasonably reproduce experimental properties such as diffusion constants, dielectric decrements, and excess heats of mixing.

### 4.3.3   Yoo et al. force-field

As discussed in the section 1, MD simulations of $Mg^{2+}$ ions with DNA have resulted in considerable artifacts on employing AMBER and CHARMM force fields [208, 209]. Yoo et al. performed the DNA simulations with $Na^+$, $Mg^{2+}$ counterions along with $Cl^-$ coions and attempted to correct the imperfections in the standard parametrization in the CHARMM force-field, via systematic optimization of the cation–anion specific interaction parameters, in particular, monovalent cation–anion LJ $\sigma$ parameters (referred to as NBFIX corrections) in order to match the resultant osmotic pressure with that obtained from experiments [208].
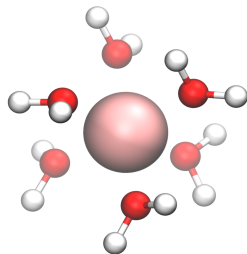
Figure 4.9: Simulation snapshot of the Mg-hexahydrate complex $Mg(H_2O)_6^{2+}$ from current analysis. $Mg^{2+}$ cation is represented by the pink sphere at the center along with six surrounding water molecules in the complex. The model is adopted from Yoo et al. [208]

In the case of $Mg^{2+}$, their reparametrization scheme focused on the six water molecules from the first solvation shell of the ions. Even though a $Mg^{2+}$ ion and those six water molecules are not covalently bonded, they considered Mg-hexahydrate complex $(Mg(H_2O)_6^{2+})$ to remain intact within the time scale of their MD simulations, since the lifetime of a water molecule within the first solvation shell of $Mg^{2+}$ is found to be $\sim 10\,\mu s$ [353]. From a simulation standpoint, in order to distinguish these six water molecules of the first solvation shell of $Mg^{2+}$ from bulk water and thereby enable application of NBFIX corrections to the oxygens of the first solvation shell water, each $Mg^{2+}$ ion and the six surrounding water molecules were collectively treated as $Mg(H_2O)_6^{2+}$ complex, as shown in Fig. 4.9.

### 4.3.4 Electronic continuum correction (ECC)

Divalent cations such as $Mg^{2+}$ represent a considerable challenge for the empirical non-polarizable force-field calculations since they strongly polarize the medium around and even trigger charge-transfer effects [301, 354, 355]. One of the promising ways of improving this scenario is the use of ECC, which considers the fast electronic polarization in a mean field way [214, 301]. Numerically, ECC is implemented via scaling the ionic charges [214]. This approach has been used in previous works to dramatically improve the description of ion pairing in calcium chloride [301], calcium acetate [356] and magnesium chloride [218] ionic solutions. This approach has been applied here by using the GAFF force-field and rescaling the charges dPGS sulphate groups by ECC, while $Mg^{2+}$, $Na^+$ and $Cl^-$ ions have been treated by ECCR charge rescaling, which means along with scaling the charges, decreasing the ion size by scaling LJ $\sigma$ parameters [301]. The radius of each ion needs to be further slightly decreased, compared with the original full charges model, in order to maintain the appropriate ion–water distances [218]. The detailed description of the concept of ECC can be found in the section 3.2.6.1.

Apart from the above mentioned force-fields, we also apply OPLS [191] force-field, used by Aryal and Ganesan [357], who studied $Mg^{2+}$, $K^+$ and water diffusivities in a charged sulphated copolymer membrane. The interaction between the sulphate charged groups and $Mg^{2+}$ in their system, resembles to that in our system of $G_2$-dPGS with $Mg^{2+}$ ions.

### 4.3.5 Atomistic simulations methods

The protocol for all simulations in this study is the same as the one described in the section 4.1.1, except the application of the force-fields and the corresponding compatible atomic partial charges. Mamatkulov [217] and Kirkwood–Buff Integral (KBI) (Naleem et al. [201]) force-fields are specifically designed for ions, hence the parametrization for dendritic polyglycerol (dPG) part in dPGS, $i.e.$, the core scaffold of the dPGS without the terminal sulphate groups, has been kept intact according to the GAFF force-field. Electronic continuum correction (ECCR) essentially rescales the atomic partial charges of dPGS and the surrounding ions, therefore GAFF force-field parametrization has been retained for this simulation as well.

$Mg^{2+}$, $Na^+$, and $Cl^-$ ions in the system are referred to with subscripts $++$, $+$ and $-$, respectively. The $G_2$-dPGS is accompanied by the corresponding number of $Na^+$ counterions $N_s = 24$ electrically neutralizing the macromolecule. The number of salt ions $i$ ($i = ++, +, -$) in a simulation box volume $V$ is denoted as $n_i$, while the corresponding total salt concentrations are denoted as $c_i^0 = n_i/V$. Bulk concentrations $c_i^b$ ($i = ++, +, -$) are calculated from the radial density distributions in far-field after the equilibration. Mamatkulov, KBI and ECCR force-fields have been applied to both the cases of $c_{++}^0 = 15$ mM and 30 mM, while OPLS and $Mg(H_2O)_6^{2+}$ force-fields are employed only for the case of $c_{++}^0 = 30$ mM. $c_-^0$ is fixed close to 150 mM for all simulations, in order to mimic physiological ionic composition, and $c_+^0$ is adjusted in order to maintain electroneutrality in the simulation box. All simulations have box sizes $\sim 10$ nm and are performed till $\sim 80$–100 ns.

### 4.3.6 Density distribution functions

Fig. 4.10 shows the radial density distributions dPGS sulphur atoms (representing the COM of the terminal sulphate groups), $Mg^{2+}$ and $Na^+$ ions with respect to the dPGS-COM, and as calculated according to several force-fields. Similar to the case of the monovalent salt in Fig. 4.2(a), the radial density of the terminal sulphur is inhomogeneous with pronounced peaks as a result of the excluded volume interactions along with bond
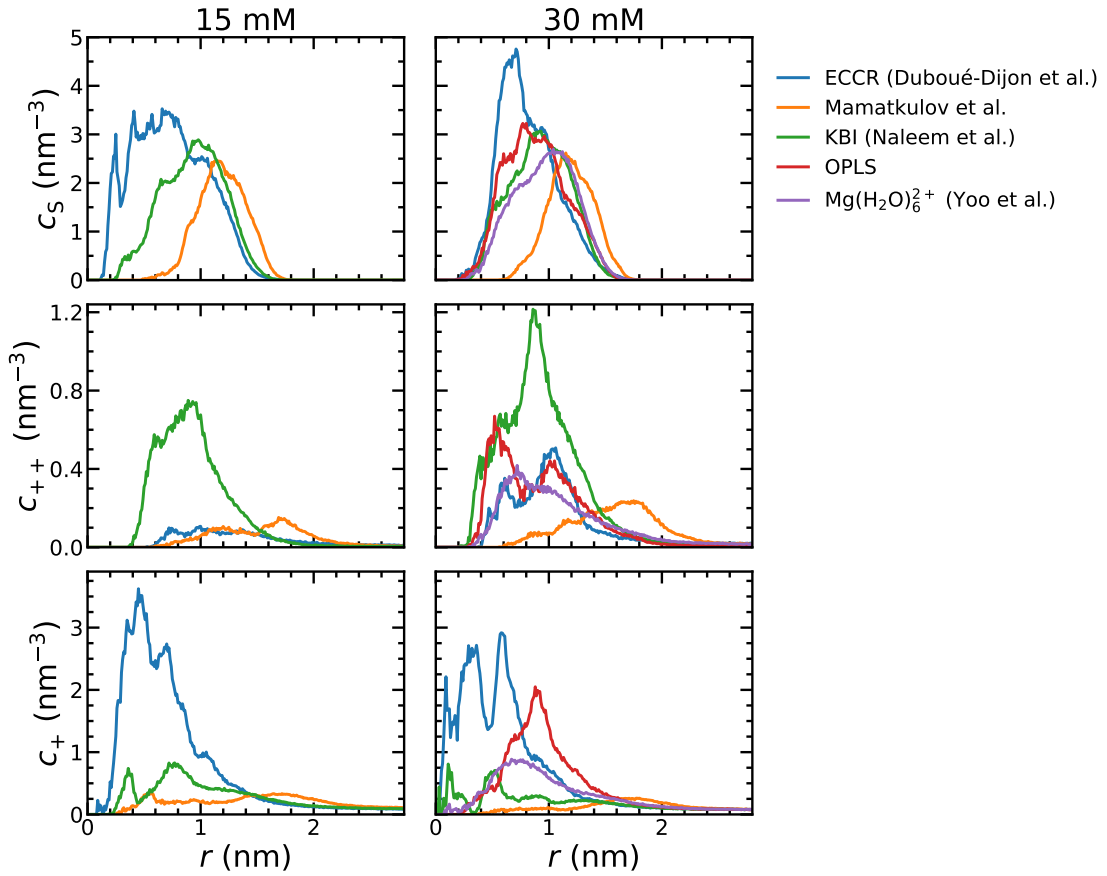
Figure 4.10: The quantitative comparison (in $nm^{-3}$) of radial density distributions of dPGS sulphur, $Mg^{2+}$ and $Na^+$ between charge rescaled (ECCR [218]) and non-polarizable force-fields (Mamatkulov et al. [217], KBI [201], OPLS [357] and $Mg(H_2O)_6^{2+}$ [208]). The reference used for the distributions is the dPGS-COM. The profiles are shown for the $Mg^{2+}$ salt concentrations $c_{++}^0 = 15$ mM and 30 mM.

constraints and charge repulsion, however, the peak location varies depending on the force-field. According to ECCR approach, the rescaled charges on the sulphate groups are $-0.75e$, which indicates lower intramolecular sulphate–sulphate repulsion as compared to non-rescaled charges ($-1e$), leading to enhanced backfolding effect and shrinking of the dPGS size. It can be seen that this peak location does not change for ECCR, KBI and Mamatkulov force-fields, on going from $c_{++}^0 = 15$ mM to 30 mM. Looking at the $c_{++}^0 = 30$ mM case, the overall peak location for sulphur distribution ranges $\sim 0.7 -$ 1.2 nm, which is somewhat lower than that for the case of monovalent salt (1.2 nm). This could be attributed to the introduction of $Mg^{2+}$ ions bridging the oppositely charged sulphate groups and increasing the inter-sulphate group attraction. As discussed in the section 4.1.2.1, the major peak position of the sulphur distribution is used to define the intrinsic dPGS radius $r_d$. The values of $r_d$ according to different force-fields are given in Table 4.6.

Fig. 4.10 further shows the radial number density distributions of $Mg^{2+}$ ions $c_{++}(r)$

| | $c_{++}^0$ | $c_+^0$ | $c_{++}^b$ | $c_+^b$ | $n_{++}$ | $r_d$ | $r_{eff}$ |
|---|---|---|---|---|---|---|---|
| ECCR[218] | 14.98 | 162.17 | 11.77 | 142.37 | 9 | 1.01 | 1.44 |
| | 30.45 | 132.77 | 23.55 | 114.12 | 18 | 1.00 | 1.52 |
| Mamatkulov[217] | 15.87 | 168.34 | 7.87 | 149.02 | 9 | 1.40 | 1.93 |
| | 28.23 | 163.07 | 17.35 | 143.46 | 16 | 1.37 | 1.93 |
| KBI[201] | 15.10 | 163.75 | 5.23 | 148.32 | 9 | 1.10 | 1.75 |
| | 31.33 | 132.54 | 15.50 | 127.87 | 18 | 1.08 | 1.75 |
| OPLS[357] | 33.34 | 142.53 | 24.80 | 113.35 | 18 | 1.07 | 1.62 |
| $Mg(H_2O)_6^{2+}$[208] | 30.55 | 131.28 | 22.25 | 116.91 | 18 | 1.12 | 1.43 |

Table 4.6: The summary of structural and electrostatic parameters of $G_2$-dPGS evaluated from the simulations employing non-polarizable and charge rescaled (ECCR) force-fields. $c_i^0$ ($i = ++$ ($Mg^{2+}$), $+$($Na^+$) and $-$($Cl^-$)) denotes total salt concentration while $c_i^b$ denotes the bulk concentration measured from the density distribution of the respective species in far-field. $n_{++}$ is the total number of $Mg^{2+}$ ions in the simulation box and $r_d$ is the dPGS bare radius calculated as radius of gyration of the sulphur atoms with respect to dPGS-COM. $r_{eff}$ and $Z_{eff}$ correspond to the effective radius and the effective charge valency of $G_2$-dPGS respectively, calculated using the Alexander prescription (*cf.* Sec. 3.1.2.4.1). Concentrations and radii are expressed in mM and nm, respectively.

according to different force-fields. While the distributions in the short-range differ based on a force-field, all distribution decay in an exponential (DH-like or Yukawa) fashion. Looking at both $c_{++}^0 = 15$ mM and 30 mM cases, it can be clearly seen that the KBI profiles largely overestimate the magnitude, compared to ECCR and Mamatkulov ones. In $c_{++}^0 = 15$ mM case, KBI shows a clear single-peak distribution with the peak location coincident with that of the corresponding sulphur distribution, which indicates that dPGS–$Mg^{2+}$ interaction is largely dominated by the interaction of $Mg^{2+}$ cations with the dPGS sulphate groups, implying electrostatics playing a major role in the interaction. ECCR and Mamatkulov profiles, on the other hand, display much lower magnitude, indicating overall lower $Mg^{2+}$ intake by dPGS. In the case of ECCR, $Mg^{2+}$ with its rescaled charge of $1.5e$ represents enhanced electronic polarization of surrounding water, decreasing its interaction strength with sulphate groups. The case of $c_{++}^0 = 30$ mM shows the diversity of the $Mg^{2+}$ density distribution around $G_2$-dPGS, according to different force-fields. This further highlights the earlier discussed issue regarding the parametrization of divalent ions in the molecular simulations. Except OPLS, all the force-fields show mostly a single-peak distributions. The double-peak OPLS profile shows the attractive interaction between $Mg^{2+}$ and the bonded oxygen atoms in the dPGS core, which is also slightly echoed by ECCR profile.

Na$^+$ density distribution $c_+(r)$ is further shown in Fig. 4.10. For both the cases of $c_{++}^0 = 15$ mM and 30 mM, ECCR and KBI profiles show enhanced Na$^+$ penetration in the dPGS interior. In the ECCR scaling of Na$^+$ ions, apart from charge rescaling, their ionic radii are also reduced, compared with the original full charges model, in order to retain proper Na$^+$–water distance. The reduced sizes enable Na$^+$ ions to penetrate the dPGS core. Another reason for this profile according to ECCR approach is the significant backfolding of the sulphate groups in the dPGS core, attracting more Na$^+$ ions in that region.

### 4.3.7 Electrostatic properties of G$_2$-dPGS

Adopting the implicit-water approach (*cf.* Sec. 3.2.5.2.2), Fig. 4.11 displays $Z_{\mathrm{acc}}(r)$ profiles around G$_2$-dPGS-COM, for all force-fields, and are represented in the form of the cumulative charge normalized by the G$_2$-dPGS bare charge $Z_{\mathrm{eff}}/Z_{\mathrm{d}}$. Note that the definition of $Z_{\mathrm{acc}}$ here (Eq. (3.66)) additionally incorporates Mg$^{2+}$ cations apart from Na$^+$ and Cl$^-$ ions according to its definition in the case of monovalent salt (*cf.* Sec. 4.1.3.2).

The magnitudes and locations of the peaks of the profiles vary depending on the force-field, however, similar to the case of monovalent salt, we observe the charge renormalization effect in action for all force-fields, as we see the gradually increasing charge build-up of the dPGS atoms (mostly sulphate groups) with $r$, eventually getting dominated by the charge accumulation due to the counterions. As a result, the profile attain a maximum and then they exponentially decline to zero at bulk. It is worth noting that, compared to the case of $c_{++}^0 = 15$ mM, $Z_{\mathrm{acc}}$ magnitude in $c_{++}^0 = 30$ mM case decreases, indicating that the increase in $c_{++}^0$ further charge renormalizes the dPGS. Adopting the Alexander prescription, Fig. 4.12 displays the natural logarithm of electrostatic potential profiles in a rescaled form $\ln|r\phi(r)|$. The values of the effective radii $r_{\mathrm{eff}}$ and charges $Z_{\mathrm{eff}}$ are then obtained, corresponding to each force-field and are listed in the Tables 4.6 and 4.7 respectively. Table 4.7 additionally shows the values of the effective potentials $\phi_{\mathrm{eff}}$, as well as the number of condensed ions on G$_2$-dPGS, $N_{++}^{\mathrm{b}}$ and $N_+^{\mathrm{b}}$. The slope of $\ln|r\phi|$ profile in the far-field gives the inverse of the Debye length $\kappa$ in the bulk. The different slopes thus show the different ionic strengths measured in the bulk due to ion-partitioning, owing to the canonical ensemble, which is a unique attribute of the force-field. The corresponding bulk concentrations of Mg$^{2+}$ and Na$^+$ cations $c_i^{\mathrm{b}}$ are listed in Table 4.6. This issue can be circumvented by increasing the simulation box size so that the condensed counterions do not make a change in their bulk concentration.
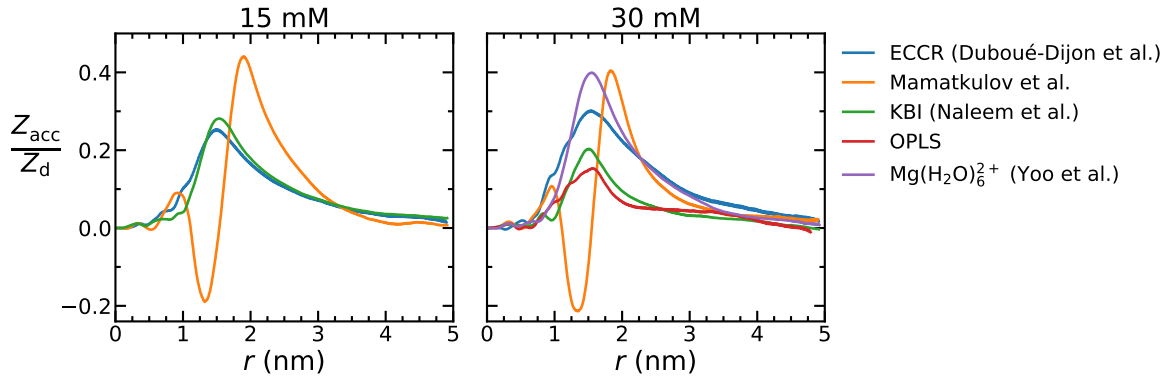
Figure 4.11: The accumulated charge valency distribution $Z_{acc}(r)$ as a summation of all the charged species (dPGS atoms and all ions), excluding water *i.e.* "implicit-water" approach. (*cf.* Sec. 3.2.5.2.2). For the sake of better comparison, $Z_{acc}$ is scaled by bare charge valency of $G_2$-dPGS $Z_d$ ($-18$ for ECCR due to the charge rescaled sulphate groups and $-24$ for non-polarizable force-fields). The plots are compared for the total $Mg^{2+}$ salt concentrations $c^0_{++} = 15$ mM and 30 mM.
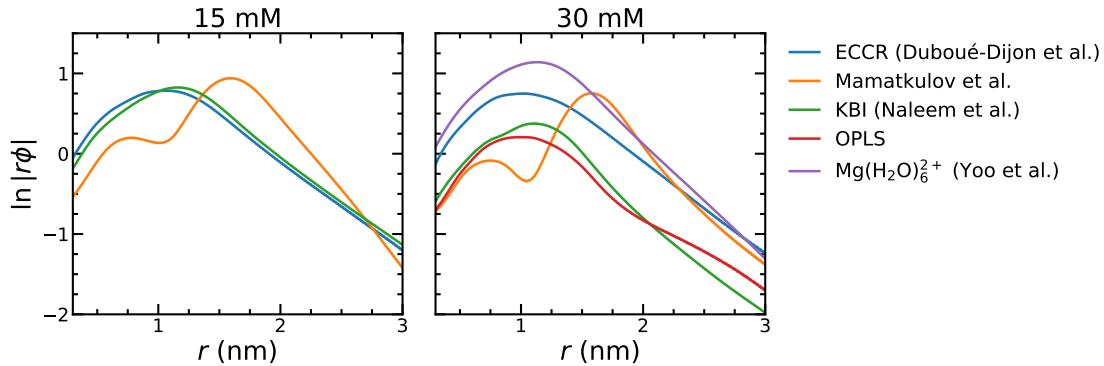


Figure 4.12: The logarithm of the rescaled electrostatic potential plotted against the distance $r$ from the dPGS-COM, according to the Alexander prescription, using the implicit-water approach. The long-range profiles are then fitted to the DH theory, in order to obtain effective electrostatic parameters for dPGS.

For both cases of $c^0_{++} = 15$ mM and 30 mM, the $Mg^{2+}$ condensation is found to be insignificant according to ECCR approach, possibly because the charge rescaling "lubricates" the electrostatic interactions. Same result is observed for $Mg(H_2O)_6^{2+}$ forcefield, which is attributed to the enhanced electrostatic multipole contribution by water molecules which are a part of the $Mg(H_2O)_6^{2+}$ complex.

Valuable insights about the competitive ion binding to dPGS can be derived by performing AA MD simulations with a fixed and reasonable force-field, at a wide range of $Mg^{2+}$ concentrations. The above analysis shows the diverse set of structural and electrostatic parameters of $G_2$-dPGS in a mixture of $Na^+$ and $Mg^{2+}$ cations, exhibited by different force-fields implemented. While there is a lack of experimental results verifying these results, we intend to satisfy our purpose to study the competitive sorption isotherm of $Mg^{2+}$ and $Na^+$ cations on dPGS, and to extract corresponding qualitative trends in the electrostatic and structural properties of dPGS, by fixing the force-field from Mamatkulov

71

| | $c_{++}^{\mathrm{b}}$ (mM) | $Z_{\mathrm{eff}}$ | $\phi_{\mathrm{eff}}$ | $N_{++}^{\mathrm{b}}$ | $N_{+}^{\mathrm{b}}$ |
|---|---|---|---|---|---|
| ECCR[218] | 11.77 | −5.92 | −1.22 | 0.88 | 12.67 |
| | 23.55 | −5.43 | −1.04 | 3.32 | 9.31 |
| Mamatkulov[217] | 7.87 | −9.06 | −1.17 | 3.47 | 8.02 |
| | 17.35 | −8.98 | −0.81 | 4.61 | 5.75 |
| KBI[201] | 5.23 | −5.75 | −0.74 | 5.41 | 7.97 |
| | 15.50 | −3.52 | −0.38 | 8.30 | 4.64 |
| OPLS[357] | 24.80 | −3.57 | −0.43 | 4.20 | 12.65 |
| $\mathrm{Mg(H_2O)_6^{2+}}$[208] | 22.25 | −8.96 | −1.82 | 2.77 | 6.05 |

Table 4.7: The electrostatic parameters of $G_2$-dPGS in a mixture of $Na^+$ and $Mg^{2+}$ cations according to different force-fields, obtained using the Alexander prescription. $\phi_{\mathrm{eff}}$ refers to the surface (effective) potential, while $N_i^{\mathrm{b}}$, ($i = ++$ ($Mg^{2+}$), $+$($Na^+$)) is the number of condensed counterions of species $i$.

et al. for our further analysis.

## 4.3.8 $G_2$-dPGS properties using Mamatkulov et al. force-field

In this section, we investigate the competitive sorption of $Mg^{2+}$ and $Na^+$ ions on $G_2$-dPGS for different $Mg^{2+}$ concentrations, with the help of AA, explicit-water MD simulations by employing Mamatkulov force-field. For different $Mg^{2+}$ bulk concentrations $c_{++}^{\mathrm{b}}$ (7, 17, 33 and 97 mM), the bulk concentration of $Cl^-$ ions $c_-^{\mathrm{b}}$ are maintained close to that in the physiological fluid, *i.e.*, $\sim 150$ mM. Considering the total charge on $G_2$-dPGS, its $Na^+$ counterions, $Mg^{2+}$ and $Cl^-$ ions in the simulation box, the concentration of $Na^+$ ions from the salt is adjusted in order to maintain the electroneutrality.

Fig. 4.13 shows the simulation results, in terms of the radial number density distributions $c_i(r)$ of dPGS sulphur, $Mg^{2+}$ and $Na^+$ counterions, the running coordination numbers of $Mg^{2+}$ and $Na^+$ counterions ($N_{\mathrm{acc},++}(r)$ and $N_{\mathrm{acc},+}(r)$), and the running total cumulative charge valency distribution $Z_{\mathrm{acc}}(r)$ (normalized with the $G_2$-dPGS bare charge valency $Z_{\mathrm{d}} = -24$) with the reference of $G_2$-dPGS-COM. The single-peak density distribution of dPGS sulphur atoms $c_{\mathrm{s}}(r)$ shows to be indifferent to the amount of $Mg^{2+}$ ions in the solution, implying that, according to Mamatkulov force-field, the intramolecular bonded, angular and dihedral interactions of sulphur with the neighbouring dPGS atoms is stronger than the non-bonded electrostatic and specific interaction of the sulphate group with ions. $Mg^{2+}$ and $Na^+$ density distributions ($c_{++}(r)$ and $c_+(r)$, respectively) show a high accumulation close to the sulphate groups, with a global maximum at distances
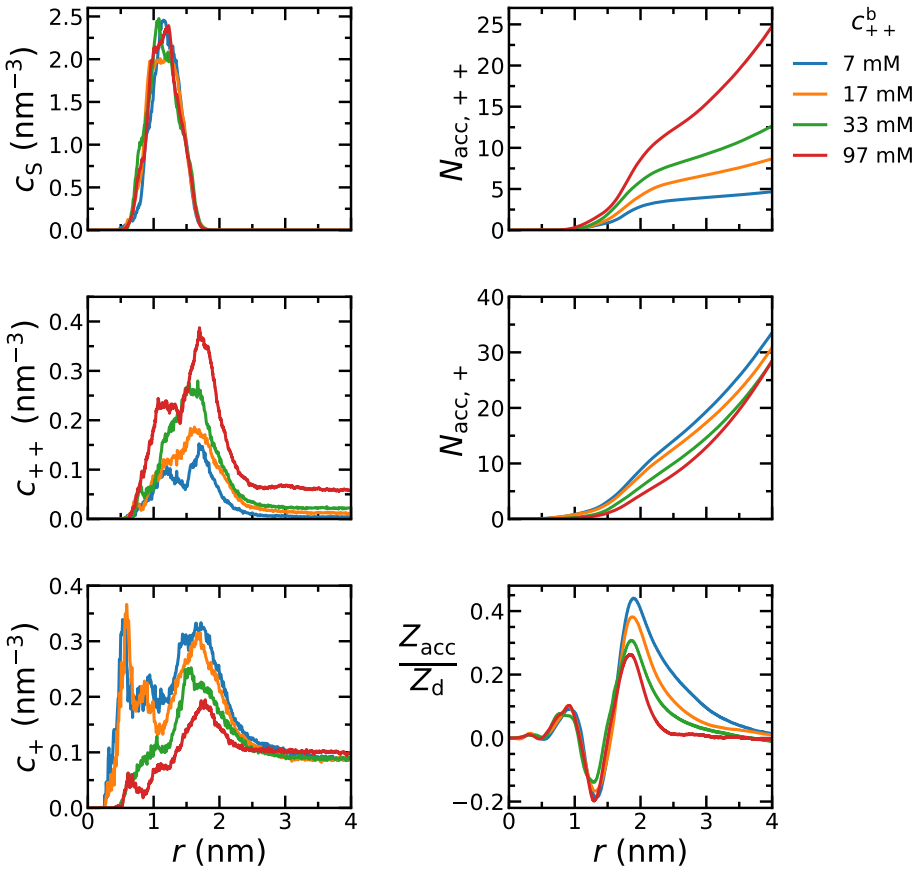
Figure 4.13: Radial density distributions around $G_2$-dPGS with $Mg^{2+}$ and $Na^+$ ions, according to Mamatkulov force field, plotted for different bulk concentrations of $Mg^{2+}$ cations $c_{++}^b$. $c_i$ ($i = $ s (sulphur), $++$ ($Mg^{2+}$), and $+$($Na^+$)) indicate the radial number density distributions. $N_{acc,i}$ denotes the running coordination number of species $i$, while $Z_{eff}/Z_d$ denotes the ratio between the effective and bare charge of $G_2$-dPGS. All distributions are plotted with the reference as dPGS-COM.

$r \sim 1.7\,$nm slightly larger than the sulphate peak (peaking roughly at $\sim 1.1\,$nm), *i.e.,* the strongest bound 'condensed' $Mg^{2+}$ and $Na^+$ counterions are distributed more on the surface layers of the dPGS. At larger distances, $r \sim 2 - 3\,$nm, a DH like decay is observable. Adding more $Mg^{2+}$ ions, $Na^+$ distribution gradually diminishes, $Mg^{2+}$ distribution gradually increases in magnitude as expected from the exchange of $Na^+$ with $Mg^{2+}$ ions within the dPGS, which is also seen in the running coordination numbers of $Mg^{2+}$ and $Na^+$ ions, $N_{acc,++}(r)$ and $N_{acc,+}(r)$. However, the $Na^+$ distribution also peaks at distances distinctively smaller than the location of the sulphate peak, roughly at $0.5 - 0.6\,$nm, for low $c_{++}^b$ (7 and 17 mM). This could be attributed to more interior binding of $Na^+$ ions with the glycerol oxygens in the dPGS core. $N_{acc,++}(r)$ distribution displays a point of inflection at $r \sim 2\,$nm indicating counterion condensation (*cf.* Sec. 3.1.2.4.2) [16]. This point of infection also exists for $N_{acc,+}(r)$, however, is not vividly distinguishable due to the large concentration of $Na^+$ ions in the simulation box. This clearly shows the stronger

| $c_{++}^{b}$ | $c_{+}^{b}$ | $n_{++}$ | $n_{+}$ | $r_{d}$ | $r_{eff}$ | $Z_{eff}$ | $\phi_{eff}$ | $N_{++}^{b}$ | $N_{+}^{b}$ |
|------|------|------|------|------|------|------|------|------|------|
| 0.00 | 160.11 | 0 | 93 | 1.39 | 1.78 | $-15.35$ | $-1.68$ | – | 8.65 |
| 7.73 | 149.03 | 9 | 98 | 1.40 | 1.93 | $-9.06$ | $-1.17$ | 3.47 | 8.02 |
| 17.35 | 143.46 | 16 | 95 | 1.37 | 1.93 | $-8.98$ | $-0.81$ | 4.61 | 5.75 |
| 33.16 | 148.80 | 27 | 95 | 1.39 | 1.95 | $-8.30$ | $-0.47$ | 5.42 | 4.89 |
| 97.33 | 154.02 | 67 | 93 | 1.40 | 1.95 | $-7.04$ | $-0.21$ | 6.71 | 3.56 |

Table 4.8: The summary of structural and electrostatic parameters of $G_2$-dPGS evaluated from applying Alexander prescription to the results obtained from simulations employing Mamatkulov et al. [217] force-field. $c_i^{b}$ ($i = ++ (Mg^{2+}), +(Na^+)$ and $-(Cl^-)$) denotes the bulk concentrations measured from the magnitude of the respective number density distribution in the long-range. $n_i$ is the total number of salt ions $i$ in the simulation box and $r_d$ is the dPGS bare radius calculated as radius of gyration of the sulphur atoms with respect to dPGS-COM. $r_{eff}$ and $Z_{eff}$ correspond to the effective radius and the effective charge valency of $G_2$-dPGS respectively. Concentrations and radii are expressed in mM and nm, respectively.

net binding affinity of $Mg^{2+}$ ions with $G_2$-dPGS, compared to that of $Na^+$ ions. $Z_{acc}/Z_d$ profile shows a decreases in magnitude with increasing $c_{++}^{b}$, implying higher charge renormalization of dPGS. $Z_{acc}(r)$ profile is then utilized to calculate the effective sizes $r_{eff}$ of $G_2$-dPGS, as well as effective charge $Z_{eff}$, potential $\phi_{eff}$, and the number of condensed counterions $N_i^{b}$ for different $c_{++}^{b}$, the values of which are given in the Table 4.8.

Table 4.8 shows that $r_{eff} \sim 1.93$ nm for all $c_{++}^{b}$, except for the monovalent case ($c_{++}^{b} = 0$ mM). It can be clearly seen that, with increasing $c_{++}^{b}$, $N_{++}^{b}$ increases while $N_{+}^{b}$ decreases, indicating ion-exchange. The values of $\phi_{eff}$ suggest that increasing $c_{++}^{b}$ leads to the neutralization of $G_2$-dPGS charge, even possibly leading to the charge reversal for higher $c_{++}^{b}$ than reported here, which is also found in literature [183, 200].

The AA MD simulations performed here provide insightful observations regarding the ionic structure around dPGS, effective charge and size of dPGS, composition of the condensed counterions, and the impact of $c_{++}^{b}$ on these attributes of the system. However, due to the lack of experimental means to produce and evaluate suitable benchmark properties, it is challenging to conclude about the quantitative aspects of these results. Future experiments in this area, hence, could be directed towards this subject in order to provide meaningful inferences. An important point to make here is also that it is vital to interpret these simulations results correctly, *i.e.*, recognizing the physicochemical effects that drive the competitive ion partitioning and quantifying the respective energy contributions with reasonable assumptions. A carefully tested and benchmarked theoretical binding model not only can fix this issue, but also circumvents the disadvantage of needing computational resources in simulations to acquire sufficient sampling. Taking this into consideration, we

aspire to build the theoretical models capturing the competitive ionic sorption on highly charged PEs (with the example of dPGS) in the next chapter.

## 4.4 Concluding remarks

In summary, AA, explicit-water MD simulations of dendritic polyglycerol sulphate are conducted. dPGS is a biomedically important PE and can be viewed as a representative of a class of highly charged dendritic macromolecules. Beyond some general characterization of ionic and hydration structure, in particular an electrostatic (surface) characterization of the dPGS was conducted in a monovalent salt (NaCl) in terms of the determination of effective charge, effective radius and surface potential using the Alexander prescription and the inflection point criterion. By comparing these several routes among each other, but also implicit versus explicit-routes of integration towards the electrostatic potential, very consistent numbers are found, within the uncertainty of the size of a water molecule. It is thus concluded that the CG models developed for the highly charged dPGS with explicit ions [114] are quite accurate from the electrostatic point of view and will thus serve in future simulations. We also extend the simulations to the physiologically relevant systems of dPGS in a mixture of divalent and monovalent salts ($MgCl_2$ and NaCl). Several recently developed force-fields for $Mg^{2+}$ cations were tested for our system and the competitive sorption isotherm of $Mg^{2+}$ and $Na^+$ cations on dPGS, along with corresponding qualitative trends in the electrostatic and structural properties of dPGS were studied. Such study will serve the interpretations of the dPGS and related dendritic PEs' action in biological context (*e.g.*, interacting with proteins [IV] or membranes) to understand and optimize their proven selective binding properties and efficacy in the medical treatment of inflammatory diseases.

# 5    Competitive sorption of monovalent and divalent ions by highly charged globular macromolecules

As per the discussion initiated in the section 4.3, a highly charged globular macromolecule, *e.g.*, a dendritic PE or charged nanogel, in a physiological electrolyte solution containing mixed, monovalent and divalent counterions, gets almost charge neutralized with a certain composition of condensed counterions, *i.e.*, a certain ratio between the sorbed mono- and divalent ions. This ratio can play a crucial role for charged macromolecules in biological media for their desired function. A theoretical prediction of such a sorption ratio is challenging because of the competition of electrostatic (valency), ion-specific, and binding saturation effects. In this chapter, we devise and discuss a few approximate mean-field continuum and discrete binding site models to predict such an equilibrium sorption ratio by extending and combining established electrostatic binding theories such as Donnan, Langmuir, Manning as well as PB approaches, to systematically study the competitive sorption between mono- and divalent counterions to the macromolecule. We compare and fit our models to CG computer simulation data of the competitive ion uptake by the globular PE dendritic polyglycerol sulphate (dPGS). The latter has a high potential to serve in macromolecular carrier applications in biological systems and at the same time constitutes a good model system for a highly charged macromolecule. We finally use the simulation-informed models to extrapolate and predict electrostatic features such as the effective charge as a function of the divalent ion concentration for a wide range of dPGS generations (sizes). Note that the descriptions and figures in this chapter are taken almost directly from our previous publication [II].

The theoretical models presented here are generally formulated for globular charged macromolecules and include ion-specific effects in a parametric way and can thus be straightforwardly modified or adapted to other charged globules, where mono-/divalent ion-exchange plays a role. In particular, we begin with the simple Donnan model, modified for ion-specific uptake, assuming that the electrostatic potential and the ionic concentrations are constant within the macromolecule phase and the bulk phase [358, 359, 360]. Despite being simple, still, for the mixed case of monovalent and divalent ions the resulting composition is a non-trivial result. We continue with the mean-field PB model, widely used in colloidal science and electrochemistry [2, 250, 361, 362, 363], and with

the limitations well known and discussed, in particular the neglect of electrostatic and steric correlations [173, 183, 364, 365, 366], or ion-specific sorption effects [180, 225, 226, 367, 368, 369, 370, 371, 372, 373]. The model has also been implemented to address the problem of competitive counterion binding in a mixed salt for the cases of linear PEs such as DNA [174, 374, 375, 376, 377] and planar geometries [378]. We also devise a two-state approximation model for an ion condensation around a charged globule. The two-state approach was firstly used in the Oosawa–Manning model [233, 234] for the counterion condensation around PE chains, according to which, counterions in a solution can be classified into two categories: 'free' counterions, which are able to explore the whole solution volume $V$ and the 'condensed' (or 'bound') counterions, which are localized within a small volume surrounding the PE macromolecule. An equivalent model for an impenetrable sphere with a surface charge was developed by Manning (*cf.* Sec. 3.1.2.4.4), where the number of condensed counterions on the macromolecule per bare unit surface charge is obtained by a free energy minimization, pointing to the competition between electrostatic binding of counterions to the macromolecule and their dissociation entropy [120]. We extend this model by introducing a discrete binding site model by considering the finite configurational volume of the ion in the condensed state and that the macromolecule has a finite number of charged binding sites by adopting the mixing entropy from the works of McGhee and von Hippel [379]. Ion-binding models in the same spirit have been developed in the past to describe the ionization equilibrium of linear PEs in monovalent salt [23, 380, 381], multivalent salt [382] and in mixtures of mono- and divalent salts [178]. All our models are compared to molecular simulations and used to study systematically the key electrostatic features of a highly charged globule, such as the effect of competitive sorption on the variation of the number of condensed monovalent and divalent counterions, effective charge, and its variation with divalent ion concentration.

## 5.1 Coarse-grained computer simulations

### 5.1.1 Simulation methods, force-fields, and systems

The CG monomer-resolved models of the dPGS macromolecule have been developed previously [114] and maintain the essential dPGS structural and electrostatic features with affordable computing expense. In brief, the dPGS branching units ($C_3H_5O-$) and inner core ($C_3H_5-$) (both of which are a part of the glycerol chemical group, respectively), and the terminal sulphate groups ($-OSO_3$) are individually represented by the CG segments

(a) $c_{++}^0 = 0.98\,\text{mM}$     (b) $c_{++}^0 = 3.75\,\text{mM}$     (c) $c_{++}^0 = 14.94\,\text{mM}$          (d)
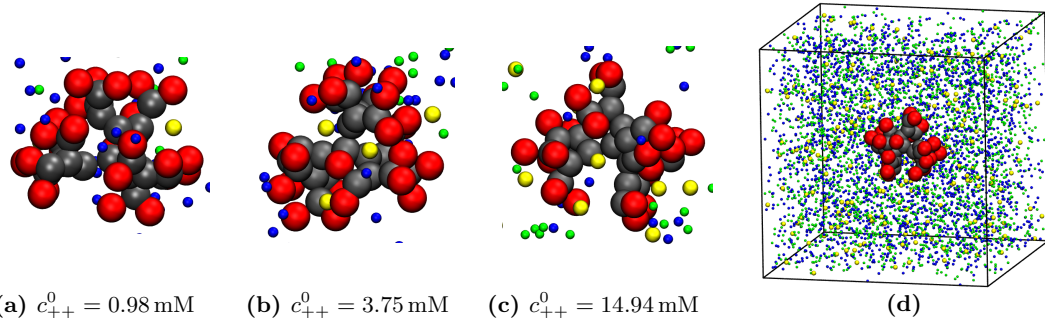
Figure 5.1: Panels (a), (b) and (c) show CG simulation snapshots of $G_2$-dPGS in a mixture of ions at the divalent cation (DC) concentrations of 0.98 mM, 3.75 mM and 14.94 mM, respectively, while the monovalent salt concentration $c_+^0$ is at 150.37 mM. The red beads depict the charged terminal sulphate groups ($-OSO_3$), which represent the binding sites of dPGS, the gray beads depict the neutral glycerol ($C_3H_5O-$) branching units, and yellow, blue and green spheres refer to DCs, monovalent cations (MCs) and monovalent anions, respectively. (d) Snapshot of the whole simulation box containing the CG model of $G_2$-dPGS and a mixture of salts of MCs and DCs. The box is cubic with a side length $L = 30$ nm. The sizes of spheres/beads in all panels are not to scale.

of specific type. The gross number of the CG segments is equal to the dendrimer polymerization $N_g = 3 \times 2^{n+1} - 2$ of generation index $n$. Only the terminal segments are charged with $-1e$ (where $e$ is the elementary charge), leading to the dPGS bare valency $|Z_n| = 3 \times 2^{n+1}$. The CG segments are connected by bonded and angular potentials both in harmonic form. In the previous work [114] we only studied monovalent ions. Here we extend it to study the competitive uptake of mono- and divalent ions for generations 2 and 4. The bare charge valencies of the $G_2$-dPGS are thus $Z_d = Z_{n=2} = -24$ and $Z_d = Z_{n=4} = -96$. Snapshots are shown in Fig. 5.1.

The non-bonded interactions between CG beads are described by the LJ potential together with the Lorentz–Berthelot mixing rules. In particular, the energy parameter $\epsilon_{LJ} = 0.1\,k_BT$ and the diameter $\sigma_{LJ} = 0.4$ nm are set identical for all ions (mono- and divalent) and thus any ion-specific effects are not explicitly included. In our simulations we place the dPGS in the center of a periodically repeated cubic box with a volume of $V$ (side-length of $L = 30$ nm). The solvent is implicitly assumed as a dielectric continuum with a dielectric constant $\varepsilon_w = 78$. The CG simulations employ the stochastic dynamics (SD) integrator in GROMACS 4.5.5 as in our previous work [114].

All simulations are performed in the canonical ensemble. The divalent cations (DCs), monovalent cations (MCs) and monovalent anions in the system are referred to with subscripts $++$, $+$ and $-$, respectively. The dPGS is accompanied by the corresponding number of monovalent counterions $N_s$ (24 for $G_2$-dPGS and 96 for $G_4$-dPGS) electrically neutralizing the macromolecule and having the same chemical identity as the MCs of the salt. The number of salt ions $i$ ($i = ++, +, -$) is denoted as $n_i$, while the corresponding

total salt concentrations are denoted as $c_i^0 = n_i/V$. Bulk concentrations are defined as $c_i^{\rm b} = (n_i - N_i^{\rm b})/(V - v_{\rm eff})$ (for $i = ++, -$) and $c_+^{\rm b} = (n_+ + N_{\rm s} - N_+^{\rm b})/(V - v_{\rm eff})$, where $v_{\rm eff} = 4\pi r_{\rm eff}^3/3$ is the volume enclosed by the effective radius $r_{\rm eff}$ of dPGS and $N_i^{\rm b}$ is the number of ions $i$ condensed (bound) on the dPGS. The definitions of both $r_{\rm eff}$ and $N_i^{\rm b}$ are adopted from the Alexander prescription (*cf.* Sec. 3.1.2.4.1).

The simulations are performed at the DC concentrations $c_{++}^0$ of 0.98, 2.95, 3.75, 9.96 and 14.94 mM. G$_2$-dPGS simulation snapshots for different $c_{++}^0$ values are shown in Fig. 5.1(a)–(c), while the whole simulation box is displayed in Fig. 5.1(d). The MC concentration $c_+^0$ is fixed at 150.37 mM and the monovalent anion concentration is adjusted in a way to ensure electroneutrality in the simulation box. The total ionic strength $I = \frac{1}{2}\sum_i z_i^2 c_i^{\rm b}$ ($i = +, ++, -$ with the charge valency $z_i$) ranges from 150.5 mM to 195 mM. The corresponding Debye screening length $\kappa^{-1} = \sqrt{8\pi l_{\rm B} I}$ (where $l_{\rm B}$ is the Bjerrum length) ranges from 0.8 nm ($c_{++}^{\rm b} = 0$ and $c_+^{\rm b} = 150.5$ mM) to 0.7 nm ($c_{++}^{\rm b} = 14.94$ and $c_+^{\rm b} = 150.5$ mM). As a reference, we also perform CG simulations in the limit of only monovalent salt, with concentrations $c_+^0$ of 10.02, 25.06 and 150.37 mM.

## 5.1.2 Simulation results: Radial density distributions

The dPGS structure and its response to the addition of the DCs, is examined by the density distribution of the terminal sulphate beads $c_{\rm s}(r)$ as a function of the distance $r$ from the dPGS-COM for different DC concentrations $c_{++}^0$, as shown in Fig. 5.2. Interestingly, the presence of DCs does not lead to a notable change in the dPGS structure. Instead, the $c_{\rm s}(r)$ profiles in the operated range of $c_{++}^0$ and for both G$_2$-dPGS and G$_4$-dPGS are reasonably coincident. Fig. 5.2(a) shows that for G$_2$-dPGS, a single-peak distribution is found, indicating that most of the sulphate beads reside on the molecular surface. However, in Fig. 5.2(b), a bimodal distribution is seen for G$_4$-dPGS with a small peak at $r \simeq 0.6$ nm. This backfolding phenomenon, contributing to a dense-core arrangement due to the dense macromolecular shell [60], is also found in our previous works [114, I] and has been detected for other terminally charged CG dendrimer models [97, 98, 106, 107]. After the major peak, $c_{\rm s}(r)$ gradually subsides to zero. The location where the charge density $c_{\rm s}(r)$ falls to 150 mM, which we set as the physiological NaCl concentration, is defined as the bare (intrinsic) radius of dPGS $r_{\rm d}$ [1], shown as vertical dashed blue lines in Fig. 5.2. The $r_{\rm d}$ values for G$_2$-dPGS and G$_4$-dPGS are obtained as 1.40 nm and 2.11 nm, respectively. Fig. 5.2(b) also shows that a slight shift in the location of the major peak

---

[1]$r_{\rm d}$ in our previous works (chapter 4) is defined as the location of the major peak of the sulphate density distribution [114, I].

and an enrichment of the lower peak appears as $c_{++}^0$ increases, indicating a slow shrinking of the dPGS molecule due to the condensation of DCs (see Fig. 5.3).
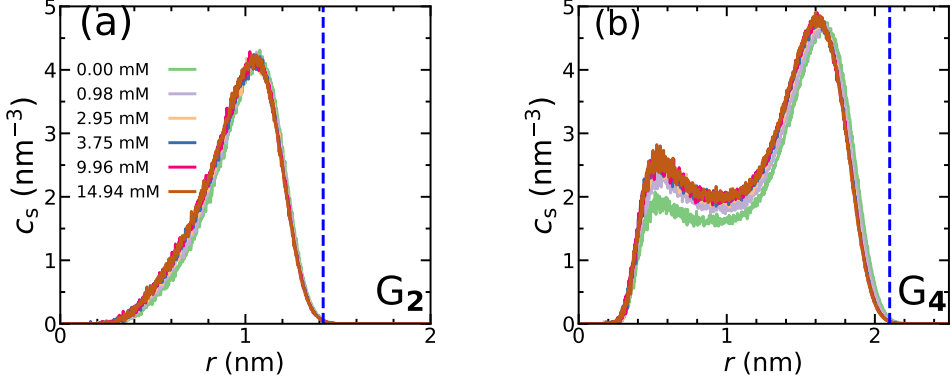


Figure 5.2: Radial density distributions $c_s(r)$ of the terminal sulphate groups of dPGS as a function of the distance $r$ from the COM of (a) $G_2$-dPGS and (b) $G_4$-dPGS, obtained from the CG computer simulations. The curves are plotted for different DC concentrations $c_{++}^0$ (see legend). The blue vertical dashed lines denote the dPGS bare radius $r_d$ (1.4 nm for $G_2$-dPGS and 2.1 nm for $G_4$-dPGS) defined as the location where $c_s(r)$ falls to the physiological threshold of 150 mM. The monovalent cation concentration $c_+^0$ is fixed to 150.37 mM.
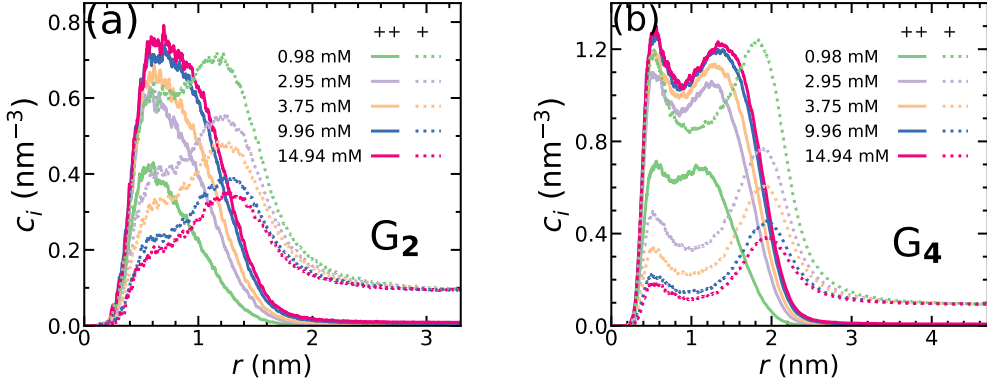


Figure 5.3: Radial density distributions $c_i(r)$ ($i = +, ++$) of counterion species $i$ as a function of the distance $r$ from the COM of (a) $G_2$-dPGS and (b) $G_4$-dPGS. The curves are plotted for different DC concentrations $c_{++}^0$ (see legend). The solid and dotted lines depict the density distributions of DCs and MCs, respectively.

Figs. 5.3(a) and (b) show the cation density distributions $c_i(r)$ ($i = +, ++$) for $G_2$-dPGS and $G_4$-dPGS, respectively. Let us focus first on $G_2$ in Fig. 5.3(a). The MC distribution $c_+(r)$ shows a high accumulation of counterions close to the sulphate groups, with a global maximum at distances $r \sim 1.2$ nm slightly larger than the sulphate peak (peaking roughly at $\sim 1$ nm). This means that the most strongly bound 'condensed' MCs are distributed more on the surface layers of the dPGS. At larger distances, $r \sim 2$ nm, a DH like decay is observed. Adding more DCs, the MC distribution gradually diminishes, as expected from the exchange of MCs with DCs within the dPGS. However, interestingly, the DC

distribution peaks at distances distinctively smaller than the location of the sulphate peak, roughly $0.5 - 0.6$ nm shifted towards the dPGS center away from the peak of the MC distribution. This more interior binding might be attributed to different binding mechanisms between DCs and sulphate, *e.g.*, bridging of two sulphate groups by one DC, which might be sterically favored closer to the dPGS core. These subtle structural effects may have important consequences in the context of the counterion-release mechanism driving the dPGS–protein binding [IV], which should be interesting for future studies. The ion profiles for $G_4$ shown in Fig. 5.3(b) show qualitatively the same behavior but are broader and double-peaked because of the significant sulfate backfolding as previously presented in Fig. 5.2(b).

It is worth noting that simulations of DCs in general are more challenging than for MCs only. DC are more heavily hydrated than MCs (*e.g.*, $Mg^{2+}$ and $Na^+$ ions) [383, 384], therefore future studies should scrutinize the ionic size used in the implicit solvent. Furthermore, quantum mechanical charge transfer effects as a result of the ion-induced powerful electronic polarization of the surrounding media [385], which are much more prevalent in the case of DCs [301, 307] than MCs, may also be subsumed in ionic sizes in the implicit water. These model details may subtly change the density profiles shown in Figs. 5.3(a) and (b). However, the effects on total competitive uptake should be relatively minor as they are dominantly driven by valency and electrostatic correlations, and size effects are typically of second order importance.

Using the density distributions of the charged entities shown above, the electrostatic properties of dPGS can be studied in the presence of the mixture of DCs and MCs. The analysis methods described in the section 5.1.3 are used to define the effective radius $r_{\text{eff}}$, charge valency $Z_{\text{eff}}$ and potential $\phi_{\text{eff}}$ of dPGS.

### 5.1.3 Structural and electrostatic properties of dPGS

Same as the analysis done for the section 4.3.7, the implicit-water approach described in the section 3.2.5.2.2 is used to calculate the electrostatic potential $\phi$ (scaled by $k_{\text{B}}T/e$) with the charged species in the system as dPGS sulphate beads ($s$), DCs ($++$), MCs ($+$) and monovalent coions ($-$). Then the Alexander prescription [15, 17, 129, 130, 386] (*cf.* Sec. 3.1.2.4.1) is used to calculate the effective radius $r_{\text{eff}}$, charge valency $Z_{\text{eff}}$, potential $\phi_{\text{eff}}$ of dPGS and the number of condensed counterions $N_i^{\text{b}}$ ($i = ++, +$). The value of $r_{\text{eff}}$ for dPGS in the simulations for $G_2$ and $G_4$ was found to be $1.65$ nm and $2.40$ nm, respectively, under the operated concentration range in the mixture of DCs with MCs as

| | | | $G_2$ | | | | $G_4$ | | | |
|---|---|---|---|---|---|---|---|---|---|---|
| $c_{++}^0$ | $c_+^0$ | $n_{++}$ | $r_d$ | $r_{eff}$ | $Z_{eff}$ | $\phi_{eff}$ | $r_d$ | $r_{eff}$ | $Z_{eff}$ | $\phi_{eff}$ |
| 0.00 | | 0 | | | $-10.09$ | $-1.26$ | | | $-20.04$ | $-1.27$ |
| 0.98 | | 16 | | | $-8.85$ | $-1.15$ | | | $-17.75$ | $-1.14$ |
| 2.95 | 150.37 | 48 | 1.06 | 1.65 | $-7.40$ | $-0.98$ | 1.65 | 2.40 | $-14.21$ | $-0.93$ |
| 3.75 | | 61 | | | $-6.84$ | $-0.85$ | | | $-12.25$ | $-0.77$ |
| 9.96 | | 162 | | | $-6.33$ | $-0.75$ | | | $-10.11$ | $-0.62$ |
| 14.94 | | 243 | | | $-5.86$ | $-0.68$ | | | $-9.65$ | $-0.55$ |

Table 5.1: The structural and electrostatic parameters of $G_2$-dPGS (having the bare charge valency $Z_d = -24$) and $G_4$-dPGS ($Z_d = -96$) measured from the CG simulations. $r_{eff}$, $Z_{eff}$, $\phi_{eff}$ are the effective radius (expressed in nm), the charge valency and the dimensionless potential of the dPGS, respectively, as a function of the DC concentration $c_{++}^0$ (expressed in mM), evaluated via simulations. The simulation box is cubic with a side length of 30 nm. The salt concentration of MCs $c_+^0$ is set to 150.37 mM.

well as in the monovalent limit, as shown in Table 5.1. These values are different than the ones obtained in our previous work [114], which operates at $c_+^0 = 10\,\text{mM}$, unlike the current work where $c_+^0 = 150.37\,\text{mM}$. The newly obtained $r_{eff}$ values in this work are then used as an input for the Manning–McGhee–von Hippel (MMvH) model, as discussed in the section 5.2.4, to describe the competitive sorption. It is thus implicitly assumed that $r_{eff}$ does not depend on the sorption of DCs, within the operated range of DC concentrations. The same prescription will be used to define $r_{eff}$ (denoted as $r_{eff}^{PB}$) from the solutions of the Penetrable Poisson–Boltzmann (PPB) model, as discussed in the section 5.2.3. The results for $r_{eff}^{PB}$ are also shown in Table 5.2. $Z_{eff}$ and $\phi_{eff}$ obtained from simulations, which are shown in Table 5.1, indicate strong decrease in magnitude with higher $c_{++}^0$, indicating enhanced dPGS charge renormalization.

## 5.2 Theoretical models

### 5.2.1 Basic model

In our theoretical models, the macromolecule is represented as a perfect sphere with the bare radius $r_d$, the bare charge valency $Z_d$, the effective radius $r_{eff}$ and the effective charge valency $Z_{eff}$, enclosed in a spherical domain of radius $R$ and volume $V$, as shown in Fig. 5.4. The total number of charged monomers in the macromolecule is $N_s$, each of which is negatively charged with a charge valency $z_s$. All ionic species and the macromolecule are assumed to be in an aqueous bath with an implicitly modeled solvent, having a uniform dielectric constant $\epsilon_w = 78$ at a temperature $T = 298\,\text{K}$.
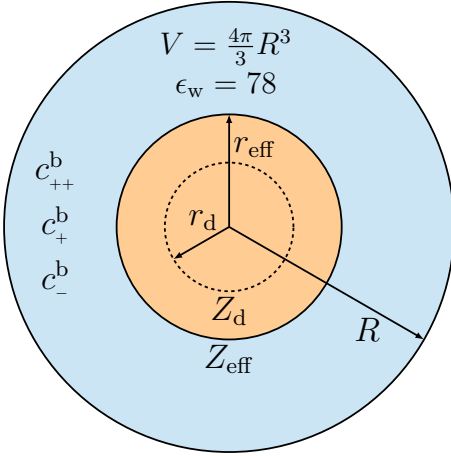
Figure 5.4: Schematic of a theoretical model representing the system shown in Fig. 5.1(d). The computational cell domain (blue) is assumed to be spherical with the same volume as that of the simulation box, $V$, and with a uniform dielectric constant of water $\epsilon_w = 78$. dPGS is assumed to be a perfect sphere (orange) at the center of the domain. The dPGS bare and effective charge valencies are $Z_d$ and $Z_{eff}$, respectively. $r_d$ is the bare radius of dPGS, while $r_{eff}$, the effective radius, representing the distance separating the electric double layer regime ($r > r_{eff}$) from the non-linear counterion 'condensation' regime ($r < r_{eff}$).

## 5.2.2 Competitive, ion-specific Donnan model (DM)

The arguably simplest model for competitive uptake is the Donnan model (*cf.* Sec. 3.1.2.5). The Donnan equilibrium assumes two strictly electroneutral and mutually exclusive regions, *i.e.*, the macromolecule region with the Donnan radius set to be the bare radius $r_d$ taken from simulations (*i.e.*, with a bare macromolecular volume $v_d = 4\pi r_d^3/3$) and total homogeneously distributed bare charge of valency $Z_d = z_s N_s$ with a concentration $c_s = N_s/v_d$ of charged groups of the macromolecule, and the bulk region outside the molecule with a bulk ion concentration $c_i^b$ ($i = +, ++, -$). Charge neutralization of the macromolecule by the counterions leads to the Donnan potential, which is a potential having a constant non-zero value in the macromolecule region. The potential in the bulk region is set to zero. The equilibrium distribution (partitioning) of ions among the regions results in the concentrations of ionic species $i$ as $c_i^m$ and $c_i^b$ in the macromolecule and bulk regions, respectively. These concentrations are related via the partition coefficient $\mathcal{K}_i$, given by

$$\mathcal{K}_i = \frac{c_i^m}{c_i^b} \qquad i = ++, +, - \tag{5.1}$$

Neglecting ion–ion correlations, an approximate expression for $\mathcal{K}_i$ can be obtained using the condition that the equilibrium electrochemical potential of ion $i$ is equal in both the

macromolecule and bulk regions, implying that

$$\ln c_i^{\mathrm{b}} = z_i \phi_{\mathrm{D}} + \ln c_i^{\mathrm{m}} + \beta \Delta \mu_{\mathrm{int},\, i} \tag{5.2}$$

where $\phi_{\mathrm{D}}$ is the dimensionless Donnan potential (scaled by $k_{\mathrm{B}}T/e$) in the macromolecule region and $\beta^{-1} = k_{\mathrm{B}}T$ is the thermal energy. With $\Delta \mu_{\mathrm{int},\, i}$ we account for additional non-electrostatic effects that can drive the sorption, *e.g.*, dispersion and hydrophobic forces in the net ion–macromolecule interaction, and is termed the ion-specific binding chemical potential of the condensed ion. The inclusion of $\Delta \mu_{\mathrm{int},\, i}$ has been considered in previous work, for example, as a term reflecting the steric ion–ion packing effects in a Donnan model for ion binding by PEs or charged hydrogels [360, 367, 368].

Eq. (5.2) with the help of Eq. (5.1) then leads to

$$\mathcal{K}_i = \frac{c_i^{\mathrm{m}}}{c_i^{\mathrm{b}}} = \mathrm{e}^{-\beta \Delta \mu_{\mathrm{bind},\, i}} = \mathrm{e}^{-\beta \Delta \mu_{\mathrm{int},\, i}} \mathrm{e}^{-z_i \phi_{\mathrm{D}}} \tag{5.3}$$

where $\Delta \mu_{\mathrm{bind},\, i}$ is the total transfer chemical potential for ion $i$ from the bulk to the macromolecule region. This allows us to define the intrinsic partition ratio for ionic species $i$ as

$$\mathcal{K}_{\mathrm{int},\, i} = \mathrm{e}^{-\beta \Delta \mu_{\mathrm{int},\, i}} \qquad i = +, ++ \tag{5.4}$$

and the Donnan partition ratio as a contribution from pure electrostatic interaction between the ion and the macromolecule environment as

$$\mathcal{K}_{\mathrm{el},\, i} = \mathrm{e}^{-z_i \phi_{\mathrm{D}}} \qquad i = +, ++ \tag{5.5}$$

The electrostatic component of total binding chemical potential of a counterion $i$ is then defined as $\beta \Delta \mu_{\mathrm{el},\, i} = -\ln \mathcal{K}_{\mathrm{el},\, i} = z_i \phi_{\mathrm{D}}$. Eq. (5.3) can then be conveniently shortened as

$$\mathcal{K}_i = \mathcal{K}_{\mathrm{el},\, i} \, \mathcal{K}_{\mathrm{int},\, i} \tag{5.6}$$

where $\mathcal{K}_i$ is shown as a composition of intrinsic and electrostatic effects. The signature assumption behind the Donnan model is the electroneutrality in the macromolecule region expressed as

$$z_{\mathrm{s}} c_{\mathrm{s}} + \sum_i z_i c_i^{\mathrm{b}} \, \mathcal{K}_i = 0 \tag{5.7}$$

Solving Eq. (5.7) for $\phi_D$ enables us to evaluate the net partition coefficient $\mathcal{K}_i$. Eq. (5.7) has no closed solution for multivalent ions, but it exists for the case of only monovalent ions in the system, $(i = \pm)$ and is given (as shown in Eq. (3.45)) as [254]

$$\phi_D = -\ln\left(-\frac{\sqrt{1 + \chi_+\chi_-} + 1}{\chi_+}\right) \tag{5.8}$$

where $\chi_i = 2\mathcal{K}_{\text{int},i}\, c_i^b/z_s c_s$. Note that $\chi_i < 0$, since the valency of charged groups $z_s$ is negative. Using Eqs. (5.3), (5.6) and (5.8), for the monovalent-only case, the number of ions of species $i(= \pm)$ partitioned into the macromolecule region is then given as

$$N_\pm^b = c_\pm^0 v_d\, \mathcal{K}_{\text{int},\pm}\left(-\frac{\sqrt{1 + \chi_+\chi_-} + 1}{\chi_+}\right)^{\pm 1} \tag{5.9}$$

To evaluate the competition between MCs and DCs in the Donnan model we evaluate Eqs. (5.3) and (5.7) numerically, *cf.* section 5.2.5.

Because of the electroneutrality assumption, the Donnan prediction for the amount of counterion sorption by the macromolecule in the monovalent-only case is given by $N_+^b = |Z| + N_-^b$. For highly charged macromolecules, *i.e.*, $\chi_i \to 0$, Eq. (5.9) trivially gives $N_+^b \simeq |Z|$. For the competitive sorption case, however, it can give a useful orientation with little effort. The Donnan model should become quantitative for high salt concentrations $(\kappa r_d \gg 1)$ for which the electroneutrality assumption is then well justified.

### 5.2.3 Ion-specific penetrable Poisson–Boltzmann (PPB) model

We now put forward a penetrable PB (PPB) model in which the charge profiles can be resolved in $r$, the radial distance from the macromolecular center. Since our charged macromolecules we have in mind (dPGS above and similar) are polymer-based with open structures and typically internally smeared out charge distributions, we opted (as in the Donnan model) for a penetrable model instead of a PB model for surface adsorption as typically used in studies of colloidal charge renormalization [115, 128, 387]. Based on the parametrization described in the basic model (Sec. 5.2.1), we assume the macromolecule as a perfect penetrable sphere with a charge valency $Z_d = z_s N_s$ and radius $r_d$, as shown in Fig. 5.4. $r_d$ is taken from the dPGS internal charge distribution obtained from simulations, *cf.* section 5.1.2 and Fig. 5.2. The charged monomers of the macromolecule, thus, have a uniform number distribution $c_s = N_s/v_d$ (where $v_d = 4\pi r_d^3/3$) within the volume $v_d$. $c_s$ is applicable only within the macromolecule domain, *i.e.*, $c_s(r) = c_s\left(1 - H(r - r_d)\right)$, where

$H(r)$ is the Heaviside-step function. As an improvement to the standard PB model, here we also consider a contribution of the intrinsic non-electrostatic ion-specific interaction $\Delta\mu_{\text{int},i}$ between the ion and the macromolecule [180, 225], analogous to Eq. (5.2) in the Donnan model above. Assuming the electrostatic potential far away from the macromolecule, $\phi(r \to R) = 0$, we first balance the chemical potential for each ion, between the bulk regime far from the macromolecule and the regime at the finite distance $r$ from the center of the macromolecule

$$\ln c_i^{\text{b}} = z_i\phi(r) + \ln c_i(r) + \beta\Delta\mu_{\text{int},i}(r), \tag{5.10}$$

which is similar to Eq. (5.2), but in a distance-resolved manner. $\Delta\mu_{\text{int},i}$ is considered on a local level, i.e., $\Delta\mu_{\text{int},i}(r) = \Delta\mu_{\text{int},i}\left(1 - H(r - r_{\text{d}})\right)$. The Boltzmann ansatz then becomes

$$c_i(r) = c_i^{\text{b}}\, e^{-z_i\phi(r) - \beta\Delta\mu_{\text{int},i}(r)} \tag{5.11}$$

The distance-resolved electrostatic potential can be calculated from Eq. (5.11) together with the Poisson's equation as

$$\nabla^2\phi(r) = -4\pi l_{\text{B}}\left(\sum_i z_i c_i(r) + z_{\text{s}}c_{\text{s}}(r)\right) \qquad i = ++, +, - \tag{5.12}$$

which establishes the PPB model including ion-specific binding effects. The boundary conditions used are $(\mathrm{d}\phi/\mathrm{d}r)\,(r \to 0) = 0$ and $(\mathrm{d}\phi/\mathrm{d}r)\,(r \to R) = 0$.

An effective radius for dPGS is calculated independently for this model (labeled $r_{\text{eff}}^{\text{PB}}$) using the Alexander prescription (cf. Sec. 3.1.2.4.1) on the obtained potential $\phi$, the same recipe used to calculate $r_{\text{eff}}$ from simulations, cf. section 5.1.3. The values of $r_{\text{eff}}^{\text{PB}}$ for $\text{G}_2$-dPGS and $\text{G}_4$-dPGS are obtained as $1.42\,\text{nm}$ and $2.36\,\text{nm}$, respectively, under the operated range of $c_{++}^0$ and at $c_+^0 = 150.37\,\text{mM}$. The $r_{\text{eff}}^{\text{PB}}$ values are thus found to be close to those obtained from the simulations, as shown in Table 5.2. The effective surface potential of the macromolecule is then given by $\phi_{\text{eff}}^{\text{PB}} = \phi(r_{\text{eff}}^{\text{PB}})$. The number of bound ions of species $i$ within $r_{\text{eff}}$, is then given by

$$N_i^{\text{b}} = \int_0^{r_{\text{eff}}} c_i(r)\,4\pi r^2\,\mathrm{d}r \qquad i = +, ++ \tag{5.13}$$

The corresponding effective charge valency $Z_{\text{eff}}^{\text{PB}}$ is calculated using Eq. (3.66). The PPB

equations are solved numerically, *cf.* section 5.2.5.

The PPB model operates in terms of the volume sorption of ions in the macromolecule with no entropic penalty, *i.e.*, the PE acts as an infinite reservoir able to uptake unlimited amount of counterions. However, there is an upper limit to the amount of counterions that can be sorbed by the real-world PEs, owing to the steric constraints [173, 226, 363, 366]. Taking it into consideration, we present a variant of the PPB model assigning the entropic penalty to the binding counterions. This entropic cost is incorporated in a Langmuir form, thus, naming the model as the Penetrable Poisson–Langmuir (PPL) model, presented in Appendix B.1.

## 5.2.4 Manning–McGhee–von Hippel (MMvH) binding model

In this section, we introduce a model based on a discrete two-state (condensed or free) perspective for the counterions, built to capture the essential physics of PE–ion binding in an accurate but minimalistic fashion. The model is an extension of ideas by Manning [120] (*cf.* Sec. 3.1.2.4.4), in which ion-condensation on charged spherical surfaces was described on a mean-field free energy level as a competition between the charging (Born) self-energy of the macromolecule in salt solution and the entropy cost of binding for one-component counterions. Here, we extend this model to the case of mixtures of MCs and DCs, including binding saturation for a fixed number of binding sites like in Langmuir isotherms. The extension of the latter to binary binding of one or two binding sites by mono- or divalent solutes, respectively, was put forward buy McGhee and von Hippel [379]. Therefore, we name the model Manning–McGhee–von Hippel binding model (MMvH).

Following Manning [120], we treat the macromolecule as an impenetrable sphere of radius $r_{\text{eff}}$ and charge valency $Z_{\text{d}} = z_s N_s$ taken from simulations, and extend the Manning's model into a discrete binding site model, where the $N_{\text{s}}$ charged monomers act as a finite collection of discrete binding sites for both the MCs and DCs. For the case of the DCs, two adjacent charged monomers can collectively act as a single binding site for a DC. The resulting combinatorial ways to arrange the bound MCs and DCs lead to mixing entropies worked out by McGhee and von Hippel [379]. Pertaining to the canonical ensemble, we fix the total number of salt ions $n_i$, the corresponding concentrations $c_i^0$ ($i = ++, +, -$), the number of monovalent counterions $N_{\text{s}}$ to the macromolecule, the total number of binding sites on the macromolecule and the total domain volume $V$. The coions in this model simply serve the function of maintaining electroneutrality in the total domain and their explicit sorption is neglected.

A counterion $i$ ($= +, ++$) is assumed to bind to the macromolecule and to occupy $f_i$ consecutive (spatially adjacent) charged terminal groups of the macromolecule. We designate $f_+ = 1$ and $f_{++} = 2$ for MCs and DCs, respectively, implying that, in a bound state, one MC occupies only one charged terminal group, while one DC occupies two consecutive charged terminal groups, owing to the fact that each terminal group has a charge valency $z_s = -1$. Consider at a given state, $N_+^b$ MCs and $N_{++}^b$ DCs are bound to the macromolecule. The *binding density*, *i.e.*, the number of bound counterions per charged terminal group is then $N_+^b/N_s$ and $N_{++}^b/N_s$ for MCs and DCs, respectively. By multiplying with $f_i$, we then define the fraction of the binding sites occupied by the counterions, *i.e.*, coverages $\Theta_+ = f_+ N_+^b/N_s = N_+^b/N_s$ and $\Theta_{++} = f_{++} N_{++}^b/N_s = 2N_{++}^b/N_s$. Thus, the total number of binding sites on the macromolecule available for MCs, is $N_+ = N_s/f_+ = N_s$, and those available for DCs, is $N_{++} = N_s/f_{++} = N_s/2$. The effective charge valency of the macromolecule is then $Z_{\text{eff}} = -N_s + N_+^b + 2N_{++}^b = -N_s(1 - \Theta_+ - \Theta_{++})$. The total Helmholtz free energy $\mathcal{F}_{\text{tot}}$ depends on the coverages $\Theta_+$ and $\Theta_{++}$ and the ionic concentrations $c_i^0$. The coverages can then be obtained by minimizing $\mathcal{F}_{\text{tot}}$ simultaneously with respect to $\Theta_+$ and $\Theta_{++}$. The total Helmholtz free energy $\mathcal{F}_{\text{tot}}$ is given by the expression

$$\mathcal{F}_{\text{tot}} = \mathcal{F}_{\text{el}} + \mathcal{F}_{\text{tr}} + \mathcal{F}_{\text{mix}} + \mathcal{F}_{\text{int}} \tag{5.14}$$

where the four additive contributions, $\mathcal{F}_{\text{el}}$, $\mathcal{F}_{\text{tr}}$, $\mathcal{F}_{\text{mix}}$ and $\mathcal{F}_{\text{int}}$ are defined respectively as (*i*) electrostatic (Born) self-energy of charge renormalized macromolecule, (*ii*) ideal gas entropy of free ions in the bulk regime, (*iii*) mixing entropy of the condensed counterions in the macromolecule, and (*iv*) the non-electrostatic ion-specific binding free energy between the condensed counterion and the corresponding binding site on the macromolecule.

The Born charging self-energy of the macromolecule immersed in an electrolyte solution associated with the Debye screening length $\kappa^{-1}$, refers to the work required to charge the macromolecule from its electroneutral to a certain charged state. Following Manning, such a charged state is associated with the effective charge $Z_{\text{eff}}e$, corresponding to the sum of the intrinsic bare charge of the macromolecule $Z_d$ and its captive, neutralizing counterions [120]. Thus, the expression for the Born charging free energy of the macro-molecule (or the self energy of the charge renormalized macromolecule) per monovalent binding site is thus expressed as (*cf.* Sec. 3.1.2.4.4)

$$\beta \mathcal{F}_{\text{el}} = \frac{Z_{\text{eff}}^2 l_B}{2N_s r_{\text{eff}}(1 + \kappa r_{\text{eff}})} = \frac{\zeta}{2}(1 - \Theta_+ - \Theta_{++})^2 \tag{5.15}$$

where $\zeta/2$ is the Born free energy per monovalent binding site in the absence of counterion condensation, and $\zeta$ is given for surface charging by [224]

$$\zeta = \frac{N_s l_B}{r_{eff}(1 + \kappa r_{eff})} \tag{5.16}$$

Considering the effective volume of dPGS $v_{eff}$ to be very small compared to the total volume $V$ ($v_{eff} \ll V$), the bulk concentrations of MCs and DCs are given by

$$
\begin{aligned}
c_+^b &= c_+^0 + \frac{N_+(1 - \Theta_+)}{V} \\
c_{++}^b &= c_{++}^0 - \frac{N_{++}\Theta_{++}}{V}
\end{aligned} \tag{5.17}
$$

owing to the depletion of the ions in the bulk due to partitioning. $c_+^b$ above is calculated considering the monovalent counterions remaining in the solution, in the salt-free limit. We assume that no anions are bound to the macromolecule binding sites, hence their bulk concentration is assumed to be the same as their salt concentration, i.e., $c_-^b = c_-^0$.

The ideal gas free energy of free cations in the bulk, normalized by the number of monovalent binding sites $N_s$, is given as

$$
\begin{aligned}
\beta \mathcal{F}_{tr} = -\frac{S_{id}}{N_s k_B} &= \sum_{i=+,++} \left( \frac{n_i - N_i^b}{N_s} \right) \left( \ln c_i^b \Lambda_i^3 - 1 \right) \\
&= \sum_{i=+,++} \left( \frac{n_i - N_i \Theta_i}{N_s} \right) \left[ \ln \left( c_i^0 \Lambda_i^3 - \frac{N_i \Theta_i \Lambda_i^3}{V} \right) - 1 \right]
\end{aligned} \tag{5.18}
$$

where $\Lambda_i$ and $n_i$ are the thermal (de Broglie) wavelength and the number of salt ions $i$.

The bound DCs and MCs can occupy the binding sites on the macromolecule in different proportions, and can distribute among the occupied sites in multiple ways at a certain bound coverages $\Theta_+$ and $\Theta_{++}$. We exert constraints to such possibilities of binding compositions and configurations, such that, (i) one bound DC can only bind to two adjacent monovalent binding sites, (ii) all non-overlapping configurations between the bound ions are possible, (iii) there are no designated binding sites for DCs, and (iv) the position of the bound DC can be shifted by a single adjacent monovalent binding site. The number of possible combinatorial binding arrangements under these constraints, adopted from the

work by McGhee and von Hippel [379], is given by

$$
W = \frac{\gamma_+^{N_+^{\mathrm{b}}} \gamma_{++}^{N_{++}^{\mathrm{b}}} (N_{\mathrm{s}} - N_{++}^{\mathrm{b}})!}{N_+^{\mathrm{b}}! N_{++}^{\mathrm{b}}! (N_{\mathrm{s}} - 2N_{++}^{\mathrm{b}} - N_+^{\mathrm{b}})!}
\tag{5.19}
$$

where we define $\gamma_i = v_i^0 / \Lambda_i^3$ in terms of the effective configurational volume $v_i^0$ in the bound state [325]. $v_i^0$ takes into account the rotational and vibrational degrees of freedom of a bound counterion $i$. We now define the free energy associated with the partition function $W$, normalized by the number of monovalent binding sites $N_{\mathrm{s}}$, as the free energy of mixing of the bound ions per binding site,

$$
\begin{aligned}
\beta \mathcal{F}_{\mathrm{mix}} = -\frac{S_{\mathrm{mix}}}{N_{\mathrm{s}} k_{\mathrm{B}}} = &-\frac{1}{N_{\mathrm{s}}} \ln W \\
\simeq &\; \Theta_+ \ln \Theta_+ + \frac{\Theta_{++}}{2} \ln \frac{\Theta_{++}}{2} - \left(1 - \frac{\Theta_{++}}{2}\right) \ln \left(1 - \frac{\Theta_{++}}{2}\right) \\
&+ (1 - \Theta_+ - \Theta_{++}) \ln(1 - \Theta_+ - \Theta_{++}) - \Theta_+ \ln \frac{v_+^0}{\Lambda_+^3} - \frac{\Theta_{++}}{2} \ln \frac{v_{++}^0}{\Lambda_{++}^3}
\end{aligned}
\tag{5.20}
$$

where the Stirling approximation has been used for the logarithm of the factorials. This description of condensed counterion entropy is different than the ion-binding models proposed in previous works for linear PE [23, 380, 381] in terms of the localization of counterions within volume $v_i^0$.

We express this intrinsic interaction $\mathcal{F}_{\mathrm{int}}$ by the intrinsic binding chemical potential $\Delta \mu_{\mathrm{int}, i}$ of each bound ion $i$. The sum of such interactions for all bound ions, normalized by the total number of monovalent binding sites gives

$$
\begin{aligned}
\beta \mathcal{F}_{\mathrm{int}} &= \frac{1}{N_{\mathrm{s}}} \left( N_+^{\mathrm{b}} \beta \Delta \mu_{\mathrm{int},+} + N_{++}^{\mathrm{b}} \beta \Delta \mu_{\mathrm{int},++} \right) \\
&= \Theta_+ \beta \Delta \mu_{\mathrm{int},+} + \frac{\Theta_{++}}{2} \beta \Delta \mu_{\mathrm{int},++}
\end{aligned}
\tag{5.21}
$$

The equilibrium coverages $\Theta_i$ are then obtained by the minimization condition

$$
\frac{\partial}{\partial \Theta_i} \mathcal{F}_{\mathrm{tot}} \overset{!}{=} 0 \qquad i = +, ++
\tag{5.22}
$$

This leads to the relation

$$
\Delta \mu_{\mathrm{tr}, i} + \Delta \mu_{\mathrm{el}, i} + \Delta \mu_{\mathrm{mix}, i} + \Delta \mu_{\mathrm{int}, i} = 0 \qquad i = +, ++
\tag{5.23}
$$

where $\Delta \mu_{\mathrm{tr}, i}$ denotes the translational entropy change associated with one ion $i$ when it

transfers from the bulk environment to the bound state in the macromolecule. $\Delta\mu_{\mathrm{el},i}$ is the *electrostatic binding chemical potential* and $\Delta\mu_{\mathrm{mix},i}$ is the *mixing chemical potential*. Eq. (5.23), similar to the PPB (Eq. (5.10)) and DM (Eq. (5.2)) models, indicates the counterion chemical potential components contributing to its condensation on the macromolecule. The expressions for the constituent chemical potential contributions in Eq. (5.23) are given by

$$
\begin{aligned}
\beta\Delta\mu_{\mathrm{tr},i} &= -\ln c_i^{\mathrm{b}} v_i^0 \qquad\qquad && i = +, ++ \\
\beta\Delta\mu_{\mathrm{el},i} &= -z_i\zeta(1 - \Theta_+ - \Theta_{++}) && i = +, ++ \\
\beta\Delta\mu_{\mathrm{mix},i} &=
\begin{cases}
\ln\dfrac{\Theta_{++}(2 - \Theta_{++})}{4(1 - \Theta_+ - \Theta_{++})^2} & i = ++ \\[3ex]
\ln\dfrac{\Theta_+}{(1 - \Theta_+ - \Theta_{++})} & i = +
\end{cases}
\end{aligned}
\tag{5.24}
$$

Using Eqs. (5.23) and (5.24) leads to the final form of the MMvH model, given by

$$
K_{++} = v_{++}^0 \mathcal{K}_{\mathrm{int},++} \mathrm{e}^{2\zeta(1 - \Theta_+ - \Theta_{++})} = \frac{\Theta_{++}(2 - \Theta_{++})}{4c_{++}^{\mathrm{b}}(1 - \Theta_+ - \Theta_{++})^2}
\tag{5.25}
$$

$$
K_+ = v_+^0 \mathcal{K}_{\mathrm{int},+} \mathrm{e}^{\zeta(1 - \Theta_+ - \Theta_{++})} = \frac{\Theta_+}{c_+^{\mathrm{b}}(1 - \Theta_+ - \Theta_{++})}
\tag{5.26}
$$

where $K_i$ are the *equilibrium binding constant* associated with the binding of ion $i$ to its corresponding binding site on the macromolecule. The relationship between $K_i$, the total binding chemical potential $\Delta\mu_{\mathrm{bind},i}$ and the total partition ratio $\mathcal{K}_i$ is given as

$$
\beta\Delta\mu_{\mathrm{bind},i} = -\ln\frac{K_i}{v_i^0} = -\ln\mathcal{K}_i \qquad i = +, ++
\tag{5.27}
$$

Or in other words, referring back to Eq. (5.6),

$$
\mathcal{K}_i = \mathcal{K}_{\mathrm{int},i}\,\mathcal{K}_{\mathrm{el},i} = \mathcal{K}_{\mathrm{int},i}\,\mathrm{e}^{z_i\zeta(1 - \Theta_+ - \Theta_{++})}
\tag{5.28}
$$

where the electrostatic contribution of the total partition ratio is defined as

$$
\mathcal{K}_{\mathrm{el},i} = \mathrm{e}^{-\beta\Delta\mu_{\mathrm{el},i}} = \mathrm{e}^{z_i\zeta(1 - \Theta_+ - \Theta_{++})} \qquad i = +, ++
\tag{5.29}
$$

From Eq. (5.27), for a given magnitude of $K_i$, the absolute magnitude of $\Delta\mu_{\mathrm{bind},i}$ depends

on $v_i^0$, which we calculate from our simulations and predict respective values of $\Delta\mu_{\mathrm{bind},\,i}$.

Finally, we consider the limit of the MMvH model for vanishing DCs (MCs only). Without DCs, we have

$$
\begin{aligned}
\beta\Delta\mu_{\mathrm{tr}} &= -\ln c_+^{\mathrm{b}} v_+^0 \\
\beta\Delta\mu_{\mathrm{el}} &= -\zeta(1 - \Theta_+) \\
\beta\Delta\mu_{\mathrm{mix}} &= \ln \frac{\Theta_+}{(1 - \Theta_+)}
\end{aligned}
\tag{5.30}
$$

Combining Eqs. (5.23) and (5.30) leads to the Manning–Langmuir model (ML)

$$
K_+ = v_+^0 \mathcal{K}_{\mathrm{int},\,+} \mathrm{e}^{\zeta(1-\Theta_+)} = \frac{\Theta_+}{c_+^{\mathrm{b}}(1 - \Theta_+)}
\tag{5.31}
$$

The McGhee–von Hippel combinatorics here reduces to the standard one-component Langmuir picture, *i.e.*, the right-hand-side of Eq. (5.31) reflects the Langmuir isotherm. The standard Langmuir model is thus extended to include charging free energies by ion condensation (charge renormalization) and ion-specific binding. From another perspective, it extends the Manning model for the counterion condensation on spheres [120, 121] to include ion-specific effects as well as the saturation of binding sites in terms of the translation entropy of the condensed ions.

Future extensions of the MMvH model could include an extra level of competition between adsorbed ions explicitly, namely through a non-linear term in Eq. (5.20) (of the type used in the regular solution theory or the Flory–Huggins approximation in polymer theories) that describes the interaction between two adsorbed ions in proximal positions (sites). The effects of this generalization in a different context can be found in a study on ion induced lamellar-lamellar phase transition in charged surfactant systems. [388] In general, this type of competition results in non-continuous adsorption equilibria and could be interesting in the present context.

### 5.2.5 Numerical evaluation

The PPB model, with the assumption of the uniform intrinsic macromolecular volume charge distribution $c_{\mathrm{s}}(r)e$ and with the knowledge of the bare radius $r_{\mathrm{d}}$ of the macromolecule inherited from simulations, generates the distance-resolved number density profiles of charged species, similar to Fig. 5.3. Hence, it performs the same analysis as that for simulations (*cf.* Sec. 5.1.3), to calculate the effective radius $r_{\mathrm{eff}}$ and other electrostatic

properties of the macromolecule, such as $Z_{\text{eff}}$, $\phi_{\text{eff}}$, etc. The Donnan model (DM) also assumes uniform sulfate charge density $c_{\text{s}}(r)e$ and requires the knowledge of the electroneutrality radius, which is taken as $r_{\text{d}}$ from simulations as an input parameter, similar to the PPB model. The MMvH (ML) model, on the other hand, assumes the macromolecule as a hard sphere with a uniform surface charge distribution. The effective radius of the hard sphere $r_{\text{eff}}$ is taken from simulations as an input parameter. The results from the DM, PPB and MMvH (ML) models and simulations are compared in terms of the coverages $\Theta_i$ ($i = ++, +$), which are defined as $\Theta_i = N_i^{\text{b}}/N_i$, where $N_i^{\text{b}}$ is the number of condensed counterions $i$ and $N_i$ is the corresponding number of binding sites available on dPGS, defined in the section 5.2.4. Since the PPB model deals with a volume sorption, while the DM model deals with the ion partitioning between two electroneutral phases, "coverage" $\Theta_i$ in these cases are interpreted as a load or an extent of neutralization of dPGS. For the DM, PPB and MMvH (ML) models, the intrinsic partition coefficients $\mathcal{K}_{\text{int},i}$ for both ions ($i = ++, +$) are unknowns and taken as fitting parameters in order to match the coverages from the simulations, which are described in the section 5.1.1. Regarding the PPB and DM models, we make a further assumption that intrinsic non-electrostatic ion–binding site interaction for the MCs is identical to that for the monovalent anions, i.e., $\mathcal{K}_{\text{int},+} = \mathcal{K}_{\text{int},-}$.

Mathematically, the PPB model represents a boundary-value problem having a second order differential equation (Eq. (5.12)) non-linear in the electrostatic potential paired with the boundary conditions, while the MMvH model (Eqs. (5.25) and (5.26)) represents two non-linear simultaneous equations in coverages $\Theta_+$ and $\Theta_{++}$. Both PPB and MMvH models are evaluated self consistently for the potential and coverages, respectively. To solve Eq. (5.12), we employ the `solve_bvp` function in the SciPy library (version 1.3.1) from Python (version 3.7.4), which solves a boundary-value problem for a system of ordinary differential equations using the fourth order collocation algorithm [389]. The bulk concentration $c_i^{\text{b}}$ is obtained using the law of conservation of mass in an iterative manner, cf. Appendix B.1.0.1. Eqs. (5.25) and (5.26) are solved using `fsolve` function from the SciPy library, which is also used to evaluate the DM model (Eq. (5.7)) representing the single non-linear equation in the Donnan potential $\phi_{\text{D}}$.

The effective configurational volume $v_i^0$ of bound counterions, used in the MMvH model is assumed to be equal for both counterions, i.e., $v_{++} = v_+ = v_0$. It is worth considering that the volume $v_0$ depends on the precise nature of the bound state and it is infeasible to have its knowledge in experiments due to unknown microscopic details, although it can be computed using simulations [IV, 390]. According to the convention in experiments,

the standard volume is defined as $v_0 = 1\,\mathrm{M}^{-1} \simeq 1.6\,\mathrm{nm}^3$, corresponding to the standard concentration $c^{\mathrm{std}} = 1\,\mathrm{M}$ [257, 258, 259]. In this case, the total binding chemical potential $\Delta\mu_{\mathrm{bind},\,i}$ can be referred to as the standard binding energy $\Delta G^0$ [258, 259].

## 5.3 Results and discussion

### 5.3.1 Monovalent limit: Theoretical comparison and best fit to simulations
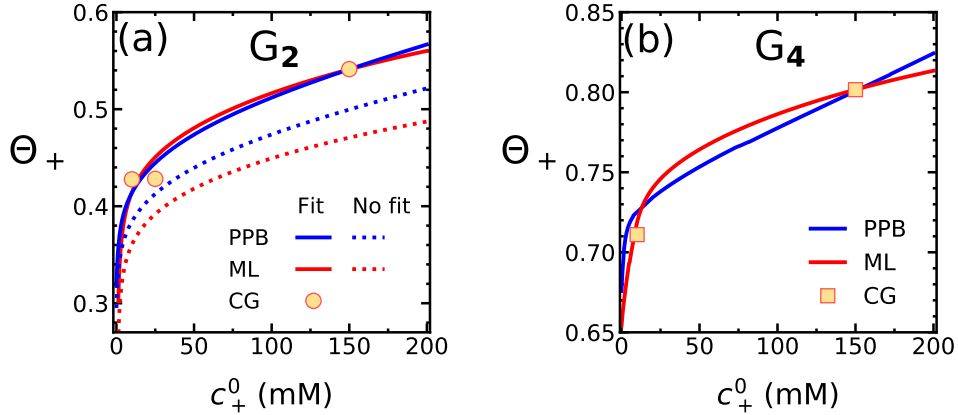


Figure 5.5: Model predictions [PPB (Eq. (5.12)) and ML (Eq. (5.31))] of the coverage $\Theta_+$ of MCs in the monovalent limit, as a function of the MC concentration $c_+^0$, compared with simulations (circle and square symbols). (a) For the case of $G_2$-dPGS, the dotted lines represent the results for vanishing intrinsic binding chemical potential $\Delta\mu_{\mathrm{int},\,+}$, while the solid lines show the results obtained by fitting $\Delta\mu_{\mathrm{int},\,+}$ to the simulations (yellow circles). The fitted $\Delta\mu_{\mathrm{int},\,+}$ values obtained for the PPB and ML models are $-0.45\,k_{\mathrm{B}}T$ and $-1.81\,k_{\mathrm{B}}T$, respectively. The ML model uses the configurational volume $v_0 = 1.04\,\mathrm{M}^{-1}$ as obtained from our previous CG simulations [IV]. (b) Comparison of binding coverages obtained by ML and PPB models for $G_2$-dPGS and $G_4$-dPGS. The dashed lines denote the model results fitted to $G_4$-dPGS simulations (yellow squares). The fitted values of $\Delta\mu_{\mathrm{int},\,+}$ obtained for PPB and ML models are $-0.56\,k_{\mathrm{B}}T$ and $-1.85\,k_{\mathrm{B}}T$, respectively, fairly close to those obtained for $G_2$-dPGS. The configurational binding volume for $G_4$ is fixed to $v_0 = 0.57\,\mathrm{M}^{-1}$ and is obtained from our previous simulations [IV].

Considering the monovalent limit as reference case, we now start with the application of aforementioned theoretical binding models. Fig. 5.5(a) shows the predictions of the PPB and ML (monovalent-only limit of MMvH) models for the variation of the binding coverage of MCs, $\Theta_+$, as a function of the MC concentration, $c_+^0$. It can be observed that $\Theta_+$ increases sharply for a small increase in $c_+^0$ from 0 to $\sim 10\,\mathrm{mM}$, while it increases gradually for larger $c_+^0$. This is attributed to the combined contribution of the electrostatics and an entropy of a bound counterion, facilitating condensation. In the low $c_+^0$ regime, the bare charge of $G_2$-dPGS is weakly renormalized, and some of the dPGS binding sites are unoccupied. This leaves a high propensity of condensation for new incoming counterions.

This can be conveniently explained via the ML model. Referring to Eq. (5.31), the increase in the condensation of MCs at the limit of low $c_+^0$, $\lim_{c_+^0 \to 0} \mathrm{d}\Theta_+/\mathrm{d}c_+^0$ is directly proportional to the total binding constant $K_+$, while at high $c_+^0$, $\lim_{c_+^0 \to \infty} \mathrm{d}\Theta_+/\mathrm{d}c_+^0 = 0$. This implies that at low $c_+^0$, the resultant low coverage $\Theta_+$ leads to a high electrostatic driving force for condensation as well as entropy of a bound counterion, thus a high amount of condensation. On the other hand, at high $c_+^0$, the macromolecule charge is almost entirely renormalized and most of the binding sites are occupied, resulting in hardly any increase in condensation.

Comparing the coverage profiles from PPB and ML models that neglect ion-specific effects, $i.e.$, with $\Delta\mu_{\mathrm{int},+} = 0$ (dotted curves), we find that the PPB coverage values are close to the ML values in the low $c_+^0$ regime, however, attain higher values than the ML counterpart at high $c_+^0$. This is attributed to the effects of discrete binding sites incorporated in the ML model, in the form of the configurational volume $v_0$ (here, we used $v_0 = 1.04$ M$^{-1}$ obtained from our previous simulations [IV]). The PPB model, on the other hand, assumes the condensed ions as point charges, leaving no entropic penalty for new incoming counterions as they condense on the binding sites. Another reason is that the PPB model also incorporates, to some extent, the non-linear effects in the electrostatic interactions, which are not considered in the DH-level Born energy used in the ML model. Both models, however, underestimate the simulations if we do not include corrections via $\Delta\mu_{\mathrm{int},+}$. The reason is likely the approximative treatments of the electrostatic energy in both models, PPB and ML, which are mean-field and do not include the discrete nature of the charged binding sites and the complex spatial charge correlations inside the macromolecule. The DM model, in addition to these assumptions, takes the macroscopic view of macromolecule and bulk phases in a segregated form. The model then predicts the ion partitioning while imposing electroneutralities of phases. In that respect, for highly charged macromolecules like dPGS, the DM model predicts $N_+^{\mathrm{b}} \simeq N_{\mathrm{s}}$, implying $\Theta_+ \simeq 1$. This plot is not shown, since it does not provide a useful insight for us in the context of counterion condensation. The case of salt concentration $c_+^0 = 0$ is referred to as the counterion-only case, and gives $\Theta_+ \sim 0.28$ for the PPB model. Note that $\Theta_+$ in this limit is system specific, since the size of the simulation box/computational domain determines the counterion concentration and subsequently the coverage. The coverage $\Theta_+$ in the ML model in this limit is undefined, since the electrostatic binding energy of MCs depends on the screening length $\kappa^{-1}$, which is undefined in this model in the absence of the salt.

In the next step, $\Theta_+$ values for PPB and ML models are fitted (bold curves in Fig. 5.5(a)) to the simulation results for G$_2$-dPGS in the monovalent limit by allowing ion-specific ef-

fects in the counterion–macromolecule binding, *i.e.*, $\Delta\mu_{\text{int},+}$ as a fitting parameter. The values of $\Delta\mu_{\text{int},+}$ are found to be $-0.45\,k_{\text{B}}T$ and $-1.81\,k_{\text{B}}T$ for PPB and ML models, respectively. Recall that the simulations have not really included ion-specific effects in terms of specific hydration phenomena, etc., still, they include excluded-volume, dispersion attraction, and importantly, all electrostatic charge–charge correlations, not captured in the mean-field theories. Hence, the ion-specific fitting parameters can be viewed in general as correction factors, including all ionic contributions that are beyond the mean-field treatment of the PPB and ML models. The larger fitting parameter for ML than PPB (in the absolute value) may indicate the higher level of approximations in the ML model. Having the models now informed using the benchmark data from simulations, they can be utilized to predict the binding at other ion concentrations.

Fig. 5.5(b) shows the numerical fitting of $\Theta_+$ values (dashed curves) to those obtained from $G_4$-dPGS simulations. The values of $\Delta\mu_{\text{int},+}$ as a fitting parameter are $-0.56\,k_{\text{B}}T$ and $-1.85\,k_{\text{B}}T$ for PPB and ML models, respectively, which are close to those obtained for $G_2$-dPGS, within the error difference of $\sim 0.1\,k_{\text{B}}T$. The ML model fits better to both $G_2$-dPGS and $G_4$-dPGS CG results than the PPB model at large $c_+^0$, which may indicate that the dPGS charge in the simulations acts more as finite binding sites, as assumed in the ML model.

## 5.3.2   Divalent case: Theoretical comparison and best fit to simulations

We now aspire to use the obtained $\Delta\mu_{\text{int},+}$ to inform the MMvH and PPB models with the help of the reference data obtained from simulations, in order to capture the competitive ion binding in a mixture of MCs and DCs. The models fitted to the benchmark data can then be used to predict the binding coverages $\Theta_{++}$ and $\Theta_+$ for different dPGS generations and salt concentrations. In practice, we perform the numerical fitting of $\Theta_{++}$ and $\Theta_+$ obtained from the MMvH and PPB models to those from simulations, by fixing $\Delta\mu_{\text{int},+}$ for MCs obtained from the monovalent-only case, and then subsequently fitting $\Delta\mu_{\text{int},++}$ for DCs. The values of $\Delta\mu_{\text{int},+}$ for MCs obtained from the monovalent limit are, for a given binding model (ML or PPB), found to be approximately independent of the dPGS generation (with $\sim 0.1\,k_{\text{B}}T$ as margin of error). Therefore, $\Delta\mu_{\text{int},+}$ is averaged over generations ($G_2$ and $G_4$), as shown in Table 5.3. Fig. 5.6 depicts the behavior of MMvH, PPB and the DM model in terms of the binding coverages $\Theta_i$, in a mixture of DCs and MCs. The MMvH model uses the effective configurational volumes $v_0 = 1.04\,\text{M}^{-1}$

97
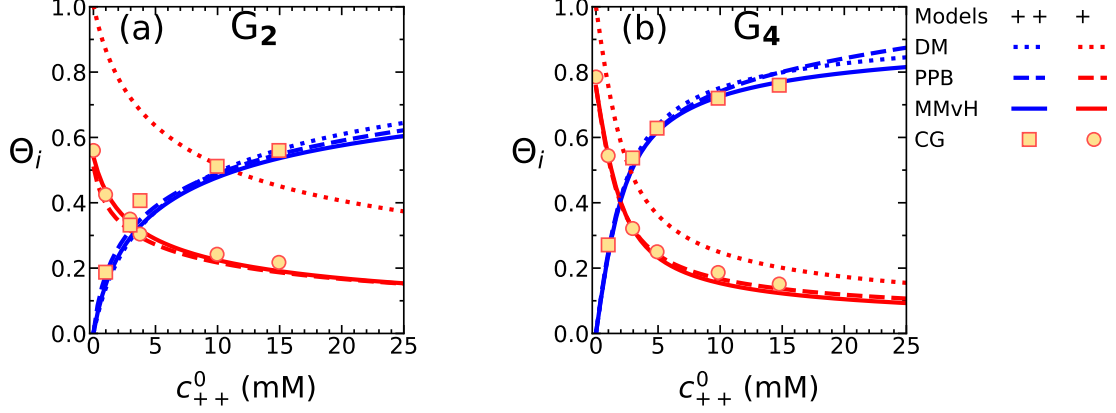
Figure 5.6: Coverages $\Theta_+$ and $\Theta_{++}$ on $G_2$-dPGS and $G_4$-dPGS obtained from the application of all models (MMvH, PPB, DM) as a function of the DC concentration $c_{++}^0$ in a mixture of DCs and MCs. The MC concentration, $c_+^0 = 150.37$ mM. Model $\Theta_i$ are fitted to simulations using the intrinsic binding chemical potentials $\Delta\mu_{\mathrm{int},i}$ as fitting parameters. The values of $\Delta\mu_{\mathrm{int},i}$ are obtained to be $-2.73\,k_\mathrm{B}T$ ($G_2$-dPGS) and $-2.98\,k_\mathrm{B}T$ ($G_4$-dPGS) for MMvH model, whereas $-1.77\,k_\mathrm{B}T$ ($G_2$-dPGS) and $-1.98\,k_\mathrm{B}T$ ($G_4$-dPGS) for PPB model. The effective configurational volumes $v_0$ used in the MMvH model are 1.04 M$^{-1}$ and 0.57 M$^{-1}$ for $G_2$-dPGS and $G_4$-dPGS, respectively, and are obtained from our previous simulations [IV]. The yellow circle and square symbols denote the coverages $\Theta_+$ and $\Theta_{++}$, respectively, obtained from simulations.

and 0.57 M$^{-1}$ for $G_2$-dPGS and $G_4$-dPGS, respectively, as obtained from our previous simulations [IV]. At low DC concentration, *i.e.* in the monovalent limit, MCs act as the only counterions to the macromolecule, resulting in the highest MC coverage $\Theta_+$. In this limit at $c_+^0 = 150.37$ mM, both MMvH and PPB models show $\Theta_+ \simeq 0.57$ for $G_2$-dPGS, and $\Theta_+ \simeq 0.8$ for $G_4$-dPGS. As $c_{++}^0$ increases, more DCs bind to the macromolecule and more of the previously bound MCs get released into the bulk. Table 5.2 shows the resultant effective charge valency $Z_{\mathrm{eff}}^{\mathrm{PB}}$ and potential $\phi_{\mathrm{eff}}^{\mathrm{PB}}$ of $G_2$-dPGS and $G_4$-dPGS evaluated by the PPB model. Quantitatively consistent with the $Z_{\mathrm{eff}}$ and $\phi_{\mathrm{eff}}$ obtained from simulations, $Z_{\mathrm{eff}}^{\mathrm{PB}}$ and $\phi_{\mathrm{eff}}^{\mathrm{PB}}$ show a strong decrease in magnitude with a higher $c_{++}^0$, depicting higher dPGS charge renormalization.

Corresponding to the fitting of binding coverages $\Theta_i$ on $G_2$-dPGS and $G_4$-dPGS binding sites, as shown in Fig. 5.6, the resulting $\Delta\mu_{\mathrm{int},++}$ values are calculated as $-2.73\,k_\mathrm{B}T$ ($G_2$) and $-2.98\,k_\mathrm{B}T$ ($G_4$) for the MMvH model, whereas $-1.77\,k_\mathrm{B}T$ ($G_2$) and $-1.98\,k_\mathrm{B}T$ ($G_4$) for the PPB model. Table 5.3 shows the values of $\Delta\mu_{\mathrm{int},++}$ averaged over $G_2$-dPGS and $G_4$-dPGS cases. It can be observed that both $\Delta\mu_{\mathrm{int},++}$ and $\Delta\mu_{\mathrm{int},+}$ values from the MMvH model exceed (in magnitude) those from the PPB model across the whole $c_{++}^0 \sim 0 - 25$ mM range. This can again be attributed to higher approximations in the electrostatic partition coefficient designed in the MMvH model, based on the DH charging free energy, as compared to that from the PPB model, incorporating non-linear effects in

| $c_{++}^0$ | G$_2$ | | | G$_4$ | | |
|---|---|---|---|---|---|---|
| | $r_{\text{eff}}^{\text{PB}}$ | $Z_{\text{eff}}^{\text{PB}}$ | $\phi_{\text{eff}}^{\text{PB}}$ | $r_{\text{eff}}^{\text{PB}}$ | $Z_{\text{eff}}^{\text{PB}}$ | $\phi_{\text{eff}}^{\text{PB}}$ |
| 0.00 | | $-11.72$ | $-1.32$ | | $-23.60$ | $-1.56$ |
| 0.98 | | $-9.79$ | $-1.12$ | | $-20.03$ | $-1.38$ |
| 2.95 | 1.42 | $-8.89$ | $-0.88$ | 2.36 | $-15.54$ | $-1.05$ |
| 3.75 | | $-8.29$ | $-0.83$ | | $-14.34$ | $-0.97$ |
| 9.96 | | $-7.03$ | $-0.57$ | | $-8.86$ | $-0.60$ |
| 14.94 | | $-6.36$ | $-0.46$ | | $-6.13$ | $-0.44$ |

Table 5.2: The structural and electrostatic parameters of G$_2$-dPGS and G$_4$-dPGS measured from the ion-specific penetrable PB (PPB) model (see Sec. 5.2.3). $r_{\text{eff}}^{\text{PB}}$, $Z_{\text{eff}}^{\text{PB}}$ and $\phi_{\text{eff}}^{\text{PB}}$ are the effective radii (expressed in nm), charge valencies and potentials of the dPGS, evaluated as a function of the DC concentration $c_{++}^0$ (expressed in mM). The MC concentration $c_+^0$ is set to 150.37 mM.

| Model | $\Delta\mu_{\text{int},i}\ (k_{\text{B}}T)$ | |
|---|---|---|
| | $++$ | $+$ |
| DM | 5.13 | 3.37 |
| PPB | $-1.87$ | $-0.50$ |
| MMvH ($v_0$ CG) | $-2.85$ | $-1.83$ |
| MMvH ($v_0$ Std.) | $-2.86$ | $-1.44$ |

Table 5.3: The values of the intrinsic component of the binding chemical potential $\Delta\mu_{\text{int},i}$ ($i = +, ++$) for the dPGS counterions for the Donnan (DM), PPB and MMvH models, obtained by the simultaneous numerical fit of the CG simulation coverages $\Theta_+$ and $\Theta_{++}$ to those obtained from the models (See Fig. 5.6). The $\Delta\mu_{\text{int},i}$ values for a particular counterion species are averaged over G$_2$ and G$_4$ dPGS generations. The MMvH model results are calculated for the configurational volume of a counterion in the bound state $v_0$ obtained from simulations and for $v_0 = 1\,\text{M}^{-1}$, which is the standard value typically considered in experimental evaluations of the standard binding energy [257]. The values of $v_0$ obtained from the simulations are 1.04 M$^{-1}$ and 0.57 M$^{-1}$ for G$_2$ and G$_4$-dPGS, respectively [IV].

the electrostatic potential in the macromolecule vicinity. The standard intrinsic chemical potentials $\Delta\mu_{\text{int},i}^0$ after fitting the MMvH model $\Theta_i$ with those from simulations are also given in Table 5.3.

Unlike the other models, we simultaneously fit both $\Delta\mu_{\text{int},+}$ and $\Delta\mu_{\text{int},++}$ to perform numerical fitting of $\Theta_+$ and $\Theta_{++}$ obtained from the DM model with the simulation data. As shown in Table 5.3, the values of $\Delta\mu_{\text{int},+}$ and $\Delta\mu_{\text{int},++}$ for the model turn out large and positive compared with those from other models, since the DM model tries to neutralize the entire dPGS charge via the electroneutrality condition in the dPGS phase. The DM fits for $\Theta_+$ differ to an extent with those from simulations, while those for $\Theta_{++}$ are found to be reasonably good. The DM, however, provides better fits for $\Theta_+$ in the case of G$_4$-dPGS as compared to G$_2$-dPGS. This is attributed to the bigger size of G$_4$-dPGS, which better

satisfies the criterion $\kappa r_{\mathrm{d}} \gg 1$, under which the DM electroneutrality condition holds comparatively well.
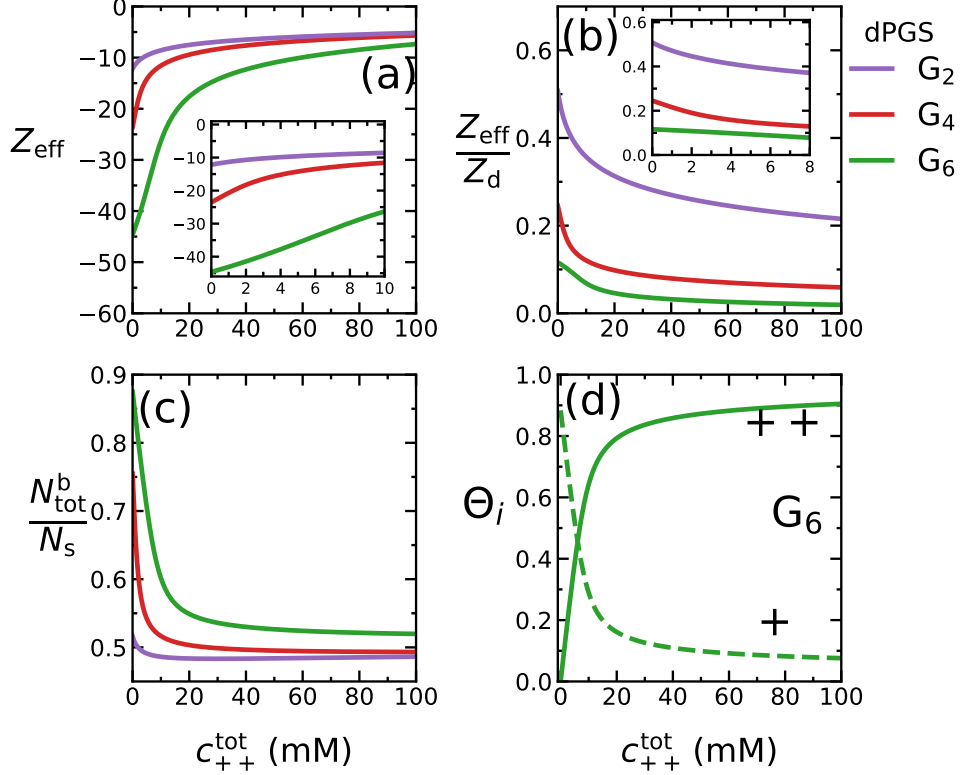


Figure 5.7: MMvH model predictions in a mixture of DCs and MCs. (a) The variation in the effective charge of dPGS with dPGS generation as a function of $c_{++}^0$. (b) The effect of the dPGS generation on the ratio of the effective charge to bare charge $Z_{\mathrm{eff}}/Z_{\mathrm{d}}$ of dPGS as a function of $c_{++}^0$. The inset shows the smaller range of DCs concentrations, close to the physiological concentration range for the DCs ($Ca^{2+}$ and $Mg^{2+}$ cations). (c) The variation in the total number of condensed counterions $N_{\mathrm{tot}}^{\mathrm{b}} = N_+^{\mathrm{b}} + N_{++}^{\mathrm{b}}$, normalized by the total number of MC binding sites $N_{\mathrm{s}}$, plotted as a function of $c_{++}^0$ for different dPGS generations. (d) Predicted values of binding coverages $\Theta_+$ and $\Theta_{++}$ for MCs vs. DCs competitive binding on $G_6$-dPGS. The MC concentration $c_+^0$ is fixed to 150.37 mM. The intrinsic binding chemical potentials for DCs and MCs are fixed to the values averaged over generations ($G_2$ and $G_4$), $\Delta\mu_{\mathrm{int},++} = -2.85\,k_{\mathrm{B}}T$ and $\Delta\mu_{\mathrm{int},+} = -1.83\,k_{\mathrm{B}}T$, which are taken from simultaneous fitting of both coverages $\Theta_i$ ($i = +, ++$) to simulations (See Table 5.3). The configurational binding volume $v_0$ is fixed to 0.80 M$^{-1}$, the mean of the binding volumes obtained for $G_2$ and $G_4$-dPGS from our previous simulations [IV].

Having established the model frameworks by informing $\Delta\mu_{\mathrm{int},i}$ by fitting the coverages $\Theta_i$ to those from simulations and averaging the values of obtained $\Delta\mu_{\mathrm{int},i}$ over generations (See Table 5.3), we finally utilize their predictive ability to explore the electrostatic characterization of dPGS for different generations and salt concentrations. As an example, Fig. 5.7(d) shows the MMvH model predictions for the binding coverages $\Theta_+$ and $\Theta_{++}$ for the case of a competitive ion binding on $G_6$-dPGS, similar to Fig. 5.6 on $G_2$-dPGS and $G_4$-dPGS. We also study the effective charge valency $Z_{\mathrm{eff}}$ of dPGS along with the composition of condensed ions on the molecule. Figs. 5.7(a) and 5.7(b) show the variation of the

effective charge valency $Z_{\text{eff}}$ of $G_2$-dPGS and its normalized form $Z_{\text{eff}}/Z_{\text{d}}$, respectively, as a function of the DC concentration $c_{++}^0$, as predicted by the MMvH model. It can be clearly seen from Fig. 5.7(a) that the introduction of DCs leads to a net charge renormalization of dPGS, which further decreases its $Z_{\text{eff}}$. The inset shows that, with reference to the monovalent limit, the dPGS effective charge is $30-35\%$ further renormalized upon introducing DCs in the range of $1-4\,\text{mM}$, which is close to the physiological concentration range for calcium(II) ions. Fig. 5.7(b) shows that the fraction of the bare dPGS charge that gets renormalized increases with the dPGS generation. The inset shows the variation for $c_{++}^0$ varying from $0\,\text{mM}$ to $10\,\text{mM}$. The rate of dPGS charge renormalization with respect to $c_{++}^0$ is the highest at the low $c_{++}^0$ regime and subsides as $c_{++}^0$ increases, since the charge renormalized dPGS results in lower electrostatic binding chemical potential $\Delta\mu_{\text{el},i}$. The reduced amount of renormalization is not attributed to the ion packing, which is evident from Fig. 5.7(c) showing the total number of condensed ions (including both DCs and MCs) per dPGS sulphate group. As $c_{++}^0$ increases, the total number of condensed ions decreases, indicating that the ion packing effects diminish as $c_{++}^0$ increases. The decrease in the amount of renormalization thus predominantly has electrostatic origin. Fig. 5.7(a) shows that $80-90\%$ of the dPGS bare charge is renormalized as $c_{++}^0$ increases from $0-100\,\text{mM}$, however, the total number of condensed counterions effectively decreases, according to Fig. 5.7(c). This in effect would significantly hamper the binding affinity of protein with dPGS. It has been well established through our previous works that the dPGS–protein complexation is dominantly influenced by the release of a few MCs that were highly confined due to heavy charge renormalization [IV]. The introduction of DCs, however, decreases the confinement of these condensed counterions, thus less counterions to be released during dPGS-protein binding. In addition, the heavy charge renormalized dPGS leads to lower electrostatic contribution to its overall binding affinity with the protein or any other multivalent ligand.

## 5.4   Conclusion

In this chapter, we have addressed the biologically and industrially relevant problem of the competitive sorption of mono- vs. divalent counterions into a highly charged globular PE, with direct comparison to CG simulations of the dendritic macromolecule dPGS. Beyond simple Donnan and ion-specific penetrable PB models, we introduced a two-state discrete binding site model (MMvH) applicable for heterogeneous ligand systems (counterions with mixed valencies/stoichiometries). The broad classification of surrounding counterions as

"bound" and "free" gives the MMvH model a computationally unique advantage over the PPB model, which involves the calculation of the distance-resolved counterion density profiles. The fitting results with simulations highlight the key differences in the MMvH and PPB models. Although being on a mean-field level, the PPB model incorporates non-linear electrostatic effects, which become more prominent near the surface of dPGS, delivering a relatively accurate picture of the dPGS-counterion electrostatic binding affinity, compared to the MMvH model, which approximates dPGS-counterion electrostatic interaction on a linearized PB (DH) level by absorbing these non-linear electrostatic effects into the effective charge valency $Z_{\text{eff}}$ of dPGS. On the contrary, the MMvH model provides more accurate values of the extent of counterion adsorption $\Theta$ at high concentrations (*i.e.*, in the binding site saturation regime) than the PPB model. The reason is that the MMvH model assumes discrete binding sites, whereas the PPB model treats dPGS charge as continuum and allows an unlimited uptake of counterions, which is not realistic.

Future extensions of the MMvH model could include an extra level of competition between adsorbed ions explicitly, namely through a non-linear term in Eq. (5.20) (of the type used in the regular solution theory or the Flory–Huggins approximation in polymer theories) that describes the interaction between two adsorbed ions in proximal positions (sites). The effects of this generalization in a different context can be found in a study on ion induced lamellar-lamellar phase transition in charged surfactant systems [388]. In general, this type of competition results in non-continuous adsorption equilibria and could be interesting in the present context.

The simplest presented model, the Donnan model (DM) extended for ion-specific effects, is also useful for a quick, qualitative prediction of the adsorption ratio. Per construction it should become more accurate for large globules and/or large salt concentrations (for which the globule size becomes larger than the DH screening length), where the electroneutrality condition is better justified.

The models presented in this work can be used to accurately extrapolate and predict the competitive ionic sorption in experiments for a wide range of salt concentrations and salt compositions. They can be also easily generalized to more ionic components and valencies. The electroneutrality radius required for the DM model and the intrinsic macromolecular charge distribution required for the PPB model as an input parameter (in the form of the bare radius $r_{\text{d}}$), are taken from simulations. However, they can also be derived by measuring the form factors from, *e.g.*, neutron scattering [391, 392]. The MMvH (or ML in the monovalent case) model requires the effective radius $r_{\text{eff}}$ of the macromolecule as

an input parameter, which besides simulations, can also be derived from independent experiments such as electrophoresis and fitting structure factors (of non-dilute colloidal suspensions) by Derjaguin–Verwey–Landau–Overbeek (DLVO) interactions [361, 393]. As we showed, $r_{\text{eff}}$ can also be obtained using PB models and related theories provided the intrinsic macromolecular charge distribution is available.

# 6 Competitive ion sorption: Isothermal titration calorimetry vs. theory

The isothermal titration calorimetry (ITC) is one of the essential and widely used tools in the area of substrate–ligand interactions, such as PE–protein [IV], PE–ion pairs [394, 395] etc. ITC mechanism greatly facilitates the direct observation of the biological macromolecular interactions and allows one to explore their thermodynamics in terms of the heat of complexation/binding [396]. However, a suitable binding model is required to analyse the data and to interpret it correctly, which then gives highly accurate values of several important quantities such as the binding affinity (binding constant) $K$ [134, 257, 325, 397, 398, 399, IV]. The underlying mechanism behind the PE–ligand binding involves a complex interplay between the electrostatic, solvation and steric effects. Previous works, interestingly, seem to indicate that most of the energy contributions related to the change in the solvation of the PE and ligands as a result of the binding, cancel out (the phenomenon well known as the enthalpy–entropy cancellation [134, 136, 142, 400, 401, 402]) and that the binding constant is mainly determined by the electrostatic effects [133, 134, 403, IV]. This justifies the suitability of the electrostatic binding models described in the previous chapter to the ITC data, in order to derive meaningful interpretation. Previous chapter presents several key binding models that describe the competitive ion uptake by highly charged globular PEs such as dPGS. The models are fairly transferable to other simulation or experimental studies on this phenomenon. In this chapter, we present a particular study of the competitive binding of $Mg^{2+}$ and $Na^+$ cations on the $G_2$-dPGS via ITC. The ITC data in the form of the heat exchange during the titration is then mapped to the amount of $Mg^{2+}$ uptake by dPGS using the two component ligand binding model presented in section 3.4 and fitted with the penetrable PB (PPB) and Manning–McGhee– von Hippel (MMvH) models presented in the previous chapter. The intrinsic binding chemical potentials $\Delta\mu_{int,i}$ ($i = ++ (Mg^{2+})$, $+ (Na^+)$), obtained as fitting parameters are then interpreted. Also the challenges faced in the experimental measurements and the fitting of the binding models to the experimental data are addressed.

## 6.1 Parameters in the ITC experiment

The dPGS is obtained by the sulphation of a fractionated hyperbranched polyglycerol [404, 405]. Synthetic dPGS is a dendritic polymer with low polydispersity, compared to the

perfect dendrimers discussed in previous chapters. Second generation of dPGS (G$_2$-dPGS) has been used for the analysis. Table 6.1 gives the details about the synthetic G$_2$-dPGS sample used in the current ITC experiments, in terms of its number-averaged total molecular weight $M_{n,dPGS}$, number-averaged core weight $M_{n,dPG}$, etc. The Degree of Sulphation (DS) can be determined from the weight percentage of sulfur [405, 406].

| dPGS | G$_2$ |
|---|---|
| $M_{n,dPG}$ (kD) | 2.6 |
| $M_{n,dPGS}$ (kD) | 6.5 |
| DS (%) | 97 |
| $N_s$ | 34 |
| $r_d$ (nm) | 1.41 |
| $r_{eff}$ (nm) | 1.65 |

Table 6.1: Properties of dPGS. DS: degree of sulphation determined from elemental analysis. $N_s$ represents the number of terminal sulphate groups. $M_{n,dPG}$ is the number-averaged molecular weight of the dPG core. The number-averaged molecular weight $M_{n,dPGS}$ was calculated from the respective dPG core and sulphate groups. The bare radius $r_d$ of G$_2$-dPGS (perfect version) is taken from simulations (cf. Table. 5.1 in Chapter 5). The effective radius $r_{eff}$ of G$_2$-dPGS is then calculated using the Alexander prescription [15, 17, 129, 130] (cf. Sec. 3.1.2.4.1).

ITC experiments were conducted on a Microcal VP-ITC instrument (Microcal, Northampton, MA, USA), with a cell volume of 1.43 ml and a syringe volume of 280 $\mu$l. All samples (including both the titrant and the analyte) used in the measurements were prepared in a buffer solution of 10 mM MOPS and a known NaCl concentration $c_+^0$ in order to derive a fixed ionic strength after the final injection of the MgCl$_2$ titrant. Therefore, $c_+^0$ remains constant throughout the titration. The titrant and analyte are aqueous solutions of MgCl$_2$ (with a known concentration $c_{++,t}^0$) + NaCl/MOPS and G$_2$-dPGS (with a known concentration $c_d$) + NaCl/MOPS, respectively. The pH of each solution was fixed to 7.2.

Three separate titration runs were carried out for different sets of $c_{++,t}^0$, $c_+^0$ and $c_d$ values, which are shown in Table 6.2. The table also shows the Mg$^{2+}$ concentration $c_{++,f}^0$ in the cell at the end of the titration run. For each titration run, MgCl$_2$ buffer solution was titrated with 35 successive injections of 8 $\mu$l each into the cell containing the dPGS solution. The stirring rate of 307 rpm was set with a time interval of 300 s between each injection. The measurements were performed at 30°C. Before each experiment all samples were degassed and thermostatted for several minutes at 1°C below the experimental temperature.

Three separate isotherms corresponding to three separate titrations depicting the competitive ion sorption of Mg$^{2+}$ and Na$^+$ cations on dPGS are then obtained from ITC

experiments in the form of the heat exchange signal $Q(x)$ as a function of the molar ratio $x = c_{++}^0/c_d$. The two component ligand binding model described in section 3.4 is then used to map the ITC isotherms $Q(x)$ to the number of condensed $Mg^{2+}$ cations $N_{++}^b(x)$.

| | | | | | PPB | | MMvH | |
|---|---|---|---|---|---|---|---|---|
| Titration | $c_{++,f}^0$ | $c_{++,t}^0$ | $c_+^0$ | $c_d$ | $\Delta\mu_{int,+}$ | $\Delta\mu_{int,++}$ | $\Delta\mu_{int,+}$ | $\Delta\mu_{int,++}$ |
| | (mM) | (mM) | (mM) | (mM) | $(k_BT)$ | $(k_BT)$ | $(k_BT)$ | $(k_BT)$ |
| 1 | 0.8 | 5.0 | 9.10 | 0.0200 | | | | |
| 2 | 1.7 | 10.0 | 6.40 | 0.0389 | 1.85 | 1.28 | 1.58 | 0.59 |
| 3 | 2.5 | 15.2 | 4.00 | 0.0638 | | | | |

Table 6.2: The total $Mg^{2+}$ concentration in the titrant ($c_{++,t}^0$), in the cell at the end of the titration ($c_{++,f}^0$), $Na^+$ concentration $c_+^0$ and $G_2$-dPGS concentration $c_d$, in the solution during the three titration runs. Concentration of MOPS is maintained at 10 mM, rendering the total ionic strength of the buffer as $c_+^0 + 10$ mM. The table also shows the intrinsic binding chemical potentials $\Delta\mu_{int,i}$ ($i = +, ++$) for the dPGS counterions for the PPB and MMvH models, obtained by the numerical fitting of $N_{++}^b$ with those obtained from ITC (*cf.* Fig. 6.3 and Sec. 6.3.2).

## 6.2 Application of PPB and MMvH models

The ITC-obtained binding isotherms $N_{++}^b(x)$ are then fitted with the PPB and MMvH models introduced in sections 5.2.3 and 5.2.4, respectively, using $\Delta\mu_{int,+}$ and $\Delta\mu_{int,++}$ as fitting parameters. It is worth noting that, according to the fitting protocol implemented in chapter 5, first $\Delta\mu_{int,+}$ is obtained by fitting the CG binding coverages to those obtained from the model in the monovalent limit, and then while fixing the obtained $\Delta\mu_{int,+}$, $\Delta\mu_{int,++}$ is obtained in the divalent case by fitting the MC and DC coverages. In the case of ITC, however, $Na^+$–$G_2$-dPGS binding isotherm in the monovalent limit is unavailable. Therefore, the ITC $N_{++}^b(x)$ is fitted to that obtained from the model using the simultaneous fitting of $\Delta\mu_{int,+}$ and $\Delta\mu_{int,++}$. The bare radius $r_d$ of $G_2$-dPGS (perfect version) is taken from simulations (*cf.* Table. 5.1 in Chapter 5). The effective radius $r_{eff}$ of $G_2$-dPGS is then calculated (*cf.* Table 6.1) using the Alexander prescription [15, 17, 129, 130] (*cf.* Sec. 3.1.2.4.1) and comes out to be approximately constant during each titration step. This result is consistent with that obtained for the PPB model and CG simulations in Chapter 5. $r_{eff}$ is then used to calculate the number of bound ions $N_i^b$ to the dPGS for the PPB model (*cf.* Eq. (5.13) in Chapter 5), and is also used as an input parameter for the MMvH model. The MMvH model, being the canonical model, inherently conserves the amount of ionic species in the solution after partitioning. Similarly, the PPB model is a cell model and the ionic bulk concentrations $c_i^b$ are obtained as a result of the partitioning,
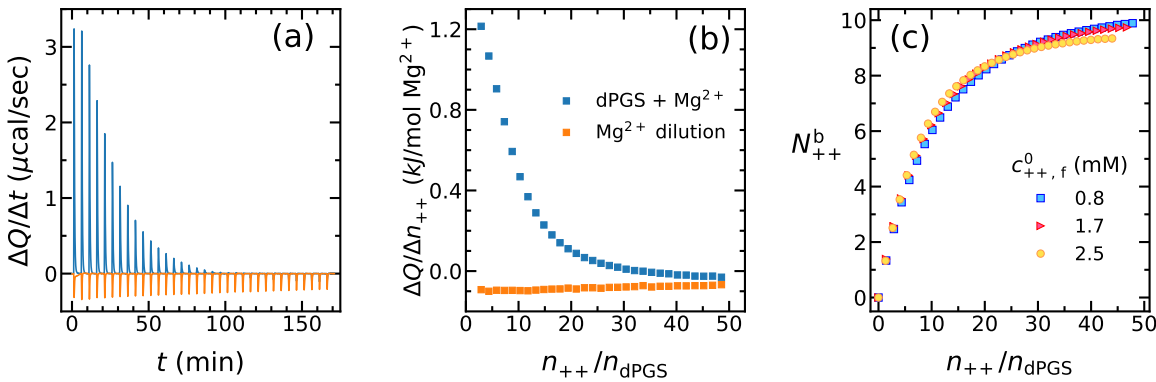
Figure 6.1: (a) Real-time data of the rate of ITC heat exchange during the dPGS–$Mg^{2+}$ titration obtained at 5 mM NaCl, 10 mM MOPS buffer with $pH = 7.2$ at 298 K. The blue and orange peaks represent the heat exchange during the sorption and the $Mg^{2+}$ solvation/dilution, respectively. (b) The corresponding titration isotherm (blue squares) and $Mg^{2+}$ solvation (orange squares) obtained by integrating the peaks in panel (a), *i.e.*, in the form of the incremental heat exchange per mol of $Mg^{2+}$ ions added into the solution $\Delta Q(x)/\Delta n_{++}$. (c) The dPGS–$Mg^{2+}$ binding isotherm for the three titration runs, represented in terms of the number of bound $Mg^{2+}$ cations $N^{\mathrm{b}}_{++}(x)$. $N^{\mathrm{b}}_{++}(x)$ are obtained by transforming the binding isotherms $\Delta Q(x)/\Delta n_{++}$, which in turn are obtained by subtracting the $Mg^{2+}$ solvation isotherms from the titration isotherms, like in panel (b).

in an iterative manner, as shown in Appendix B.1.0.1. Further details about the model assumptions are given in section 5.2.5 of chapter 5.

## 6.3 Results and discussion

### 6.3.1 Analysis by ITC

Fig. 6.1(a) and (b) show the experimental results with an example of those obtained from the titration run 1. Fig. 6.1(a) shows the heat flow in the form of the titration peaks (blue) and the heat exchanged as a result of the dilution/solvation of an equal amount of $Mg^{2+}$ ions (orange), with time. It can be seen that the titration peaks are endothermic, while the $Mg^{2+}$ dilution peaks are exothermic. Integration of these peaks leads to the heat exchange per mol of $Mg^{2+}$ ions added to the cell $\Delta Q(x)/\Delta n_{++}$, as a function of the total molar ratio of $Mg^{2+}$ ions and dPGS molecules $n_{++}/n_{\mathrm{dPGS}}$ in the cell, as shown in Fig. 6.1(b). In order to precisely capture the physics of dPGS–$Mg^{2+}$ binding, the $Mg^{2+}$-dilution heat is then subtracted from the titration heat to obtain the $Mg^{2+}$–dPGS sorption isotherm $\Delta Q(x)/\Delta n_{++}$, which is then transformed into the isotherm in the form of the number of bound $Mg^{2+}$ ions $N^{\mathrm{b}}_{++}(x)$ per dPGS molecule, as shown in Fig. 6.1(c). Fig. 6.1(c) shows the ITC-obtained $N^{\mathrm{b}}_{++}(x)$ for the three titration runs. It can be seen that the increase in the $Mg^{2+}$ binding to dPGS is the highest at low $c^0_{++}$,
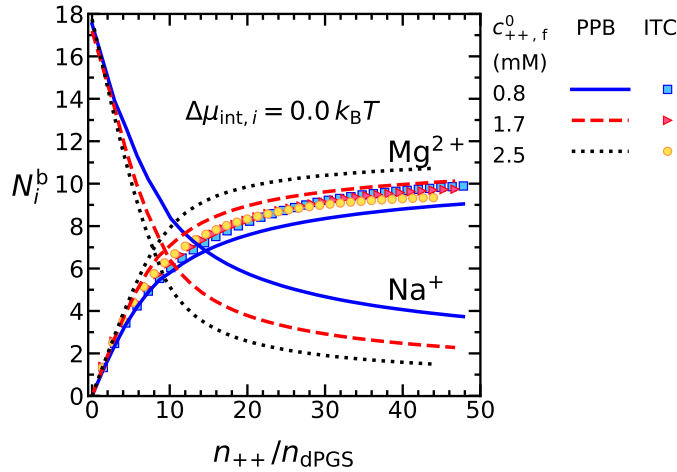
Figure 6.2: The binding isotherm $N_i^b(x)$ ($i = ++, +$) (*i.e.*, the number of bound counterions on G$_2$-dPGS) obtained from the application of the PPB model (lines) and from ITC (symbols) as a function of the titration steps measured in terms of the number of moles of Mg$^{2+}$ ions per mol of G$_2$-dPGS $n_{++}/n_{dPGS}$ in the solution. PPB obtained $N_{++}^b$ are independently evaluated with the intrinsic binding chemical potentials $\Delta\mu_{int, i} = 0$. Three titration runs are performed, which are addressed with the final Mg$^{2+}$ concentrations at the end of the titrations $c_{++,f}^0 = 0.8$ mM, $1.7$ mM and $2.5$ mM. Na$^+$ and dPGS concentrations during the runs are shown in the Table 6.2.

while it subsides as $c_{++}^0$ increases. $N_{++}^b(x)$ also does not increase with the increase in the total Mg$^{2+}$ concentration $c_{++,f}^0$. This could be attributed to the limitations in the measurement of the heat exchange in the VP-ITC calorimeter during the titration. It is worth noting that the dPGS–Mg$^{2+}$ interaction here is an example of a low binding affinity. The calorimetric measurements depend on the number of bound Mg$^{2+}$ ions, and the distinction between the solutions with the Mg$^{2+}$ concentrations $c_{++,f}^0$ within the range of 0.8 and 2.5 mM is, unfortunately, too subtle for the VP-ITC calorimeter.

## 6.3.2   Application of binding models

We now compare the binding isotherms $N_{++}^b(x)$ obtained from the ITC experiments with the PPB model. Fig. 6.2 shows the ITC-obtained $N_{++}^b(x)$ for the three titration runs (also shown in Fig. 6.1(c)), along with $N_i^b(x)$ for both Mg$^{2+}$ and Na$^+$ ions obtained from the PPB model at identical conditions. The PPB model here neglects the ion-specific effects, *i.e.*, $\Delta\mu_{int, i} = 0$. It can be observed that the increase in the Mg$^{2+}$ sorption and Na$^+$ desorption, *i.e.*, $dN_{++}^b/dx$ and $dN_+^b/dx$ respectively, is the highest at low Mg$^{2+}$ concentrations $c_{++}^0$. This can be accredited to the combined effect of the electrostatics of Mg$^{2+}$–dPGS binding, and the entropy gain in the release of previously bound Na$^+$ cations in the bulk, facilitating the Mg$^{2+}$ condensation. In the low $c_{++}^0$ (or $x = n_{++}/n_{dPGS}$) regime, Na$^+$ cations act as the only counterions to the dPGS (monovalent limit). In this case, the

dPGS charge is weakly renormalized and some of the dPGS binding sites are available for binding. This incentivizes the newly binding $Mg^{2+}$ cations to occupy these binding sites. Simultaneously, owing to the high density of the binding sites that are occupied with $Na^+$ cations, it is entropically favourable for the release of the bound $Na^+$ cations into the bulk and replacement of the corresponding freed binding sites with the newly binding $Mg^{2+}$ cations. Fig. 6.2 shows that the amount of $Na^+$ cations getting desorbed from dPGS is more than that of newly binding $Mg^{2+}$ cations, *i.e.*, $\Delta N_+^b/\Delta N_{++}^b > 1$, indicating the net gain in the total ionic entropy, facilitating $Mg^{2+}$ condensation. Therefore, as $c_{++}^0$ increases, more $Mg^{2+}$ cations bind to the dPGS and more of the previously bound $Na^+$ cations get released into the bulk. In the large $c_{++}^0$ regime, however, the dPGS charge is highly renormalized and fewer binding cites are occupied with $Na^+$ cations, resulting in the decrease in the condensation $dN_{++}^b/dx$ and the desorption $dN_+^b/dx$. As can be seen in Fig. 6.2, PPB model indicates that $N_{++}^b(x)$ increases and $N_+^b(x)$ decreases with the increase in $c_{++,f}^0$ (different titration runs), *i.e.*, increase in the amount of $Mg^{2+}$ ions per dPGS molecule in the solution. Fig. 6.2 illustrates fairly close comparison of the PPB with the ITC isotherms for different titration runs. Approximately $8 - 10$ $Mg^{2+}$ cations are condensed and $14 - 16$ previously condensed $Na^+$ cations are released in the bulk, respectively, at the end of the titrations. The comparison between the PPB and ITC isotherms is then attempted to be improvised by numerically fitting them using the intrinsic ion-specific binding chemical potentials of the cations $\Delta\mu_{int,i}$ ($i = ++, +$) used in the PPB model, as fitting parameters.

Fig. 6.3 shows the PPB isotherms numerically fitted with the ITC isotherms. $N_{++}^b(x)$ in particular in the low $c_{++}^0$ regime are more accurately fitted. In the low $c_{++}^0$ limit, where only $Na^+$ cations act as counterions, 12 $Na^+$ cations are bound to dPGS, resulting in the corresponding effective charge valency of the dPGS $Z_{eff}$ as $-22$. The variation in $Z_{eff}$ is discussed in detail in Fig. 6.4(a). The PPB isotherm suggests that approximately $8.5-9.5$ $Mg^{2+}$ cations are condensed and $10.8-11.5$ previously condensed $Na^+$ cations are released in the bulk, respectively, at the end of the titrations. Approximately $50\%$ ion-exchange occurs as the molar ratio $x$ reaches 6, indicating that most portion of the ion-exchange occurs during the first few titration steps. The PPB fitting parameters are obtained as $\Delta\mu_{int,+} = 1.85\,k_BT$ and $\Delta\mu_{int,++} = 1.28\,k_BT$ (*cf.* Table 6.2). Apart from the PPB model, we also perform the numerical fitting of ITC isotherms with that obtained from the MMvH model. The respective fitting parameters are obtained as $\Delta\mu_{int,+} = 1.58\,k_BT$ and $\Delta\mu_{int,++} = 0.59\,k_BT$ (*cf.* Table 6.2).

Fig. 6.4(a) shows the binding isotherms obtained from the fitted PPB and MMvH
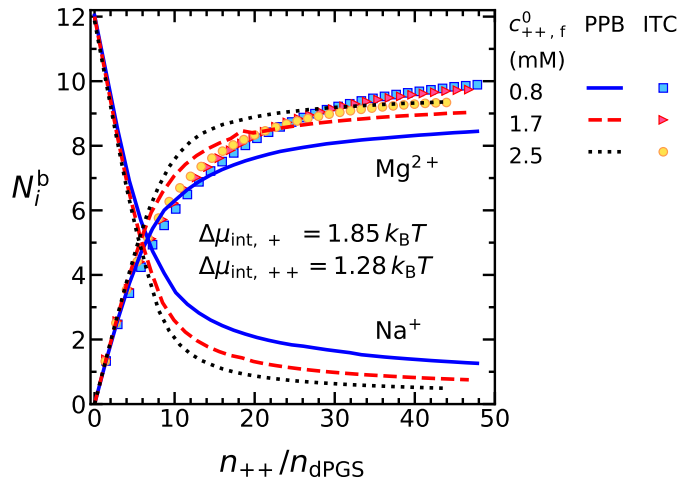
Figure 6.3: The binding isotherm $N_i^b(x)$ ($i = ++, +$) obtained from the application of the PPB model (lines) and from ITC (symbols) as a function of the titration steps measured in terms of the number of moles of $Mg^{2+}$ ions per mol of $G_2$-dPGS $n_{++}/n_{dPGS}$ in the solution. Three titration runs are performed, which are addressed with the final $Mg^{2+}$ concentrations $c_{++}^0$ at the end of the titrations $c_{++,f}^0 = 0.8\,mM$, $1.7\,mM$ and $2.5\,mM$. $Na^+$ and dPGS concentrations during the runs are shown in the Table 6.2. PPB obtained $N_{++}^b$ are fitted to those obtained from ITC using the intrinsic binding chemical potentials $\Delta\mu_{int,+} = 1.85\,k_BT$ and $\Delta\mu_{int,++} = 1.28\,k_BT$.

models in the form of $Z_{eff}$. It can be seen that the dPGS is effectively charge renormalized at the end of the titration. However, as expected, considering the isotherms shown in Fig. 6.3, $dZ_{eff}/dx$ decreases as $c_{++}^0$ increases. Both model isotherms perform reasonably close to each other. In the monovalent limit, *i.e.*, at $c_{++}^0 = 0$, $Z_{eff}$ according to the PPB model converges to $-22$, while it meets $-21.5$ according to the MMvH model. This difference could be attributed to the non-linear effects considered in the PPB electrostatic interactions (resulting in higher condensed ions), which are not incorporated in the DH-level Born energy used in the MMvH model (*cf.* Chapter 5). Taking into account the bare charge valency of the $G_2$-dPGS used in this study as $-34$ (*cf.* Table 6.1), the extent of the total charge renormalization of dPGS at the end of the titration ranges from $53 - 57\%$, considering both models.

Fig. 6.4(b) shows the binding isotherms in terms of the composition of the $Mg^{2+}$ and $Na^+$ cations in the condensed state plotted as a function of that in the bulk, evaluated by the PPB model, which can be interpreted as a "phase diagram" of the counterions. It can be observed that, at the start of the titration, *i.e.*, at $c_{++}^0 \sim 0$, the rate of enrichment of $Mg^{2+}$ cations binding to dPGS vs. that of $Na^+$ cations is high, which is expected looking at Fig. 6.3 and also due to a high resultant depletion of $Mg^{2+}$ cations in the bulk. As $c_{++}^0$ increases, $c_{++}^b$ also increases and less $Mg^{2+}$ cations bind to dPGS per released $Na^+$ cation from its bound state, resulting in the decrease in the slopes of the composition curves in
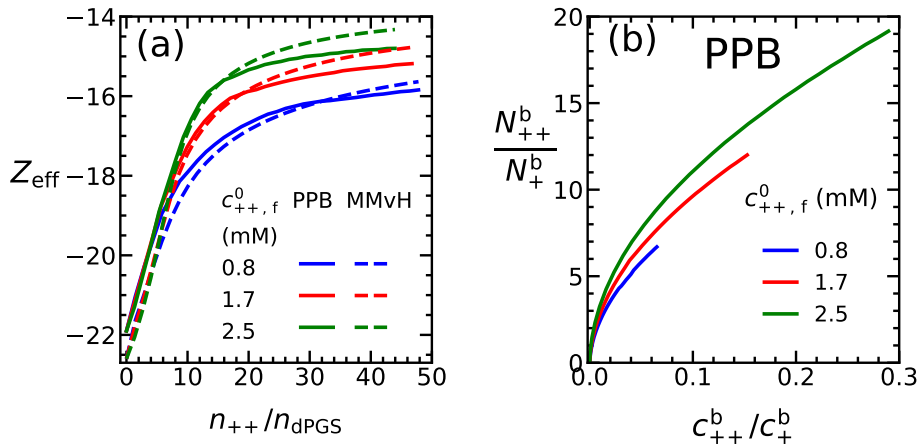
Figure 6.4: (a) Comparison of effective charge valency $Z_{\text{eff}}$ profiles predicted from MMvH and PPB models. The profiles are obtained using the $Na^+$ and $Mg^{2+}$ bound ions from Fig. 6.3. The profiles are calculated as a function of the titration steps measured in terms of the number of moles of $Mg^{2+}$ ions per $G_2$-dPGS molecule $n_{++}/n_{\text{dPGS}}$ in the solution. (b) A "phase diagram" depicting the composition of bound counterions on dPGS as a function of their composition in the bulk, evaluated by the PPB model.

Fig. 6.4(b).

## 6.4 Conclusion

In this chapter, we have presented a study of the competitive ion binding on a highly charged globular polyelectrolyte with the exemplification of $Mg^{2+}$ and $Na^+$ ion-exchange on the $G_2$-dPGS, studied using ITC. ITC measurements carried out at a range of dPGS, $Na^+$ and $Mg^{2+}$ concentrations indicate a high $Mg^{2+}$ sorption in a low $c_{++}^0$ range, while the saturation in binding occurs at a high $c_{++}^0$ range. The ITC binding isotherm is then compared and fitted with the theoretical binding models, *viz.*, the PPB and the MMvH models, presented in chapter 5. There is a rapid ion-exchange during the initial stages of the titration, while the exchange slows down at the later stages when the dPGS is significantly charge renormalized. We ascertain that this ion-exchange is driven by $Mg^{2+}$–dPGS electrostatic interaction, as well as the entropic gain due to the simultaneous release of previously bound $Na^+$ cations, while the energetic effects due to solvation/desolvation are canceled out [134, 136, 142, 400, 401, 402].

However, it is clear that the biomolecular complexation/binding processes involving PE–ion, PE–PE systems are complex, and the ITC attempts to observe these processes, however, only indirectly by probing into the incremental heat exchange occurring during the binding equilibrium. In that sense, theoretical binding models such as the PPB and MMvH models take into account the microscopic interaction details, and thus are helpful

in meaningfully complimenting the ITC results. This perspective can help in the possible developments of more intricate binding models that are directly applicable to fit the ITC results.

# 7 Summary of the thesis and outlook

## 7.1 Summary of the thesis

Dendritic PEs are known to be the emerging class of functional PEs, having attracted considerable interest in the scientific community in the last years, due to their versatility in bioapplications. In this thesis, we conducted a systematic characterization of the electrostatic and hydration properties of the dendritic PEs in a monovalent salt, and described a competitive sorption of mono- vs. divalent counterions into highly charged globular PEs, with the exemplification of dPGS. The electrostatic properties of dPGS are quantified in terms of its effective charge and size, which are described with the help of both the simulations and well-established theoretical frameworks such as the Debye–Hückel theory and the concept of counterion condensation. Also, several theoretical models based on the standard PB, Donnan, Manning, Langmuir models are devised and discussed to describe the effective charge of dPGS during the competitive ionic sorption.

In particular, in the chapter 4, owing to the charged renormalization of dPGS induced by the condensed counterions, we address the challenges of how to obtain a well-defined effective charge and surface potential of the dPGS for practical applications using the implicit- and explicit-solvent approaches applied to the explicit-water, AA MD computer simulations. Atomic specificity provides us a deeper insight into the effective pair interaction between dPGS and counterions, and allows us to characterize dPGS by calculating the molecular distributions. Furthermore, explicit treatment of water allows us to observe the equilibrium properties of the hydration structures around charged species, and rationalizing the energetics of dPGS–water interaction. To electrostatically characterize dPGS, we discuss well-known methods in the literature which are constructed for simple charged hard spheres with smooth surfaces, *viz.*, Alexander prescription on the electrostatic potential and on the counterion PMF obtained from simulation and the inflection point criterion. We find that the charge renormalization effect on dPGS strengthens with the generation, and consequently, effective charge has much weaker dependence on the dPGS generation than the bare charge. It is concluded that all approaches give consistent values for the effective charge and size but within an uncertainty window of the size of one water molecule. Furthermore, the nature of the dPGS–water interaction was studied. The PE–water interaction depends very specifically on the physicochemical properties of the interaction environment. It was found that there is a net repulsion between the dPGS and

water, which can be attributed to the hydrophobic dPGS scaffold and weakly attractive sulphate–water interaction compared to water–water interaction, due to the chaotropic nature of the monovalent sulphate groups.

Having completed the systematic depiction of the dPGS electrostatics in a monovalent salt, the growing number of its bioapplications highlight the importance to study its interactions with a mixture of mono- and divalent counterions, available in the *in vivo* environment, and the resultant competitive ion sorption. In the chapter 4, we thus perform the explicit water, AA MD simulations of dPGS with $Na^+$, $Mg^{2+}$, and $Cl^-$ ions. Given that the conventional non-polarizable AA force-fields struggle to model multivalent ions, owing to their ability to polarize surrounding media [200, 201, 204, 208], we evaluate the performances of several recently advanced divalent ion force-fields optimized to ensure a reasonable balance between ion–ion, ion–water and water–water interactions [201, 208, 217, 218] and their effect on the dPGS electrostatic attributes. While it is challenging to conclude the simulation results in a quantitative way due to the unavailability of the suitable benchmark properties from experiments, qualitative trends show that the effective charge and potential reach a saturation level as $Mg^{2+}$ concentration increases, while the effective size remains unchanged.

In the chapter 5, we tackle the same problem of the competitive ion sorption via theoretical modeling in a more generic fashion by representing dPGS as a part of highly charged globular PEs. We modify a few existing electrostatic binding theories such as Donnan, Langmuir, Manning and Poisson–Boltzmann approaches and present a few transferable ion binding models. We then inform these models via the coarse-grained computer simulation data, and use the models to predict the competitive ionic sorption for different salt concentrations and PEs of different sizes. Such knowledge can help predict the biological immune response to the PE, its metabolic fate, and the efficacy of the PE drug in different environments for biomedical and biotechnological applications. In particular, we present the novel two-state discrete binding site model for a binary heterogeneous ligand system with a reasonable accuracy and a computational advantage over the standard PB theory and simulations.

In the chapter 6, we now use the opportunity to utilize the binding models presented in the chapter 5 to quantitatively rationalize the isotherms of the competitive binding of $Mg^{2+}$ and $Na^+$ cations to dPGS, obtained via ITC experiments. Here, the ITC obtained information in the form of the heat signals as a function of the $Mg^{2+}$ concentration are mapped to the number of bound counterions and the effective charge of dPGS. It is found that there is a rapid ion-exchange during the initial stages of the titration. The driving

force behind this is attributed to the presence of unoccupied dPGS binding sites and the entropy gain in the release of $Na^+$ cations. The ion-exchange slows down in the later stages of titration, when the dPGS is significantly charge renormalized.

## 7.2 Outlook

### 7.2.1 Multivalent ion force-field

In principle, AA, explicit water MD simulations have a great advantage over the standard electrostatic binding models (*e.g.* Donnan, PB, etc.) in unraveling the physics of the binding features and complex biological systems by enabling one to probe into unprecedented time and length scales. However, as discussed before, this comes with a critical part of the simulation setup– the choice of an accurate, reliable and reproducible force-field for the system, which depends on the system properties of interest. This issue is particularly pressing in the case of classical non-polarizable force-fields designed for multivalent ions. As shown in the chapter 4, we tested several recently developed force-fields for divalent cations and observed diverse set of results in terms of the dPGS electrostatic attributes. In future works, therefore, focus could be directed towards more elaborate strategies such as the implementation of polarizable force-fields [210, 211, 212], which have been extensively developed in a simple and efficient form, since the past decade.

### 7.2.2 Improvements in binding models

In the chapter 5, we presented several approximate binding models (MMvH and PPB models in particular) capturing the competitive ionic sorption on highly charged globular PEs, which can provide reliable predictions of PE properties in experiments. There is also a considerable room for improvement in these models, particularly in the modeling of electrostatic charging free energy of the PE. The MMvH model treats the macromolecular charging on a DH level, while the PPB model incorporates non-linear electrostatic effects arising at the macromolecular surface, and between sulphate groups and counterions. Both models, however, are on a mean-field level, and thus neglect the complex spatial charge correlations inside the PE. Other non-electrostatic effects such as steric correlations are considered in the MMvH model, however on the two-body level. The PPB model, on the other hand, assumes the ions as point charges, neglecting the steric contributions. These approximations consequently cause the corrections due to the electrostatic and steric correlations to be collectively incorporated in the intrinsic counterion binding chemical

potential $\Delta\mu_{\text{int},i}$, when the models are fitted to simulation results, rendering it difficult to separate these effects from the single ion-specific effects during binding. Some of the other effects that both models do not incorporate are the fluctuations arising from the interactions among the free ions in the bulk, and the fluctuations in the dielectric constant of the medium near the PE. Future binding models can thus improve these models in this respect, in order to refine and accurately depict the physics of competitive ionic sorption. The MMvH model can also be extended to the mixture of different species of ligands binding to the same PE. Mathematical formulations in that regard can be derived with reference to the work by McGhee and von Hippel [379]. One of the purposes behind the development of the presented models, however, was to capture the essential physics behind the competitive binding in a minimalistic fashion, which both models indeed comply with.

# Appendices

# A Charge and hydration structure of dendritic polyelectrolytes: Molecular simulations of polyglycerol sulphate

## A.1 dPGS with monovalent salt

### A.1.1 Forcefield parameters

GAFF force-field [326, 327] is employed to characterize atomistic interaction properties in all simulations. The bonded and nonbonded parameters for atoms in the system are displayed in the Tables A.1–A.4 below. Partial charges are summarized in Fig. A.1.

### A.1.2 Calculation of atomic partial charges

While the restrained electrostatic potential (RESP) [407, 408] at HF/6-31G* is the default charge approach applied in the Amber protein force fields [326], this charge scheme needs to run ab initio optimization at HF/6-31G* level which prevents it from being used in handling large molecules such as dPGS. Alternatively, the partial charges for dPGS atoms were calculated from AM1-BCC quantum mechanical scheme [328] which is much cheaper than HF/6-31G* RESP and compatible with GAFF [326]. The antechamber package [327, 329] from USCF Chimera software (Ver. 1.11.2) [330] is used to assign the partial charges.

| Atomtype | $\sigma$(nm) | $\epsilon$(kJ mol$^{-1}$) | Description |
|----------|----------|----------|-------------|
| C | 0.340 | 0.458 | sp3 carbon |
| CS | 0.340 | 0.458 | sp3 $\alpha$-carbon to sulphate |
| OS | 0.300 | 0.711 | ether and ester oxygen |
| OB | 0.300 | 0.711 | sulphate oxygen connecting sulphate to dPG |
| O | 0.296 | 0.878 | sulphate oxygen |
| S | 0.356 | 1.046 | sulphate sulfur |
| H1 | 0.247 | 0.066 | hydrogen connected to $\alpha$-carbon to sulphate |
| HC | 0.265 | 0.066 | hydrogen connected to carbon |
| NA | 0.333 | 0.011 | Na$^+$ ion |
| CL | 0.440 | 0.418 | Cl$^-$ ion |

Table A.1: Atom identities and corresponding nonbonded LJ parameters used for dPGS molecule and ions in the simulation for GAFF forcefield.
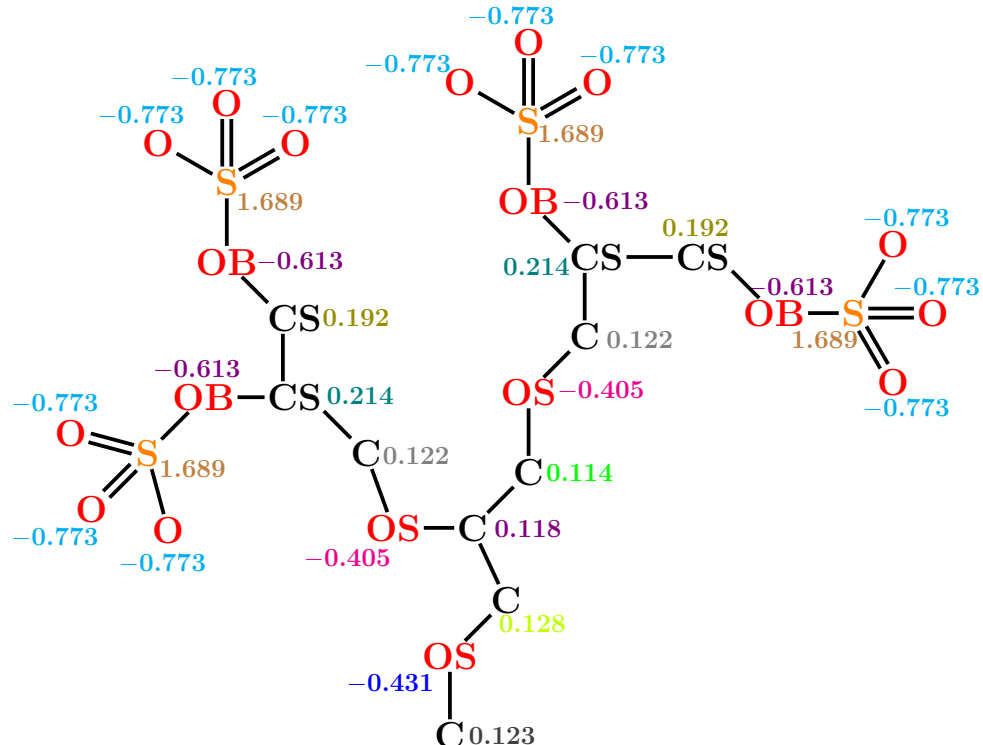


Figure A.1: The atomistic structure and AM1–BCC partial charges (in units of $e$) for one of the three repeating main branches of G$_1$-dPGS (*cf*. Fig. 1.2(a)). All accompanying hydrogens of carbons are assigned a partial charge of 0.045$e$ each.

| Angles | $k^{\theta}_{ijk}(\text{kJ mol}^{-1})$ | $\theta_{ijk}(°)$ |
|---|---|---|
| C–C–C | 528.86 | 110.63 |
| C–C–CS | 528.86 | 110.63 |
| C–CS–CS | 528.86 | 110.63 |
| C–C–OS | 418.40 | 109.50 |
| CS–C–OS | 567.35 | 108.42 |
| C–CS–OB | 567.35 | 108.42 |
| CS–CS–OB | 567.35 | 108.42 |
| C–OS–C | 519.65 | 113.41 |
| CS–OB–S | 496.22 | 109.55 |
| OB–S–O | 624.25 | 107.84 |
| O–S–O | 624.25 | 119.82 |
| H1–CS–OB | 425.09 | 108.82 |
| H1–CS–CS | 388.27 | 110.07 |
| H1–CS–C | 388.27 | 110.07 |
| H1–CS–H1 | 328.02 | 109.55 |
| HC–C–HC | 329.70 | 108.35 |
| HC–C–C | 388.27 | 110.05 |
| HC–C–CS | 388.27 | 110.05 |
| HC–C–OS | 425.93 | 108.70 |

Table A.3: Angular parameters for atoms in dPGS

| Bonds | $k^{b}_{ij}(\text{kJ mol}^{-1}\ \text{nm}^{-2})$ | $b_{ij}(\text{nm})$ |
|---|---|---|
| C–C | 253 634.0 | 0.154 |
| C–CS | 253 634.0 | 0.154 |
| CS–CS | 253 634.0 | 0.154 |
| C–OS | 252 295.2 | 0.144 |
| CS–OB | 252 295.2 | 0.144 |
| OB–S | 297 064.0 | 0.157 |
| S–O | 452 792.0 | 0.146 |
| C–HC | 282 252.6 | 0.109 |
| CS–H1 | 281 081.1 | 0.109 |

Table A.2: Bond parameters for atoms in dPGS

| Dihedrals | $\phi_s(°)$ | $k_\phi(\text{kJ mol}^{-1})$ | Mult iplicity (n) |
|---|---|---|---|
| C–C–C–OS | 0.00 | 0.651 | 3 |
| CS–CS–C–OS | 0.00 | 0.651 | 3 |
| C–CS–CS–OB | 0.00 | 0.651 | 3 |
| OS–C–C–OS | 0.00 | 0.651 | 3 |
| OS–C–CS–OB | 0.00 | 0.651 | 3 |
| OB–CS–CS–OB | 0.00 | 0.651 | 3 |
| C–OS–C–C | 180.0 | 0.418 | 2 |
| C–OS–C–CS | 180.0 | 0.418 | 2 |
| C–CS–OB–S | 0.00 | 1.604 | 3 |
| CS–CS–OB–S | 0.00 | 1.604 | 3 |
| CS–OB–S–O | 180.0 | 5.020 | 2 |
| HC–C–C–HC | 0.00 | 0.620 | 3 |
| HC–C–CS–H1 | 0.00 | 0.620 | 3 |
| H1–CS–CS–H1 | 0.00 | 0.620 | 3 |
| HC–C–C–C | 0.00 | 0.670 | 3 |
| H1–CS–CS–C | 0.00 | 0.670 | 3 |
| HC–C–CS–CS | 0.00 | 0.670 | 3 |
| HC–C–OS–C | 0.00 | 1.604 | 3 |
| H1–CS–OB–S | 0.00 | 1.604 | 3 |
| HC–C–C–OS | 0.00 | 1.046 | 1 |
| H1–CS–C–OS | 0.00 | 1.046 | 1 |
| H1–CS–CS–OS | 0.00 | 1.046 | 1 |
| HC–C–CS–OS | 0.00 | 1.046 | 1 |
| HC–C–CS–OB | 0.00 | 1.046 | 1 |
| H1–CS–CS–OB | 0.00 | 1.046 | 1 |

Table A.4: Dihedral parameters for atoms in dPGS

### A.1.3 Explicit vs. implicit water integration: Cumulative charge and electrostatic fields

Figs. A.2 and A.3 show the comparison of explicit and implicit water approaches in terms of the ratio of the net cumulative charge and the dielectric constant $Z_{\mathrm{acc}}(r)/\varepsilon_{\mathrm{r}}$ and the resultant electrostatic field $eE(r)$ as a function of the distance from dPGS-COM, for all generations. Evidently, explicit-water profiles consist of a spacially correlated noise which stems from the integrated noise from the radial charge density of water. This radial charge density is obtained by summing the individual charge densities of hydrogen and oxygen atoms of water. Given an illustrative example of an electroneutral system,
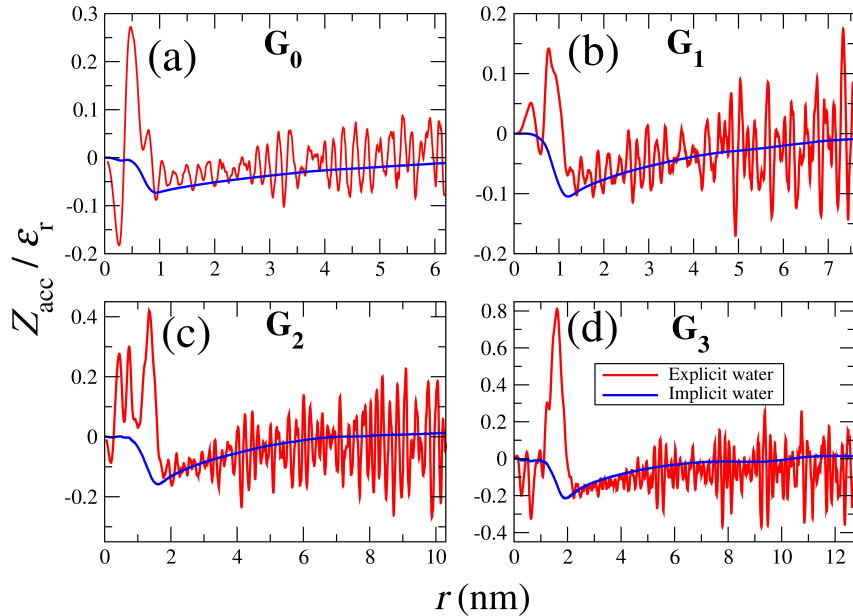


Figure A.2: Comparison of the ratio of the net cumulative charge distribution and the dielectric constant with respect to dPGS-COM between implicit and explicit-water. $\varepsilon_{\mathrm{r}} = 72$ for the implicit water approach while for explicit-water, $\varepsilon_{\mathrm{r}} = 1$.

suppose we have $\langle N \rangle$ positive and negative charges each. The difference of positive and negative charges on average is zero. However their statistical uncertainty (noise) scales as $\sim \sqrt{\langle N \rangle}$, which indicates that higher the charge density, higher is the uncertainty. This effect can normally be seen in the systems with large number of water molecules. Since dPGS is a highly charged molecule, we used significantly large sizes of simulation box (listed in Table 4.1) in order to ensure that the bulk regime is reached and thus the electroneutrality in the long-range. However the downside of this strategy is an increase in the statistical uncertainty in the charge calculations of water while implementing an explicit-water approach, due to consequently large number of water molecules in the box.

This effect can be nullified by more time averaging, thus performing longer simulations.
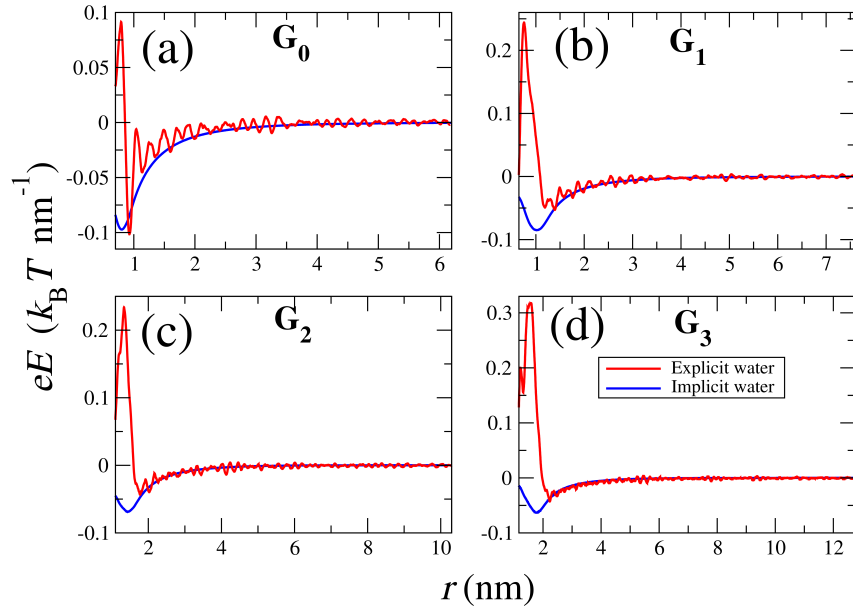


Figure A.3: Comparison of electrostatic field profiles with respect to dPGS-COM between implicit and explicit-water.

# B Competitive partitioning of mono- versus di-valent ions in highly charged macromolecules

## B.1 Ion-specific Penetrable Poisson–Langmuir (PPL) model

The PPB model (*cf.* Sec. 5.2.3) operates in terms of the volume sorption of ions in the macromolecule, *i.e.*, the PE acts as an infinite reservoir able to uptake unlimited amount of counterions. However, there is an upper limit to the amount of counterions that can be sorbed by the real-world PEs, owing to the steric constraints [173, 226, 363, 366]. Taking it into consideration, we here present a modification to the PPB model assigning the entropic penalty to the binding counterions. Several such modifications have been suggested in the past in terms of the Stern layer modifications [409, 410] of the PB approach, the numerical solutions of the hypernetted chain integral equations [411], and using analytical modifications in the PB theory assuming finite size of ions [173, 226, 363, 366]. We incorporate the entropic cost for the binding ions here in a Langmuir form, thus, naming the model as the PPL model describing the competitive ion binding. We assume the macromolecule as a perfect penetrable sphere with a charge valency $Z_\mathrm{d} = z_\mathrm{s} N_\mathrm{s}$ and radius $r_\mathrm{eff}$, as shown in Fig. 5.4. $r_\mathrm{eff}$ is taken from the simulations, *cf.* section 5.1.3. The charged monomers of the macromolecule, thus, have a uniform number distribution $c_\mathrm{s} = N_\mathrm{s}/v_\mathrm{eff}$ (where $v_\mathrm{eff} = 4\pi r_\mathrm{eff}^3/3$) within the volume $v_\mathrm{eff}$. We now balance the chemical potential for each ion, between the bulk regime far from the macromolecule and the regime at the finite distance $r$ from the center of the macromolecule

$$\ln c_i^\mathrm{b} = \beta\Delta\mu_{\mathrm{int},i}(r) + \beta\Delta\mu_\mathrm{excl}(r) + z_i\phi(r) + \ln c_i(r) \tag{B.1}$$

where the meanings of the terminologies are described in the section 5.2.3. $\Delta\mu_\mathrm{excl}$ is a chemical potential associated with the ion-ion packing effects leading to the Boltzmann ansatz as

$$c_i(r) = c_i^\mathrm{b}\, \mathrm{e}^{-z_i\phi(r)-\beta\Delta\mu_{\mathrm{int},i}(r)-\beta\Delta\mu_\mathrm{excl}(r)} \tag{B.2}$$

where the distance-resolved profiles of the intrinsic ion-specific effects $\Delta\mu_{\mathrm{int},i}(r)$ and $\mu_\mathrm{excl}(r)$ are expressed in terms of the Heaviside step function as $\Delta\mu_{\mathrm{int},i}(r) =$

## Appendix B. Competitive partitioning of mono- versus divalent ions in highly charged macromolecules

$\Delta\mu_{\text{int},i}\left(1 - H(r - r_{\text{eff}})\right)$ and $\mu_{\text{excl}}(r) = \mu_{\text{excl}}\left(1 - H(r - r_{\text{eff}})\right)$. $\Delta\mu_{\text{excl}}$ is treated on a $\mathcal{B}_2$ (two-body) level in the limit of low bound ion packing fraction $\eta$, and is expressed as $\beta\Delta\mu_{\text{excl}} = 8\eta$, representing the free energy of transferring one hard sphere to an environment of hard spheres (condensed counterions) only interacting via excluded volume effects, and with a packing fraction $\eta$ [254]. We assume that the excluded volume interaction between same species of ions is the same as that for different species, i.e., the second virial coefficient $\mathcal{B}_{2,ii} = \mathcal{B}_{2,ij} = \mathcal{B}_2$. Hence $\eta$ can be expressed as

$$\eta = \frac{N_{\text{tot}}^b \mathcal{B}_2}{4 v_{\text{eff}}} \tag{B.3}$$

where $N_{\text{tot}}^{\text{b}}$ is the total number of condensed counterions to the macromolecule, i.e., $N_{\text{tot}}^{\text{b}} = \sum_i N_i^{\text{b}}$ and the number of condensed counterions of species $i$, $N_i^{\text{b}}$ is given by

$$N_i^{\text{b}} = \int_0^{r_{\text{eff}}} c_i(r) 4\pi r^2 \, \mathrm{d}r \tag{B.4}$$

The partition coefficient associated with ion-ion excluded volume interactions, $\mathcal{K}_{\text{excl}}$ can be given as

$$\mathcal{K}_{\text{excl}} = \mathrm{e}^{-\beta\Delta\mu_{\text{excl}}} = \mathrm{e}^{-8\eta} \tag{B.5}$$

In the limit of a small packing fraction, i.e., $\eta \to 0$, Eq. (B.5) can be approximated as

$$\mathcal{K}_{\text{excl}} \simeq 1 - 8\eta = 1 - 2\mathcal{B}_2 \sum_i c_i^{\text{m}} = 1 - 2\mathcal{B}_2 \frac{\sum_i N_i^{\text{b}}}{v_{\text{eff}}} \tag{B.6}$$

where $c_i^{\text{m}} = N_i^{\text{b}}/v_{\text{eff}}$ is the number density of ion $i$ in a bound state. The number density profile $c_i(r)$ can then be expressed as

$$c_i(r) = \begin{cases} c_i^{\text{b}} \, \mathrm{e}^{-z_i\phi(r) - \beta\Delta\mu_{\text{int},i}(r)} \left(1 - 2\mathcal{B}_2 \sum_i c_i^{\text{m}}\right) & r < r_{\text{eff}} \\ c_i^{\text{b}} \, \mathrm{e}^{-z_i\phi(r)} & r \geqslant r_{\text{eff}} \end{cases} \tag{B.7}$$

The distance-resolved electrostatic potential can be calculated from the PB equation as

$$\nabla^2\phi(r) = -4\pi l_{\text{B}} \left(\sum_i z_i c_i(r) + z_{\text{s}} c_{\text{s}}(r)\right) \qquad i = ++, +, - \tag{B.8}$$

## B.1. Ion-specific Penetrable Poisson–Langmuir (PPL) model

where the number density of charged monomers of the macromolecule, $c_{\mathrm{s}}$, is expressed in terms of the Heaviside step function as $c_{\mathrm{s}}(r) = c_{\mathrm{s}}\left(1 - H(r - r_{\mathrm{eff}})\right)$. After solving Eq. (B.8) and using the boundary conditions as $(\mathrm{d}\phi/\mathrm{d}r)(r \to 0) = 0$ and $\phi(r \to R) = 0$, we use Eqs. (B.4) and (B.7) to express $c_i^{\mathrm{m}}$ as

$$
\begin{aligned}
c_i^{\mathrm{m}} &= \frac{1}{v_{\mathrm{eff}}} \int_0^{r_{\mathrm{eff}}} c_i(r) 4\pi r^2 \, \mathrm{d}r \\
&= c_i^{\mathrm{b}} \, \mathrm{e}^{-\beta \Delta \mu_{\mathrm{int},\,i}} \left(1 - 2\mathcal{B}_2 \sum_i c_i^{\mathrm{m}}\right) \frac{1}{v_{\mathrm{eff}}} \int_0^{r_{\mathrm{eff}}} \mathrm{e}^{-z_i \phi(r)} 4\pi r^2 \, \mathrm{d}r \\
&= c_i^{\mathrm{b}} \, \mathcal{K}_{\mathrm{int},\,i} \mathcal{K}_{\mathrm{el},\,i} \left(1 - 2\mathcal{B}_2 \sum_i c_i^{\mathrm{m}}\right)
\end{aligned}
\tag{B.9}
$$

where $\mathcal{K}_{\mathrm{int},\,i} = \mathrm{e}^{-\beta \Delta \mu_{\mathrm{int},\,i}}$ and

$$
\mathcal{K}_{\mathrm{el},\,i} = \mathrm{e}^{-\beta \Delta \Phi_i} = \frac{1}{v_{\mathrm{eff}}} \int_0^{r_{\mathrm{eff}}} \mathrm{e}^{-z_i \phi(r)} 4\pi r^2 \, \mathrm{d}r
\tag{B.10}
$$

. Summing up the LHS in Eq. (B.9) for all ionic species $i$ gives

$$
\begin{aligned}
\sum_i c_i^{\mathrm{m}} &= \sum_i c_i^{\mathrm{b}} \, \mathcal{K}_{\mathrm{int},\,i} \mathcal{K}_{\mathrm{el},\,i} \left(1 - 2\mathcal{B}_2 \sum_i c_i^{\mathrm{m}}\right) \\
\implies \sum_i c_i^{\mathrm{m}} &= \frac{\sum_i c_i^{\mathrm{b}} \mathcal{K}_{\mathrm{int},\,i} \mathcal{K}_{\mathrm{el},\,i}}{1 + 2\mathcal{B}_2 \sum_i c_i^{\mathrm{b}} \, \mathcal{K}_{\mathrm{int},\,i} \mathcal{K}_{\mathrm{el},\,i}}
\end{aligned}
\tag{B.11}
$$

Eq. (B.7) can then be rewritten as

$$
c_i(r) = \begin{cases} \dfrac{c_i^{\mathrm{b}} \, \mathcal{K}_{\mathrm{int},\,i} \, \mathrm{e}^{-z_i \phi(r)}}{1 + v_0 \sum_i c_i^{\mathrm{b}} \, \mathcal{K}_{\mathrm{int},\,i} \mathcal{K}_{\mathrm{el},\,i}} & r < r_{\mathrm{eff}} \\[4mm] c_i^{\mathrm{b}} \, \mathrm{e}^{-z_i \phi(r)} & r \geqslant r_{\mathrm{eff}} \end{cases}
\tag{B.12}
$$

where $v_0 = 2\mathcal{B}_2$, *i.e.*, the excluded volume treatment is set to be equivalent to Langmuir treatment, where the bound ion is considered as ideal gas particle having a configurational freedom (volume) of $2\mathcal{B}_2$, allowing it to freely move around in one of the $N_i$ bounding boxes for respective condensed counterions.

## Appendix B. Competitive partitioning of mono- versus divalent ions in highly charged macromolecules

### B.1.0.1 Calculation of bulk concentration

The bulk concentration of divalent and monovalent counterions $c_i^{\mathrm{b}}$ is updated during each injection in the following way.:

1. Solve PB equation (Eq. (B.8)) (Unknown parameter $c_i^{\mathrm{b}}$ is guessed from the outcome of previous concentration input/ITC injection.)

2. Find $c_{++}^0$ and iterate

   Total known molar concentration of $Mg^{2+}$ per molar concentration of dPGS: $c_{++}^0$

   The total amount of $Mg^{2+}$ is conserved within the titration volume $V$ (spherical cell of radius $R$).

   $$\int_0^R c_{++}(r)4\pi r^2 \mathrm{d}r = c_{++}^{\mathrm{b}}\int_0^R e^{-2\phi(r)-\beta\Delta\mu_{\mathrm{int},\,++}(r)}4\pi r^2\mathrm{d}r \overset{!}{=} c_{++}^0\left(\frac{4\pi}{3}R^3\right) \quad (B.13)$$

   $$\implies c_{++}^{\mathrm{b}} = \frac{c_{++}^0\left(\frac{4\pi}{3}R^3\right)}{\int_0^R e^{-2\phi(r)-\beta\Delta\mu_{\mathrm{int},\,++}(r)}4\pi r^2\mathrm{d}r} \quad (B.14)$$

   Substitute $c_{++}^{\mathrm{b}}$ back in Eq. (5.12) and repeat steps 1 and 2 till $c_{++}^{\mathrm{b}}$ is converged.

3. Calculate bound $Mg^{2+}$ ions after convergence of $c_{++}^{\mathrm{b}}$ using Eq. (B.4), and use $c_{++}^{\mathrm{b}}$ as initial guess for next injection.
   Follow the same steps for the convergence of the bulk $Na^+$ concentration $c_+^{\mathrm{b}}$.

# List of tables

# List of figures

# List of abbreviations

AA      all-atom

CG      coarse-grained

COM   center-of-mass

DCs    divalent cations

DH      Debye–Hückel

DLVO  Derjaguin–Verwey–Landau–Overbeek

DM      Donnan model

dPG    dendritic polyglycerol

dPGS  dendritic polyglycerol sulphate

DS      Degree of Sulphation

ECC   Electronic Continuum Correction

GAFF  General Amber Force Field

ITC    isothermal titration calorimetry

KBI    Kirkwood–Buff Integral

LJ      Lennard-Jones

MCs   monovalent cations

MD     Molecular Dynamics

ML     Manning–Langmuir model

MMvH  Manning–McGhee–von Hippel

PAMAM  Polyamidoamine

PB      Poisson–Boltzmann

PBC    periodic boundary conditions

PEs     Polyelectrolytes

PETIM  Poly(propyl ether imine)

PMF    Potential of Mean Force

PPB    Penetrable Poisson–Boltzmann

PPL    Penetrable Poisson–Langmuir

PTX    Paclitaxel

RDF    Radial distribution function

SASA   Solvent Accessible Surface Area

SPC/E  Simple Point Charge-Extended

VSE    solvent excluded volume

# Bibliography

[1] H Boroudjerdi, Y Kim, A Naji, R Netz, X Schlagberger, and A Serr. "Statics and dynamics of strongly charged soft matter". *Phys. Rep.* 416.3-4 (2005), pp. 129–199.

[2] M. Rubinstein and G. A. Papoian. "Polyelectrolytes in biology and soft matter". *Soft Matter* 8.36 (2012), p. 9265.

[3] C. Holm, P. Kékicheff, and R. Podgornik. *Electrostatic Effects in Soft Matter and Biophysics*. Vol. 46. Springer Science & Business Media, 2001.

[4] M. Muthukumar. "50th Anniversary Perspective : A Perspective on Polyelectrolyte Solutions". *Macromolecules* 50.24 (2017), pp. 9528–9560.

[5] A. Katchalsky. "Polyelectrolytes and Their Biological Interactions". *Biophys. J.* 4.1 (1964), pp. 9–41.

[6] S Förster and M Schmidt. "Polyelectrolytes in Solution". *Adv. Polym. Sci.* 120 (1995), pp. 51–133.

[7] A. Dobrynin and M. Rubinstein. "Theory of polyelectrolytes in solutions and at surfaces". *Prog. Polym. Sci.* 30.11 (2005), pp. 1049–1118.

[8] S. Liu, K. Ghosh, and M. Muthukumar. "Polyelectrolyte solutions with added salt: A simulation study". *J. Chem. Phys.* 119.3 (2003), pp. 1813–1823.

[9] M. Rooman and R. Wintjens. "Protein-DNA Interactions". *eLS*. Chichester, UK: John Wiley & Sons Ltd, 2015, pp. 1–11.

[10] J. M. Park, B. B. Muhoberac, P. L. Dubin, and J. Xia. "Effects of protein charge heterogeneity in protein-polyelectrolyte complexation". *Macromolecules* 25.1 (1992), pp. 290–295.

[11] S. Han et al. "Protein- Protein Recognition Control by Modulating Electrostatic Interactions". *J. Proteome Res.* 9.6 (2010), pp. 3118–3125.

[12] X. Xu. "Molecular modeling of the complexation of proteins with strong anionic polyelectrolytes". PhD thesis. Humboldt-Universität zu Berlin, Mathematisch-Naturwissenschaftliche Fakultät, 2018.

[13] H. Gohlke and G. Klebe. "Approaches to the description and prediction of the binding affinity of small-molecule ligands to macromolecular receptors". *Angew. Chem.* 41.15 (2002), pp. 2644–2676.

[14] A. Chremos and J. F. Douglas. "Counter-ion distribution around flexible polyelectrolytes having different molecular architecture". *Soft Matter* 12.11 (2016), pp. 2932–2941.

[15] S. Alexander, P. M. Chaikin, P. Grant, G. J. Morales, P. Pincus, and D. Hone. "Charge renormalization, osmotic pressure, and bulk modulus of colloidal crystals: Theory". *J. Chem. Phys.* 80.11 (1984), pp. 5776–5781.

[16] L. Belloni. "Ionic condensation and charge renormalization in colloidal suspensions". *Colloids Surf., A* 140.1 (1998), pp. 227–243.

[17] L. Bocquet, E. Trizac, and M. Aubouy. "Effective charge saturation in colloidal suspensions". *J. Chem. Phys.* 117.17 (2002), pp. 8138–8152.

[18] S. Förster, M. Schmidt, and M. Antonietti. "Experimental and theoretical investigation of the electrostatic persistence length of flexible polyelectrolytes at various ionic strengths". *J. Phys. Chem.* 96.10 (1992), pp. 4008–4014.

[19] A. Dobrynin, R. H. Colby, and M. Rubinstein. "Scaling Theory of Polyelectrolyte Solutions". *Macromolecules* 28.6 (1995), pp. 1859–1871.

[20] J. R. Wenner, M. C. Williams, I. Rouzina, and V. A. Bloomfield. "Salt Dependence of the Elasticity and Overstretching Transition of Single DNA Molecules". *Biophys. J.* 82.6 (2002), pp. 3160–3169.

[21] E. Raspaud, M. Olvera de la Cruz, J.-L. Sikorav, and F. Livolant. "Precipitation of DNA by Polyamines: A Polyelectrolyte Behavior". *Biophys. J.* 74.1 (1998), pp. 381–393.

[22] S. Liu and M. Muthukumar. "Langevin dynamics simulation of counterion distribution around isolated flexible polyelectrolyte chains". *J. Chem. Phys.* 116.22 (2002), pp. 9975–9982.

[23] M. Muthukumar. "Theory of counter-ion condensation on flexible polyelectrolytes: Adsorption mechanism". *J. Chem. Phys.* 120 (2004), pp. 9343–9350.

[24] J. Rühe et al. "Polyelectrolyte brushes". *Polyelectrolytes with Defined Molecular Architecture I.* Springer, 2004, pp. 79–150.

[25] P. Pincus. "Colloid stabilization with grafted polyelectrolytes". *Macromolecules* 24.10 (1991), pp. 2912–2919.

[26] O. Borisov, T. Birshtein, and E. Zhulina. "Collapse of grafted polyelectrolyte layer". *J. Phys. II (Paris)* 1.5 (1991), pp. 521–526.

[27] E. B. Zhulina, T. M. Birshtein, and O. V. Borisov. "Theory of Ionizable Polymer Brushes". *Macromolecules* 28.5 (1995), pp. 1491–1499.

[28] E. B. Zhulina, J. Klein Wolterink, and O. V. Borisov. "Screening Effects in a Polyelectrolyte Brush: Self-Consistent-Field Theory". *Macromolecules* 33.13 (2000), pp. 4945–4953.

[29] P. K. Jha, J. W. Zwanikken, F. A. Detcheverry, J. J. de Pablo, and M. Olvera de la Cruz. "Study of volume phase transitions in polymeric nanogels by theoretically informed coarse-grained simulations". *Soft Matter* 7 (13 2011), pp. 5965–5975.

[30] J. Hua, M. K. Mitra, and M. Muthukumar. "Theory of volume transition in polyelectrolyte gels with charge regularization". *The Journal of Chemical Physics* 136.13 (2012), p. 134901.

[31] J. Landsgesell, D. Sean, P. Kreissl, K. Szuttor, and C. Holm. "Modeling Gel Swelling Equilibrium in the Mean Field: From Explicit to Poisson–Boltzmann Models". *Phys. Rev. Lett.* 122 (20 2019), p. 208002.

[32] S Förster and M. Schmidt. "Polyelectrolytes in solution". *Physical Properties of Polymers.* Vol. 120. Berlin, Heidelberg: Springer, 1995.

[33] G. S. Manning. "Poisson's ratio for a polyelectrolyte". *Soft Matter* 8.36 (2012), p. 9334.

[34]  H. G. M. Van de Steeg, M. A. Cohen Stuart, A. De Keizer, and B. H. Bijsterbosch. "Polyelectrolyte adsorption: a subtle balance of forces". *Langmuir* 8.10 (1992), pp. 2538–2546.

[35]  M. A. G. Dahlgren, A. Waltermo, E. Blomberg, P. M. Claesson, L. Sjoestroem, T. Aakesson, and B. Joensson. "Salt effects on the interaction between adsorbed cationic polyelectrolyte layers: theory and experiment". *J. Phys. Chem.* 97.45 (1993), pp. 11769–11775.

[36]  R. R. Netz and J. F. Joanny. "Complexation between a semiflexible polyelectrolyte and an oppositely charged sphere". *Macromolecules* 32.26 (1999), pp. 9026–9040.

[37]  R. Hariharan, C. Biver, J. Mays, and W. B. Russel. "Ionic Strength and Curvature Effects in Flat and Highly Curved Polyelectrolyte Brushes". *Macromolecules* 31.21 (1998), pp. 7506–7513.

[38]  D. I. Gittins and F. Caruso. "Tailoring the Polyelectrolyte Coating of Metal Nanoparticles". *J. Phys. Chem. B* 105.29 (2001), pp. 6846–6852.

[39]  F. Caruso. "Hollow capsule processing through colloidal templating and self-assembly". *Chem. Eur. J.* 6.3 (2000), pp. 413–419.

[40]  G Decher, J. D. Hong, and J Schmitt. "Buildup of ultrathin multilayer films by a self-assembly process: III. Consecutively alternating adsorption of anionic and cationic polyelectrolytes on charged surfaces". *Thin Solid Films* 210-211.211 (1992), pp. 831–835.

[41]  G. Decher. "Fuzzy Nanoassemblies: Toward Layered Polymeric Multicomposites". *Science* 277.5330 (1997), pp. 1232–1237.

[42]  G. Ladam, P. Schaad, J. C. Voegel, P. Schaaf, G. Decher, and F. Cuisinier. "In Situ Determination of the Structural Properties of Initially Deposited Polyelectrolyte Multilayers". *Langmuir* 16.3 (2000), pp. 1249–1255.

[43]  R. A. McAloney, M. Sinyor, V. Dudnik, and M. C. Goh. "Atomic Force Microscopy Studies of Salt Effects on Polyelectrolyte Multilayer Film Morphology". *Langmuir* 17.21 (2001), pp. 6655–6663.

[44]   S. T. Dubas and J. B. Schlenoff. "Swelling and Smoothing of Polyelectrolyte Multilayers by Salt". *Langmuir* 17.25 (2001), pp. 7725–7727.

[45]   A. Hugerth, N. Caram-Lelham, and L.-O. Sundelöf. "The effect of charge density and conformation on the polyelectrolyte complex formation between carrageenan and chitosan". *Carbohydr. Polym.* 34.3 (1997), pp. 149–156.

[46]   L Rusu-Balaita, J Desbrieres, and M Rinaudo. "Formation of a biocompatible polyelectrolyte complex: Chitosan-hyaluronan complex stability". *Polym. Bull.* 50.1-2 (2003), pp. 91–98.

[47]   R. G. Winkler, M. O. Steinhauser, and P. Reineker. "Complex formation in systems of oppositely charged polyelectrolytes: a molecular dynamics simulation study". *Phys. Rev. E* 66.2 (2002), p. 021802.

[48]   A. Kudlay and M. Olvera de la Cruz. "Precipitation of oppositely charged polyelectrolytes in salt solutions". *J. Chem. Phys.* 120.1 (2004), pp. 404–412.

[49]   M. Mende, G. Petzold, and H.-M. Buchhammer. "Polyelectrolyte complex formation between poly(diallyldimethyl-ammonium chloride) and copolymers of acrylamide and sodium-acrylate". *Colloid Polym. Sci.* 280.4 (2002), pp. 342–351.

[50]   E. Spruijt, A. H. Westphal, J. W. Borst, M. A. Cohen Stuart, and J. van der Gucht. "Binodal compositions of polyelectrolyte complexes". *Macromolecules* 43.15 (2010), pp. 6476–6484.

[51]   J. van der Gucht, E. Spruijt, M. Lemmers, and M. A. Cohen Stuart. "Polyelectrolyte complexes: Bulk phases and colloidal systems". *J. Colloid Interface Sci.* 361.2 (2011), pp. 407–422.

[52]   P. M. Biesheuvel and M. A. Cohen Stuart. "Electrostatic free energy of weakly charged macromolecules in solution and intermacromolecular complexes consisting of oppositely charged polymers". *Langmuir* 20.7 (2004), pp. 2785–2791.

[53]   S. Perry, Y. Li, D. Priftis, L. Leon, and M. Tirrell. "The Effect of Salt on the Complex Coacervation of Vinyl Polyelectrolytes". *Polymers (Basel).* 6.6 (2014), pp. 1756–1772.

[54] J. Dernedde et al. "Dendritic polyglycerol sulfates as multivalent inhibitors of inflammation". *Proc. Natl. Acad. Sci. U. S. A.* 107.46 (2010), pp. 19679–19684.

[55] J. Khandare, M. Calderón, N. M. Dagiaa, and R. Haag. "Multifunctional dendritic polymers in nanomedicine: opportunities and challenges". *Chem. Soc. Rev.* 41 (2012), p. 2824.

[56] D. Gröger et al. "Synthesis and Biological Evaluation of Radio and Dye Labeled Amino Functionalized Dendritic Polyglycerol Sulfates as Multivalent Anti-Inflammatory Compounds". *Bioconjug. Chem.* 24.9 (2013), pp. 1507–1514.

[57] D. Maysinger et al. "Dendritic Polyglycerol Sulfate Inhibits Microglial Activation and Reduces Hippocampal CA1 Dendritic Spine Morphology Deficits". *Biomacromolecules* 16 (2015), pp. 3073–3082.

[58] S. Reimann, D. Gröger, C. Kühne, S. B. Riese, J. Dernedde, and R. Haag. "Shell Cleavable Dendritic Polyglycerol Sulfates Show High Anti-Infl ammatory Properties by Inhibiting L-Selectin Binding and Complement Activation". *Adv. Healthc. Mater.* 4 (2015), pp. 2154–2162.

[59] C. C. Lee, J. A. MacKay, J. M. Fréchet, and F. C. Szoka. "Designing dendrimers for biological applications". *Nat. Biotechnol.* 23 (2005), pp. 1517–1526.

[60] M. Ballauff and C. N. Likos. "Dendrimers in Solution: Insight from Theory and Simulation". *Angew. Chem., Int. Ed.* 43 (2004), p. 2998.

[61] W. Tian and Y. Ma. "Theoretical and computational studies of dendrimers as delivery vectors". *Chem. Soc. Rev.* 42 (2013), p. 705.

[62] S. Kanchi, G. Suresh, U. D. Priyakumar, K. Ayappa, and P. K. Maiti. "Molecular dynamics study of the structure, flexibility, and hydrophilicity of PETIM dendrimers: a comparison with PAMAM dendrimers". *J. Phys. Chem. B* 119.41 (2015), pp. 12990–13001.

[63] D. A. Tomalia et al. "A new class of polymers: starburst-dendritic macromolecules". *Polym. J.* 17.1 (1985), pp. 117–132.

[64]  L. Yang and S. R. P. da Rocha. "PEGylated, NH$_2$-Terminated PAMAM Dendrimers: A Microscopic View from Atomistic Computer Simulations". *Mol. Pharm.* 11.5 (2014), pp. 1459–1470.

[65]  P. Kesharwani, V. Gajbhiye, and N. K. Jain. "A review of nanocarriers for the delivery of small interfering RNA". *Biomaterials* 33.29 (2012), pp. 7138–7150.

[66]  P. Kesharwani, S. Banerjee, U. Gupta, M. C. I. Mohd Amin, S. Padhye, F. H. Sarkar, and A. K. Iyer. "PAMAM dendrimers as promising nanocarriers for RNAi therapeutics". *Mater. Today* 18.10 (2015), pp. 565–572.

[67]  B Klajnert and M Bryszewska. "Dendrimers: properties and applications." *Acta Biochim. Pol.* 48.1 (2001), pp. 199–208.

[68]  Y.-q. Ma et al. "Theoretical and computational studies of dendrimers as delivery vectors". *Chem. Soc. Rev.* 42.2 (2013), pp. 705–727.

[69]  C. C. Lee, J. A. MacKay, J. M. Fréchet, and F. C. Szoka. "Designing dendrimers for biological applications". *Nat.* 23.12 (2005), pp. 1517–1526.

[70]  P. K. Maiti, T. Çagin, G. Wang, and W. A. Goddard. "Structure of PAMAM Dendrimers: Generations 1 through 11". *Macromolecules* 37.16 (2004), p. 6236.

[71]  A. M. Naylor, W. A. Goddard, G. E. Kiefer, and D. A. Tomalia. "Starburst dendrimers. 5. Molecular shape control". *J. Am. Chem. Soc.* 111.6 (1989), pp. 2339–2341.

[72]  I. Lee, B. D. Athey, A. W. Wetzel, W. Meixner, and J. James R. Baker. "Structural molecular dynamics studies on polyamidoamine dendrimers for a therapeutic application: effects of pH and generation". *Macromolecules* 35.11 (2002), pp. 4510–4520.

[73]  M. Han, P. Chen, and X. Yang. "Molecular dynamics simulation of PAMAM dendrimer in aqueous solution". *Polymer* 10.25 (2005), p. 3481.

[74]  P. K. Maiti, T. T. Çagin, S.-T. Lin, and W. A. Goddard. "Effect of Solvent and pH on the Structure of PAMAM Dendrimers". *Macromolecules* 38.3 (2005), pp. 979–991.

[75] P. M. Paulo, J. N. C. Lopes, and S. M. Costa. "Molecular dynamics simulations of charged dendrimers: Low-to-intermediate half-generation PAMAMs". *J. Phys. Chem. B* 111.36 (2007), pp. 10651–10664.

[76] P. K. Maiti and R. Messina. "Counterion Distribution and $\zeta$-Potential in PAMAM Dendrimer". *Macromolecules* 41 (2008), p. 5002.

[77] P. K. Maiti, T. Çagin, S.-T. Lin, and W. A. Goddard. "Effect of solvent and pH on the structure of PAMAM dendrimers". *Macromolecules* 38.3 (2005), pp. 979–991.

[78] S.-T. Lin, P. K. Maiti, and W. A. Goddard. "Dynamics and thermodynamics of water in PAMAM dendrimers at subnanosecond time scales". *J. Phys. Chem. B* 109.18 (2005), pp. 8663–8672.

[79] H. Lee, J. R. Baker, and R. G. Larson. "Molecular dynamics studies of the size, shape, and internal structure of 0% and 90% acetylated fifth-generation polyamidoamine dendrimers in water and methanol". *J. Phys. Chem. B* 110.9 (2006), pp. 4014–4019.

[80] P. K. Maiti and W. A. Goddard. "Solvent quality changes the structure of G8 PAMAM dendrimer, a disagreement with some experimental interpretations". *J. Phys. Chem. B* 110.51 (2006), pp. 25628–25632.

[81] C. Wu. "pH response of conformation of poly (propylene imine) dendrimer in water: a molecular simulation study". *Mol. Simulat.* 36.14 (2010), pp. 1164–1172.

[82] C. Jana, G Jayamurugan, R. Ganapathy, P. K. Maiti, N Jayaraman, and A. Sood. "Structure of poly (propyl ether imine) dendrimer from fully atomistic molecular dynamics simulation and by small angle X-ray scattering". *J. Chem. Phys.* 124.20 (2006), p. 204719.

[83] B. Wu et al. "Structured water in polyelectrolyte dendrimers: Understanding small angle neutron scattering results through atomistic simulation". *J. Chem. Phys.* 136.14 (2012), p. 144901.

[84] S. Huißmann, C. N. Likos, and R. Blaak. "Explicit vs implicit water simulations of charged dendrimers". *Macromolecules* 45.5 (2012), pp. 2562–2569.

[85] M. Muratt and G. S. Grest. "Molecular Dynamics Study of Dendrimer Molecules in Solvents of Varying Quality". *Macromolecules* 29 (1996), p. 1278.

[86] P. Welch and M. Muthukumar. "Tuning the Density Profile of Dendritic Polyelectrolytes". *Macromolecules* 31.17 (1998), p. 5892.

[87] S. V. Lyulin, L. J. Evers, P. van der Schoot, A. A. Darinskii, A. V. Lyulin, and M. A. J. Michels. "Effect of Solvent Quality and Electrostatic Interactions on Size and Structure of Dendrimers. Brownian Dynamics Simulation and Mean-Field Theory". *Macromolecules* 37.12 (2004), pp. 3049–3063.

[88] S. V. Lyulin, A. A. Darinskii, A. V. Lyulin, and M. A. J. Michels. "Computer Simulation of the Dynamics of Neutral and Charged Dendrimers". *Macromolecules* 37.12 (2004), pp. 4676–4685.

[89] G. Giupponi and D. M. A. Buzza. "Monte Carlo simulation of dendrimers in variable solvent quality". *J. Chem. Phys.* 120.21 (2004), p. 10290.

[90] H. Lee and R. G. Larson. "Molecular Dynamics Simulations of PAMAM Dendrimer-Induced Pore Formation in DPPC Bilayers with a Coarse-Grained Model". *J. Phys. Chem. B* 110.37 (2006), pp. 18204–18211.

[91] H. Lee and R. G. Larson. "Coarse-grained molecular dynamics studies of the concentration and size dependence of fifth- and seventh-generation PAMAM dendrimers on pore formation in DMPC bilayer". *J. Phys. Chem. B* 112.26 (2008), pp. 7778–7784.

[92] H. Lee and R. G. Larson. "A molecular dynamics study of the structure and interparticle interactions of polyethylene glycol-conjugated PAMAM dendrimers". *J. Phys. Chem. B* 113.40 (2009), pp. 13202–13207.

[93] L. Chong, F. Aydin, and M. Dutt. "Implicit solvent coarse-grained model of polyamidoamine dendrimers: Role of generation and pH". *J. Comput. Chem.* 37.10 (2016), pp. 920–926.

[94] A. A. Gurtovenko, S. V. Lyulin, M. Karttunen, and llpo Vattulainen. "Molecular dynamics study of charged dendrimers in salt-free solution: Effect of counterions". *J. Chem. Phys.* 124 (2006), p. 094904.

[95]    R. Blaak, S. Lehmann, and C. N. Likos. "Charge-Induced Conformational Changes of Dendrimers". *Macromolecules* 41 (2008), pp. 4452–4458.

[96]    P. Carbone and L. Lue. "Prediction of Bulk Density and Molecular Packing in Model Dendrimers with Different Chain Stiffness". *Macromolecules* 43 (2010), pp. 9191–9197.

[97]    S. Huißmann, A. Wynveen, C. N. Likos, and R. Blaak. "The effects of pH, salt and bond stiffness on charged dendrimers". *J. Phys.: Condens. Matter* 22.23 (2010), p. 232101.

[98]    S. Huißmann, A. Wynveen, C. N. Likos, and R. Blaak. "Conformations of high-generation dendritic polyelectrolytes". *J. Mat. Chem.* 20 (2010), pp. 10486–10494.

[99]    W. Tian and Y. Ma. "pH-responsive dendrimers interacting with lipid membranes". *Soft Matter* 8 (2012), p. 2627.

[100]   A. K. Das and P.-Y. Hsiao. "Charged Dendrimers in Trivalent Salt Solutions under the Action of DC Electric Fields". *J. Phys. Chem. B* 118 (2014), pp. 6265–6276.

[101]   P. Welch and M. Muthukumar. "Dendrimer-Polyelectrolyte Complexation: A Model Guest-Host System". *Macromolecules* 33 (2000), p. 6159.

[102]   D. A. Lenz, R. Blaak, and C. N. Likos. "Structural properties of dendrimer-colloid mixtures". *J. Phys.: Condens. Matter* 24 (2012), p. 284119.

[103]   J. S. Kłos and J.-U. Sommer. "Properties of Dendrimers with Flexible Spacer-Chains: A Monte Carlo Study". *Macromolecules* 42 (2009), p. 4878.

[104]   P. K. Maiti, Y. Li, T. Çagin, and W. A. Goddard. "Structure of polyamidoamide dendrimers up to limiting generations: A mesoscale description". *J. Chem. Phys.* 130 (2009), p. 144902.

[105]   W. Tian and Y. Ma. "Coarse-grained molecular simulation of interacting dendrimers". *Soft Matter* 7 (2011), p. 500.

[106]   J. S. Kłos and J.-U. Sommer. "Simulations of Terminally Charged Dendrimers with Flexible Spacer Chains and Explicit Counterions". *Macromolecules* 43.9 (2010), pp. 4418–4427.

[107]  J. S. Kłos and J.-U. Sommer. "Monte Carlo simulations of charged dendrimer-linear polyelectrolyte complexes and explicit counterions". *J. Chem. Phys.* 134 (2011), p. 204902.

[108]  J. S. Kłos and J.-U. Sommer. "Simulations of Neutral and Charged Dendrimers in Solvents of Varying Quality". *Macromolecules* 46 (2013), pp. 3107–3117.

[109]  S. Huißmann, C. N. Likos, and R. Blaak. "Explicit vs Implicit Water Simulations of Charged Dendrimers". *Macromolecules* 45 (2012), p. 2562.

[110]  W. Tian and Y. Ma. "Effects of valences of salt ions at various concentrations on charged dendrimers". *Soft Matter* 6 (2010), p. 1308.

[111]  A. Sousa-Herves et al. "Dendritic polyglycerol sulfate as a novel platform for paclitaxel delivery: pitfalls of ester linkage". *Nanoscale* 7 (2015), pp. 3923–3932.

[112]  J. Vonnemann et al. "Polyglycerolsulfate Functionalized Gold Nanorods as Optoacoustic Signal Nanoamplifiers for In Vivo Bioimaging of Rheumatoid Arthritis". *Theranostics* 4.6 (2014), pp. 629–641.

[113]  J. Dernedde et al. "Dendritic polyglycerol sulfates as multivalent inhibitors of inflammation". *Proc. Natl. Acad. Sci.* 107.46 (2010), pp. 19679–19684.

[114]  X. Xu, Q. Ran, R. Haag, M. Ballauff, and J. Dzubiella. "Charged dendrimers revisited: Effective charge and surface potential of dendritic polyglycerol sulfate". *Macromolecules* 50.12 (2017), pp. 4759–4769.

[I]  R. Nikam, X. Xu, M. Ballauff, M. Kanduč, and J. Dzubiella. "Charge and Hydration Structure of Dendritic Polyelectrolytes: Molecular Simulations of Polyglycerol Sulphate". *Soft Matter* 14.21 (2018), pp. 4300–4310.

[115]  H. Ohshima, T. W. Healy, and L. R. White. "Accurate analytic expressions for the surface charge density/surface potential relationship and double-layer potential distribution for a spherical colloidal particle". *J. Colloid Interface Sci.* 90 (1982), pp. 17–26.

[116]  B. H. Zimm and M. L. Bret. "Counter-Ion Condensation and System Dimensionality". *J. Biomol. Struct. Dyn.* 1 (1983), pp. 461–471.

Bibliography

[117]   L. Belloni, M. Drifford, and P. Turq. "Counterion diffusion in polyelectrolyte solutions". *Chem. Phys.* 83.1-2 (1984), pp. 147–154.

[118]   G. V. Ramanathan. "Counterion condensation in micellar and colloidal solutions". *J. Chem. Phys.* 88.6 (1988), p. 3887.

[119]   R. R. Netz and H. Orland. "Variational charge renormalization in charged systems". *Eur. Phys. J. E* 11.3 (2003), pp. 301–311.

[120]   G. S. Manning. "Counterion Condensation on Charged Spheres, Cylinders, and Planes". *J. Phys. Chem. B* 111.29 (2007), pp. 8554–8559.

[121]   D. A. J. Gillespie, J. E. Hallett, O. Elujoba, A. F. Che Hamzah, R. M. Richardson, and P. Bartlett. "Counterion condensation on spheres in the salt-free limit". *Soft Matter* 10.4 (2014), pp. 566–577.

[122]   F. Carlsson, P. Linse, and M. Malmsten. "Monte Carlo Simulations of Polyelectrolyte–Protein Complexation". *J. Phys. Chem. B* 105.38 (2001), pp. 9040–9049.

[123]   M. Jonsson and P. Linse. "Polyelectrolyte–macroion complexation. I. Effect of linear charge density, chain length, and macroion charge". *J. Chem. Phys.* 115 (2001), p. 3406.

[124]   M. Jonsson and P. Linse. "Polyelectrolyte–macroion complexation. II. Effect of chain flexibility". *J. Chem. Phys.* 115 (2001), p. 10975.

[125]   A. B. Kayitmazer, D. Seeman, B. B. Minsky, P. L. Dubin, and Y. Xu. "Protein–polyelectrolyte interactions". *Soft Matter* 9 (2013), pp. 2553–2583.

[126]   C. Yigit, J. Heyda, M. Ballauff, and J. Dzubiella. "Like-charged protein–polyelectrolyte complexation driven by charge patches". *J. Chem. Phys.* 143 (2015), p. 064905.

[127]   S. Yu et al. "Interaction of Human Serum Albumin with short polyelectrolytes: A study by calorimetry and computer simulation". *Soft Matter* 11 (2015), p. 4630.

[IV]   X. Xu, Q. Ran, P. Dey, R. Nikam, R. Haag, M. Ballauff, and J. Dzubiella. "Counterion-Release Entropy Governs the Inhibition of Serum Proteins by Polyelectrolyte Drugs". *Biomacromolecules* 19.12 (2018), pp. 409–416.

[128]  H. Ohshima. "Donnan potential and surface potential of a spherical soft particle in an electrolyte solution". *J. Colloid Interface Sci.* 323.1 (2008), pp. 92–97.

[129]  E. Trizac, L. Bocquet, and M. Aubouy. "Simple Approach for Charge Renormalization in Highly Charged Macroions". *Phys. Rev. Lett.* 89.24 (2002), p. 248301.

[130]  A. Diehl and Y. Levin. "Effective charge of colloidal particles". *J. Chem. Phys.* 121.23 (2004), pp. 12100–12103.

[131]  D. P. Mascotti and T. M. Lohman. "Thermodynamic extent of counterion release upon binding oligolysines to single-stranded nucleic acids." *Proc. Natl. Acad. Sci.* 87.8 (1990), pp. 3142–3146.

[132]  G. S. Manning and J. Ray. "Counterion Condensation Revisited". *J. Biomol. Struct. Dyn.* 16.2 (1998), pp. 461–476.

[133]  Q. Ran et al. "Interaction of human serum albumin with dendritic polyglycerol sulfate: Rationalizing the thermodynamics of binding". *J. Chem. Phys.* 149.16 (2018), p. 163324.

[134]  X. Xu and M. Ballauff. "Interaction of Lysozyme with a Dendritic Polyelectrolyte: Quantitative Analysis of the Free Energy of Binding and Comparison to Molecular Dynamics Simulations". *J. Phys. Chem. B* 123.39 (2019), pp. 8222–8231.

[135]  E. Barratt, R. J. Bingham, D. J. Warner, C. A. Laughton, S. E. V. Phillips, and S. W. Homans. "Van der Waals Interactions Dominate Ligand–Protein Association in a Protein Binding Site Occluded from Solvent Water". *J. Am. Chem. Soc.* 127.33 (2005), pp. 11827–11834.

[136]  D. H. Leung, R. G. Bergman, and K. N. Raymond. "Enthalpy–Entropy Compensation Reveals Solvent Reorganization as a Driving Force for Supramolecular Encapsulation in Water". *J. Am. Chem. Soc.* 130.9 (2008), pp. 2798–2805.

[137]  P. Setny, R. Baron, and J. A. McCammon. "How can hydrophobic association be enthalpy driven?" *J. Chem. Theory Comput.* 6.9 (2010), pp. 2866–2871.

[138]  R. Baron, P. Setny, and J. A. McCammon. "Water in cavity-ligand recognition". *J. Am. Chem. Soc.* 132.34 (2010), pp. 12091–12097.

[139] J. M. Fox, M. Zhao, M. J. Fink, K. Kang, and G. M. Whitesides. "The Molecular Origin of Enthalpy/Entropy Compensation in Biomolecular Recognition". *Annu. Rev. Biophys.* 47.1 (2018), pp. 223–250.

[140] B. Breiten et al. "Water Networks Contribute to Enthalpy/Entropy Compensation in Protein–Ligand Binding". *J. Am. Chem. Soc.* 135.41 (2013), pp. 15579–15584.

[141] L. Jen-jacobson, L. E. Engler, J. T. Ames, M. R. Kurpiewski, and A. Grigorescu. "Thermodynamic Parameters of Specific and Nonspecific Protein-DNA Binding". *Supramol. Chem.* 12.2 (2000), pp. 143–160.

[142] L. Jen-Jacobson, L. E. Engler, and L. A. Jacobson. "Structural and Thermodynamic Strategies for Site-Specific DNA Binding Proteins". *Structure* 8.10 (2000), pp. 1015–1023.

[143] L. E. Engler, P. Sapienza, L. F. Dorner, R. Kucera, I. Schildkraut, and L. Jen-Jacobson. "The energetics of the interaction of BamHI endonuclease with its recognition site GGATCC11". *J. Mol. Biol.* 307.2 (2001), pp. 619–636.

[144] P. J. Sapienza, T. Niu, M. R. Kurpiewski, A. Grigorescu, and L. Jen-Jacobson. "Thermodynamic and Structural Basis for Relaxation of Specificity in Protein-DNA Recognition". *J. Mol. Biol.* 426.1 (2014), pp. 84–104.

[145] S. Friesen, G. Hefter, and R. Buchner. "Cation Hydration and Ion Pairing in Aqueous Solutions of $MgCl_2$ and $CaCl_2$". *J. Phys. Chem. B* 123.4 (2019), pp. 891–900.

[146] J. F. Da Silva and R. J. P. Williams. *The Biological Chemistry of the Elements: The Inorganic Chemistry of Life.* Oxford University Press, 2001.

[147] R. A. Meyers and R. A. Meyers. *Encyclopedia of Molecular Cell Biology and Molecular Medicine.* Wiley Online Library, 2004.

[148] R. H. Kretsinger, V. N. Uversky, and E. A. Permyakov. *Encyclopedia of Metalloproteins.* Springer, 2013.

[149] D. E. Owens and N. A. Peppas. "Opsonization, biodistribution, and pharmacokinetics of polymeric nanoparticles." *Int. J. Pharm.* 307.1 (2006), pp. 93–102.

Bibliography

[150]  T. Cedervall et al. "Understanding the nanoparticle-protein corona using methods to quantify exchange rates and affinities of proteins for nanoparticles". *Proc. Natl. Acad. Sci.* 104.7 (2007), pp. 2050–2055.

[151]  S. Lindman, I. Lynch, E. Thulin, H. Nilsson, K. A. Dawson, and S. Linse. "Systematic investigation of the thermodynamics of HSA adsorption to N-iso-propylacrylamide/N-tert-butylacrylamide copolymer nanoparticles. Effects of particle size and hydrophobicity." *Nano Lett.* 7.4 (2007), pp. 914–20.

[152]  M. P. Monopoli, C. Åberg, A. Salvati, and K. A. Dawson. "Biomolecular coronas provide the biological identity of nanosized materials". *Nat. Nanotechnol.* 7.12 (2012), pp. 779–786.

[153]  F. Wang, L. Yu, M. P. Monopoli, P. Sandin, E. Mahon, A. Salvati, and K. A. Dawson. "The biomolecular corona is retained during nanoparticle uptake and protects the cells from the damage induced by cationic nanoparticles until degraded in the lysosomes". *Nanomedicine: Nanotechnology, Biology and Medicine* 9.8 (2013), pp. 1159–1168.

[154]  M. C. Lo Giudice, L. M. Herda, E. Polo, and K. A. Dawson. "In situ characterization of nanoparticle biomolecular interactions in complex biological media by flow cytometry". *Nat. Commun.* 7.1 (2016), p. 13475.

[155]  L. Boselli, E. Polo, V. Castagnola, and K. A. Dawson. "Regimes of Biomolecular Ultrasmall Nanoparticle Interactions". *Angew. Chemie Int. Ed.* 56.15 (2017), pp. 4215–4218.

[156]  I. Pochard, A. Foissy, and P. Couchot. "Conductometric and microcalorimetric analysis of the alkaline-earth/alkali-metal ion exchange onto polyacrylic acid". *Colloid Polym. Sci.* 277.9 (1999), pp. 818–826.

[157]  L. Birnhack, O. Keller, S. C. Tang, N. Fridman-Bishop, and O. Lahav. "A membrane-based recycling process for minimizing environmental effects inflicted by ion-exchange softening applications". *Sep. Purif. Technol.* 223.April (2019), pp. 24–30.

[158] Y Kobuchi, H Motomura, Y Noma, and F Hanada. "Application of ion exchange membranes to the recovery of acids by diffusion dialysis". *J. Membr. Sci.* 27.2 (1986), pp. 173–179.

[159] T. Sata. "New applications of ion exchange membranes". *Macromolecules 1992*. VSP Utrecht, 1993, p. 451.

[160] T. Sata, T. Sata, and W. Yang. "Studies on cation-exchange membranes having permselectivity between cations in electrodialysis". *J. Memb. Sci.* 206.1-2 (2002), pp. 31–60.

[161] S. A. Pabit, X. Qiu, J. S. Lamb, L. Li, S. P. Meisburger, and L. Pollack. "Both helix topology and counterion distribution contribute to the more effective charge screening in dsRNA compared with dsDNA". *Nucleic Acids Res.* 37.12 (2009), pp. 3887–3896.

[162] S. A. Pabit, S. P. Meisburger, L. Li, J. M. Blose, C. D. Jones, and L. Pollack. "Counting Ions around DNA with Anomalous Small-Angle X-ray Scattering". *J. Am. Chem. Soc.* 132.46 (2010), pp. 16334–16336.

[163] G. C. Wong and L. Pollack. "Electrostatics of Strongly Charged Biological Polymers: Ion-Mediated Interactions and Self-Organization in Nucleic Acids and Proteins". *Annu. Rev. Phys. Chem.* 61.1 (2010), pp. 171–189.

[164] S. Kirmizialtin, S. A. Pabit, S. P. Meisburger, L. Pollack, and R. Elber. "RNA and Its Ionic Cloud: Solution Scattering Experiments and Atomically Detailed Simulations". *Biophys. J.* 102.4 (2012), pp. 819–828.

[165] J. Ostrowska-Czubenko. "Competitive binding of $Na^+$ and $Ca^{2+}$ ions to teichoic acid analogues". *Colloid Polym. Sci.* 280.11 (2002), pp. 1015–1020.

[166] J. Yoo and A. Aksimentiev. "Competitive Binding of Cations to Duplex DNA Revealed through Molecular Dynamics Simulations". *J. Phys. Chem. B* 116.43 (2012), pp. 12946–12954.

Bibliography

[167] T. J. Robbins, J. D. Ziebarth, and Y. Wang. "Comparison of monovalent and divalent ion distributions around a DNA duplex with molecular dynamics simulation and a Poisson-Boltzmann approach". *Biopolymers* 101.8 (2014). Ed. by J. A. McCammon, pp. 834–848.

[168] M. J. Stevens. "Simple simulations of DNA condensation". *Biophys. J.* 80.1 (2001), pp. 130–139.

[169] A. A. Pais, M. G. Miguel, P. Linse, and B. Lindman. "Polyelectrolytes confined to spherical cavities". *J. Chem. Phys.* 117.3 (2002), pp. 1385–1394.

[170] M. Majtyka and J. Kłos. "Monte Carlo simulations of a charged dendrimer with explicit counterions and salt ions". *Phys. Chem. Chem. Phys.* 9.18 (2007), pp. 2284–2292.

[171] W. D. Tian and Y. Q. Ma. "Molecular dynamics simulations of a charged dendrimer in multivalent salt solution". *J. Phys. Chem. B* 113.40 (2009), pp. 13161–13170.

[172] T. Das, D. Bratko, L. B. Bhuiyan, and C. W. Outhwaite. "Polyelectrolyte solutions containing mixed valency ions in the cell model: A simulation and modified Poisson–Boltzmann study". *J. Chem. Phys.* 107.21 (1997), pp. 9197–9207.

[173] I. Borukhov, D. Andelman, and H. Orland. "Steric effects in electrolytes: A modified Poisson–Boltzmann equation". *Phys. Rev. Lett.* 79.3 (1997), pp. 435–438.

[174] Y. Burak, G. Ariel, and D. Andelman. "Competition between condensation of monovalent and multivalent ions in DNA aggregation". *Curr. Opin. Colloid Interface Sci.* 9.1-2 (2004), pp. 53–58.

[175] P. Biesheuvel and M. van Soestbergen. "Counterion volume effects in mixed electrical double layers". *J. Colloid Interface Sci.* 316.2 (2007), pp. 490–499.

[176] G. Tresset. "Generalized Poisson-Fermi formalism for investigating size correlation effects with multiple ions". *Phys. Rev. E - Stat. Nonlinear, Soft Matter Phys.* 78.6 (2008), pp. 1–9.

[177] P. González-Mozuelos and M. O. de la Cruz. "Ion condensation in salt-free dilute polyelectrolyte solutions". *J. Chem. Phys.* 103.8 (1995), pp. 3145–3157.

[178] A. Kundagrami and M. Muthukumar. "Theory of competitive counterion adsorption on flexible polyelectrolytes: Divalent salts". *J. Chem. Phys.* 128 (2008), p. 244901.

[179] R. Kumar and G. H. Fredrickson. "Theory of polyzwitterion conformations". *J. Chem. Phys.* 131.10 (2009), p. 104901.

[180] I. Kalcher, J. C. F. Schulz, and J. Dzubiella. "Ion-Specific Excluded-Volume Correlations and Solvation Forces". *Phys. Rev. Lett.* 104.9 (2010), p. 097802.

[181] P. S. Kuhn, Y. Levin, and M. C. Barbosa. "Polyelectrolyte solutions with multivalent salts". *Phys. A Stat. Mech. its Appl.* 266.1-4 (1999), pp. 413–419.

[182] S. Gavryushov and P. Zielenkiewicz. "Multivalent Ion Distribution around a Cylindrical Polyion: Contribution of Polarization Effects Due to Difference between Dielectric Properties of the Macromolecule's Interior and the Aqueous Solvent". *J. Phys. Chem. B* 101.5 (1997), pp. 792–797.

[183] A. P. dos Santos, A. Diehl, and Y. Levin. "Colloidal charge renormalization in suspensions containing multivalent electrolyte". *J. Chem. Phys.* 132.10 (2010), p. 104105.

[184] J. Arenzon, J. Stilck, and Y. Levin. "Simple model for attraction between like-charged polyions". *Eur. Phys. J. B* 12.1 (1999), pp. 79–82.

[185] A. Naji, A. Arnold, C. Holm, and R. R. Netz. "Attraction and unbinding of like-charged rods". *Europhys. Lett.* 67.1 (2004), pp. 130–136.

[186] M. Kanduč, A. Naji, and R. Podgornik. "Counterion-mediated weak and strong coupling electrostatic interaction between like-charged cylindrical dielectrics". *J. Chem. Phys.* 132.22 (2010), p. 224703.

[187] N. Adžić and R. Podgornik. "Titratable macroions in multivalent electrolyte solutions: Strong coupling dressed ion approach". *J. Chem. Phys.* 144.21 (2016), p. 214901.

[188] W. D. Cornell et al. "A Second Generation Force Field for the Simulation of Proteins, Nucleic Acids, and Organic Molecules". *J. Am. Chem. Soc.* 117.19 (1995), pp. 5179–5197.

[189]   A. D. MacKerell et al. "All-Atom Empirical Potential for Molecular Modeling and Dynamics Studies of Proteins". *J. Phys. Chem. B* 102.18 (1998), pp. 3586–3616.

[190]   W. F. van Gunsteren et al. "Biomolecular simulation: the GROMOS96 manual and user guide". *Vdf Hochschulverlag AG an der ETH Zürich, Zürich* 86 (1996).

[191]   W. L. Jorgensen and J. Tirado-Rives. "The OPLS [optimized potentials for liquid simulations] potential functions for proteins, energy minimizations for crystals of cyclic peptides and crambin". *J. Am. Chem. Soc.* 110.6 (1988), pp. 1657–1666.

[192]   I. V. Leontyev and A. A. Stuchebrukhov. "Electronic continuum model for molecular dynamics simulations". *J. Chem. Phys.* 130.8 (2009), p. 085102.

[193]   W. L. Ash, M. R. Zlomislic, E. O. Oloo, and D. P. Tieleman. "Computer simulations of membrane proteins". *Biochim. Biophys. Acta - Biomembr.* 1666.1-2 (2004), pp. 158–189.

[194]   I. Nezbeda, F. Moučka, and W. R. Smith. "Recent progress in molecular simulation of aqueous electrolytes: force fields, chemical potentials and solubility". *Mol. Phys.* 114.11 (2016), pp. 1665–1690.

[195]   F. Moučka, I. Nezbeda, and W. R. Smith. "Molecular simulation of aqueous electrolytes: Water chemical potential results and Gibbs-Duhem equation consistency tests". *J. Chem. Phys.* 139.12 (2013), p. 124505.

[196]   Z. Mester and A. Z. Panagiotopoulos. "Mean ionic activity coefficients in aqueous NaCl solutions from molecular dynamics simulations". *J. Chem. Phys.* 142.4 (2015), p. 044507.

[197]   Z. Mester and A. Z. Panagiotopoulos. "Temperature-dependent solubilities and mean ionic activity coefficients of alkali halides in water from molecular dynamics simulations". *J. Chem. Phys.* 143.4 (2015), p. 044505.

[198]   A. Benavides, J. Aragones, and C Vega. "Consensus on the solubility of NaCl in water from computer simulations using the chemical potential route". *J. Chem. Phys.* 144.12 (2016), p. 124504.

[199] M. Kohns, S. Reiser, M. Horsch, and H. Hasse. "Solvent activity in electrolyte solutions from molecular simulation of the osmotic pressure". *J. Chem. Phys.* 144.8 (2016), p. 084112.

[200] A. Kubíčková, T. Křížek, P. Coufal, M. Vazdar, E. Wernersson, J. Heyda, and P. Jungwirth. "Overcharging in Biological Systems: Reversal of Electrophoretic Mobility of Aqueous Polyaspartate by Multivalent Cations". *Phys. Rev. Lett.* 108.18 (2012), p. 186101.

[201] N. Naleem, N. Bentenitis, and P. E. Smith. "A Kirkwood-Buff derived force field for alkaline earth halide salts". *J. Chem. Phys.* 148.22 (2018), p. 222828.

[202] I. S. Joung and T. E. Cheatham. "Determination of Alkali and Halide Monovalent Ion Parameters for Use in Explicitly Solvated Biomolecular Simulations". *J. Phys. Chem. B* 112.30 (2008), pp. 9020–9041.

[203] J. Åqvist. "Ion-water interaction potentials derived from free energy perturbation simulations". *J. Phys. Chem.* 94.21 (1990), pp. 8021–8024.

[204] S. Mamatkulov and N. Schwierz. "Force fields for monovalent and divalent metal cations in TIP3P water based on thermodynamic and kinetic properties". *J. Chem. Phys.* 148.7 (2018).

[205] J. G. Kirkwood and F. P. Buff. "The statistical mechanical theory of solutions. I". *J. Chem. Phys.* 19.6 (1951), pp. 774–777.

[206] P. G. Kusalik and G. N. Patey. "The thermodynamic properties of electrolyte solutions: Some formal results". *J. Chem. Phys.* 86.9 (1987), pp. 5110–5116.

[207] A. P. Lyubartsev and A. Laaksonen. "Osmotic and activity coefficients from effective potentials for hydrated ions". *Phys. Rev. E* 55.5 (1997), pp. 5689–5696.

[208] J. Yoo and A. Aksimentiev. "Improved Parametrization of $Li^+$, $Na^+$, $K^+$, and $Mg^{2+}$ Ions for All-Atom Molecular Dynamics Simulations of Nucleic Acid Systems". *J. Phys. Chem. Lett.* 3.1 (2012), pp. 45–50.

[209] J. Yoo, J. Wilson, and A. Aksimentiev. "Improved model of hydrated calcium ion for molecular dynamics simulations using classical biomolecular force fields". *Biopolymers* 105.10 (2016), pp. 752–763.

[210] H. Yu et al. "Simulating Monovalent and Divalent Ions in Aqueous Solution Using a Drude Polarizable Force Field". *J. Chem. Theory Comput.* 6.3 (2010), pp. 774–786.

[211] J. Huang, P. E. M. Lopes, B. Roux, and A. D. MacKerell. "Recent Advances in Polarizable Force Fields for Macromolecules: Microsecond Simulations of Proteins Using the Classical Drude Oscillator Model". *J. Phys. Chem. Lett.* 5.18 (2014), pp. 3144–3150.

[212] Z. Jing, C. Liu, R. Qi, and P. Ren. "Many-body effect determines the selectivity for Ca 2+ and Mg 2+ in proteins". *Proc. Natl. Acad. Sci.* 115.32 (2018), E7495–E7501.

[213] I. V. Leontyev and A. A. Stuchebrukhov. "Electronic Polarizability and the Effective Pair Potentials of Water". *J. Chem. Theory Comput.* 6.10 (2010), pp. 3153–3161.

[214] I. Leontyev and A. Stuchebrukhov. "Accounting for electronic polarization in non-polarizable force fields". *Phys. Chem. Chem. Phys.* 13.7 (2011), p. 2613.

[215] Y. Luo and B. Roux. "Simulation of Osmotic Pressure in Concentrated Aqueous Salt Solutions". *J. Phys. Chem. Lett.* 1.1 (2010), pp. 183–189.

[216] S. Mamatkulov, M. Fyta, and R. Netz. "Force fields for divalent cations based on single-ion and ion-pair properties". *J. Chem. Phys.* 138.138 (2013), pp. 24505–124507.

[217] S. Mamatkulov, K. F. Rinne, R. Buchner, R. Netz, and D. J. Bonthuis. "Water-separated ion pairs cause the slow dielectric mode of magnesium sulfate solutions". *J. Chem. Phys.* 148.22 (2018), p. 222812.

[218] E. Duboué-Dijon, P. E. Mason, H. E. Fischer, and P. Jungwirth. "Hydration and Ion Pairing in Aqueous $Mg^{2+}$ and $Zn^{2+}$ Solutions: Force-Field Description Aided by Neutron Scattering Experiments and Ab Initio Molecular Dynamics Simulations". *J. Phys. Chem. B* 122.13 (2018), pp. 3296–3306.

[219] J.-P. Hansen and I. R. McDonald. *Theory of Simple Liquids*. Elsevier, 1990.

[220] A. Ben-Naim. *Molecular Theory of Solutions*. Oxford University Press, 2006.

[221] J. E. Mayer. *Equilibrium Statistical Mechanics*. Vol. 1. Elsevier, 2013.

[222] W. G. McMillan Jr and J. E. Mayer. "The statistical thermodynamics of multi-component systems". *J. Chem. Phys.* 13.7 (1945), pp. 276–305.

[223] P. Chaikin and T. Lubensky. *Principles of Condensed Matter Physics*. Vol. 1. Cambridge university press Cambridge, 2000.

[224] D. McQuarrie. *Statistical mechanics*. University Science Books, 2000.

[225] I. Kalcher, J. C. F. Schulz, and J. Dzubiella. "Electrolytes in a nanometer slab-confinement: Ion-specific structure and solvation forces". *J. Chem. Phys.* 133.16 (2010), p. 164511.

[226] D. Ben-Yaakov, D. Andelman, D. Harries, and R. Podgornik. "Beyond standard Poisson–Boltzmann theory: ion-specific interactions in aqueous solutions". *J. Phys. Condens. Matter* 21.42 (2009), p. 424106.

[227] H.-J. Butt, K. Graf, and M. Kappl. *Physics and Chemistry of Interfaces*. John Wiley & Sons, 2013.

[228] W. C. K. Poon and D. Andelman. *Soft Condensed Matter Physics in Molecular and Cell Biology*. Ed. by W. Poon and D. Andelman. CRC Press, 2006.

[229] P Debye and E Hückel. "De la theorie des electrolytes. I. abaissement du point de congelation et phenomenes associes". *Phy. Z.* 24.9 (1923), pp. 185–206.

[230] H. Yukawa. "On the Interaction of Elementary Particles. I". *Proc. Phys. Math. Soc. Jpn.* 17 (1935), p. 48.

Bibliography

[231]  N. Hoffmann, C. N. Likos, and J.-P. Hansen. "Linear screening of the electrostatic potential around spherical particles with non-spherical charge patterns". *Mol. Phys.* 102.9-10 (2004), pp. 857–867.

[232]  R. M. Fuoss, A. Katchalsky, and S. Lifson. "The Potential of an Infinite Rod-Like Molecule and the Distribution of the Counter Ions". *Proc. Natl. Acad. Sci.* 37.9 (1951), pp. 579–589.

[233]  G. S. Manning. "Limiting laws and counterion condensation in polyelectrolyte solutions. I. Colligative Properties". *J. Chem. Phys.* 51.3 (1969), p. 924.

[234]  F. Oosawa. *Polyelectrolytes*. New York: Marcel Dekker, 1971, p. 158.

[235]  E. Trizac and G. Téllez. "Onsager-Manning-Oosawa Condensation Phenomenon and the Effect of Salt". *Phys. Rev. Lett.* 96.3 (2006), p. 038302.

[236]  M. L. Bret and B. H. Zimm. "Distribution of counterions around a cylindrical polyelectrolyte and Manning's condensation theory". *Biopolymers* 23.2 (1984), pp. 287–312.

[237]  T. Alfrey, P. W. Berg, and H. Morawetz. "The counterion distribution in solutions of rod-shaped polyelectrolytes". *J. Polym. Sci. Part B Polym. Phys.* 34.3 (1996), pp. 395–399.

[238]  G. S. Manning. "The critical onset of counterion condensation: A survey of its experimental and theoretical basis". *Berichte der Bunsengesellschaft für Phys. Chemie* 100.6 (1996), pp. 909–922.

[239]  M. Deserno, C. Holm, and S. May. "Fraction of Condensed Counterions around a Charged Rod: Comparison of Poisson–Boltzmann Theory and Computer Simulations". *Macromolecules* 33.1 (2000), pp. 199–206.

[240]  G. S. Manning. "Counterion condensation theory constructed from different models". *Phys. A Stat. Mech. its Appl.* 231.1-3 (1996), pp. 236–253.

[241]  A. V. Dobrynin and M. Rubinstein. "Counterion Condensation and Phase Separation in Solutions of Hydrophobic Polyelectrolytes". *Macromolecules* 34.6 (2001), pp. 1964–1972.

[242]  A. Deshkovski, S. Obukhov, and M. Rubinstein. "Counterion Phase Transitions in Dilute Polyelectrolyte Solutions". *Phys. Rev. Lett.* 86.11 (2001), pp. 2341–2344.

[243]  M. J. Stevens and K. Kremer. "Structure of salt-free linear polyelectrolytes". *Phys. Rev. Lett.* 71.14 (1993), pp. 2228–2231.

[244]  J. Barrat and J. Joanny. "Theory of polyelectrolyte solutions". *Adv. Chem. Phys.* 94 (1996), pp. 1–66.

[245]  G. V. Ramanathan. "Statistical mechanics of electrolytes and polyelectrolytes. III. The cylindrical Poisson–Boltzmann equation". *J. Chem. Phys.* 78.6 (1983), pp. 3223–3232.

[246]  A. Diehl and Y. Levin. "Statistics versus dynamics: two methods for calculating the effective charge of colloidal particles". *J. Phys. Condens. Matter* 17.45 (2005), S3309–S3316.

[247]  S. Gavryushov and P. Linse. "Effective interaction potentials for alkali and alkaline earth metal ions in SPC/E water and prediction of mean ion activity coefficients". *J. Phys. Chem. B* 110.22 (2006), pp. 10878–10887.

[248]  J. Perkyns and B. M. Pettitt. "A site–site theory for finite concentration saline solutions". *J. Chem. Phys.* 97.10 (1992), pp. 7656–7666.

[249]  I. Kalcher and J. Dzubiella. "Structure-thermodynamics relation of electrolyte solutions". *J. Chem. Phys.* 130.13 (2009), p. 134507.

[250]  E. J. W. Verwey. "Theory of the Stability of Lyophobic Colloids". *J. Phys. Chem.* 51.3 (1947), pp. 631–636.

[251]  F. Donnan. "Theorie der Membrangleichgewichte und Membranpotentiale bei Vorhandensein von nicht dialysierenden Elektrolyten. Ein Beitrag zur physikalisch-chemischen Physiologie." *Zeitschrift für Elektrochemie und Angewandte Physikalische Chemie* 17.14 (1911), pp. 572–581.

[252]  F. G. Donnan. "The Theory of Membrane Equilibria." *Chem. Rev.* 1.1 (1924), pp. 73–90.

[253]   A. Philipse and A. Vrij. "The Donnan equilibrium: I. On the thermodynamic foundation of the Donnan equation of state". *J. Phys. Condens. Matter* 23.19 (2011), p. 194106.

[254]   C. Yigit, N. Welsch, M. Ballauff, and J. Dzubiella. "Protein sorption to charged microgels: Characterizing binding isotherms and driving forces". *Langmuir* 28.40 (2012), pp. 14373–14385.

[255]   M Volmer and P Mahnert. "Über die Auflösung fester Körper in Flüssigkeitsoberflächen und die Eigenschaften der dabei entstehenden Schichten". *Z. Phys. Chem.* 115.1 (1925), pp. 239–252.

[256]   R. I. Masel. *Principles of Adsorption and Reaction on Solid Surfaces*. Vol. 3. John Wiley & Sons, 1996.

[257]   P. W. Atkins and J. De Paula. *Physical Chemistry*. W. H. Freeman and Company, 2010.

[258]   M. Gilson and H.-X. Zhou. "Calculation of Protein-Ligand Binding Affinities". *Annu. Rev. Biophys.* 36.1 (2007), pp. 21–42.

[259]   I. J. General. "A Note on the Standard State's Binding Free Energy". *J. Chem. Theory Comput.* 6.8 (2010), pp. 2520–2524.

[260]   D. Van Der Spoel, E. Lindahl, B. Hess, G. Groenhof, A. E. Mark, and H. J. Berendsen. "GROMACS: fast, flexible, and free". *J. Comput. Chem.* 26.16 (2005), pp. 1701–1718.

[261]   B. Hess, C. Kutzner, D. Van Der Spoel, and E. Lindahl. "GROMACS 4: algorithms for highly efficient, load-balanced, and scalable molecular simulation". *J. Chem. Theory Comput.* 4.3 (2008), pp. 435–447.

[262]   S. Pronk et al. "GROMACS 4.5: a high-throughput and highly parallel open source molecular simulation toolkit". *Bioinformatics* (2013), btt055.

[263]  S. Pall, M. J. Abraham, C. Kutzner, B. Hess, and E. Lindahl. "Tackling exascale software challenges in molecular dynamics simulations with GROMACS". *International Conference on Exascale Applications and Software*. Springer. 2014, pp. 3–27.

[264]  H. A. Lorentz. "Über die Anwendung des Satzes vom Virial in der kinetischen Theorie der Gase". *Ann. Phys.* 248.1 (1881), pp. 127–136.

[265]  B. Hess, H. Bekker, H. J. C. Berendsen, and J. G. E. M. Fraaije. "LINCS: A Linear Constraint Solver for Molecular Simulations". *J. Comput. Chem.* 18.12 (1997), pp. 1463–1472.

[266]  R. A. Lippert et al. "A common, avoidable source of error in molecular dynamics integrators". *J. Chem. Phys.* 126.4 (2007), p. 046101.

[267]  D. Van Der Spoel and P. J. van Maaren. "The origin of layer structure artifacts in simulations of liquid water". *J. Chem. Theory Comput.* 2.1 (2006), pp. 1–11.

[268]  S. Cheluvaraja and H. Meirovitch. "Stability of the free and bound microstates of a mobile loop of $\alpha$-amylase obtained from the absolute entropy and free energy". *J. Chem. Theory Comput.* 4.1 (2008), pp. 192–208.

[269]  H. J. Berendsen, J. v. Postma, W. F. van Gunsteren, A. DiNola, and J. R. Haak. "Molecular dynamics with coupling to an external bath". *J. Chem. Phys.* 81.8 (1984), pp. 3684–3690.

[270]  S. Nosé. "A molecular dynamics method for simulations in the canonical ensemble". *Mol. Phys.* 52.2 (1984), pp. 255–268.

[271]  W. G. Hoover. "Canonical dynamics: Equilibrium phase-space distributions". *Phys. Rev. A* 31.3 (1985), p. 1695.

[272]  H. C. Andersen. "Molecular dynamics simulations at constant pressure and/or temperature". *J. Chem. Phys.* 72.4 (1980), pp. 2384–2393.

[273]  G. Bussi, D. Donadio, and M. Parrinello. "Canonical sampling through velocity rescaling". *J. Chem. Phys.* 126.1 (2007), p. 014101.

[274] M. Parrinello and A. Rahman. "Polymorphic transitions in single crystals: A new molecular dynamics method". *J. Appl. Phys.* 52.12 (1981), pp. 7182–7190.

[275] S. Nosé and M. Klein. "Constant pressure molecular dynamics for molecular systems". *Mol. Phys.* 50.5 (1983), pp. 1055–1076.

[276] T. Darden, D. York, and L. Pedersen. "Particle mesh Ewald: An N. log (N) method for Ewald sums in large systems". *J. Chem. Phys.* 98.12 (1993), pp. 10089–10092.

[277] U. Essmann, L. Perera, M. L. Berkowitz, T. Darden, H. Lee, and L. G. Pedersen. "A smooth particle mesh Ewald method". *J. Chem. Phys.* 103.19 (1995), pp. 8577–8593.

[278] P. G. Kusalik and I. M. Svishchev. "The spatial structure in liquid water". *Science* 265.5176 (1994), pp. 1219–1221.

[279] J. W. Gibbs. *The Collected Works of J. Willard Gibbs-Volume 1: Thermodynamics*. Yale University Press, 1945.

[280] F. P. Buff. "The spherical interface. I. Thermodynamics". *J. Chem. Phys.* 19.12 (1951), pp. 1591–1594.

[281] V. A. Parsegian, R. P. Rand, and D. C. Rau. "[3] Macromolecules and water: Probing with osmotic stress". *Methods Enzymol.* Vol. 259. Elsevier, 1995, pp. 43–94.

[282] R. Defay, A. Bellemans, and I. Prigogine. "Surface tension and adsorption" (1966).

[283] B Widom. "Remarks on the Gibbs adsorption equation and the van der Waals, Cahn-Hilliard theory of interfaces". *Physica A* 95.1 (1979), pp. 1–11.

[284] V. Parsegian, R. Rand, and D. Rau. "Osmotic stress, crowding, preferential hydration, and binding: a comparison of perspectives". *Proc. Natl. Acad. Sci. U.S.A.* 97.8 (2000), pp. 3987–3992.

[285] S. Toxvaerd. "Statistical mechanical and quasithermodynamic calculations of surface densities and surface tension". *Mol. Phys.* 26.1 (1973), pp. 91–99.

[286] F. M. Floris. "Nonideal effects on the excess volume from small to large cavities in TIP4P water". *J. Phys. Chem. B* 108.41 (2004), pp. 16244–16249.

# Bibliography

[287]  F. M. Floris. "Effect of increasing pressure on excess volumes for cavities in TIP4P water". *J. Mol. Liq.* 222 (2016), pp. 38–46.

[288]  A. Y. Ben-Naim. *Statistical Thermodynamics for Chemists and Biochemists*. Springer Science & Business Media, 2013.

[289]  D. Ben-Amotz, F. O. Raineri, and G. Stell. "Solvation thermodynamics: theory and applications". *J. Phys. Chem. B* 109.14 (2005), pp. 6866–6878.

[290]  D. E. Smith, L. Zhang, and A. Haymet. "Entropy of association of methane in water: a new molecular dynamics computer simulation". *J. Am. Chem. Soc.* 114.14 (1992), pp. 5875–5876.

[291]  S. Lüdemann, R. Abseher, H. Schreiber, and O. Steinhauser. "The temperature-dependence of hydrophobic association in water. pair versus bulk hydrophobic interactions". *J. Am. Chem. Soc.* 119.18 (1997), pp. 4206–4213.

[292]  S. Shimizu and H. S. Chan. "Temperature dependence of hydrophobic interactions: A mean force perspective, effects of water density, and nonadditivity of thermodynamic signatures". *J. Chem. Phys.* 113.11 (2000), pp. 4683–4700.

[293]  R. O. Dror et al. "Pathway and mechanism of drug binding to G-protein-coupled receptors". *Proc. Natl. Acad. Sci.* 108.32 (2011), pp. 13118–13123.

[294]  D. E. Shaw et al. "Atomic-level characterization of the structural dynamics of proteins". *Science* 330.6002 (2010), pp. 341–346.

[295]  P. L. Freddolino, A. S. Arkhipov, S. B. Larson, A. McPherson, and K. Schulten. "Molecular dynamics simulations of the complete satellite tobacco mosaic virus". *Structure* 14.3 (2006), pp. 437–449.

[296]  P. C. Whitford, S. C. Blanchard, J. H. Cate, and K. Y. Sanbonmatsu. "Connecting the kinetics and energy landscape of tRNA translocation on the ribosome". *PLOS Comput. Biol.* 9.3 (2013), e1003003.

[297]  J. A. Lemkul, J. Huang, B. Roux, and A. D. MacKerell. "An Empirical Polarizable Force Field Based on the Classical Drude Oscillator Model: Development History and Recent Applications". *Chem. Rev.* 116.9 (2016), pp. 4983–5013.

[298] M. Karplus and J. A. McCammon. "Molecular dynamics simulations of biomolecules". *Nat. Struct. Mol. Biol.* 9.9 (2002), p. 646.

[299] G. Hummer, L. R. Pratt, and A. E. Garcia. "Free energy of ionic hydration". *J. Phys. Chem.* 100.4 (1996), pp. 1206–1215.

[300] M. Vener, I. Leontyev, Y. A. Dyakov, M. Basilevsky, and M. Newton. "Application of the linearized MD approach for computing equilibrium solvation free energies of charged and dipolar solutes in polar solvents". *J. Phys. Chem. B* 106.50 (2002), pp. 13078–13088.

[301] M. Kohagen, P. E. Mason, and P. Jungwirth. "Accurate Description of Calcium Solvation in Concentrated Aqueous Solutions". *J. Phys. Chem. B* 118.28 (2014), pp. 7902–7909.

[302] A. Saxena and D. Sept. "Multisite ion models that improve coordination and free energy calculations in molecular dynamics simulations". *J. Chem. Theory Comput.* 9.8 (2013), pp. 3538–3542.

[303] C. Oostenbrink, A. Villa, A. E. Mark, and W. F. Van Gunsteren. "A biomolecular force field based on the free enthalpy of hydration and solvation: the GROMOS force-field parameter sets 53A5 and 53A6". *J. Comput. Chem.* 25.13 (2004), pp. 1656–1676.

[304] L. X. Dang and D. E. Smith. "Comment on "Mean force potential for the calcium–chloride ion pair in water"[J. Chem. Phys. 99, 4229 (1993)]". *J. Chem. Phys.* 102.8 (1995), pp. 3483–3484.

[305] P. Bjelkmar, P. Larsson, M. A. Cuendet, B. Hess, and E. Lindahl. "Implementation of the CHARMM force field in GROMACS: analysis of protein stability effects from correction maps, virtual interaction sites, and water models". *J. Chem. Theory Comput.* 6.2 (2010), pp. 459–466.

[306] F Bruni, S Imberti, R Mancinelli, and M. Ricci. "Aqueous solutions of divalent chlorides: ions hydration shell and water structure". *J. Chem. Phys.* 136.6 (2012), p. 064520.

[307] M. Pavlov, P. E. M. Siegbahn, and M. Sandström. "Hydration of Beryllium, Magnesium, Calcium, and Zinc Ions Using Density Functional Theory". *J. Phys. Chem. A* 102.1 (1998), pp. 219–228.

[308] E. Pluhařová, P. E. Mason, and P. Jungwirth. "Ion Pairing in Aqueous Lithium Salt Solutions with Monovalent and Divalent Counter-Anions". *J. Phys. Chem. A* 117.46 (2013), pp. 11766–11773.

[309] G. A. Kaminski, H. A. Stern, B. Berne, and R. A. Friesner. "Development of an accurate and robust polarizable molecular mechanics force field from ab initio quantum chemistry". *J. Phys. Chem. A* 108.4 (2004), pp. 621–627.

[310] S. Patel, A. D. Mackerell Jr, and C. L. Brooks III. "CHARMM fluctuating charge force field for proteins: II protein/solvent properties from molecular dynamics simulations using a nonadditive electrostatic model". *J. Comput. Chem.* 25.12 (2004), pp. 1504–1514.

[311] G. Lamoureux, E. Harder, I. V. Vorobyov, B. Roux, and A. D. MacKerell Jr. "A polarizable model of water for molecular dynamics simulations of biomolecules". *Chem. Phys. Lett.* 418.1-3 (2006), pp. 245–249.

[312] P. E. Lopes, J. Huang, J. Shim, Y. Luo, H. Li, B. Roux, and A. D. MacKerell Jr. "Polarizable force field for peptides and proteins based on the classical drude oscillator". *J. Chem. Theory Comput.* 9.12 (2013), pp. 5430–5449.

[313] J. W. Ponder et al. "Current status of the AMOEBA polarizable force field". *J. Phys. Chem. B* 114.8 (2010), pp. 2549–2564.

[314] A. G. Donchev et al. "Assessment of performance of the general purpose polarizable force field QMPFF3 in condensed phase". *J. Comput. Chem.* 29.8 (2008), pp. 1242–1249.

[315] A. Donchev, V. Ozrin, M. Subbotin, O. Tarasov, and V. Tarasov. "A quantum mechanical polarizable force field for biomolecular interactions". *Proc. Natl. Acad. Sci.* 102.22 (2005), pp. 7829–7834.

[316]  P. E. Mason, E. Wernersson, and P. Jungwirth. "Accurate Description of Aqueous Carbonate Ions: An Effective Polarization Model Verified by Neutron Scattering". *J. Phys. Chem. B* 116.28 (2012), pp. 8145–8153.

[317]  S. Kmiecik, D. Gront, M. Kolinski, L. Wieteska, A. E. Dawid, and A. Kolinski. "Coarse-grained protein models and their applications". *Chem. Rev.* 116.14 (2016), pp. 7898–7936.

[318]  H. I. Ingólfsson, C. A. Lopez, J. J. Uusitalo, D. H. de Jong, S. M. Gopal, X. Periole, and S. J. Marrink. "The power of coarse graining in biomolecular simulations". *Wiley Interdiscip. Rev. Comput. Mol. Sci.* 4.3 (2014), pp. 225–248.

[319]  M. J. Boniecki et al. "SimRNA: a coarse-grained method for RNA folding simulations and 3D structure prediction". *Nucleic Acids Res.* 44.7 (2016), e63–e63.

[320]  D. A. Potoyan, A. Savelyev, and G. A. Papoian. "Recent successes in coarse-grained modeling of DNA". *Wiley Interdiscip. Rev. Comput. Mol. Sci.* 3.1 (2013), pp. 69–83.

[321]  R. Baron, D. Trzesniak, A. H. de Vries, A. Elsener, S. J. Marrink, and W. F. van Gunsteren. "Comparison of Thermodynamic Properties of Coarse-Grained and Atomic-Level Simulation Models". *ChemPhysChem* 8.3 (2007), pp. 452–461.

[322]  C. A. López, A. J. Rzepiela, A. H. De Vries, L. Dijkhuizen, P. H. Hünenberger, and S. J. Marrink. "Martini coarse-grained force field: extension to carbohydrates". *J. Chem. Theory Comput.* 5.12 (2009), pp. 3195–3210.

[323]  K. R. Hadley and C. McCabe. "Coarse-grained molecular models of water: a review". *Mol. Simulat.* 38.8-9 (2012), pp. 671–681.

[324]  M. Pierce, C. Raman, and B. Nall. "Isothermal titration calorimetry of protein–protein interactions". *Methods* 19.2 (1999), pp. 213–221.

[325]  X. Xu and J. Dzubiella. "Probing the protein corona around charged macromolecules : interpretation of isothermal titration calorimetry by binding models and computer simulations". *Colloid Polym. Sci.* 298 (2020), pp. 747–759.

[326] J. Wang, R. M. Wolf, J. W. Caldwell, P. A. Kollman, and D. A. Case. "Development and testing of a general amber force field". *J. Comput. Chem.* 25.9 (2004), pp. 1157–1174.

[327] J. Wang, W. Wang, P. A. Kollman, and D. A. Case. "Automatic atom type and bond type perception in molecular mechanical calculations". *J. Mol. Graphics Modell.* 25.2 (2006), pp. 247–260.

[328] A. Jakalian, D. B. Jack, and C. I. Bayly. "Fast, efficient generation of high-quality atomic charges. AM1-BCC model: II. Parameterization and validation". *J. Comput. Chem.* 23.16 (2002), pp. 1623–1641.

[329] J. Wang, W. Wang, P. A. Kollman, and D. A. Case. "Antechamber: an accessory software package for molecular mechanical calculations". *J. Am. Chem. Soc.* 222 (2001), U403.

[330] E. F. Pettersen, T. D. Goddard, C. C. Huang, G. S. Couch, D. M. Greenblatt, E. C. Meng, and T. E. Ferrin. "UCSF Chimera—a visualization system for exploratory research and analysis". *J. Comput. Chem.* 25.13 (2004), pp. 1605–1612.

[331] H. Berendsen, J. Grigera, and T. Straatsma. "The missing term in effective pair potentials". *J. Phys. Chem.* 91.24 (1987), pp. 6269–6271.

[332] B. Hess, H. Bekker, H. J. Berendsen, J. G. Fraaije, et al. "LINCS: a linear constraint solver for molecular simulations". *J. Comput. Chem.* 18.12 (1997), pp. 1463–1472.

[333] S. Huißmann, A. Wynveen, C. N. Likos, and R. Blaak. "The effects of pH, salt and bond stiffness on charged dendrimers". *J. Phys.: Condens. Matter* 22.23 (2010), p. 232101.

[334] S. Huißmann, C. N. Likos, and R. Blaak. "Conformations of high-generation dendritic polyelectrolytes". *J. Mater. Chem.* 20.46 (2010), pp. 10486–10494.

[335] J. Kłos and J.-U. Sommer. "Simulations of terminally charged dendrimers with flexible spacer chains and explicit counterions". *Macromolecules* 43.9 (2010), pp. 4418–4427.

Bibliography

[336]  J. Kłos and J.-U. Sommer. "Simulations of neutral and charged dendrimers in solvents of varying quality". *Macromolecules* 46.8 (2013), pp. 3107–3117.

[337]  Y. Zhang and Z. Xu. "Atomic radii of noble gas elements in condensed phases". *Am. Mineral.* 80.7-8 (1995), pp. 670–675.

[338]  Q. R. Huang, P. L. Dubin, C. N. Moorefield, and G. R. Newkome. "Counterion Binding on Charged Spheres: Effect of pH and Ionic Strength on the Mobility of Carboxyl-Terminated Dendrimers". *J. Phys. Chem. B* 104 (2000), pp. 898–904.

[339]  D. J. Tobias and J. C. Hemminger. "Getting specific about specific ion effects". *Science* 319.5867 (2008), pp. 1197–1198.

[340]  R. Zangi. "Can salting-in/salting-out ions be classified as chaotropes/kosmotropes?" *J. Phys. Chem. B* 114.1 (2009), pp. 643–650.

[341]  K. D. Collins and M. W. Washabaugh. "The Hofmeister effect and the behaviour of water at interfaces". *Q. Rev. Biophys* 18.4 (1985), pp. 323–422.

[342]  Y. Zhang and P. S. Cremer. "Interactions between macromolecules and ions: the Hofmeister series". *Curr. Opin. Chem. Biol.* 10.6 (2006), pp. 658–663.

[343]  W. Kunz. "Specific ion effects in colloidal and biological systems". *Curr. Opin. Colloid In.* 15.1-2 (2010), pp. 34–39.

[344]  J. Shelley, K. Watanabe, and M. L. Klein. "Simulation of a sodium dodecylsulfate micelle in aqueous solution". *Int. J. Quantum Chem.* 38.S17 (1990), pp. 103–117.

[345]  X. Tang, P. H. Koenig, and R. G. Larson. "Molecular Dynamics Simulations of Sodium Dodecyl Sulfate Micelles in Water - The Effect of the Force Field". *J. Phys. Chem. B* 118 (2014), pp. 3864–3880.

[346]  D. A. Evans. "History of the Harvard ChemDraw Project". *Angew. Chem. Int. Ed.* 53.42 (2014), pp. 11140–11145.

[347]  D. Beglov and B. Roux. "Finite representation of an infinite bulk system: Solvent boundary potential for computer simulations". *J. Chem. Phys.* 100.12 (1994), pp. 9050–9063.

[348] C. S. Babu and C. Lim. "Empirical Force Fields for Biologically Active Divalent Metal Cations in Water". *J. Phys. Chem. A* 110.2 (2006), pp. 691–699.

[349] D. A. Pearlman et al. "AMBER, a package of computer programs for applying molecular mechanics, normal mode analysis, molecular dynamics and free energy calculations to simulate the structural and energetic properties of molecules". *Comput. Phys. Commun.* 91.1-3 (1995), pp. 1–41.

[350] D. Horinek, S. I. Mamatkulov, and R. R. Netz. "Rational design of ion force fields based on thermodynamic solvation properties". *J. Chem. Phys.* 130.12 (2009), p. 124507.

[351] M. Fyta, I. Kalcher, J. Dzubiella, L. Vrbka, and R. R. Netz. "Ionic force field optimization based on single-ion and ion-pair solvation properties". *J. Chem. Phys.* 132.2 (2010), p. 024911.

[352] M. Fyta and R. R. Netz. "Ionic force field optimization based on single-ion and ion-pair solvation properties: Going beyond standard mixing rules". *J. Chem. Phys.* 136.12 (2012), p. 124103.

[353] K. M. Callahan, N. N. Casillas-Ituarte, M. Roeselova", H. C. Allen, and D. J. Tobias. "Solvation of Magnesium Dication: Molecular Dynamics Simulation and Vibrational Spectroscopic Study of Magnesium Chloride in Aqueous Solutions". *J. Phys. Chem. A* 114.15 (2010), pp. 5141–5148.

[354] D. V. Sakharov and C. Lim. "Zn Protein Simulations Including Charge Transfer and Local Polarization Effects". *J. Am. Chem. Soc.* 127.13 (2005), pp. 4921–4929.

[355] M. Soniat, L. Hartman, and S. W. Rick. "Charge Transfer Models of Zinc and Magnesium in Water". *J. Chem. Theory Comput.* 11.4 (2015), pp. 1658–1667.

[356] T. Martinek et al. "Calcium ions in aqueous solutions: Accurate force field description aided by ab initio molecular dynamics and neutron scattering". *J. Chem. Phys.* 148.22 (2018), p. 222813.

[357] D. Aryal and V. Ganesan. "Diffusivity of Mono-and Divalent Salts and Water in Polyelectrolyte Desalination Membranes". *J Phys Chem B* 122.33 (2018), pp. 8098–8110.

[II]    R. Nikam, X. Xu, M. Kanduč, and J. Dzubiella. "Competitive sorption of monovalent and divalent ions by highly charged globular macromolecules". *J. Chem. Phys.* 153.4 (2020), p. 044904.

[358]   P. J. Basser and A. J. Grodzinsky. "The Donnan model derived from microstructure". *Biophys. Chem.* 46.1 (1993), pp. 57–68.

[359]   A. Moncho-Jordá and J. Dzubiella. "Swelling of ionic microgel particles in the presence of excluded-volume interactions: a density functional approach". *Phys. Chem. Chem. Phys.* 18.7 (2016), pp. 5372–5385.

[360]   S. Ahualli, A. Martín-Molina, and M. Quesada-Pérez. "Excluded volume effects on ionic partitioning in gels and microgels: a simulation study". *Phys. Chem. Chem. Phys.* 16.46 (2014), pp. 25483–25491.

[361]   J. N. Israelachvili. *Intermolecular and Surface Forces*. 2nd ed. Academic Press London; San Diego, 1991.

[362]   A. W. Adamson and A. P. Gast. *Physical Chemistry of Surfaces*. Vol. 15. Interscience New York, 1967.

[363]   I. Borukhov, D. Andelman, and H. Orland. "Adsorption of large ions from an electrolyte solution: A modified Poisson–Boltzmann equation". *Electrochim. Acta* 46.2-3 (2000), pp. 221–229.

[364]   M Eigen and E Wicke. "The thermodynamics of electrolytes at higher concentration". *J. Phys. Chem.* 58.9 (1954), pp. 702–714.

[365]   V. Kralj-Iglič and A Iglič. "A Simple Statistical Mechanical Approach to the free Energy of the Electric Double Layer Including the Excluded Volume Effect". *J. Phys. II* 6.4 (1996), pp. 477–491.

[366]   N. Cuvillier, M. Bonnier, F. Rondelez, D. Paranjape, M. Sastry, and P. Ganguly. "Adsorption of multivalent ions on charged Langmuir monolayers". *Prog. Colloid Polym. Sci.* 105.1 (1997), pp. 118–125.

[367] R. Chudoba, J. Heyda, and J. Dzubiella. "Tuning the collapse transition of weakly charged polymers by ion-specific screening and adsorption". *Soft Matter* 14.47 (2018), pp. 9631–9642.

[368] A. Moncho-Jordá and I. Adroher-Benítez. "Ion permeation inside microgel particles induced by specific interactions: From charge inversion to overcharging". *Soft Matter* 10.31 (2014), pp. 5810–5823.

[369] E. R. A. Lima, D. Horinek, R. R. Netz, E. C. Biscaia, F. W. Tavares, W. Kunz, and M. Boström. "Specific Ion Adsorption and Surface Forces in Colloid Science". *J. Phys. Chem. B* 112.6 (2008), pp. 1580–1585.

[370] P. Koelsch et al. "Specific ion effects in physicochemical and biological systems: Simulations, theory and experiments". *Colloids Surfaces A Physicochem. Eng. Asp.* 303.1-2 (2007), pp. 110–136.

[371] H. I. Okur et al. "Beyond the Hofmeister series: Ion-specific effects on proteins and their biological functions". *J. Phys. Chem. B* 121.9 (2017), pp. 1997–2014.

[372] P. Lo Nostro and B. W. Ninham. "Hofmeister phenomena: An update on ion specificity in biology". *Chem. Rev.* 112.4 (2012), pp. 2286–2322.

[373] N. Schwierz, D. Horinek, and R. R. Netz. "Anionic and cationic hofmeister effects on hydrophobic and hydrophilic surfaces". *Langmuir* 29.8 (2013), pp. 2602–2614.

[374] S.-w. W. Chen and B. Honig. "Monovalent and Divalent Salt Effects on Electrostatic Free Energies Defined by the Nonlinear Poisson–Boltzmann Equation: Application to DNA Binding Reactions". *J. Phys. Chem. B* 101.44 (1997), pp. 9113–9118.

[375] I. Rouzina and V. A. Bloomfield. "Competitive electrostatic binding of charged ligands to polyelectrolytes: practical approach using the non-linear Poisson–Boltzmann equation". *Biophys. Chem.* 64.1-3 (1997), pp. 139–155.

[376] V. K. Misra, K. A. Sharp, R. A. Friedman, and B. Honig. "Salt Effects on Ligand-DNA Binding". *J. Mol. Biol.* 238.2 (1994), pp. 245–263.

[377] M. D. Paulsen, B. Richey, C. F. Anderson, and M. Record. "The salt dependence of the preferential interaction coefficient in dna solutions as determined by grand canonical monte carlo simulations". *Chem. Phys. Lett.* 139.5 (1987), pp. 448–452.

[378] I. Rouzina and V. A. Bloomfield. "Competitive Electrostatic Binding of Charged Ligands to Polyelectrolytes: Planar and Cylindrical Geometries". *J. Phys. Chem.* 100.10 (1996), pp. 4292–4304.

[379] J. D. McGhee and P. H. von Hippel. "Theoretical aspects of DNA-protein interactions: Co-operative and non-co-operative binding of large ligands to a one-dimensional homogeneous lattice". *J. Mol. Biol.* 86 (1974), pp. 469–489.

[380] P. Flory. "Molecular configuration of polyelectrolytes". *J. Chem. Phys.* 21.1 (1953), pp. 162–163.

[381] E. Raphael and J. F. Joanny. "Annealed and quenched polyelectrolytes". *EPL* 13.7 (1990), pp. 623–628.

[382] R. A. G. Friedman and G. S. Manning. "Polyelectrolyte effects on site-binding equilibria with application to the intercalation of drugs into DNA". *Biopolymers* 23.12 (1984), pp. 2671–2714.

[383] R. H. Stokes and R. A. Robinson. "Ionic Hydration and Activity in Electrolyte Solutions". *J. Am. Chem. Soc.* 70.5 (1948), pp. 1870–1878.

[384] Y. Marcus and G. Hefter. "Ion Pairing". *Chem. Rev.* 106.11 (2006), pp. 4585–4621.

[385] Y. Yao, M. L. Berkowitz, and Y. Kanai. "Communication: Modeling of concentration dependent water diffusivity in ionic solutions: Role of intermolecular charge transfer". *J. Chem. Phys.* 143.24 (2015), p. 241101.

[386] E. Trizac, L. Bocquet, M. Aubouy, and H. H. von Grünberg. "Alexander's Prescription for Colloidal Charge Renormalization". *Langmuir* 19.9 (2003), pp. 4027–4033.

[387] F. T. Wall and J. Berkowitz. "Numerical Solution to the Poisson-Boltzmann Equation for Spherical Polyelectrolyte Molecules". *J. Chem. Phys.* 26.1 (1957), pp. 114–122.

[388]    D. Harries, R. Podgornik, V. A. Parsegian, E. Mar-Or, and D. Andelman. "Ion in-
        duced lamellar-lamellar phase transition in charged surfactant systems". *J. Chem.
        Phys.* 124.22 (2006), p. 224702.

[389]    J. Kierzenka and L. F. Shampine. "A BVP solver based on residual control and the
        Maltab PSE". *ACM Transactions on Mathematical Software* 27.3 (2001), pp. 299–
        316.

[390]    S. Yu et al. "Interaction of human serum albumin with short polyelectrolytes: a
        study by calorimetry and computer simulations". *Soft Matter* 11 (2015), pp. 4630–
        4639.

[391]    D. Boris and M. Rubinstein. "A Self-Consistent Mean Field Model of a Starburst
        Dendrimer: Dense Core vs Dense Shell". *Macromolecules* 29.22 (1996), pp. 7251–
        7260.

[392]    I. Berndt, J. S. Pedersen, and W. Richtering. "Temperature-Sensitive Core–Shell
        Microgel Particles with Dense Shell". *Angew. Chemie Int. Ed.* 45.11 (2006), pp. 1737–
        1741.

[393]    R. J. Hunter. *Foundations of Colloid Science.* Oxford University Press, Oxford,
        2001.

[394]    D. Matulis, I. Rouzina, and V. A. Bloomfield. "Thermodynamics of DNA binding
        and condensation: isothermal titration calorimetry and electrostatic mechanism".
        *J. Mol. Biol.* 296.4 (2000), pp. 1053–1063.

[395]    C. G. Sinn, R. Dimova, and M. Antonietti. "Isothermal Titration Calorimetry of
        the Polyelectrolyte/Water Interaction and Binding of $Ca^{2+}$: Effects Determining
        the Quality of Polymeric Scale Inhibitors". *Macromolecules* 37.9 (2004), pp. 3444–
        3450.

[396]    B. W. Sigurskjold. "Exact Analysis of Competition Ligand Binding by Displace-
        ment Isothermal Titration Calorimetry". *Anal. Biochem.* 277.2 (2000), pp. 260–
        266.

[397] I. Jelesarov and H. R. Bosshard. "Isothermal titration calorimetry and differential scanning calorimetry as complementary tools to investigate the energetics of biomolecular recognition". *J. Mol. Recognit.* 12.1 (1999), pp. 3–18.

[398] A. Velázquez Campoy and E. Freire. "ITC in the post-genomic era... ? Priceless". *Biophys. Chem.* 115.2-3 (2005), pp. 115–124.

[399] J. B. Chaires. "Calorimetry and Thermodynamics in Drug Design". *Annu. Rev. Biophys.* 37.1 (2008), pp. 135–151.

[400] R. Lumry and S. Rajender. "Enthalpy-entropy compensation phenomena in water solutions of proteins and small molecules: A ubiquitous property of water". *Biopolymers* 9.12 (1970), pp. 1557–1559.

[401] J.-H. Ha, R. S. Spolar, and M. Record. "Role of the hydrophobic effect in stability of site-specific protein-DNA complexes". *J. Mol. Biol.* 209.4 (1989), pp. 801–816.

[402] G. Klebe. "Applying thermodynamic profiling in lead finding and optimization". *Nat. Rev. Drug Discov.* 14.2 (2015), pp. 95–110.

[403] Q. Ran, X. Xu, J. Dzubiella, R. Haag, and M. Ballauff. "Thermodynamics of the Binding of Lysozyme to a Dendritic Polyelectrolyte: Electrostatics Versus Hydration". *ACS Omega* 3.8 (2018), pp. 9086–9095.

[404] R. Haag, A. Sunder, and J.-F. Stumbé. "An Approach to Glycerol Dendrimers and Pseudo-Dendritic Polyglycerols". *J. Am. Chem. Soc.* 122.12 (2000), pp. 2954–2955.

[405] F. Paulus et al. "Structure related transport properties and cellular uptake of hyperbranched polyglycerol sulfates with hydrophobic cores". *Polym. Chem.* 5.17 (2014), pp. 5020–5028.

[406] H. Türk, R. Haag, and S. Alban. "Dendritic Polyglycerol Sulfates as New Heparin Analogues and Potent Inhibitors of the Complement System". *Bioconjug. Chem.* 15.1 (2004), p. 162.

[407] C. I. Bayly, P. Cieplak, W. Cornell, and P. A. Kollman. "A well-behaved electrostatic potential based method using charge restraints for deriving atomic charges: the RESP model". *J. Phys. Chem.* 97.40 (1993), pp. 10269–10280.

[408] P. Cieplak, W. D. Cornell, C. Bayly, and P. A. Kollman. "Application of the multimolecule and multiconformational RESP methodology to biopolymers: Charge derivation for DNA, RNA, and proteins". *J. Comput. Chem.* 16.11 (1995), pp. 1357–1377.

[409] O. Stern. "The theory of the electrolytic double-layer". *Z. Elektrochem* 30.508 (1924), pp. 1014–1020.

[410] D. Henderson. "Recent progress in the theory of the electric double layer". *Prog. Surf. Sci.* 13.3 (1983), pp. 197–224.

[411] R. Kjellander and S. Marcelja. "Double-layer interaction in the primitive model and the corresponding Poisson–Boltzmann description". *J. Phys. Chem.* 90.7 (1986), pp. 1230–1232.

# Acknowledgements

I would like to first acknowledge the fact that my four years of scientific journey would not have commenced and continued without the profound and everlasting support by my supervisor *Prof. Dr. Joachim Dzubiella.* I am forever indebted and thankful to him for believing in my potential and welcoming me to his group in Berlin, offering a meticulous and thorough help in science with an optimistic viewpoint, his scientific intuition fueled with rich expertise, pragmatism and experience, and for harbouring a healthy and friendly scientific and social environment for a fruitful discourse.

I owe special thanks to *Prof. Dr. Matthias Ballauff* for a continuous experimental cooperation, for productive scientific discussions motivated by his endless curiosity in my research work and for witty and joyful conversations.

I am forever thankful to *Won Kyu Kim, Xiao Xu, Karol Palczynski, Matej Kanduč, Richard Chudoba* and *Victor Ruiz López* for their wealth of knowledge and scientific expertise, offering me useful perspectives and for the memorable and enjoyable social discussions. My stay in their presence was a deep learning experience that will bring abundant value to my future life and career prospects.

I would like to thank all the members of the soft matter theory group, especially my former office colleagues *Mila Miletić, Chanbum Park* and *Holger-Dietrich Saßnick* for a wonderful time in the group. Also thanks to *Jacek Walkowiak* who I had a pleasure collaborating with and for sharing the experimental data with me.

Finally, I would like to express my deepest gratitude towards my family in India, for understanding my aspirations and for the limitless support and care. I dedicate this thesis to my father and mother.